Numerical Investigation of Stratified Thermal Storage Tank Applied in Adsorption Heat Pump Cycle

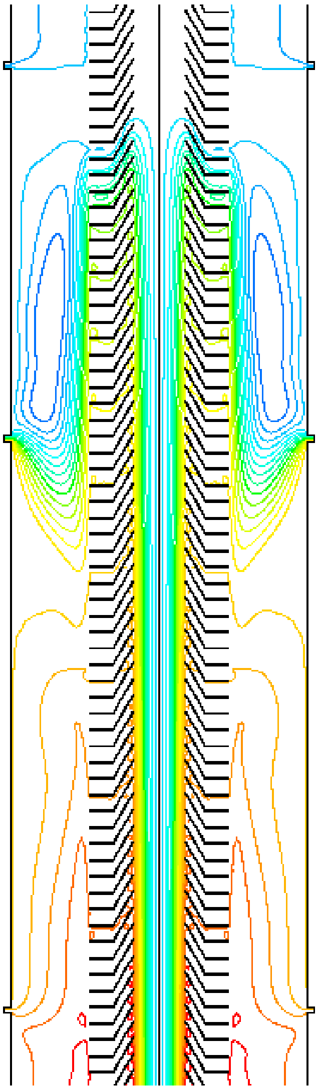

Karlsruhe 2014

Cover page: Streamlines of the charging process of TES with inlet stratification pipe for 0.2 kg/s charging mass flow rate after 32 seconds

Numerical Investigation of Stratified Thermal Storage Tank Applied in Adsorption Heat Pump Cycle

Zur Erlangung des akademischen Grades

Doktor der Ingenieurwissenschaften

der Fakultät für Maschinenbau

Karlsruher Institut für Technologie (KIT)

genehmigte
Dissertation
von

M. Sc. Hadi Taheri

Tag der mündlichen Prüfung: 07.05.2014

Hauptreferent: Prof. Dr.-Ing. Martin Gabi

Korreferenten: Prof. Dr. rer. nat. Hans-Martin Henning
Dr. rer. nat. Ferdinand Schmidt

Abstract

The current thesis contributes to the detailed numerical study of the charging process of thermal storage tank applied in adsorption heat pump cycle.

With the aid of the stratified thermal storage in the adsorption heat pump cycle, the released heat during the adsorption half cycle can be stored and be reused during the desorption half cycle. On account of this heat recovery concept, the COP (Coefficient of Performance) of the adsorption heat pump or cooling machine system can be improved.

Different geometrical variations of the stratified storage tank, different geometrical variations of stratification device, and various charging temperatures and charging mass flow rates have been investigated thoroughly by means of multitude of CFD simulations in order to analyze the influential parameters on the thermal stratification. Richardson number as a dimensionless number, which describes the importance of buoyancy forces against mixing forces, has been analyzed for selected simulations. The simulation results of a reference CFD model have been compared with corresponding experimental results.

The effective thermal conductivity during the charging process of the stratified thermal storage tank is studied based on two different points of view. The first one is the advection or macroscopic point of view, which considers the fluid bulk motion, and the next refers to turbulent diffusion or microscopic point of view, which focuses on the molecular motions in the fluid flow.

In another section of the present work, the porous medium impact on the mixing process and turbulence during the charging of thermal storage tank has been studied numerically.

To sum up, this study explores different charging systems used in thermal storage tank which is combined with adsorption heat pump cycle. The main aim of the study is to analyze the relevant instruments and conditions in order to reduce the mixing process in thermal storage tank and thereby a better stratification in storage tank, which improves the COP of the whole system.

Zusammenfassung

Die vorliegende Arbeit untersucht verschiedene Schichtbeladeeinheiten unter unterschiedlichen Ladebedingungen und geometrische Variationen von thermischen Schichtspeichern.

Mit Hilfe des thermischen Schichtspeichers im Adsorptionswärmepumpen-Zyklus kann die freigesetzte Wärme während des Adsorptionshalbzyklus gespeichert werden und während des Desorptionshalbzyklus wiederverwendet werden. Aufgrund dieses Wärmerückgewinnungskonzeptes kann die Effizienz des Adsorptionswärmepumpensystems oder Kältemaschinensystems verbessert werden.

Verschiedene Beladungsmassenströme, Temperaturdifferenzen zwischen der Beladungsströmung und dem Fluid im Inneren des Tanks sowie verschiedene Speichermedien wurden in einer Vielzahl von CFD Simulationen untersucht, um die wesentlichen Parameter der thermischen Schichtung zu ermitteln. Die Richardson-Zahl als dimensionslose Kennzahl, die die Wichtigkeit der Auftriebskräfte gegenüber den Mischungskräften beschreibt, wurde für ausgewählte Simulationen analysiert. Die Simulationsergebnisse von einigen ausgewählten Simulationen wurden mit experimentellen Ergebnissen verglichen.

In einem weiteren Teil der Arbeit wurde die effektive Wärmeleitfähigkeit der Strömung während des Beladungsprozesses als bedeutende Strömungsgröße berechnet, die den Wärmeübertragungsprozess während des Be- und Entladungsprozesses des Schichtspeichers beschreibt.

Bei der Berechnung der effektiven Wärmeleitfähigkeit wurden zwei unterschiedliche Gesichtsspunkte berücksichtigt. Einer von ihnen ist die Diffusion bzw. der mikroskopische Teil, der den Turbulenzteil der effektiven Wärmeleitfähigkeit betrachtet, und der andere ist die Advektion bzw. der makroskopische Teil, der die makroskopische Strömung in Betracht zieht.

Der Schwerpunkt eines weiteren Abschnitts der Arbeit fokussiert sich auf den Einfluss von porösen Medien auf die Mischvorgänge der Strömung im Beladungsprozess des thermischen Schichtsspeichers.

Zusammengefasst konzentriert sich die vorliegende Arbeit vor allem auf die numerische Untersuchung der verschiedenen Beladungsysteme für den Wärmespeichertank verbunden mit einem Adsorptionswärmepumpen-Zyklus. Die Untersuchung hat zum Ziel, mögliche Instrumente und Bedingungen zur Reduzierung des Mischungseffektes der Strömung zu analysieren und damit eine bessere Schichtung und eine höhere Systemeffizienz zu erreichen.

Acknowledgements

The current thesis have been completed during my Ph. D. study from June 2009 until May 2014.

I would like to sincerely thank Prof. Martin Gabi for giving me the opportunity to join his numerical research group in institute of fluid machinery, as well as supervising, mentoring and examining of my dissertation.

I would like to express my special thank to Dr. Ferdinand Schmidt, who supervised my thesis and provided a dedicated scientific support during my Ph. D. study. I am grateful and honored to have your assistance over the last years.

My special gratitude to Prof. Hans-Martin Henning for reviewing and co-examination of my thesis.

I am particularly grateful to Dr. Balazs Pritz for his valuable guidance and discussion for completion of this thesis.

I am very grateful to Dr. Franco Magagnato and Dr. Iris Pantle for their constructive support during some part of my dissertation.

I also thank all of my colleagues in institute of fluid machinery. I appreciate your guidance and detailed advice during these years. I have enjoyed our discussions and nice coffee time.

My parents have been a major source of lateral support over the whole of my educational life. I extend my special thanks to you and my sisters. I fully appreciate your encouragement, endorsement and support during the whole of my education until the successful completion of Ph. D. thesis.

I want to express my gratitude to Karlsruhe Institute of Technology for proving me the scholarship (Rektorstipendium) in order to financing my residence in Karlsruhe.

Many thanks to all my friends. I can’t list all of your names, but you know that I am grateful of you for your laugh, advice, kind conversation and encouragement especially during the challenging times over last years.

Karlsruhe, 13.05.2014

Contents

Nomenclature

Symbols

A	$[m^2]$	Surface area
a	$[-]$	Slope at the entrance of the stratification pipe opening channel
a_p	$[-]$	Center coefficient in residual equation
a_{nb}	$[-]$	Influence coefficients for the neighboring cells in residual equation
a^*	$[-]$	Turbulent viscosity damping coefficient for lower Reynolds number
b	$[-]$	Constant part of the source term in residual equation
b	$[-]$	Slope at the middle of the stratification pipe opening channel
C	$\left[\frac{J}{kg\cdot K}\right]$	Specific heat
C	$[-]$	Constant coefficient of $k-\varepsilon$ turbulence model
C_p	$\left[\frac{J}{kg\cdot K}\right]$	Specific heat at constant pressure
C_u	$[-]$	Turbulent viscosity coefficient
C_i	$[m^{-1}]$	Inertial resistance coefficient in momentum source equation
c	$[-]$	Vertical distance between opening channels of stratification pipe
D	$[-]$	Cross-diffusion term in SST $k-\omega$ turbulence model
d	$[m]$	Diameter
d_c	$[m]$	Hydraulic pore diameter in porous medium
d_e	$[m]$	Equivalent particle diameter in porous medium
E	$[J/kg]$	Specific total energy
e	$[J/kg]$	Specific internal energy
G	$[-]$	Generation term
g	$[m/s^2]$	Gravitational acceleration
H	$[m]$	Storage tank height
H_{max}	$[m]$	Maximun reaching point of flow in the stratification pipe

H_p	$[m]$	Vertical distance of the channel profile of the stratification pipe
k	$\left[\frac{W}{m \cdot K}\right]$	Thermal conductivity
k	$[m^2/s^2]$	Turbulent kinetic energy
L	$[m]$	Length scale
l	$[m]$	Length; characteristic length
N	$[-]$	Grid number
P	$[Pa]$	Pressure
Pe	$[-]$	Peclet number
Pr	$[-]$	Prandtl number
Q	$[J]$	Heat energy
Q	$[m^3/s]$	Volumetric flow rate
$\dot{q}$	$[W]$	Heat transfer rate
R	$[-]$	Scaled residual of the general variable ϕ
Re	$[-]$	Reynolds number
Ri	$[-]$	Richardson number
S	$[-]$	Source term
S_h	$[W/m^3]$	Volumetric heat source
S_{ij}	$[s^{-1}]$	Mean strain rate tensor
S_v	$[m^{-1}]$	Specific surface of the particle per unit volume in porous medium
T	$[K]$	Temperature
t	$[s]$	Time
U	$[m/s]$	Velocity scale
u	$[m/s]$	Velocity
u, v, w	$[m/s]$	Velocity components
u_τ	$[m/s]$	Friction velocity

V	$[m^3]$	Volume
V_c	$[m^3]$	Average pore volume
V_0	$[m^3]$	Body volume of the porous medium
V_v	$[m^3]$	Void volume of the porous medium
Y	$[-]$	Dissipation term
y^+	$[-]$	Dimensionless wall distance
x, y, z	$[m]$	Coordinates

Greek symbols

ρ	$[kg/m^3]$	Density
μ	$\left[\frac{kg}{m\cdot s}\right]$	Dynamic viscosity
ν	$\left[\frac{m^2}{s}\right]$	Kinematic viscosity
λ	$[-]$	pipe friction factor
γ	$\left[\frac{kg}{m\cdot s}\right]$	Second viscosity
δ_{ij}	$[-]$	Kronecker symbol
β	$[K^{-1}]$	Thermal expansion coefficient
ζ	$[-]$	Resistance coefficient
ϵ	$\left[\frac{m^2}{s}\right]$	Thermal diffusivity
Γ	$\left[\frac{m^2}{s}\right]$	Diffusion coefficient; Effective diffusivity
ε	$\left[\frac{m^2}{s^3}\right]$	Turbulent kinetic energy dissipation rate
τ	$[Pa]$	Shear stress
ΔT	$[K]$	Temperature difference
Δt	$[s]$	Time step
R_{ij}	$[Pa]$	Reynolds stress tensor

ω	$[s^{-1}]$	Turbulent kinetic energy specific dissipation rate
α	$[m^2]$	Permeability
ε	$\left[\frac{m^2}{s}\right]$	Eddy diffusivity
σ	$[-]$	Turbulent Prandtl number for turbulent variables
β	$[m^{-1}]$	Inertial resistance coefficient
η	$[-]$	Porosity of porous medium
τ_{ij}	$[Pa]$	Deviatoric stress tensor
ϕ	$[-]$	General variable
Φ	$\left[\frac{kg}{m \cdot s^3}\right]$	Dissipation function in energy equation

Subscripts

av	Average value
b	Buoyancy
$bottom$	Bottom of the storage tank
$cond$	Condenser
$conv$	Convection
$cooler$	Cooler
$cool$	Cooling machine
cs	Cross section
dl	Dimensionless
e	Specific internal energy
eff	Effective
ev	Evaporator
f	Fluid phase
$heater$	Heater
$heat$	Heat pump

hor	Horizontal
in	Inlet
$init$	Initial
k	Turbulent kinetic energy
M	Momentum
m	Field average value
nb	Neighboring cells
p	Porous medium; Pore
ref	Reference
r	Radial component
s	Porous medium skeleton; solid medium, static
str	Stratification device
T	Thermal
top	Top of the storage tank
t	Turbulent
w	Wall
x	Axial component
ϕ	Fluid variable
ε	Turbulent kinetic energy dissipation rate
ω	Turbulent kinetic energy specific dissipation rate
$3D$	Three Dimensional

Superscripts

$\bar{\phi}$	Mean value; time averaged component
$\acute{\phi}$	Fluctuating component
$\vec{\phi}$	Vector
$\dot{\phi}$	Time derivative

Abbreviations

BOS	Background Oriented Schlieren
COP	Coefficient of Performance
CFD	Computational Fluid Dynamics
DNS	Direct Numerical Simulation
LES	Large Eddy Simulation
PIV	Particle Image Velocimetry
$RANS$	Reynolds Averaged Navier-Stokes Equation
SGS	Subgrid-Scale
TES	Thermal energy storage
UDF	User defined function
1-D	One Dimensional
2-D	Two Dimensional
lpm	Liter per minute
rke	Realizable $k-\varepsilon$ turbulence model
RNG_ke	Renormalization Group $k-\varepsilon$ turbulence model
sst_k-omega	Shear stress transport $k-\omega$ turbulence model
s	Second

1 Introduction

1.1 Motivation

Energy efficiency of numerous systems with thermal storage tank is considerably influenced by thermal stratification. Thermal stratification is an issue resulted from separation of hot and cold storage medium. The separation of the hot and cold regions occurs as a result of buoyancy forces during charging and discharging operations [1]. Achieving a better stratification in the storage tank lies in the minimization of the mixing effect. Thermal stratification results from the gravity and density difference in the storage tank, which is due to the temperature gradient. The factors influencing the thermal stratification are as follows:

- Mixing effect at the inlet and outlet ports
- Heat loss to environment
- Conductive heat transfer because of temperature gradients in the fluid
- Charging mass flow rate

The mixing mechanism is controlled by thermal buoyancy and convective mixing [2]. Different parameters have some indirect influences on the thermal stratification by affecting the above mentioned factors. For example, the inlet and outlet ports position impact the stratification by controlling the convective mixing at the inlet and outlet ports. The nature of that mixing is dependent on the momentum of the inlet jet as well as the direction of the buoyancy force [3]. The flow vorticity, which is associated with the flow circulation and turbulent mixing, is another parameter influencing the mixing at the inlet and thereby the stratification. Analysis of the thermal stratification in the thermal storage tank is an important issue aiming to improve the energy efficiency, especially in solar thermal systems. In the present work, the thermal storage tank is considered to be applied in an adsorption heat pump system for heat recovery between adsorption and desorption half cycles. By utilization of the stratified storage in the adsorption heat pump system and storing of released heat during the adsorption half cycle until its reuse during the desorption half cycle, the COP (Coefficient of Performance) of the adsorption heat pump or cooling machine can be improved [4]. The main motivation for the numerical simulation of the thermal storage tank coupled with adsorption heat pump unit lies in the deep understanding of the process in the stratified storage and parameters study in order to achieve higher system COP. To reduce the mixing effect at the inlet port, different stratification charging devices are presented. One of the stratification devices patented and marketed by the German company Sailer GmbH & Co KG has been studied numerically and experimentally in a dissertation in Stuttgart university [5].

1.2 Thesis Overview

The present thesis investigates different stratification charging devices at various charging conditions and geometrical designs of the storage tank. Different charging mass flow rates, temperature differences between the charging flow and initial temperature inside of the tank, and different storage fluids are applied in a variety of simulations to explore the influencing parameters on the thermal stratification. Simulation results of some selected geometrical designs have been compared using available experimental findings. In another part of the thesis, effective thermal conductivity as a significant flow variable is computed which describes the heat transfer process in the storage tank charging and discharging. In computation of effective thermal conductivity, two different points of view are taken into account. One of them is diffusion point of view representing the turbulence part of the effective thermal conductivity and the other one is convection point of view dealing with the bulk flow motion. The focus of another section of the work is on porous medium impact investigation on the mixing decrement in the storage tank charging process. To sum up, the current thesis concentrates mainly on the examination of different charging systems for thermal storage tank applied in adsorption heat pump cycle and possible tools and conditions aiming to reduce the mixing effect and achieve better stratification.

2 Adsorption Heat Pump Cycle

2.1 Adsorption Module

The adsorption module includes the following main parts:

-Adsorber

Adsorber is a kind of heat exchanger with the task of heat transfer between the fluid flow in channel and sorption material.

-Evaporator

Evaporator is a heat exchanger that absorbs the heat through evaporation process. This process produces some useful cooling effects when applying the system as a cooling machine.

-Condenser

Condenser is a heat exchanger which releases the heat through condensing process. This process produces some useful heating effects when the system is employed as a heat pump.

-Housing, Pipe Installation, and Valves

During the adsorption and desorption, different valves are opened, and the working fluid can flow between the condenser, evaporator, and adsorber.

The underlying process of any adsorption cycle consists basically of two phases, the regeneration phase and the adsorption phase [6]. During the desorption, a high temperature driving heat desorbs the working fluid from the adsorbent. The condensation of desorbed working fluid in condenser releases heat at medium temperature. During the adsorption, the evaporated working fluid is adsorbed by adsorbent, which releases heat at medium temperature. The evaporation process is performed by a low temperature heat, which provides a useful cold in the case of cooling machine.

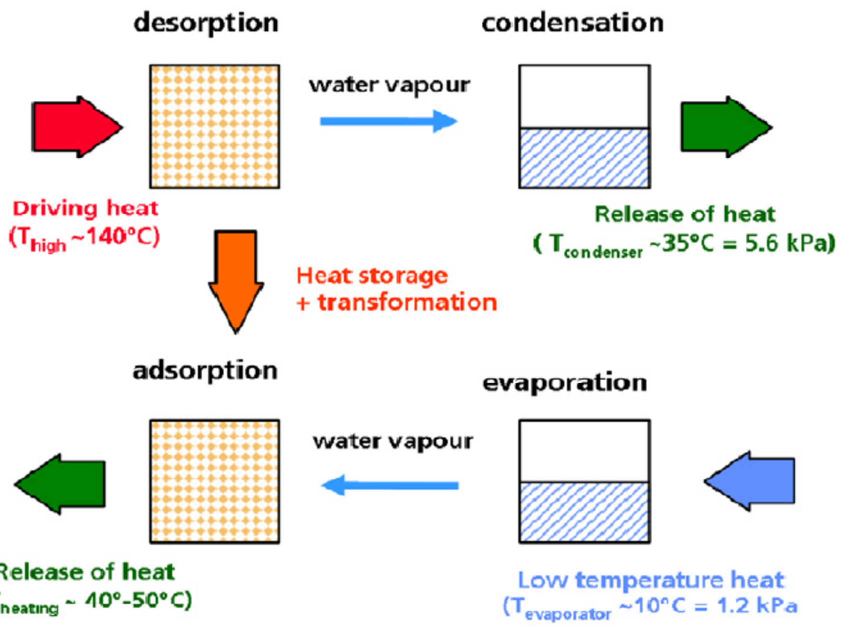

Figure 2.1: Schematic representation of adsorption process [6]

2.2 Thermal Storage Tank Coupled with Adsorption Heat Pump Cycle

The main potential of the present work is the development of the thermally-driven heat pumps and cooling machine in order to achieve more energy efficient system. Higher energy efficiency of the system lies on increasing the COP (coefficient of performance) of the thermally-driven heat pump and better system integration. By means of coupled system of thermal stratified storage tank with adsorption heat pump (stratisorp) the COP of the system can be improved. In this context, a patent has been arranged, which has an adsorption heat pump including at least one adsorber and one heat storage [7]. The whole adsorption heat pump system consists of the adsorption module and thermal storage tank with charging and discharging devices, heater cycle, and cooler cycle. The fluid flow leaving the storage tank absorbs or releases the heat in the adsorber and returns back to the storage tank again.

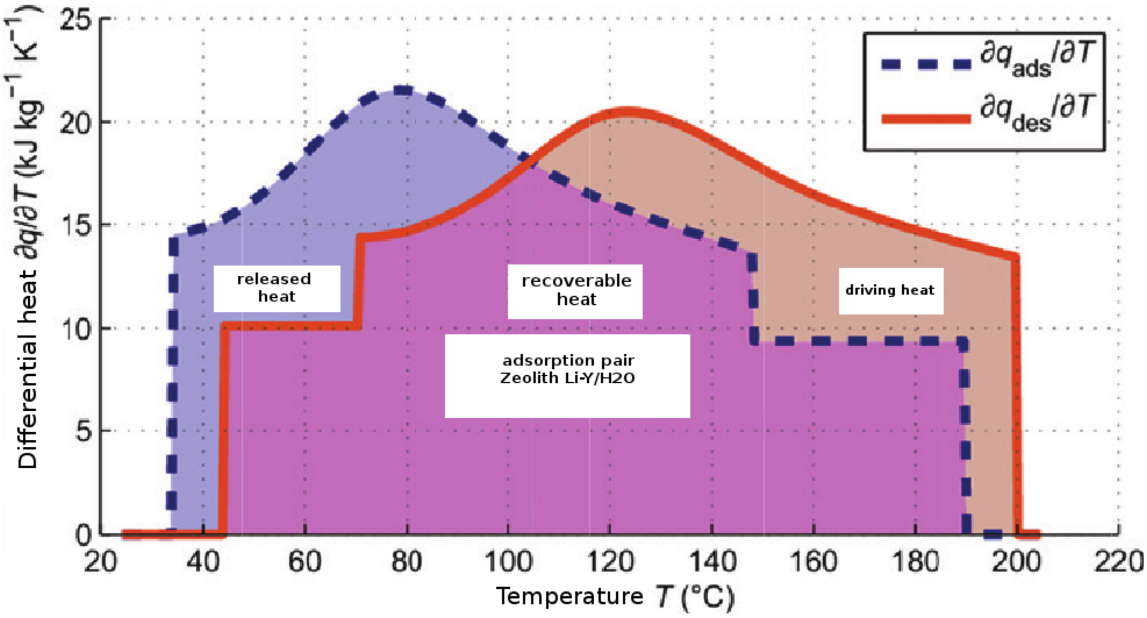

Figure 2.2: Differential heat graph for adsorption pair Zeolith Li-Y/H2O [8]

The integral of the differential desorption heat represents the heat, which is required during the desorption. Figure 2.2 demonstrates the recoverable heat between adsorption and desorption half cycles. The integral of the differential adsorption heat curve as a function of temperature represents the released heat during the adsorption and the integral of the differential desorption heat curve as a function of temperature represents the driving heat during the desorption. The development potential of the adsorption heat pump bases upon the internal heat recovery between adsorption and desorption processes.

During the adsorption, the fluid with lower temperature is taken from the relevant position in stratified storage tank and returns to the storage tank with higher temperature after absorption of released heat in adsorber. During the desorption, the fluid with higher temperature is taken from the relevant position in stratified storage tank and after releasing the heat in adsorber returns to the storage tank with lower temperature. In other words, during the adsorption, the adsorber releases the heat and then is cooled down; consequently, the adsorption material is adsorbed causing the system pressure reduction. During the desorption, adsorber will be heated up and the adsorption material will be desorbed leading to the system pressure raise.

In the ideal stratified storage tank model with plug flow charging, during adsorption phase the cold fluid layer is taken from corresponding layer in the tank and after receiving heat in adsorber, will be stored at the position of fluid layer with the same temperature in the tank. During the desorption, hot fluid layer is taken from the corresponding layer in the tank and after providing heat for adsorber returns back to the tank with lower temperature and is stored at the level with the same temperature. The timescale of an Adsorption heat pump full cycle in reality can be from 10 to 30 minutes. During this time, the adjusted boundary conditions for storage tank change continuously due to the coupling with adsorber components. Therefore, in CFD simulation, the whole process in storage tank should be simulated in an unsteady simulation, and the boundary conditions for CFD model should be changed during the cycle by means of coupled system model and storage tank CFD model. In CFD simulation, a selected part of the storage tank charging process with a specified charging flow rate and temperature has been simulated in transient way with very small time steps from 0.1 to 0.2 second.

Adsorption heat pump cycle is a periodic cycle, which means the storage tank experiences the similar situation during different cycles. The boundary condition is changed by each switching in adsorption system, before reaching a steady state situation. The process during the cycle is unsteady but the process by the end of the cycles as a whole is steady state (cyclic steady state).

The function of heater cycle is defined as provider of a part of the desorption heat, which is not covered from the released heat during of adsorption half cycle. The heat transfer fluid is extracted at the level of the heater position (heater outlet in CFD model) and after heating up, will be inserted at the top of the tank.

The function of cooler in this application is defined as a heat sink. The cooler cycle absorbs part of the released heat during the adsorption that will not be used for the desorption half cycle. This part of the heat can be used as part of useful heat in heat pump system. The heat transfer fluid is extracted at the level of cooler position (cooler outlet in CFD model) and after being cooled down will be inserted at the bottom of the tank. The COP of the system in case of heat pump and cooling machine can be defined as follows,

$$COP_{heat} = \frac{Q_{cooler}+Q_{cond}}{Q_{heater}} \tag{2.1}$$

$$COP_{cool} = \frac{Q_{ev}}{Q_{heater}} \tag{2.2}$$

The Figure 2.3 and 2.4 represent the schematic model of the storage tank coupled with the adsorption module during the adsorption and desorption half cycles [9].

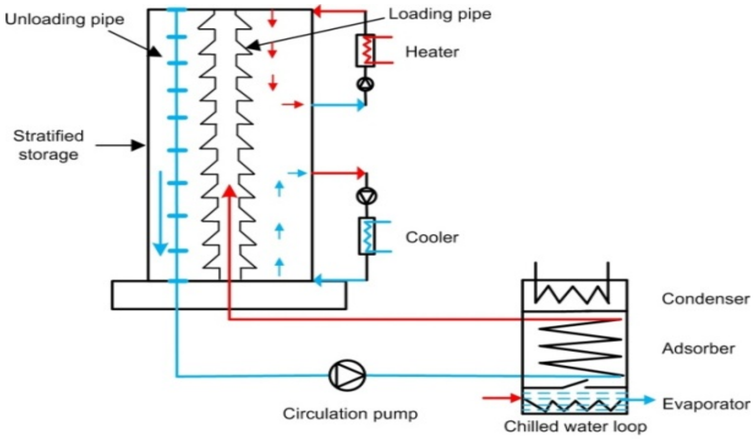

Figure 2.3: Schematic model of the storage tank coupled with adsorption module during the adsorption

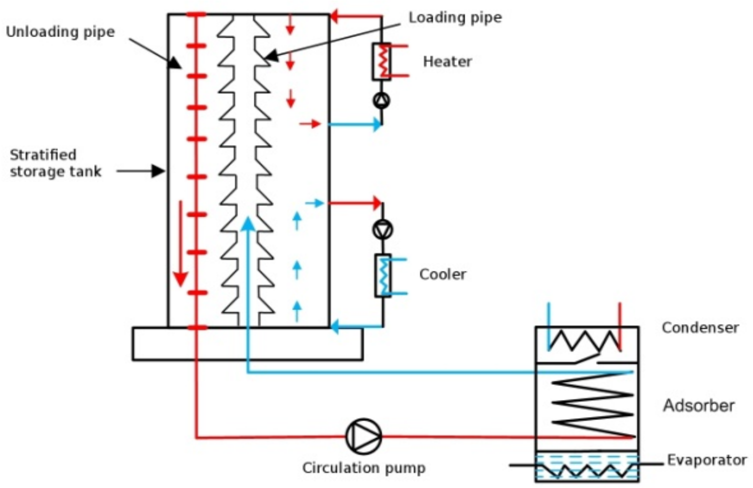

Figure 2.4: Schematic model of the storage tank coupled with adsorption module during the desorption

Mixing in the tank can affect the system COP by influencing the heater, cooler, and condenser heat. Due to mixing in the lower part of the tank, the extracted heat transfer fluid at the heater position is colder than the extracted fluid in well stratified tank. Heat transfer fluid with lower temperature needs to be heated up with higher heating energy until reaching the temperature at the top of the tank. So, the heater provided energy (Q_{heater}) increases and therewith the system COP will reduce. The similar process due to mixing is the cause of heat transfer fluid temperature reduction at the cooler position. Lower temperature of the extracted heat transfer fluid at cooler position decreases the release heat in cooler cycle (Q_{cooler}), and so the system COP will decreases. On the other hand, mixing in the tank leads to lower temperature of heat transfer fluid that enters the adsorber for desorption, and so the desorbed vapor leaving the adsorber to condenser reduces, and lower condensation heat (Q_{cond}) causes a smaller system COP. From the above arguments, it can be concluded that the system COP reduces due to mixing in the tank by influencing three variables. For this reason, the effect of mixing on system COP is strong and because of COP sensitivity to the mixing effect, it makes sense to study the mixing process in more details.

In system model, the interaction between storage tank and adsorber has been modeled by means of so-called fractional plug flow model. The plug flow model assumes no boundary layer at the wall region and considers a constant velocity profile. In this model, first a part of the plug is displaced(displacement), afterwards a new mixing temperature for every plug is calculated (dissipation) [9].

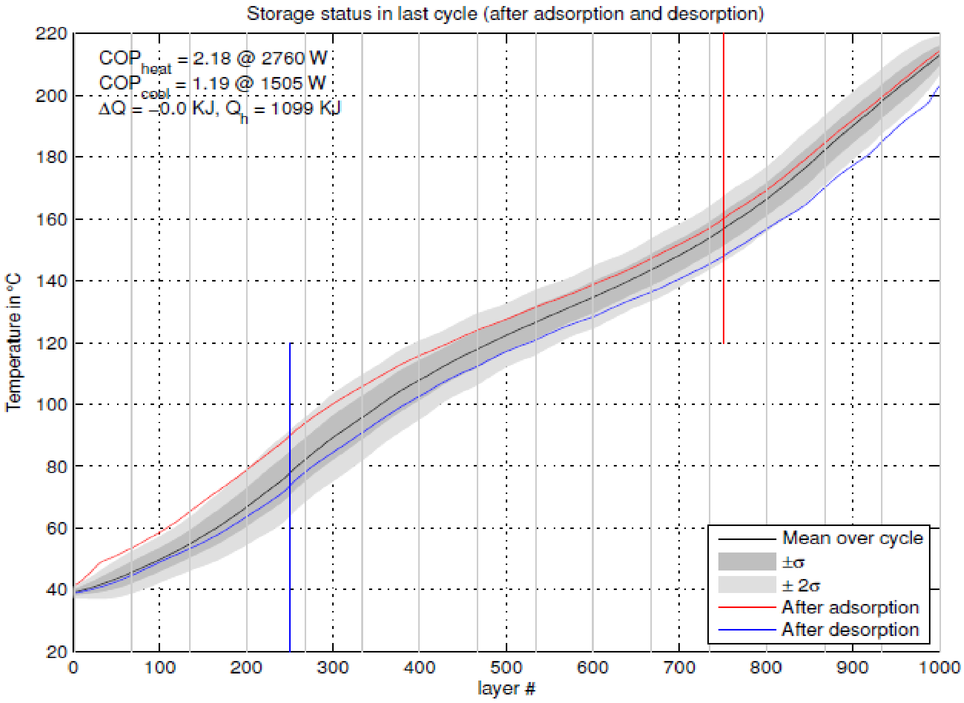

Figure 2.5: Temperature distribution in the storage tank over the cycle [9]

The main previous studies in the area of numerical study of thermal stratification focus on the solar systems thermal storage tank. Zurigat et al. (1990) studied the influence of different inlet geometries on thermal stratification in a thermocline storage tank [10]. They presented in 1992 a comprehensive experimental study to evaluate the performance of a stratified tank under variable inlet temperature conditions [11]. Cai and Stewart (1993) developed a numerical model to simulate the turbulent mixing processes of storage tank charging [12]. Davidson et al. (1994) developed a dimensionless coefficient to characterize the level of mixing in solar water storage tank [13]. Eames and Norton (1997) studied the impact of tank geometry on the thermal performance of stratified hot water storage in a numerical and experimental work [14]. Alizadeh (1999) investigated the thermal behavior of the storage tank experimentally and numerically [15]. His main concern was on the discharging process of the storage tank. Andersen and Furbo (1999) examined mixing or destratification during hot water discharge in solar storage tanks [16].

Ramsayer (2001) studied inlet flow when entering horizontally in the upper part of a hot water storage tank numerically. Furbo et al. (2003) performed the CFD simulation and experimental analysis of water jets when entering a solar storage tank [17]. Altuntop et al. (2004) analyzed the effect of different obstacles on thermal stratification in a cylindrical hot water tank numerically [18]. Shah et al. (2005) investigated the charging of the storage tank with inlet stratifiers by CFD and experimental work [19]. They also investigated the performance improvement by discharging from different levels in solar storage tank [20]. Panthalookaran et al. (2006) developed a new characterization method for stratified thermal energy stores, which was integrated into CFD-based design analysis [21]. Their new method integrates both the first and second law of thermodynamics. Andersen et al. (2007) studied a multilayer fabric stratification pipe for solar tanks [22]. Hampel et al. (2008) analyzed the thermal stratification devices for hot water thermal storage tank by means of CFD and experimental study [5]. They investigated the inlet stratification pipe effect with a limited number of operating conditions appearing in solar collector loops. Levers and Lin (2009) investigated three-dimensional flow dynamics in hot water storage tank numerically [23]. Palacios et al. (2011) investigated thermal mixing caused by the inflow from one or two round, horizontal and buoyant jets in a water storage tank, experimentally [24]. Furbo et al. (2012) presented the experimental and numerical investigations of thermal behavior in the storage tank due to the standby heat loss of the tank [25].

3 Theory and Principle of TES Numerical Investigation

3.1 Transport Mechanisms in TES

Mathematically, thermal behavior of the fluid in the tank can be modeled with the mass, momentum and energy equations [26]. Computational fluid dynamics (CFD) is a computer-based simulation to analyze the systems with fluid flow and heat transfer. By means of CFD simulation of the charging process of the thermal energy storage (TES), the momentum transport and heat transfer procedures are studied at different time of the charging process. The numerical results from solution to the flow governing transport equations provide the flow variable field at different times after charging or discharging of the TES. Different mechanisms are associated with charging process of the TES. Local mixing introduced due to the momentum diffusion at the inlet region plays a key role in mixing in the TES. In the case of turbulent flow at the inlet, turbulent diffusion acts as a parameter to increase the momentum diffusion. Convection heat transfer as a result of fluid bulk flow introduces another mechanism within the TES. Another transport mechanism in TES is the heat conduction from hot fluid layers to cold fluid layers. All these mechanisms influence the thermal performance of the energy system by impacting thermal stratification built up in the TES. In the current numerical study, the commercial CFD code Ansys Fluent 14.0 [27] has been used for the simulation of the thermal energy storage in various geometries and different charging devices. CFD Simulations with Ansys Fluent have shown promising results in previous studies in the field of solar thermal energy storage especially for turbulent flow calculations.

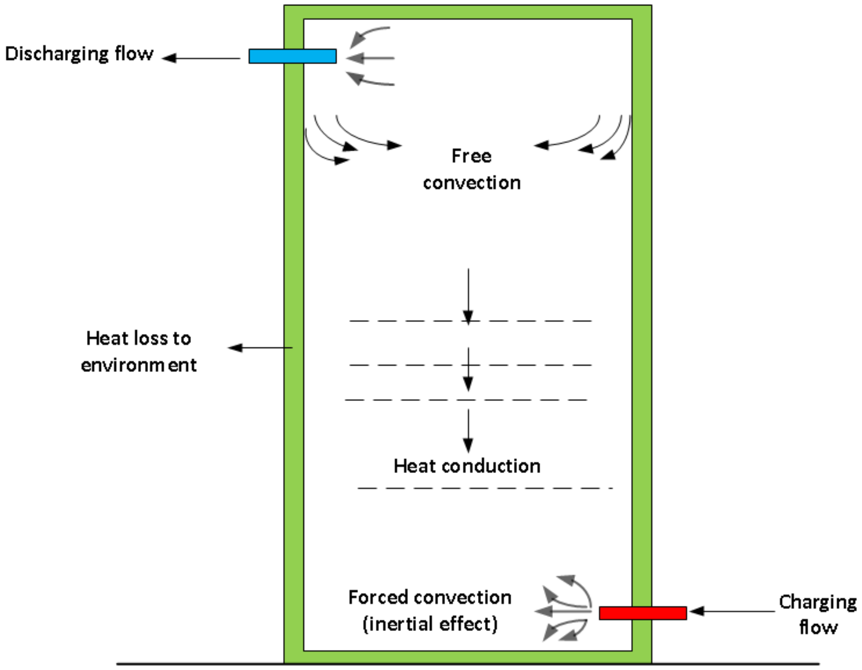

Figure 3.1: Different momentum and heat transfer mechanisms in thermal energy storage

Thermocline Thickness

Temperature stratification inside the storage tank is affected by different factors such as tank dimension (height and diameter), inlet and outlet ports location and type of the fluid [28]. Different methods have been suggested in order to analyze the stratification quality in TES. The main focus of many of them is the characterization of degree of stratification. One of these methods is thermocline thickness.

Due to buoyancy effect in TES, high temperature fluid or low density fluid rises and is collected at the top of the tank. The low temperature or high density fluid tends to move to the bottom of the tank. A thermocline region between hot and cold water region is formed. The formation of the thermocline is determined by the geometry of the tank, the inlet, the hydrodynamics, and thermal characteristics of the water flow in the tank [29]. The thickness of the thermocline determines the stratification quality in TES. Figure 3.2 demonstrates the thermocline region in a TES as a schematic representation.

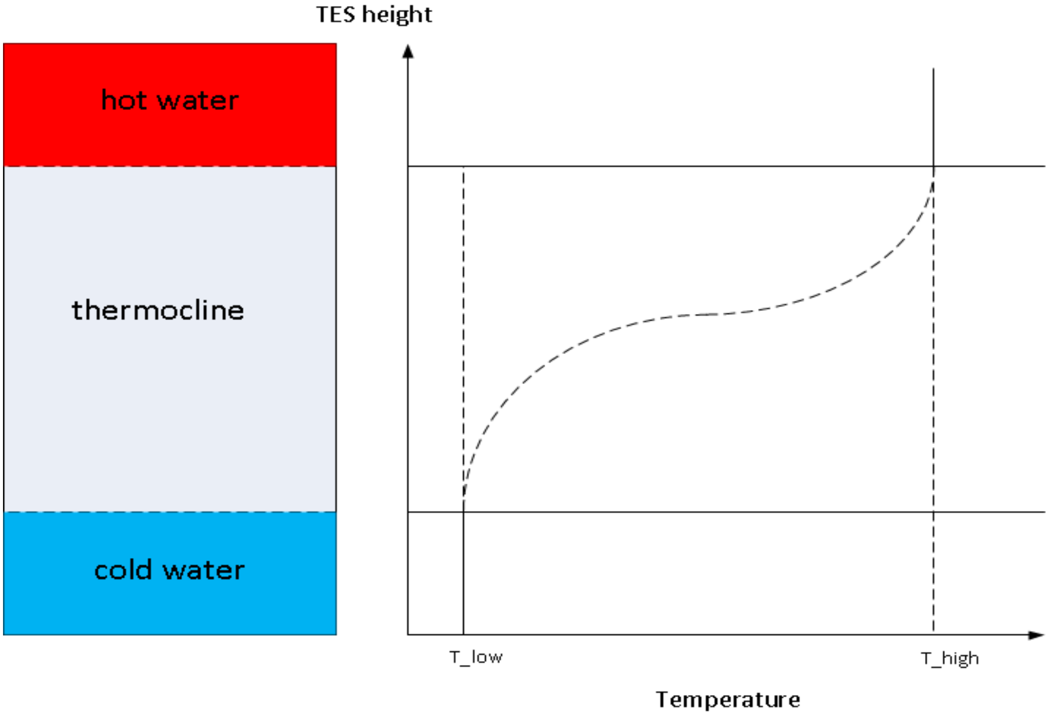

Figure 3.2: Thermocline in thermal energy storage

Temperature gradient and thermocline thickness is a regular method to characterize the degree of stratification in TES. By smaller thickness of thermocline corresponding higher temperature gradient, the mixing is less and stratification in TES is more efficient. As the thermocline thickness becomes larger, the mixing process is intensified and stratification is less efficient. Thermocline thickness is not applicable in cases with many fluid layers with different temperatures like the charging process of thermal stratified storage tank coupled with Adsorption heat pump. Initial linier temperature distribution in the tank is affected by charging process and changes at different tank height by the time. Therefore, no distinguished thermocline region can be determined.

Different Dimensionless Numbers for Characterization of TES

Different parameters can influence the thermal stratification and mixing process in the thermal storage tank. These parameters can be represented in terms of dimensionless numbers. The most important dimensionless numbers to characterize thermal stratification in a storage tank are as follows:

Reynolds Number

Reynolds number represents the ratio of the inertial force to the viscous force. At the inlet of the thermal storage tank, the Reynolds number determines the flow regime.

$$\mathrm{Re} = \frac{\rho u l_{str}}{\mu} \tag{3.1}$$

Therefore, Reynolds number at the inlet determines the laminar or turbulent flow entering in the storage tank and thereby it is a decisive parameter in the mixing process at the inlet region. In the case of stratisorp storage tank [9], Reynolds number at the inlet region has an additional impact on the suction effect at the bottom of the tank which leads to destratification.

Richardson Number

Richardson number is a suitable number to characterize stratification stability in a thermal storage tank. Generally, Richardson number expresses the ratio of natural convection to the forced convection. In thermal storage tank, Richardson number is the ratio of buoyancy forces to mixing forces and is expressed as follows:

$$Ri = \frac{g\beta l\left(T_{top} - T_{bottom}\right)}{u^2} \tag{3.2}$$

and for the storage inlet

$$Ri = \frac{(\rho - \rho_m) g l}{\rho_m u^2} \tag{3.3}$$

Where ρ_m is the average density of the fluid in the storage tank. This dimensionless number describes the stratification more qualitatively than quantitatively. With smaller value of the Richardson number, the buoyancy forces are negligible in comparison to the mixing forces, which means more mixing in the tank. With higher value of Richardson number, buoyancy forces are more important in comparison to the mixing forces. This leads to a better stratified tank in the cases, where the buoyancy and mixing forces act against each other.

In charging process of thermal storage tank, higher charging flow rate leads to smaller Richardson number at the inlet and represents stronger mixing effect in the inlet region inside of the stratification pipe.

Peclet Number

The Peclet number represents the ratio of bulk heat transfer to the conductive heat transfer. It is defined as follows:

$$Pe = \frac{u \cdot l}{\epsilon} = Re \cdot Pr \tag{3.4}$$

The Peclet number can be represented as the product of Reynolds and Prandtl numbers. Prandtl number is defined as the ratio of momentum diffusivity to thermal diffusivity. At higher Peclet numbers, the influence of bulk heat transfer is more decisive than the conductive heat transfer. Therefore, effective thermal conductivity due to convection is the influential part of the effective thermal conductivity against the diffusion part. On the other hand, with smaller Peclet number heat transfer process occurs particularly due to conduction. In this case, effective thermal conductivity due to convection has less significance than the diffusion part.

Convective Term in Substantive Derivative of Fluid Property

The rate of change of property ϕ per unit volume for a fluid particle is given by the product of the substantive derivative of ϕ and density.

$$\rho \frac{D\phi}{Dt} = \rho\left(\frac{\partial \phi}{\partial t} + \vec{u} \cdot grad\phi\right) = \frac{\partial(\rho\phi)}{\partial t} + div(\rho\phi\vec{u}) \tag{3.5}$$

The right side of the equation expresses the rate of the change in time of ϕ per unit volume plus the net flow of ϕ out of the fluid element per unit volume [30].
The differential form of transport equation for the fluid property ϕ can be found in equation

$$\frac{\partial(\rho\phi)}{\partial t} + div(\rho\phi\vec{u}) = div(\Gamma grad\phi) + S_\phi \tag{3.6}$$

This equation shows the various transport processes. The left side of the equation describes the rate of change of ϕ of fluid element (transient term) plus net rate of flow of ϕ out of fluid element (convective term), and the right side demonstrates the rate of increase of ϕ due to diffusion (diffusion term) plus rate of increase of ϕ due to sources [30] .

3.2 Basic Governing Equations of the Incompressible Newtonian Fluid Flow

The following system of equations highlight the governing equations of the time dependent three-dimensional fluid flow of a incompressible Newtonian fluid [30].

Continuity:

$$div(\vec{u}) = 0 \tag{3.7}$$

x-momentum:

$$\rho \frac{\partial u}{\partial t} + \rho div(u\vec{u}) = -\frac{\partial p}{\partial x} + div(\mu \cdot grad(u)) + S_{Mx} \tag{3.8}$$

y-momentum:

$$\rho \frac{\partial v}{\partial t} + \rho div(v\vec{u}) = -\frac{\partial p}{\partial y} + div(\mu \cdot grad(v)) + S_{My} \tag{3.9}$$

z-momentum:

$$\rho \frac{\partial w}{\partial t} + \rho div(w\vec{u}) = -\frac{\partial p}{\partial z} + div(\mu \cdot grad(w)) + S_{Mz} \tag{3.10}$$

Energy equation:

$$\rho \frac{\partial (e)}{\partial t} + \rho div(e\vec{u}) = -p \cdot div(\vec{u}) + div(k \cdot grad(T)) + \Phi + S_e \tag{3.11}$$

Where e is the specific internal energy, Φ the dissipation function, and S_M and S_e the momentum and energy source terms respectively.

All of the effects due to the viscous stresses in the internal energy equation are described by the dissipation function Φ [30].

$$\Phi = \mu\left\{2\left[\left(\frac{\partial u}{\partial x}\right)^2 + \left(\frac{\partial v}{\partial y}\right)^2 + \left(\frac{\partial w}{\partial z}\right)^2\right] + \left(\frac{\partial u}{\partial y} + \frac{\partial v}{\partial x}\right)^2 + \left(\frac{\partial u}{\partial z} + \frac{\partial w}{\partial x}\right)^2 + \left(\frac{\partial v}{\partial z} + \frac{\partial w}{\partial y}\right)^2\right\} + \gamma\left(div\vec{u}\right)^2 \tag{3.12}$$

The momentum source terms S_M are the contribution of the body forces. For example, the body forces caused by gravity would be modeled by [30]

$$S_{Mx} = 0, S_{My} = 0, S_{Mz} = -\rho g \tag{3.13}$$

γ in dissipation function is the second viscosity which has an small effect, and for gases a good working approximation can be obtained by taking the value $\gamma = -\frac{2}{3}\mu$ (Schlichting, 1979).

For 2D axisymmetric flow like the current simulation, the continuity equation is as follows [27]:

$$\frac{\partial \rho}{\partial t} + \frac{\partial}{\partial x}(\rho u_x) + \frac{\partial}{\partial r}(\rho u_r) + \frac{\rho u_r}{r} = 0 \tag{3.14}$$

Where x is the axial coordinate, r the radial coordinate, u_x the axial velocity and u_r the radial velocity.

Conservation of momentum in an inertial reference frame can be written as follows:

$$\underbrace{\rho\frac{\partial u_i}{\partial t}}_{\substack{unsteady\\term}} + \underbrace{\rho u_j\frac{\partial u_i}{\partial x_j}}_{convection} = \underbrace{-\rho g_i}_{\substack{volume\\force}} - \underbrace{\frac{\partial p}{\partial x_i}}_{pressure} + \underbrace{\frac{\partial}{\partial x_j}\left[\mu\left[(\frac{\partial u_i}{\partial x_j}+\frac{\partial u_j}{\partial x_i}) - \frac{2}{3}\frac{\partial u_l}{\partial x_l}\delta_{ij}\right]\right]}_{friction} \tag{3.15}$$

For 2-D axisymmetric flow, the axial and radial momentum conservation equations are as follows [27]:

$$\frac{\partial}{\partial t}(\rho u_x) + \frac{1}{r}\frac{\partial}{\partial x}(r\rho u_x u_x) + \frac{1}{r}\frac{\partial}{\partial r}(r\rho u_r u_x) = -\frac{\partial p}{\partial x} + \frac{1}{r}\frac{\partial}{\partial x}\left[r\mu\left(2\frac{\partial u_x}{\partial x} - \frac{2}{3}\left(\nabla\cdot\vec{u}\right)\right)\right]$$
$$+\frac{1}{r}\frac{\partial}{\partial r}\left[r\mu\left(\frac{\partial u_x}{\partial r} + \frac{\partial u_r}{\partial x}\right)\right] + S_x \tag{3.16}$$

And

$$\frac{\partial}{\partial t}(\rho u_r) + \frac{1}{r}\frac{\partial}{\partial x}(r\rho u_x u_r) + \frac{1}{r}\frac{\partial}{\partial r}(r\rho u_r u_r) = -\frac{\partial p}{\partial r} + \frac{1}{r}\frac{\partial}{\partial r}\left[r\mu\left(2\frac{\partial u_r}{\partial r} - \frac{2}{3}\left(\nabla\cdot\vec{u}\right)\right)\right]$$
$$+\frac{1}{r}\frac{\partial}{\partial x}\left[r\mu\left(\frac{\partial u_r}{\partial x} + \frac{\partial u_x}{\partial r}\right)\right] - 2\mu\frac{u_r}{r^2} + \frac{2}{3}\frac{\mu}{r}\left(\nabla\cdot\vec{u}\right) + \rho\frac{u_z^{\,2}}{r} + S_r \tag{3.17}$$

Where

$$\nabla\cdot\vec{u} = \frac{\partial u_x}{\partial x} + \frac{\partial u_r}{\partial r} + \frac{u_r}{r} \tag{3.18}$$

And u_z is the swirl velocity.

In this formulation the tensor notation is used with the indices i, j, and k which are from 1 to n as the dimension number.

In order to study the heat transfer and temperature field, the energy equation should be also solved.

The energy equation for an incompressible flow without the effect of viscous stresses and source term can be written as follows:

$$\rho\cdot C\cdot\left(\frac{\partial T}{\partial t} + \frac{\partial}{\partial x_j}\left(u_j\cdot T\right)\right) = \frac{\partial}{\partial x_j}\left(k\cdot\frac{\partial T}{\partial x_j}\right) \tag{3.19}$$

where C is the heat capacity of the fluid, and k is the fluid heat conduction coefficient.

3.3 Turbulence Modeling in CFD Simulation

Turbulence in fluid flow expresses the random and fluctuating change in fluid variables. Turbulence fluctuations have an unsteady and three-dimensional spatial character. A large energy spectrum is one of the most important physical characteristics of turbulent flows [31]. Many turbulence models have been developed, aiming at capturing the most important statistical quantities of turbulent flows, such as profiles of mean velocity, r.m.s. velocity fluctuations, etc. [32]. The flow variables in a turbulent flow can be decomposed into a steady mean value $\bar{\phi}$ and a fluctuating component ϕ' [30].

$$\phi(t) = \bar{\phi} + \phi'(t) \tag{3.20}$$

Where

$$\bar{\phi} = \frac{1}{\Delta t}\int_0^{\Delta t} \phi(t)dt \tag{3.21}$$

And the time average of the fluctuations is, by definition, zero:

$$\overline{\phi'} = \frac{1}{\Delta t}\int_0^{\Delta t} \phi'(t)dt \equiv 0 \tag{3.22}$$

Another main characteristic structure of the turbulent flows is rotational flow structures, which is called turbulent eddies with a wide range of length scales [30]. Because of the eddying motions in turbulent flows, the produced mixing procedure increases the values of diffusion coefficients for mass, momentum, and heat.

The smallest scales describing the eddy motion in turbulent flows is called Kolmogorov-scales. The Reynolds number of the smallest eddies based on their characteristic velocity and characteristic length is equal to 1; thus, the smallest scales present in a turbulent flow are those for which the inertial and viscous effects are of equal strength [30].

The largest scales describing the eddy motions are characterized by turbulent velocity scale (U_t) and turbulent length scale (L_t), so the turbulent Reynolds number can be defined as follows:

$$\mathrm{Re}_t = \frac{U_t L_t}{\nu} \tag{3.23}$$

In order to simulate the turbulent flows, the most popular methods are:

1- Direct numerical simulation (DNS)
2- Large eddy simulation (LES)
3- Reynolds-averaged Navier Stokes (RANS)

DNS

Direct numerical simulation (DNS) has recently become a powerful supplement to experimental investigations of turbulence in complex phenomena and has been shown to be capable of accurately reproducing the physics of moderate Reynolds number turbulent flows [33]. The turbulent motion consists of eddies with a wide spectrum of sizes, ranging from large eddies of the size of the flow domain corresponding to low-frequency fluctuations to much smaller eddies, at which dissipation take place, corresponding to high-frequency fluctuations [34]. In direct numerical simulation (DNS), the transient Navier-stokes equations are solved in spatial discretization. The grid should be fine enough to resolve the Kolmogorov length scales at which energy dissipation takes place and with time steps sufficiently small to resolve the period of the fastest fluctuations [30]. The aim of this kind of simulation is resolution of eddies with all length scales. To reach this aim, a grid number in order of $N_{3D} \cong \mathrm{Re}^{\frac{9}{4}}$ is usually needed. The computational requirements of the DNS are usually high and are not often used in the industrial flow simulation. By means of DNS method, turbulence parameters and their transport can be calculated in much more accurate manner. One of the important advantages of the DNS method is its capability in computation of instantaneous turbulence structures. With DNS, one can derive more turbulence statistics [35]. However, the weakness of DNS is that increasing the Reynolds number increases the computational cost and time [36].

LES

In contrast to direct numerical simulation (DNS) the Kolmogorov dissipation scale is not resolved with LES, making the computational cost of LES largely independent of the Reynolds number [37]. Transport of the mass, momentum, and energy in turbulent flow is mainly achieved by large scale eddies. In the large eddy simulation (LES), larger eddies are resolved and the effects of smaller eddies on the mean flow are modeled by means of sub-grid scale (SGS) model. A spatial filtering function separates the larger and smaller eddies. By filtering the governing equations, all scales of motion and mixing smaller than a given filter width are removed, and its influence on the resolved flow are modeled [38]. As in RANS equations, in LES is also necessary to use closure models, and due to the characteristics of the SGS (homogeneity, isotropy and no significant variations for different flows), it is more appropriate to represent them by mathematical models [39]. In the Figure 3.3, a comparison of modeling complexity and computational cost among different turbulent modeling methods is shown in a chart.

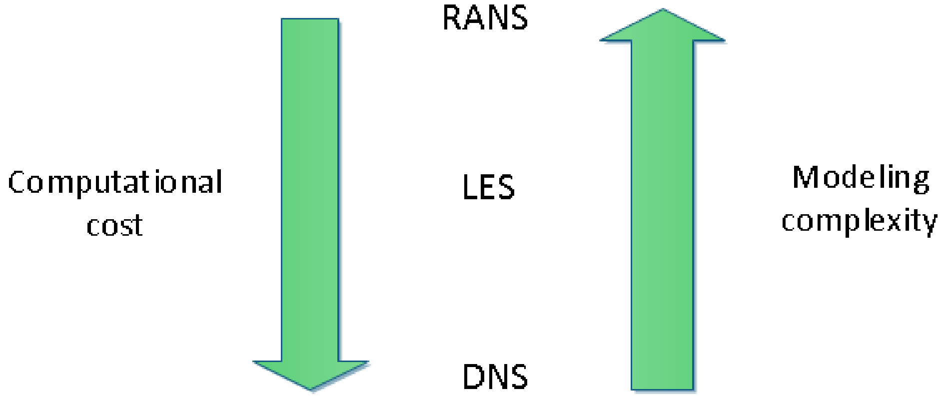

Figure 3.3: Modeling complexity and computational cost of different methods for turbulence calculation

LES requires a finer grid, cannot benefit from symmetries of the flow in space, and provides mean values only by averaging the unsteady flow field computed with small time step over a long sampling time [40]. The computational cost of the LES is expensive especially for wall-bounded flows and at high Reynolds number. That was the main motivation for development of new hybrid RANS-LES methods. A way to reduce the computational cost of LES by orders of magnitude is to combine LES equations with RANS equations used in the near wall region [41].

RANS Turbulence Models

In the RANS method of turbulence modeling the main focus is on the mean flow. The effect of the turbulence on mean flow is considered by means of additional term in the time averaged or Reynolds-averaged flow equation. In other words, this method represents a statistical description of turbulence effect by means of Reynolds averaging. The equation 3.24 shows the Reynolds-averaged Navier-Stokes (RANS) equations.

$$\frac{\partial \rho}{\partial t}+\frac{\partial}{\partial x_i}(\rho u_i)=0$$

$$\frac{\partial}{\partial t}(\rho u_i)+\frac{\partial}{\partial x_j}(\rho u_i u_j)=-\frac{\partial p}{\partial x_i}+\frac{\partial}{\partial x_j}\left[\mu\left(\frac{\partial u_i}{\partial x_j}+\frac{\partial u_j}{\partial x_i}-\frac{2}{3}\delta_{ij}\frac{\partial u_l}{\partial x_l}\right)\right]+\frac{\partial}{\partial x_j}\left(-\rho\ \overline{u_i' u_j'}\ \right) \tag{3.24}$$

Where $-\rho\overline{u_i' u_j'}$ is the Reynolds stresses term.

In order to be able to compute turbulent flows with the RANS equations, it is necessary to develop turbulence models to predict the Reynolds stresses and scalar transport terms and close the system of mean flow equation [30].

The most popular RANS turbulence models are $k-\varepsilon$, $k-\omega$, and Reynolds stress. They are classified based on the additional transport equation required for turbulent variable calculation. For instance, in $k-\varepsilon$ turbulence model, two additional transport equations are considered for turbulent kinetic energy (k) and turbulent dissipation rate (ε). Usually the $k-\omega$ model provides a better result than $k-\varepsilon$ in cases when facing smaller turbulent kinetic energy. In other words, in the near wall flow without applying the wall treatment, $k-\omega$ model leads to better results. One of the disadvantages of two-equation turbulence models like $k-\varepsilon$ and $k-\omega$ is their disability of detecting the relationship between turbulent energy production and turbulent stresses because of normal stress anisotropy.

Turbulent Viscosity Modeling in $k-\varepsilon$ and $k-\omega$ Turbulence Models

In order to relate the Reynolds stresses to the mean velocity gradients, the Boussinesq hypothesis is applied in the classical turbulence model like Spalart-Allmaras [42], $k-\varepsilon$, and $k-\omega$. This relation is shown in equation 3.25.

$$R_{ij}=-\rho\overline{u_i' u_j'}=\mu_t\left(\frac{\partial \overline{u}_i}{\partial x_j}+\frac{\partial \overline{u}_j}{\partial x_i}\right)-\frac{2}{3}\rho k\delta_{ij} \tag{3.25}$$

Therefore, the Reynolds stresses are linearly related to the mean strain rate tensor [43]. k in the Boussinesq hypothesis is the turbulent kinetic energy per unit mass and is computed by the velocity fluctuation terms.

$$k=\frac{1}{2}\left(\overline{u'^2}+\overline{v'^2}+\overline{w'^2}\right) \tag{3.26}$$

The eddy viscosity is calculated from the equation 3.27.

$$\mu_t = C_\mu \rho U_t \, L_t = \rho C_\mu \frac{k^2}{\varepsilon} \tag{3.27}$$

Where C_μ is a constant equals 0.09, and the U_t and L_t are the velocity and length scales representing the turbulent large-scales. These representative turbulent large scales are related to the turbulent kinetic energy and turbulent energy dissipation rate as follows:

$$U_t = k^{1/2} \quad L_t = \frac{k^{3/2}}{\varepsilon} \tag{3.28}$$

Therefore, the Reynolds stress term is a function of mean strain rate (S_{ij}), turbulent kinetic energy (k), turbulent energy rate of dissipation (ε), and fluid density (ρ)

$$-\rho \overline{u_i' u_j'} = R_{ij}\left[S_{ij}, k, \varepsilon, \rho\right] \tag{3.29}$$

In the non-linear $k-\varepsilon$ turbulence model, the Reynolds stress term is also dependent on the rate of change of mean strain following a fluid particle.

Different types of $k-\varepsilon$ model like Re-Normalization Group (RNG) [44] and realizable [45] increase the accuracy and reliability of the model for a wider class of flows. The RNG model has an additional term in turbulent energy dissipation rate equation, and swirling flow effect is taken into account in this model. Therefore, it results in a higher accuracy for swirling flows. Moreover, the RNG model provides a differential formula for effective viscosity that accounts for low-Reynolds number effects [27].
Realizable $k-\varepsilon$ model offers an alternative formulation for turbulent viscosity and modified transport equation for turbulent dissipation rate.

RANS Turbulence Modeling for Application in TES Simulation

During charging process of TES, flow with high inertial forces, and therefore, high Reynolds number is introduced inside of the tank. Due to different loss factors, the Reynolds number decreases further from inlet region. For this reason, relaminarization of flow is a decisive phenomenon in the charging process. The applied turbulence model in this context should be able to capture this flow characteristic as much as possible. Generally, the standard $k-\varepsilon$ model provides more accurate results at higher Reynolds number especially at the region far away from the wall. In the current application, standard $k-\varepsilon$ model can be an appropriate choice for the regions inside of the charging flow jet that have a higher Reynolds number. For the interface between charging flow jet and the fluid in surroundings and also flow in the further regions, where the Reynolds number is less, standard $k-\varepsilon$ model can provide some inaccurate results. Additionally standard $k-\varepsilon$ model doesn’t reproduce the flow structures in near wall region properly and also is not recommended for flows including separation. The modified version of $k-\varepsilon$ model like realizable and RNG suggests alternative eddy viscosity formulation and dissipation rate transport equation. Realizable $k-\varepsilon$ model shows better prediction in flows with round jet and recirculation.
On the other hand, $k-\omega$ model is more relevant for shear flow and advantageous for the near wall region and smaller Reynolds number. SST $k-\omega$ model [46] combines the advantage of $k-\varepsilon$ model in regions far from the wall and $k-\omega$ model in near wall or low Reynolds number regions. From all properties of turbulence model summarized above, it can be concluded that the realizable $k-\varepsilon$ and SST $k-\omega$ models could be appropriate choices for the current application.

Wall Treatment for Turbulent Flow

For a turbulent flow over a wall, the law of the wall is applied to calculate the average velocity of turbulent flow. Very close to the wall, viscous damping reduces the tangential velocity fluctuations, while kinematic blocking reduces the normal fluctuations [27]. Turbulence quantities close to the wall are strongly anisotropic because the turbulent velocity fluctuations normal to the wall are damped by the presence of the wall [47].
There are two different ways to model the near-wall region in Ansys Fluent.

1- wall functions approach

2- near wall model approach

Although the laminar sub-layer is very thin, its resolution strongly affects the accuracy of the solution in the entire domain [48]. In wall functions approach , the viscosity-affected inner region (viscous sublayer and buffer layer) is not resolved and semi-empirical formulas called "wall functions" are used to bridge the viscosity –affected region between the wall and the fully-turbulent region [27]. Standard wall functions are one of the biggest sources of misconceptions in turbulent flow computations, even for experienced users [49]. Turbulence model should be modified in order to consider the viscosity-affected region.
The wall function approach can only be used in flows with high Reynolds number, where the viscous sublayer is very thin. In this approach no grid point should be located in viscous sublayer. In order to make sure that no grid point is located in viscous sublayer, the dimensionless wall distance should be checked ($y^+ \geq 20$). However, almost 10 grid point should exist in boundary layer. This approach is popular because it is economical, robust, and reasonably accurate [27]. However, the wall-function performance is often poor, partly because of inappropriate implementations and partly because the schemes themselves have inherent limitations [50].
Generally ,when the viscous sublayer is resolved, wall functions cannot be used anymore for the flows with low Reynolds number, and a fine mesh in the wall region is recommended. This approach is in Ansys Fluent under Enhanced wall treatment available. In this approach, at least, one cell should exist in the viscous sublayer ($y^+ \approx 1$). But ($y^+ \leq 5$) is also acceptable. Furthermore , between 5 to 10 grid points should be located between wall and $y^+ \leq 20$ [5]. In the current study, Enhanced wall treatment has been implemented for the wall treatment, and value of y^+ is monitored in order to make sure that the viscous sub layer has been resolved.

Turbulence and Heat Transfer

Usually when modeling convective heat transfer in turbulent flows, one uses a turbulent Prandtl number for RANS approaches or a subgrid scale Prandtl number for LES approaches [51]. The effect of turbulence on the heat transfer in turbulent flow is described by eddy heat flux where the turbulent heat flux is described by turbulent Prandtl number and mean temperature gradient.
Turbulent Prandtl number is a dimensionless number which is defined as the ratio between eddy momentum diffusivity to eddy thermal diffusivity.

$$\Pr_t = \frac{\varepsilon_M}{\varepsilon_T} \tag{3.30}$$

Where ε_M and ε_T are the momentum eddy diffusivity and thermal eddy diffusivity respectively. The turbulent prandtl number is widely considered to be constant [52]. The value of turbulent Prandtl number from empirical data is 0.9.

The eddy heat flux is presented in equation 3.31 in a similar way to the Boussinesq hypothesis.

$$-\rho\overline{u_i'T'} = \frac{\mu_t}{\Pr_t}\cdot\frac{\partial\overline{T}}{\partial x_i} \tag{3.31}$$

Eddy thermal conductivity and eddy viscosity are related to each other by the following equation

$$k_t = \frac{c_p\,\mu_t}{Pr_t} \tag{3.32}$$

3.4 Effective Thermal Conductivity due to Turbulence in TES Charging Process

Convective heat transfer in TES can be influenced by two different mechanisms. One of them is the heat transfer due to the random microscopic molecular motion called heat diffusion. Another mechanism is the heat transfer because of the bulk fluid motion or so-called heat advection.

Due to turbulence and its effect on the thermal diffusion, heat transfer mechanism of diffusion is influenced by means of an additional thermal conduction coefficient. The effective thermal conductivity is defined as follows [27]:

$$k_{eff\_t} = k + \frac{c_p\mu_t}{\Pr_t} \tag{3.33}$$

In the equation 3.33 k is fluid thermal conductivity, μ_t turbulent eddy viscosity and $\Pr_t$ turbulent Prandtl number. This part of effective thermal conductivity is affected by microscopic molecular motion. Turbulence effect contributes to effective thermal conductivity by influencing the molecular diffusion. Turbulent heat transfer is modeled in ASYS Fluent CFD code by substitution of fluid thermal conductivity with turbulent effective thermal conductivity and additional modification in energy equation. Energy equation in this case is represented in equation 3.34.

$$\frac{\partial}{\partial t}(\rho E)+\frac{\partial}{\partial x_i}\left[u_i(\rho E+p)\right]=\frac{\partial}{\partial x_j}\left(k_{eff}\frac{\partial T}{\partial x_j}+u_i\left(\tau_{ij}\right)_{eff}\right)+S_h \tag{3.34}$$

In equation 3.34, E is the total Energy, k_{eff} the effective thermal conductivity, $(\tau_{ij})_{eff}$ the deviatoric stress tensor, and S_h the volumetric heat source.

$$\left(\tau_{ij}\right)_{eff} = \mu_{eff}\left(\frac{\partial\overline{u}_j}{\partial x_i}+\frac{\partial\overline{u}_i}{\partial x_j}\right)-\frac{2}{3}\mu_{eff}\frac{\partial u_l}{\partial x_l}\delta_{ij} \tag{3.35}$$

Effective viscosity (μ_{eff}) is the summation of fluid molecular viscosity and turbulent eddy viscosity calculated by means of Boussinesq hypothesis.

3.5 Effective Thermal Conductivity due to Advection in TES Charging Process

The heat transfer mechanism caused by the bulk fluid motion so-called heat Advection contributes to effective thermal conductivity with an additional part. This part of effective thermal conductivity in the storage tank simulation with inlet stratification pipe is calculated as follows:

$$\dot{q}_{conv} = \rho \cdot C_p \left(\vec{U} \cdot \vec{\nabla} T\right) dV$$

$$\dot{Q}_{conv} = \int_{V\_cs} \rho C_p \left(\vec{U} \cdot \vec{\nabla} T\right) dV$$

$$\dot{Q}_{conv} = k_{eff\_conv} \cdot A_{hor\_cs} \cdot \frac{\overline{\partial T}}{\partial x}$$

$$k_{eff\_conv} = \frac{\int_{V\_cs} \rho C_p \left(\vec{U} \cdot \nabla T\right) dV}{A_{hor\_cs} \cdot \frac{\overline{\partial T}}{\partial x}} \qquad (3.36)$$

Where A_{hor_cs} is the horizontal cross section of thermal storage tank between outer diameter of the stratification pipe and storage tank wall. $\frac{\overline{\partial T}}{\partial x}$ is the average value of the temperature gradient over the horizontal cross section of the storage tank between stratification pipe outer diameter and storage tank wall.

Buoyancy Modeling in Ansys Fluent

Due to the temperature difference and, therefore, density difference, the natural buoyancy results in a buoyancy-driven flow in TES. There are different approaches to model the buoyancy effect in solution domain. One of these approaches is Boussinesq model which considers density as a constant value in all governing equations except for the buoyancy term in momentum equation. An Steady state calculation with Boussinesq model is recommended , if the temperature difference in fluid domain is small. If the temperature difference in solution domain is relatively high, a transient calculation with another approach is recommended. In this approach, the fluid density is defined as a function of temperature and is compared with a determined reference density. In simulation of TES, the buoyancy term is modeled by means of a body-force term in momentum equation. This term is shown in equation 3.37

$$(\rho - \rho_{ref})g \qquad (3.37)$$

ρ_{ref} is reference density which is determined in the simulation setup.

This term is considered in the simulation by means of redefinition of pressure in Ansys Fluent

$$p_s' = p_s - \rho_{ref}\, g x \qquad (3.38)$$

Where p_s is the static pressure in the TES, and x is the axial coordinate [27].

Buoyancy and Turbulence

In thermal stratified fluid, the warmer fluid with lower density is located at the upper part of the storage tank and colder fluid with higher density is located at the lower part of the tank. These two regions of fluid are separated from each other by means of transition zone called thermocline. Due to density gradient in fluid, any transport of fluid particles causes an increasing in system potential energy. These fluid particles can flow back due to buoyancy forces and therewith the potential energy can be converted to kinetic energy [53]. In an stable stratified flow, the turbulent fluctuation parallel to density gradient can be damped and the fluctuation perpendicular to the gradient can be enforced [53]. As a result, the turbulent eddy viscosity can show some anisotropic behavior. In buoyancy driven flow, this effect causes some inaccuracy by implementation of RANS models that consider isotropic behavior of turbulent eddy viscosity.

Stratification Device Function

Different sucking effects can appear due to pressure differences between the charge system and the storage tank during the charging process [19, 54]. This sucking effect leads to a mixing with the charge flow and subsequently to a worse stratification behavior [55]. In the case of incompressible inviscid fluid flow, where friction by viscous forces can be negligible, Bernoulli's equation can be used for the flow description.

$$\frac{1}{2}\rho u^2 + \rho g z + P = constant$$

In case of flow with friction, some pressure losses will add an additional term to the original version of Bernoulli equation [56].

$$P_1 + \rho_1 g z_1 + \frac{\rho_1}{2} {u_1}^2 = P_2 + \rho_2 g z_2 + \frac{\rho_2}{2} {u_2}^2 \cdot (1 + \sum \zeta) \tag{3.39}$$

As an example in the pipe flow, the pressure loss can be represented by pipe friction factor. Using this pipe friction factor, a resistance coefficient can be formed [55] .

$$\zeta = \lambda \frac{l}{d} \tag{3.40}$$

The pressure difference must overcome the flow resistance due to friction forces in order to transport the flow over a determined distance. In charging systems, high negative pressure difference between charging pipe and storage tank can lead to sucking flow from storage tank to the charging pipe. The mixing of flow from the storage tank with charging flow reduces the stratification. On the other hand, a relative higher positive pressure difference between charging pipe and storage tank leads to an inflow in the storage tank.

3.6 Solution Methods Applied in the Numerical Simulation

The pressure-based solver is usually a proper choice to solve the governing equations in incompressible flows. The density-based solver is recommended for high-speed compressible flows.

In pressure based solver, two algorithms determine the way of the governing equation solution. These are segregated and coupled algorithms. In the segregated algorithm the momentum and pressure-based continuity equations are solved sequential and separated from each other. In the coupled algorithm, momentum and continuity equations are solved in a coupled manner, which has a faster convergence speed over the segregated algorithm. For the temporal discretization in transient simulation, evaluation of the unsteady term can be considered in implicit or explicit time integration methods.

3.6.1 Explicit Method

In the explicit time integration, the transient term is expressed as

$$\frac{\phi^{n+1} - \phi^n}{\Delta t} = F(\phi^n) \tag{3.41}$$

In this method, the value of ϕ^{n+1} can be expressed in terms of the existing solution values [27],

$$\phi^{n+1} = \phi^n + \Delta t F(\phi^n) \tag{3.42}$$

3.6.2 Implicit Method

In the Implicit time integration, the transient term is expressed as

$$\frac{\phi^{n+1} - \phi^{n}}{\Delta t} = F\left(\phi^{n+1}\right) \tag{3.43}$$

In this temporal discretization method, the value of ϕ^{n+1} is related to the value in neighboring cells.

$$\phi^{n+1} = \phi^{n} + \Delta t F\left(\phi^{n+1}\right) \tag{3.44}$$

The advantage of implicit method over explicit method is the stability regardless of the time step size [27]. The Implicit method has been used for temporal discretization in the simulations in current study.

4 Numerical Simulation of Flow through Porous Media

4.1 Flow Characteristic in Porous Media

Fluid flow through porous media is the interesting research area in different science branches and engineering applications like flows through packed beds and filters. In case of stratisorp storage tank, the porous medium implementation influences the stratification by consideration of two points of view. First point of view is related to the effect of porous medium to achieve more uniform velocity distribution, which draws the charging process of the TES nearer to the ideal plug flow charging model. Another point of view is related to the role of porous medium in velocity gradient reduction that leads to the decrement of turbulent kinetic energy production. The effect of the porous media on the fluid flow is the creation of resistance in flow direction. This resistance can be represented in the form of a pressure gradient. Some parameters including permeability, inertial parameter and friction factor are often used to describe the physical properties for the fluid flow in porous media [57]. In porous media, there are two methods of calculating the Reynolds number of a flow [58]. One is permeability-based method, where characteristic length for the definition of Reynolds number is defined as follows,

$$l = \sqrt{\alpha} \tag{4.1}$$

And α is porous medium permeability.

In another method, pore diameter is used as characteristic length to calculate Reynolds number [58].

$$Re_d = \frac{\rho u d_p}{\mu} \tag{4.2}$$

Where d_p is average pore diameter.

4.2 Different Flow Regime in Porous Media

Based on the Reynolds number of the flow through porous media and importance of inertial forces against viscous forces, three different flow regimes can be considered to study the flow characteristics in porous media in detail ,

1-Darcy’s regime or low Reynolds number regime:

By low Reynolds number flow through porous media, where flow is dominated with viscous forces. In such a flow regime the linear Darcy law is valid.

2-Forchheimer’s regime, or inertial zone,

By increasing of Reynolds number, inertial terms of the local flow through the pores become significant. At the lower end of this zone, the transition from the viscous force predominant laminar regime to the inertial force predominant laminar regime occurs. At the upper end of the transition zone, there is a gradual passage to turbulent flow. In this regime, the boundary layer starts to develop while an inertial core flow grows with the Reynolds number [59].

3-Froude’s regime, or turbulent zone with high Reynolds number,

In this flow regime, the inertial terms are dominant and the movement is highly unsteady and chaotic [57].

For lower Reynolds number in fluid flow, the dependency of the pressure gradient to the flow velocity can be expressed by Darcy Law which is demonstrated in equation 4.3

$$\nabla p = -\frac{\mu}{\alpha} u \tag{4.3}$$

In this equation, ∇p is pressure gradient along the flow direction, α is the permeability of the porous medium and μ the dynamic viscosity. Velocity in Darcy equation is superficial velocity and is defined as [57]

$$u = \frac{Q}{A} \tag{4.4}$$

Where Q is volumetric flow rate and A is the exposed surface area of the porous media perpendicular to the flow direction.

In higher Reynolds number, the inertial resistance in porous zone plays a significant role, and both viscous and inertial resistances both are the influential parameters in order to determine the pressure loss through porous zone. Furthermore, inertial resistance part causes a non-linier behavior between pressure gradient and flow velocity. These additional influences are considered in Forchheimer's modification of Darcy's equation.

$$\nabla p = -\left(\frac{\mu}{\alpha}u + \beta\rho u^2\right) \tag{4.5}$$

β in Forchheimer equation is the inertial resistance coefficient. The Darcy-Forchheimer based theory has been successfully applied in characterizing the behavior of both compressible and incompressible fluids [60].

Inertial and viscous resistance coefficients influence the flow governing equation through porous zone by adding a momentum source term to Navier-stokes equation. This source terms for a simple homogeneous porous medium are shown in equation 4.6

$$S_i = -\left(\frac{\mu}{\alpha}u_i + \frac{1}{2}\rho C_i |u| u_i\right) \tag{4.6}$$

In the above equation C_i is defined as

$$C_i = 2\beta \tag{4.7}$$

4.3 Calculating of Inertial and Viscous Resistance Coefficients

The momentum source term in flow governing equations is determined in CFD model by definition of inertial and viscous resistance coefficients. The coefficients are constant medium properties and can be calculated from porous media properties like porosity and pore diameter. The porosity of the porous media is defined as the ratio between the void volume and whole body volume of the porous medium [61].

$$\eta = \frac{V_v}{V_0} \tag{4.8}$$

The equation 4.8 can be rewritten as a function of densities [61].

$$\eta = 1 - \frac{\rho_p}{\rho_s} \tag{4.9}$$

Where ρ_p is the porous medium density, and ρ_s is the density of the material forming the porous medium skeleton.

The Ergun equations represent the resistance coefficients of porous medium in terms of medium porosity and another parameter called equivalent particle diameter.

With assumption of void volume in a cylindrical shape, the hydraulic diameter of pores is calculated as follows:

$d_c = 4 \cdot$ void volume available for flow/wetted surface

In terms of porosity, the d_c is expressed in equation 4.10 [62],

$$d_c = 4\frac{(1-\eta)}{\eta S_v} \tag{4.10}$$

Where S_v is the specific surface or total particle surface per volume of particle. The quantity S_v is used to define the equivalent particle diameter. Hence, the equation 4.11 expresses the dependency of porosity and pore diameter on equivalent particle diameter [62].

$$d_e = 1.5\frac{1-\eta}{\eta} d_c \tag{4.11}$$

The resistance coefficient can be calculated as follows [62]:

$$\frac{1}{\alpha} = \frac{150(1-\eta)^2}{\eta^3 d_e{}^2}$$

$$C_i = \frac{3.5}{d_e} \cdot \frac{(1-\eta)}{\eta^3} \tag{4.12}$$

5 Numerical Study of the TES Charging Process without Stratification Device

5.1 Storage Tank CFD Model

Stratification devices play an important role in the creation and retaining of stratified flow in charging process of the thermal storage tank. It is important that the hot or chilled water being stored experiences minimum mixing during the process of charging and discharging [63]. The main function of the charging device in TES can be concluded in minimization of the mixing process between warm and cold fluid.

Implementation of stratification devices enables the passive charging of the fluid inside of TES with the aim of reducing the mixing process due to the momentum effect of inflow. In order to investigate the influence of inflow momentum in stratification thoroughly, the charging process of TES without stratification device in different flow regime has been studied numerically and the findings are compared with available experimental results.

In order to compare the results from the numerical model with experimental results, a model storage tank has been built and investigated experimentally in a parallel work from Chirag Joshi. In numerical study, a simple case of the storage tank with uniform initial temperature is simulated with two different charging flow temperatures. Different momentums and heat transfer mechanisms in the charging process have been depicted in figure 3.1.

The storage tank CFD model height is 38 cm with 18 cm diameter. Flow is introduced to the tank through a ring shape inlet channel with 1cm length. A block-structured mesh with about 676000 cells is applied to simulate the charging process of the TES without stratification device.

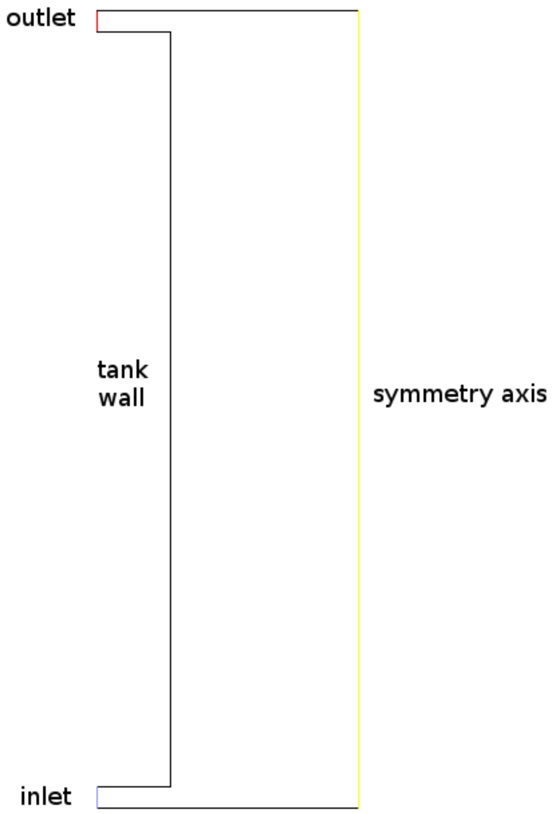

Figure 5.1: Storage tank geometry and boundary conditions applied for numerical simulation

5.2 Boundary Conditions and Solution Methods in CFD Simulation

The fluid domain in simulation has been considered to be 2-D axisymmetric. Flow inlet to the domain has been defined as mass flow inlet with specified temperature. Axis boundary condition type in Ansys Fluent has been used for defining of the axis in 2-D axisymmetric flow.

The outflow boundary condition has been used for the outlet boundary condition which applies a zero diffusion flux at the boundary and an overall mass balance. Wall boundary condition in simulations has been considered as no slip condition for shear condition and adiabatic or no heat flux for thermal condition.

Continuity and momentum equations have been solved in a coupled algorithm for pressure-velocity coupling method. Body force weighted method has been used for pressure in spatial discretization. The second order upwind scheme has been used for spatial discretization of momentum, turbulent kinetic energy, and turbulent dissipation rate equations. In addition, the second order implicit scheme has been applied for transient formulation.

5.3 Charging Process with Various Temperatures and Viscous Model

5.3.1 Initial Condition in Simulation

The solution domain has been initialized with 40 °C and flow has been injected with 20 °C ($\Delta T = 20\ K$) and 35 °C ($\Delta T = 5\ K$). In case of turbulent simulation, turbulent variables like turbulent kinetic energy and turbulent energy dissipation rate have been set to a very small value considering no initial turbulence variable as the initial condition.

5.3.2 Charging with ΔT: 20 K

5.3.2.1 Motivation for Performing Laminar and Turbulent Simulations

One of the critical issues in simulation of storage tank is whether the flow leaving the diffuser is laminar or turbulent because of its impact on mixing [64]. In this investigation, different simulations for laminar and turbulent cases have been performed because of the following reasons:

- different ranges of the Reynolds number value in storage tank charging process
- high possibility of flow regime transition from turbulent flow at the region close to inlet port to laminar flow at the region farther from inlet port

5.3.2.2 Laminar Simulation

Figure 5.3 represents the streamline for the charging of the TES with 20 K temperature difference from the fluid inside of the tank. The charging of the tank has been performed by a 3 liter per minute volume flow rate. The illustrated streamlines show the tank situation after 20 seconds charging in a laminar simulation. The main forces acting on the inflow in the inlet channel region include buoyancy forces tending to subject flow downward and inertial forces in radial direction. The charging flow enters to the TES in a radial direction channel. Charging in radial direction has the advantage of inertial effect reduction in axial direction. Therefore, less number of fluid layers can be affected by the inertial forces which lead to more mixing.

When the flow leaves the radial channel and enters the tank, the radial inertial effect works to raise the flow stream in vertical direction towards the outlet. The interaction of buoyancy and inertial forces in opposite direction can cause some recirculation region at the lower part of the tank. By means of the definition of density varying values with temperature and gravitation acceleration, the buoyancy forces are considered in the simulation.

Figure 5.2 illustrates Reynolds number analysis for charging flow rate of 3 lpm after 20 seconds charging time. In the definition of Reynolds number, characteristic length of the problem can be selected in different ways depending on the problem. Two different characteristic lengths might be used for current simulation. One of them is the perimeter of the storage tank at the inlet boundary. According to axisymmetric fluid domain, the flow enters the storage tank through the whole perimeter of the tank at the inlet surface. Another characteristic length might be the inner diameter of the tank, where ideal plug flow will move inside of the tank.

The maximum possible characteristic length, which is the outer perimeter of the tank, has been applied for Reynolds number calculation. High value of Reynolds number especially at the inlet region increases the possibility of a transition from laminar to turbulent flow, and therefore, laminar simulation is not a proper choice to resolve the flow structures more precisely. The complex vortical structures at the lower part of the tank are another proof for inappropriateness of laminar simulation.

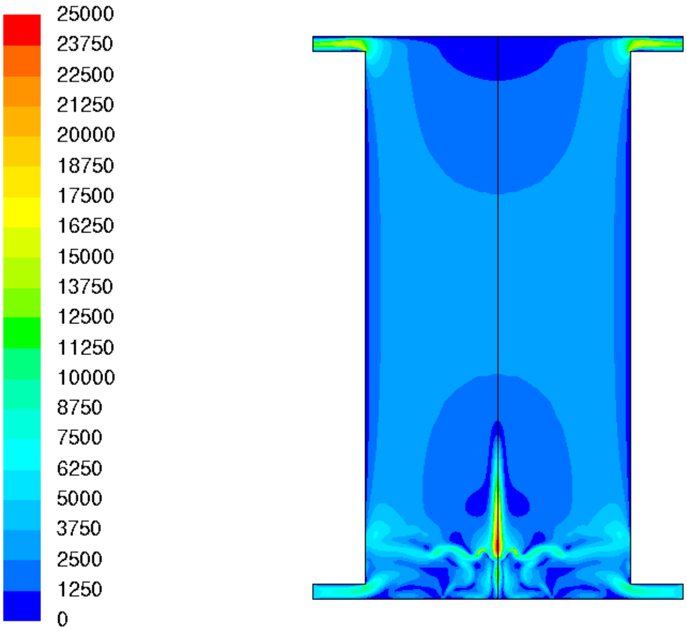

Figure 5.2: Reynolds number in storage tank after 20 s charging with 3 lpm for laminar simulation based on outer perimeter of the tank as characteristic length

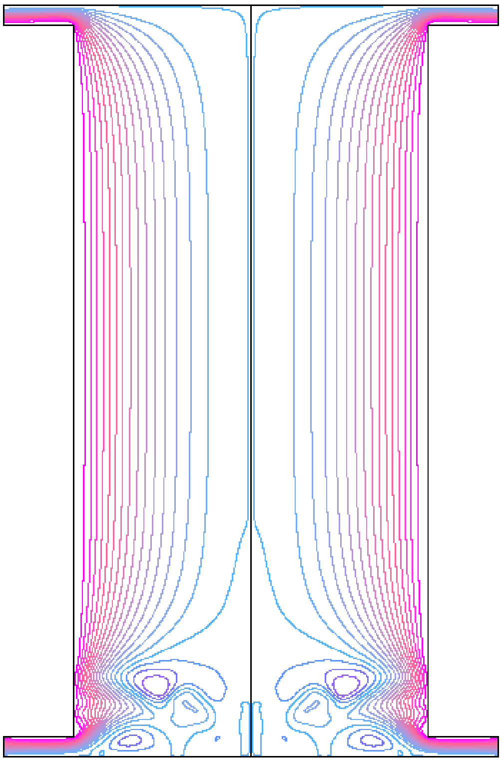

Figure 5.3: Streamline of the charging with 3 lpm and $\Delta T = 20\ K$ after 20 s in laminar simulation

5.3.2.3 Mesh Independency Study

Mesh independency study is one of the required steps to prove the accuracy of the obtained numerical results. For this study, a new finer grid has been generated to probe mesh independency of the created CFD mesh. Figure 5.4 and 5.5 represent the average temperature distribution in horizontal direction versus storage tank height for 20 and 60 seconds charging time, respectively. The temperature values in different heights of the tank have been averaged in horizontal direction for both cases with different grid sizes. These values of the coarser grid are in good agreement with the values for the finer grid in both charging time. The coarser grid with about 676000 cells can, therefore, be used for further simulations.

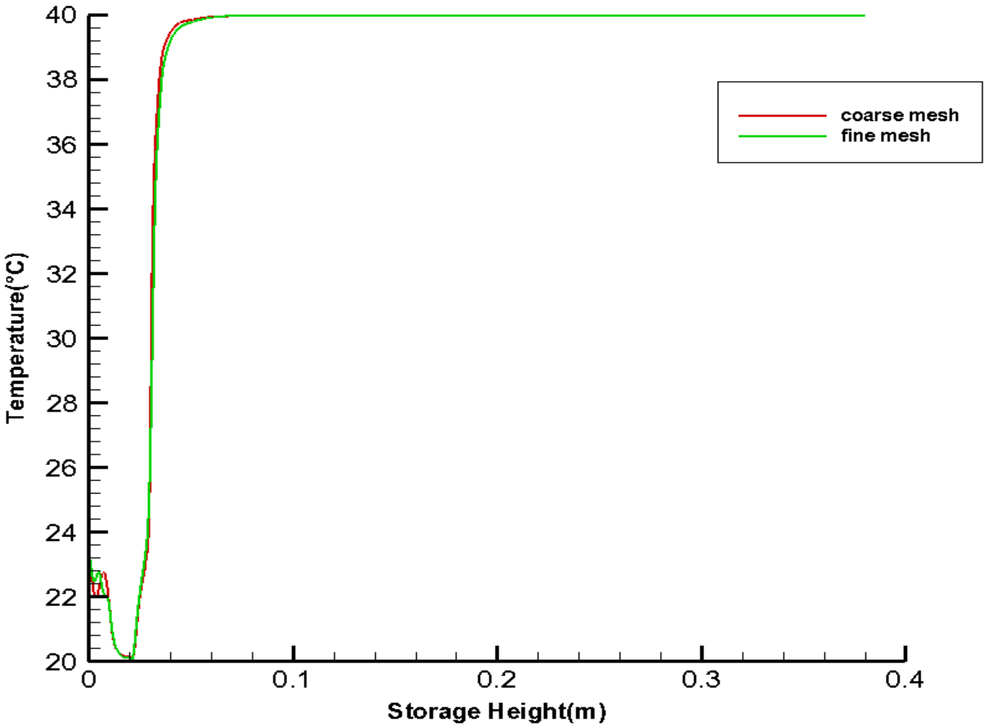

Figure 5.4: Average temperature distribution comparison between coarse and fine grid after 20 s charging with 3 lpm volume flow rate in turbulent simulation with realizable $k-\varepsilon$ model (coarse mesh: 676619 cells and fine mesh 1144157 cells)

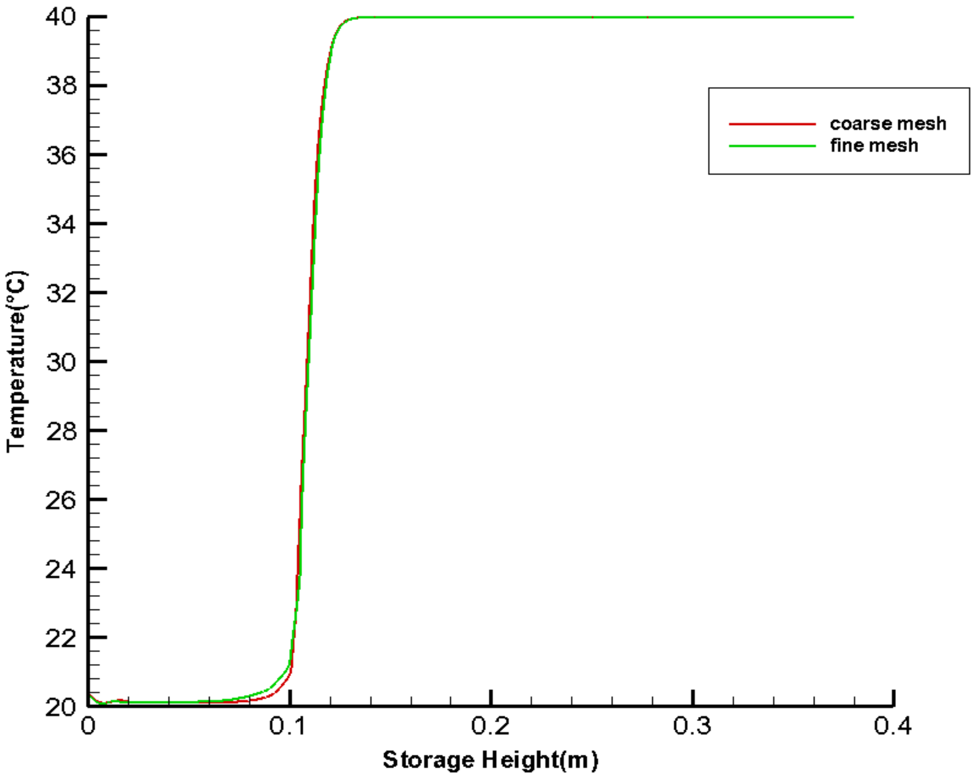

Figure 5.5: Average temperature distribution comparison between coarse and fine grid after 60 s charging with 3 lpm volume flow rate in turbulent simulation with realizable $k-\varepsilon$ model (coarse mesh: 676619 cells and fine mesh 1144157 cells)

5.3.2.4 Residual Monitoring during Calculation

In order to judge convergence of the conservation equation for a fluid variable ϕ at the cell p, the globally scaled residuals in Ansys Fluent[27] has been monitored.

$$R^{\phi} = \frac{\sum_{cellsP}\left|\sum_{nb} a_{nb}\phi_{nb} + b - a_P\phi_p\right|}{\sum_{cellsP}\left|a_p\phi_p\right|}$$

In the scaled residual equation, a_p and a_{nb} are the center coefficient and influence coefficient for the neighboring cells, respectively. b is the contribution of the constant part of the source term and boundary condition [27].

Scaled residual monitoring of the fluid variables demonstrates a good convergence process with small residual values. As it has been depicted in figure 5.7, the surface monitoring for mass flow rate at the outlet boundary also represents a converged value of mass flow rate which convinces the mass conservation in solution domain.

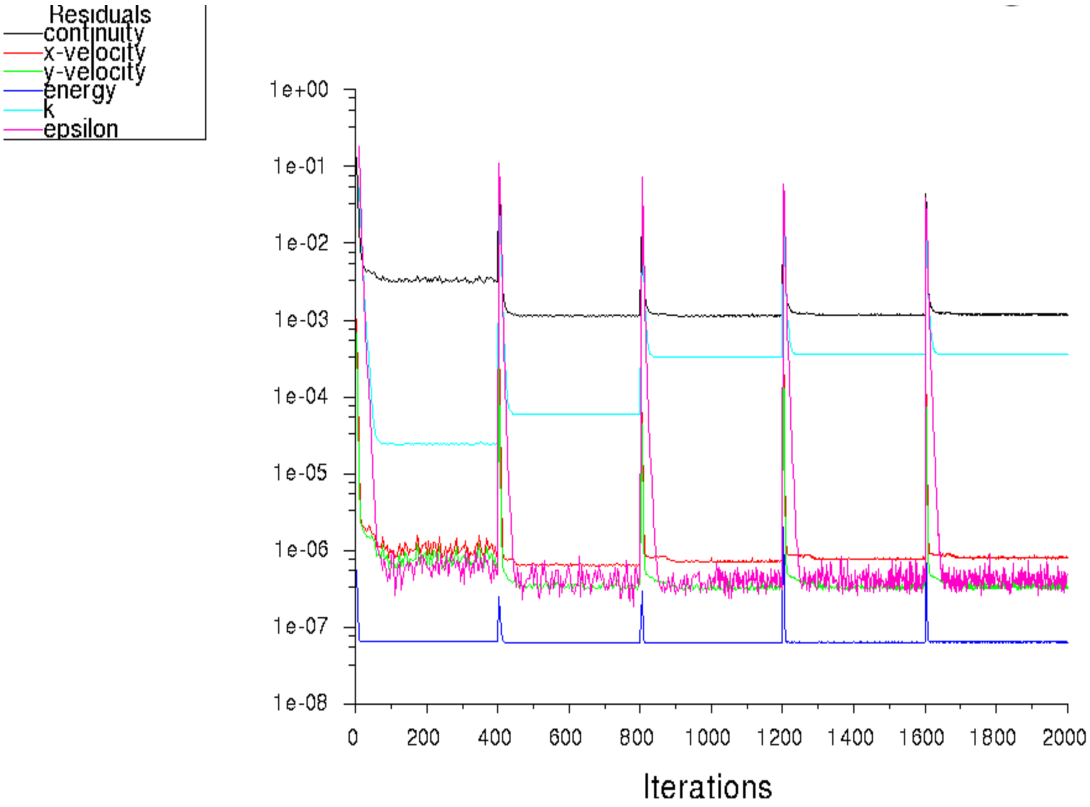

Figure 5.6: Convergence history of flow equations in transient simulation with realizable $k-\varepsilon$ model for one second simulation time with 0.2 s time step size (maximum 400 iterations per time step)

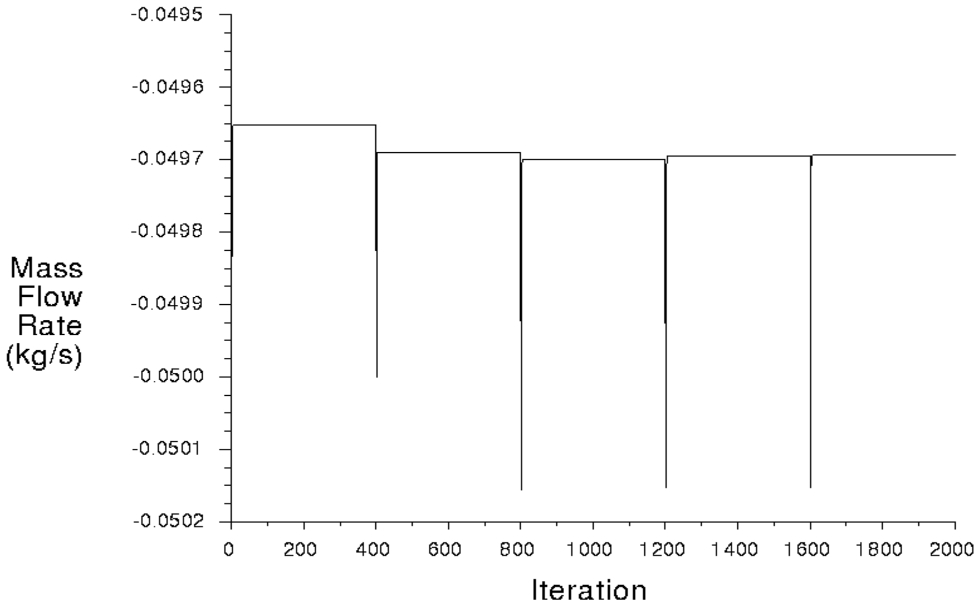

Figure 5.7: Mass flow rate convergence process at the outlet of the storage tank in transient simulation with realizable $k - \varepsilon$ model for one second simulation time with 0.2 s time step size (maximum 400 iterations per time step)

5.3.2.5 Turbulent Simulations

The possibility of transition from laminar to turbulent makes the simulation results sensitive to the viscous model. Different Reynolds-averaged Navier-stokes (RANS) turbulence models can be relevant choices for simulating the charging process of the corresponding TES.

Hence, the same simulations are performed with different RANS turbulence models in order to obtain more physical and accurate results.

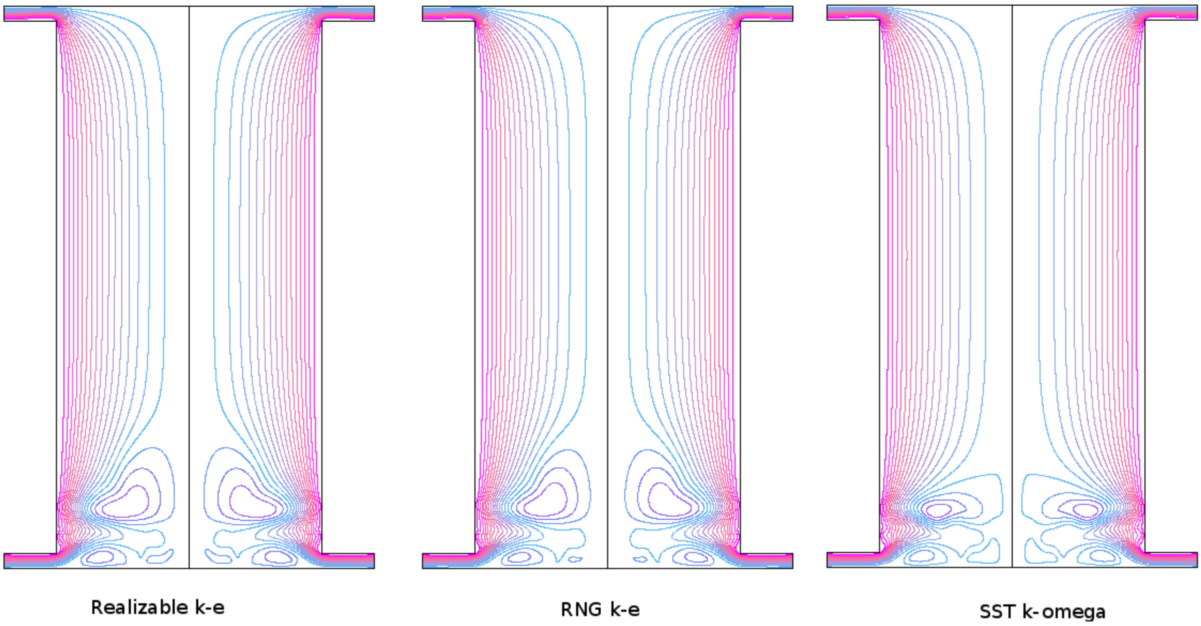

Figure 5.8: Streamline for the simulation with different RANS turbulence model after 20 s charging with $\Delta T = 20\ K$ and 3 lpm volume flow rate

According to figure 5.8, it can be concluded that after 20 seconds charging both $k-\varepsilon$ models predict recirculation region with larger length scales. Turbulent eddy viscosity field in realizable $k-\varepsilon$ model show higher values in comparison to SST $k-\omega$ model. The SST $k-\omega$ model combines the advantage of standard $k-\omega$ model in the near-wall region and $k-\varepsilon$ model in the far field. A modified definition of turbulent viscosity considering transport of turbulent shear stress in SST $k-\omega$ model causes a relative expanded field of turbulent eddy viscosity.

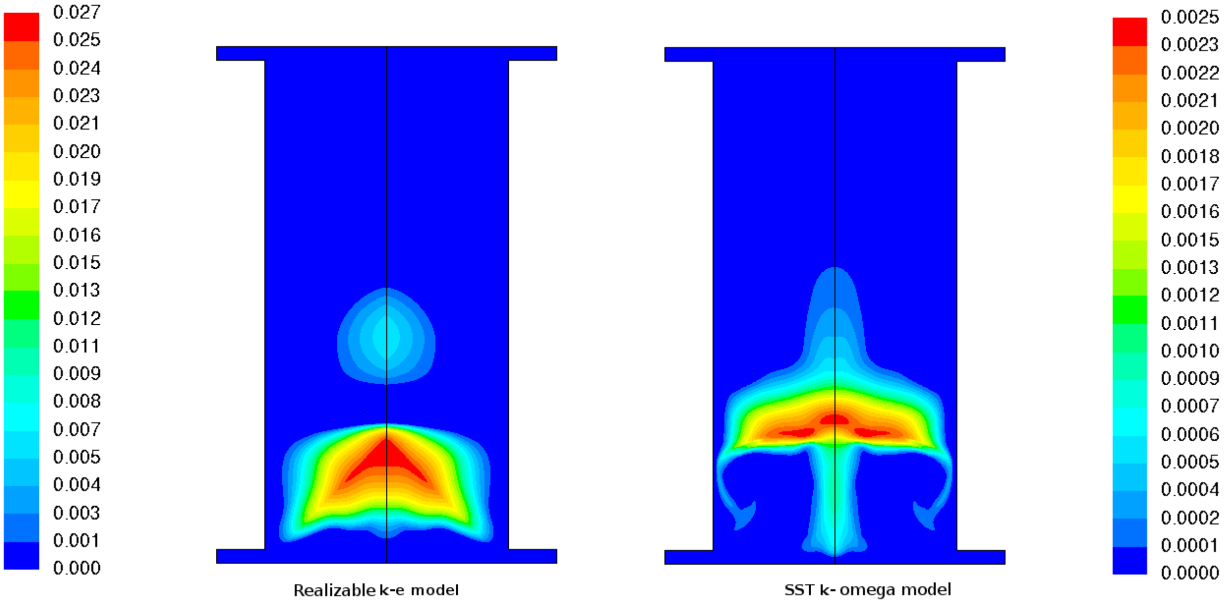

Figure 5.9: Turbulent viscosity (kg/(m.s)) comparison between realizable $k-\varepsilon$ and SST $k-\omega$ turbulence model after 60 s charging with ($\Delta T = 20\ K$) and 3 lpm volume flow rate

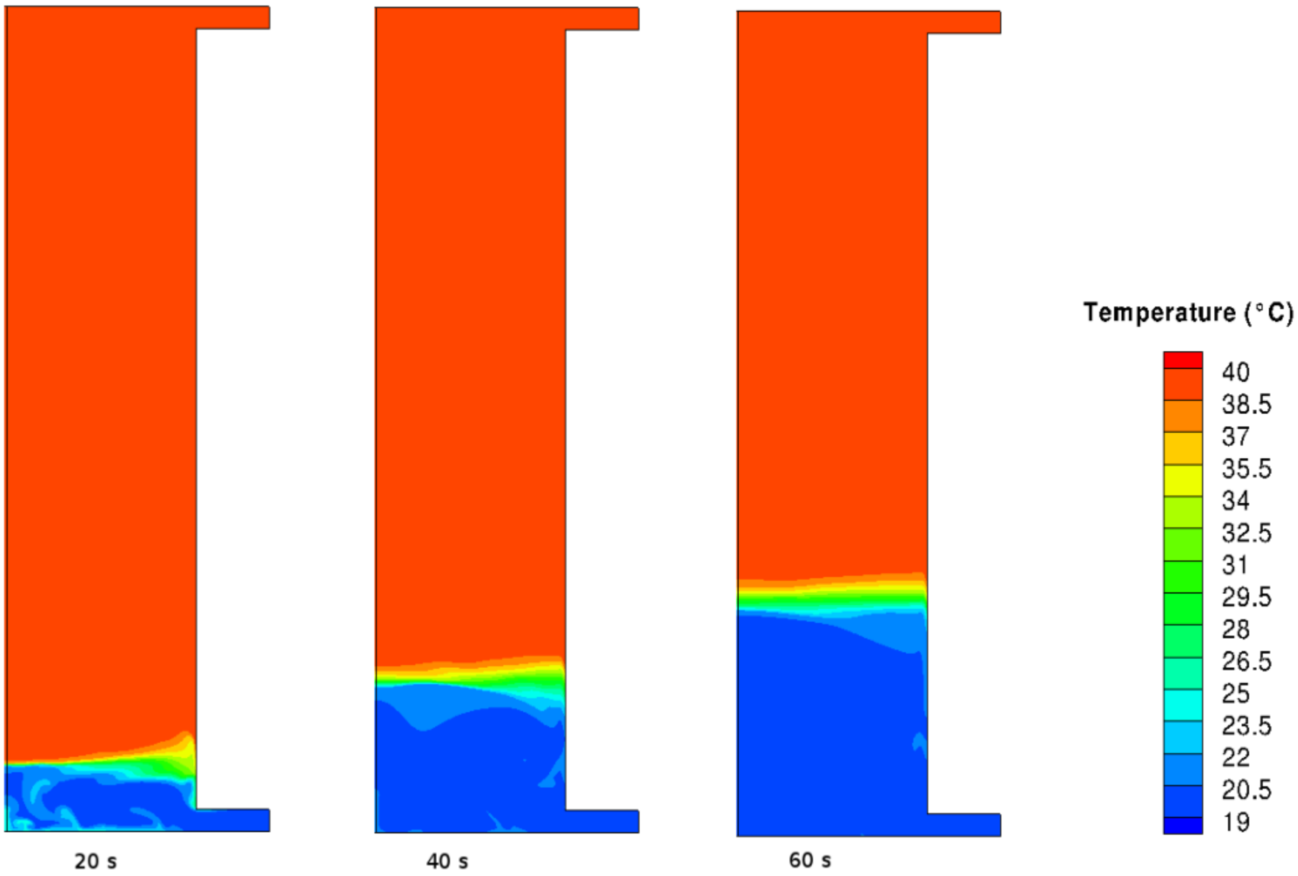

Figure 5.10: Temperature contours for simulation with realizable $k - \varepsilon$ model for charging volume flow rate of 3 lpm with ($\Delta T = 20\,K$)

As presented in Figure 5.9, the turbulent viscosity contour after 60 seconds charging shows an extension of the region with higher values in SST $k - \omega$ model. Therefore, the thermocline region after 60 seconds charging experiences higher values of the turbulent eddy viscosity. These higher values of eddy viscosity in the thermocline region result in higher effective thermal conductivity, turbulent heat transfer, and a relatively higher mixing.

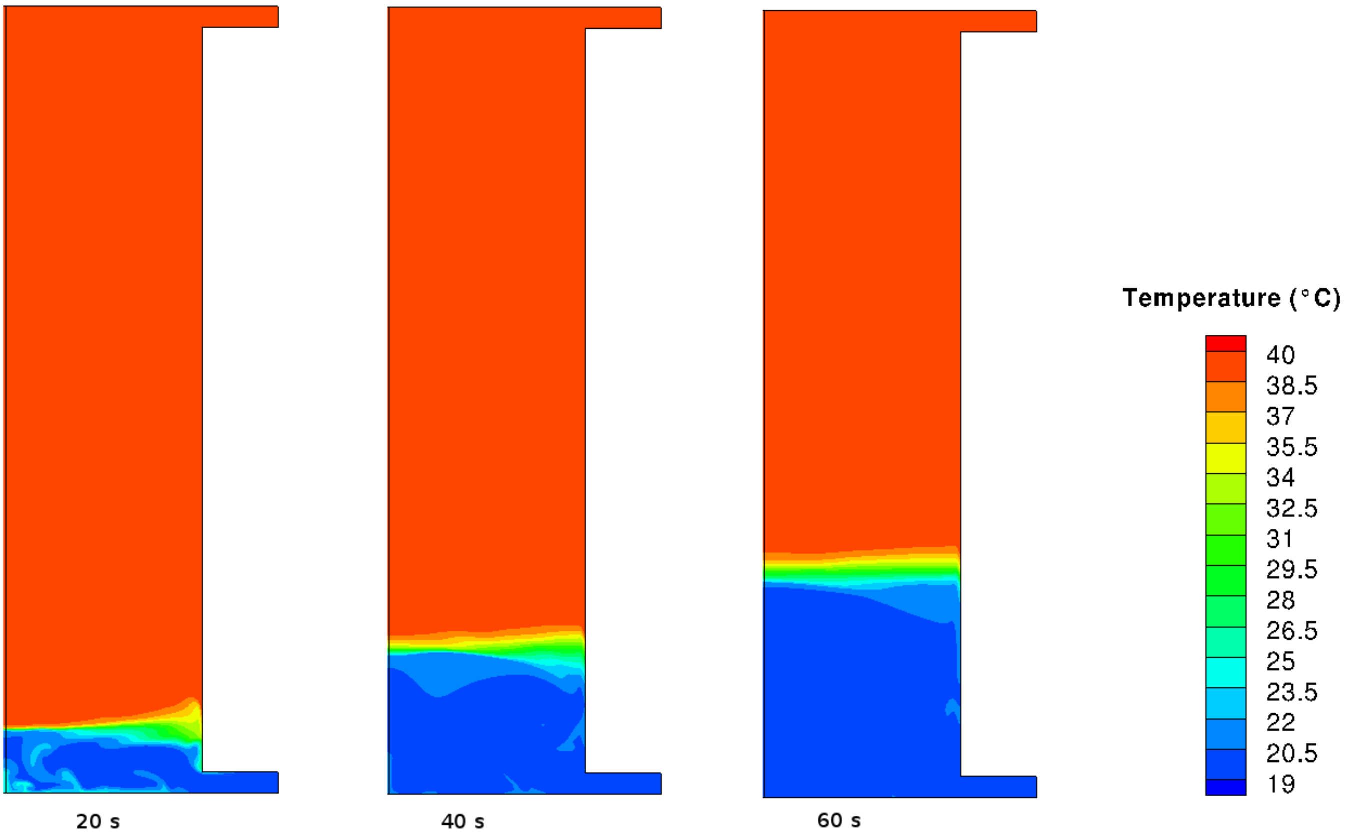

Figure 5.11: Temperature contours for simulation with RNG $k-\varepsilon$ model for charging volume flow rate of 3 lpm with ($\Delta T = 20\ K$)

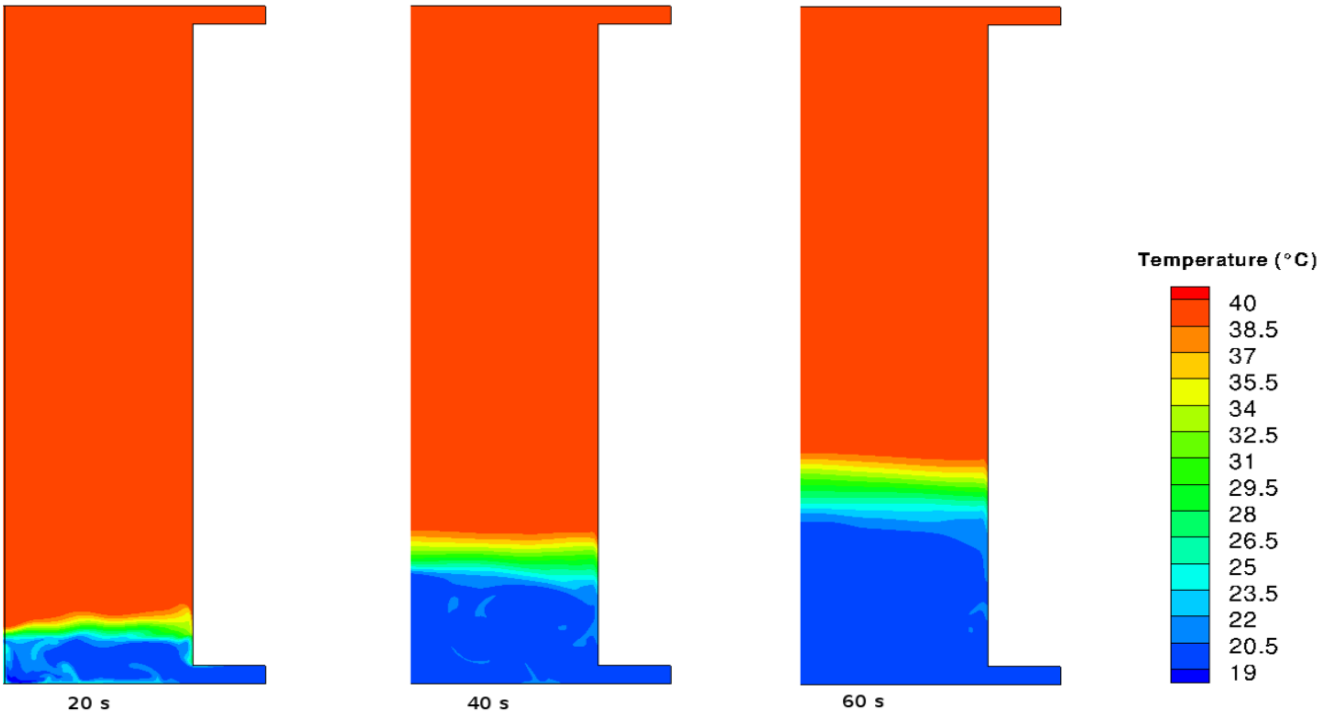

Figure 5.12: Temperature contours for simulation with SST $k-\omega$ model for charging volume flow rate of 3 lpm with ($\Delta T = 20\ K$)

Based on the temperature analysis in the tank after 60 seconds charging, it can be seen that $k-\varepsilon$ models including realizable and RNG predict thinner Thermocline in comparison to SST $k-\omega$ model. In other words, SST $k-\omega$ model predicts higher mixing in the charging process.

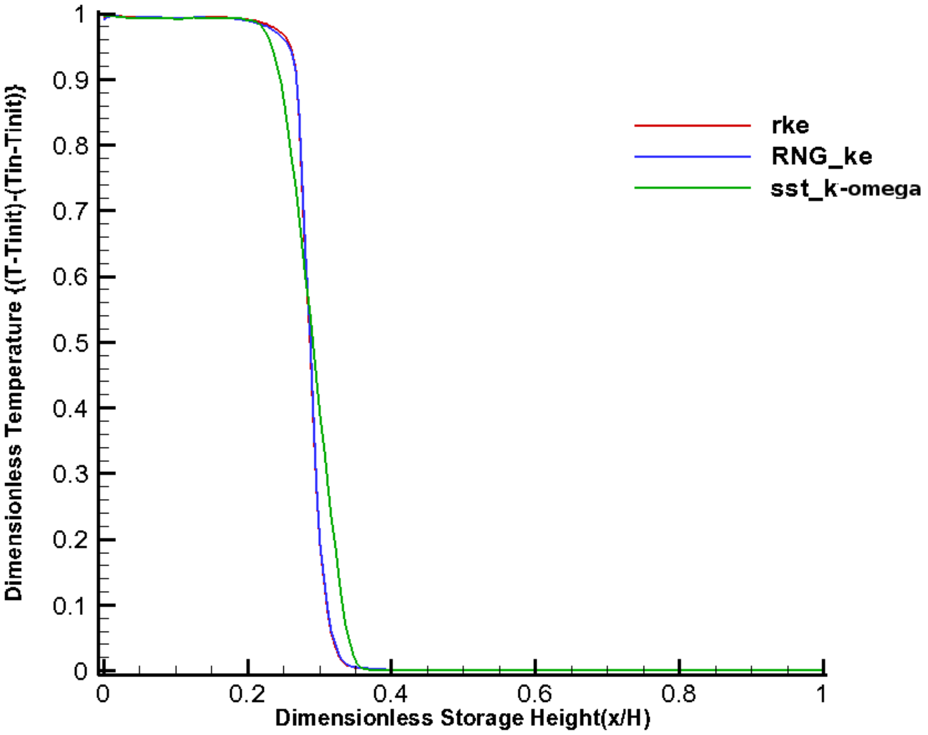

Figure 5.13: Dimensionless average temperature distribution in storage tank for charging volume flow rate 3 lpm with different turbulence models after 60 s with ($\Delta T = 20\,K$)

5.3.3 Charging with ΔT: 5 K

5.3.3.1 Laminar Simulation

As discussed in section 5.1.1, the laminar simulation seems to be an inappropriate choice for viscous model in simulation with 3lpm charging flow. Therefore, in charging with ΔT = 5 K, the simulations have been done only with different turbulence models. Since the same charging flow rate has been applied for simulation with ΔT = 5 K, the inertial forces are in the same range as the simulation with ΔT = 20 K. The buoyancy forces acting in the opposite direction, are smaller for the case with ΔT = 5 K.

5.3.3.2 Turbulent Simulations

Turbulent viscosity ratio represents the ratio between turbulent viscosity calculated by Boussinesq hypothesis and molecular viscosity of the fluid. After 20 seconds of charging, turbulent viscosity ratio contour shows that this ratio can increase until value about 26 in the lower part of the tank. It also indicates the importance of turbulence motions in this region. This contour shows the importance of turbulence and fluctuating motion at the lower part of the tank. As a consequence, an increased momentum transfer in this region causes mixing layers.

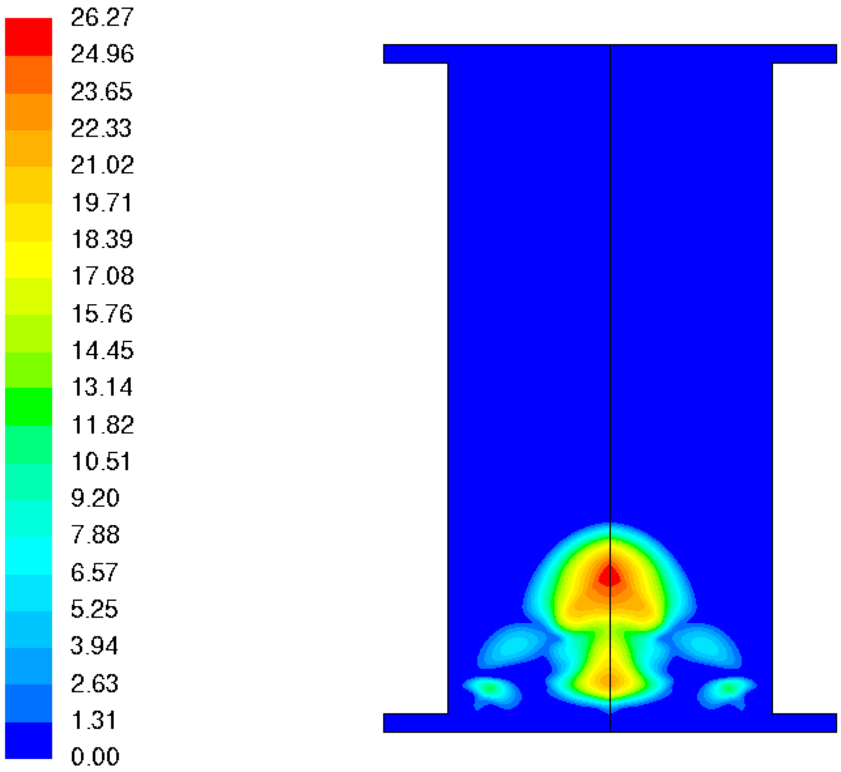

Figure 5.14: Turbulent viscosity ratio after 20 s charging for turbulent simulation with realizable $k - \varepsilon$ model for $\Delta T = 5\ K$

Figure 5.18 demonstrates the average dimensionless temperature distribution in the tank for simulation with different turbulence models. Also in the case of ΔT = 5 K, SST $k - \omega$ predicts a thicker thermocline in comparison to $k - \varepsilon$ models. One of the main differences between the SST $k - \omega$ model and standard $k - \omega$ model is the modified turbulent viscosity formulation to account for transport effects of turbulent shear stress. The modified formulation results in a more extended turbulent viscosity contours. Because of the smaller buoyancy forces in the case of ΔT = 5 K, the extended turbulent viscosity region causes a more extended temperature gradient field after each specific time of charging.

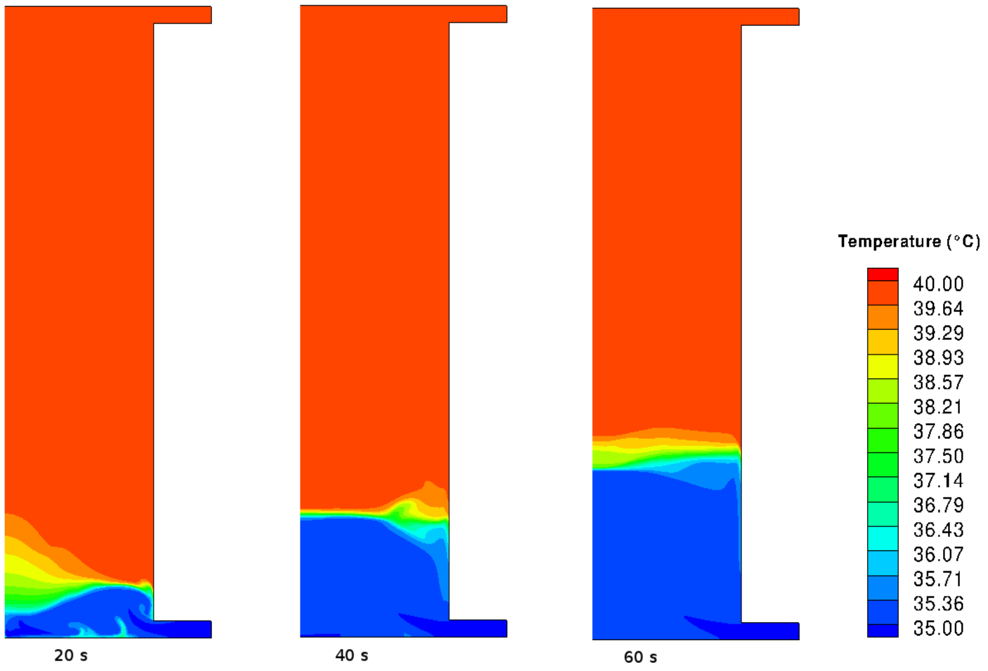

Figure 5.15: Temperature contours for simulation with realizable $k-\varepsilon$ model for charging volume flow rate of 3 lpm for $\Delta T = 5\ K$

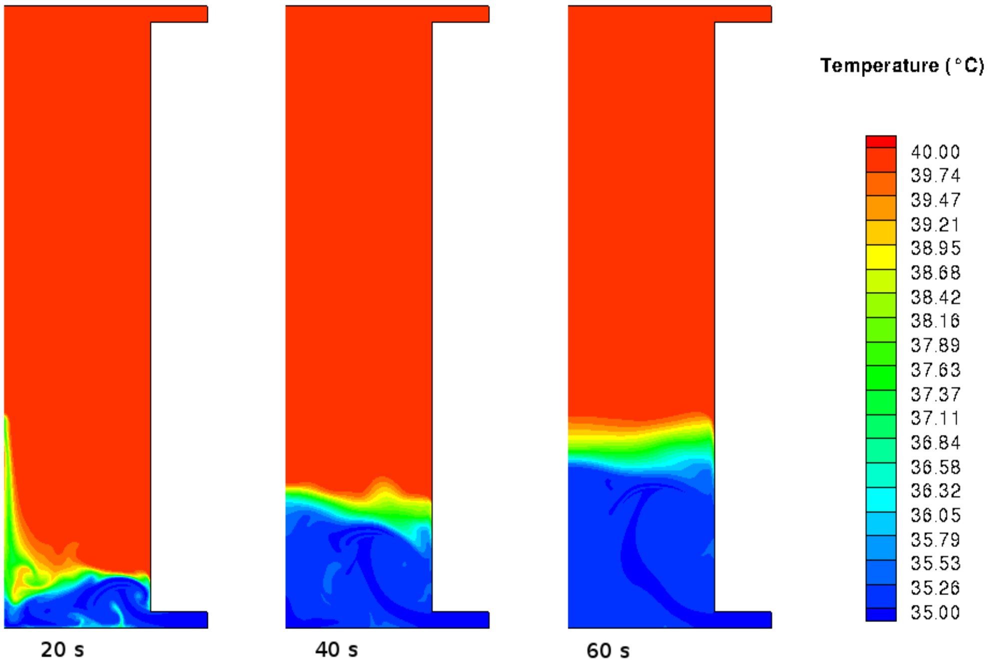

Figure 5.16: Temperature contours for simulation with SST $k-\omega$ model for charging volume flow rate of 3 lpm for $\Delta T = 5\ K$

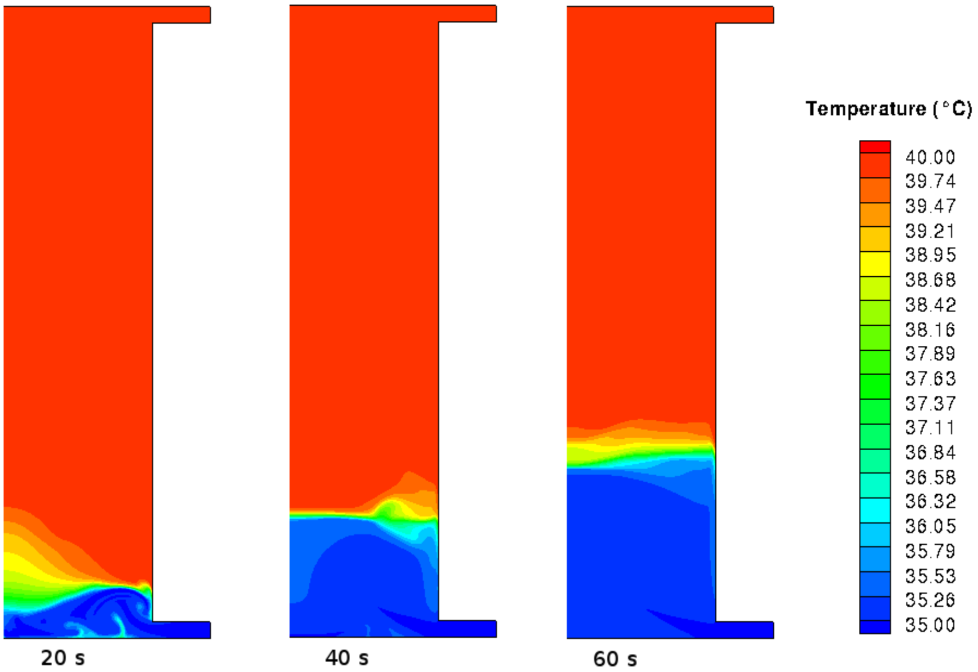

Figure 5.17: Temperature contours for simulation with RNG $k - \varepsilon$ model for charging volume flow rate of 3 lpm for $\Delta T = 5\ K$

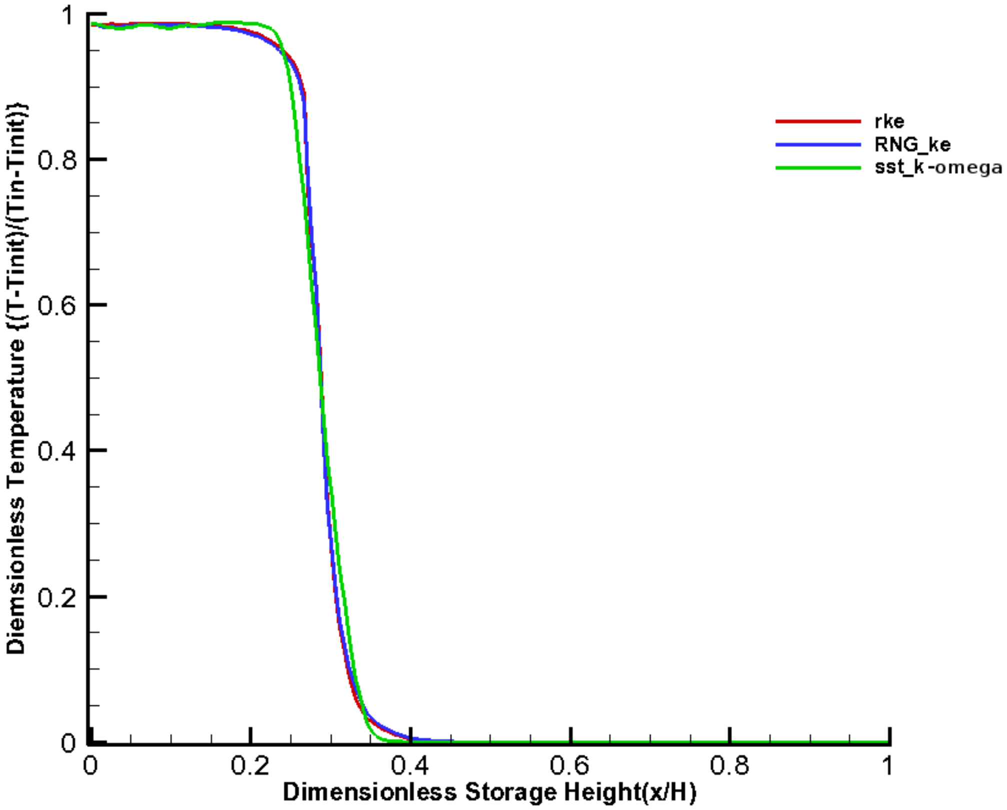

Figure 5.18: Dimensionless average temperature distribution in storage tank for charging volume flow rate of 3 lpm with different turbulence models after 60 s charging for $\Delta T = 5\ K$

5.3.4 Dimensionless Temperature Distribution in Charging Process with Different Temperature Difference

The main difference between simulations with different ΔT is in the buoyancy forces. These forces work because of the density difference between inflow and the fluid inside of the tank. In the current case, buoyancy forces work against the inertial forces which can be represented as forced convection. Richardson number, which represents the importance of natural convection to forced convection, has a higher value for the cases with higher ΔT. Therefore, inertial forces that intensify the mixing effect in the charging process can be damped stronger by the influence of buoyancy forces for higher Richardson number. On the other hand, fluctuating motion due to turbulence can be damped by the influence of buoyancy forces in higher level for higher Richardson number; therefore, momentum and heat transfer are reduced. Thus, it is expected that higher Richardson number in the current case results in more stratified storage tank. This effect can be seen in dimensionless temperature distribution comparison for ΔT = 20 K and ΔT = 5 K. Because of the smaller buoyancy forces for ΔT=5 K, momentum and heat transfer resulted from turbulent motion are higher, which leads to larger mixing layer and a thermocline with higher thickness.

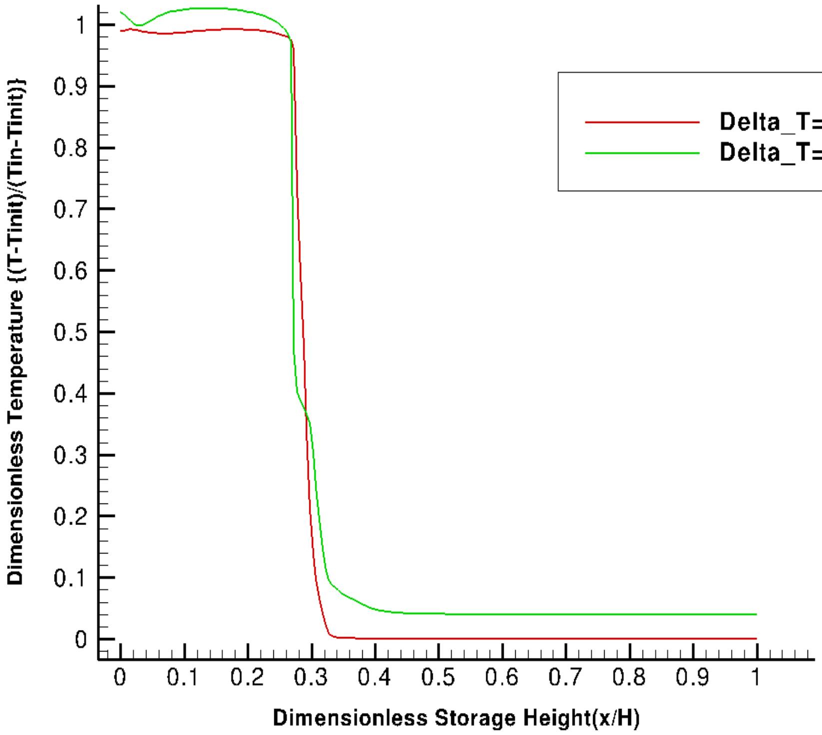

Figure 5.19: Dimensionless average temperature distribution in charging process with 3 lpm volume flow rate with $\Delta T = 20\ K$ and $\Delta T = 5\ K$

In calculation of Richardson number, the selection of characteristic length should adopt to the problem. There are two possibilities for the selection of characteristic length in the current simulation. The inlet port length and the height of the tank can be applied as characteristic length. The description of Richardson number as the ratio of natural convection and forced convection requires these two forces which works against each other. The buoyancy forces act in the vertical direction inside the tank due to the density difference between charging flow and the flow in the tank. So the height of the tank has been used as characteristic length in Richardson number calculation. In order to calculate the velocity, the volume flow rate through storage tank has been divided by the tank cross section. The average velocity in axial direction has been applied for Richardson number calculation as well.

5.3.5 Charging of TES with Higher Volume Flow Rate

Thermal stratification in storage tanks depends mainly on the flow rates of the fluid streams entering and exiting the tank, the size and location of the inlets and outlets and the volume of the tank [65]. In order to assess the impact of the inertial forces on the mixing and their significance in this context, the additional simulations with higher charging flow rate have been performed. Because of the higher Reynolds number in the whole tank and the higher possibility of a turbulent flow in a larger region of the tank, these parts of simulations have been run only with turbulence models.

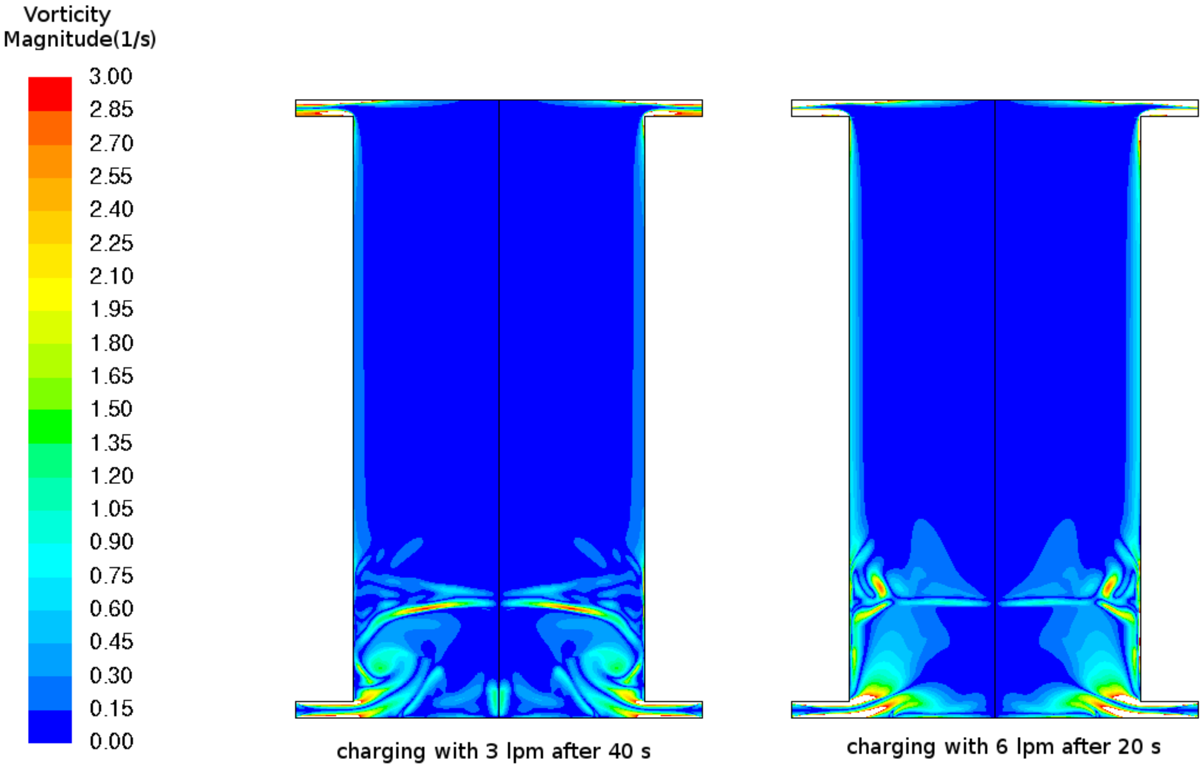

Figure 5.20: Vorticity magnitude (1/s) comparison for different charging volume flow rate with realizable $k - \varepsilon$ model and $\Delta T = 20\ K$

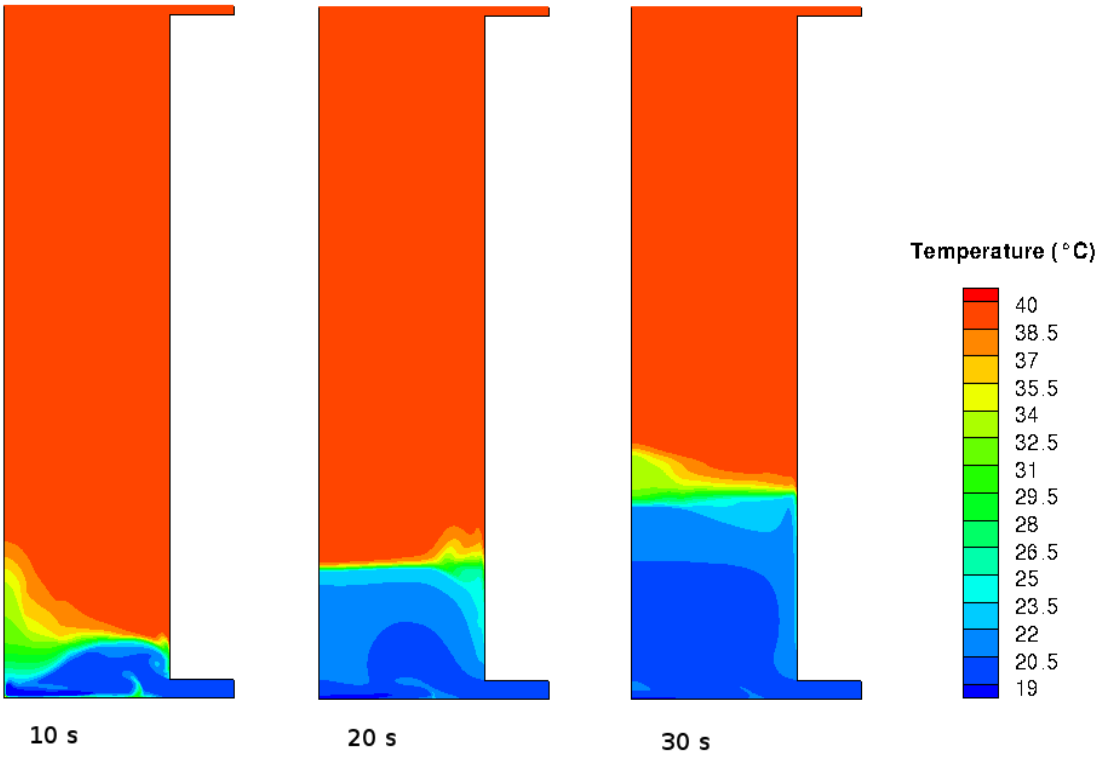

Figure 5.21: Temperature contours for simulation with realizable $k - \varepsilon$ model for charging volume flow rate of 6 lpm

A dimensionless temperature analysis has been performed for the charging with different volume flow rates. Dimensionless temperature is defined as follows:

$$T_{dl} = \frac{T - T_{init}}{T_{in} - T_{init}}$$

Figure 5.22 depicts the dimensionless temperature versus dimensionless tank height for charging mass flow rates of 3 and 6 liter per minute (lpm).

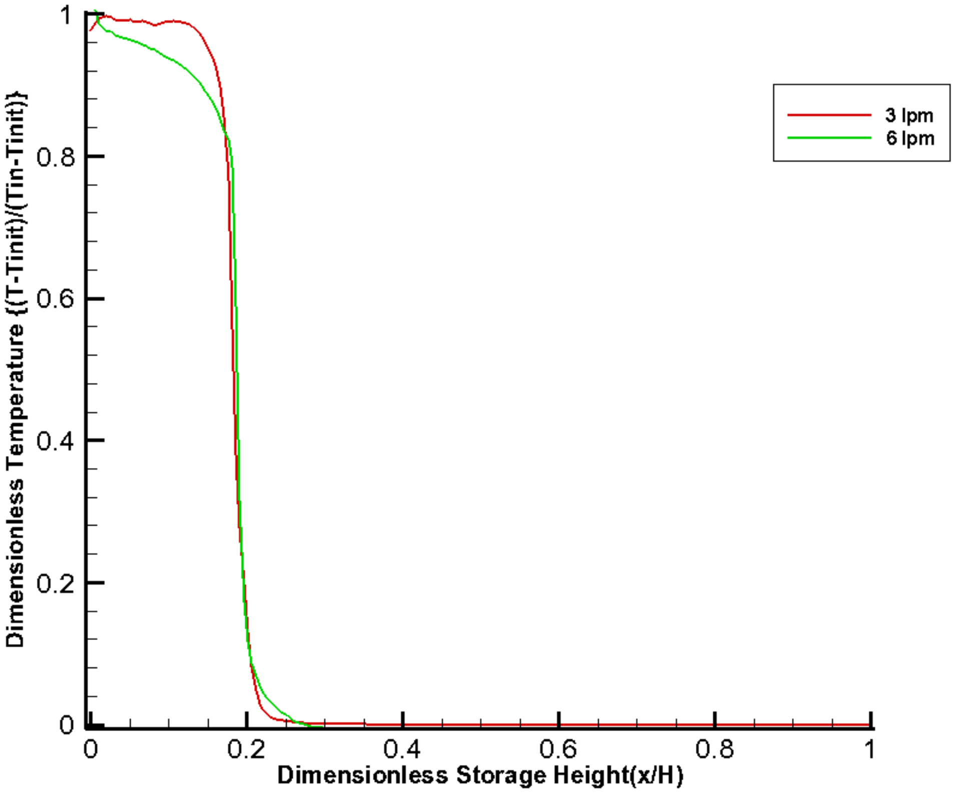

Figure 5.22: Dimensionless average temperature distribution in simulation with realizable $k - \varepsilon$ model and different charging volume flow rates for $\Delta T = 20\ K$ (3 lpm charging flow rate after 40 s and 6 lpm charging flow rate after 20 s)

Considering dimensionless temperature distribution in simulations with different charging volume flow rates, it can be concluded that thermocline thickness in the case of higher charging volume flow rate is higher than the case with lower charging volume flow rate. The main reason is the stronger mixing effect in case of higher charging flow rate due to the higher inertial forces, and consequently, higher fluctuating motion . This effect has been already observed by vorticity magnitude comparison between these two charging volume flow rates.

In simulation with higher charging volume flow rate, velocity magnitude of the flow in the shear layers is relatively higher than the simulation with lower charging flow rate. It leads to the higher velocity gradient and vorticity magnitude in a larger part of the TES, and therefore, stronger mixing.

5.4 Simulation of TES based on the Experimental Setup

5.4.1 Simulation Setup

In order to compare the results from simulation with available experimental results, new numerical model has been applied, and new simulations have been performed. One of the main deviations of the experimental setup from the numerical model is the presence of aluminum plate at the inlet port in the experimental setup. Aluminum plate has an initial temperature of 40 °C at the beginning of the charging process. The charging water flows to the tank through the inlet channel with 20 °C and is heated up in the vicinity of plate due to conduction.

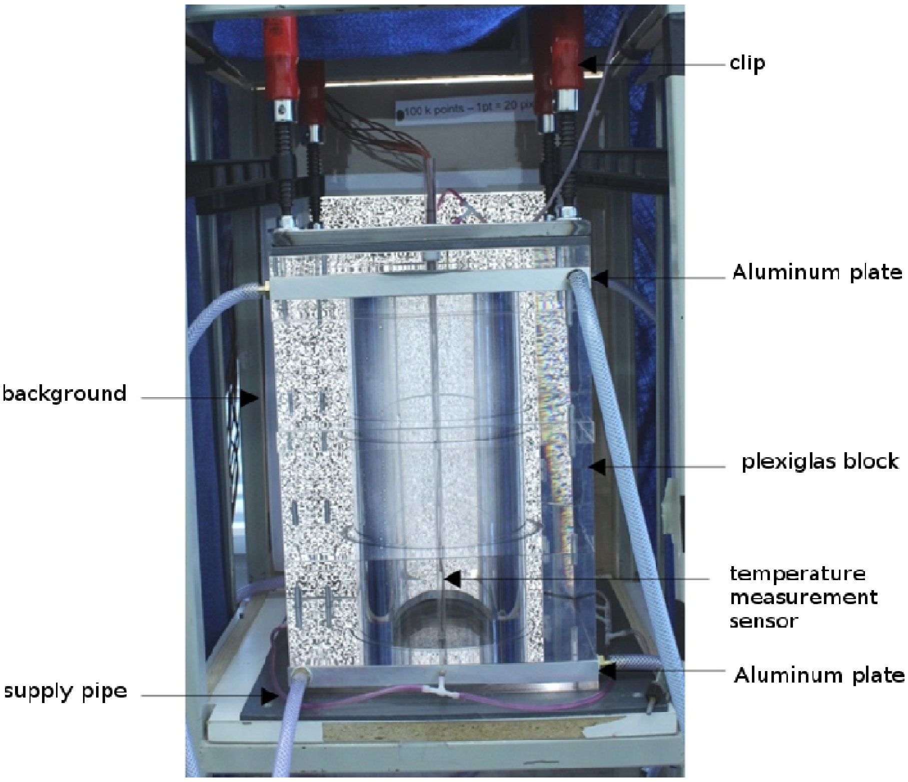

Figure 5.23: Experimental setup of the plexiglas storage tank

A block structured mesh with about 765000 quadrilateral cells has been generated in order to discretize the fluid domain. The mesh quality checking has been performed showing high quality values. The domain includes an inlet region and outlet region with two solid zones next to these regions. These two solid zones should represent the thermal effect due to the aluminum plate in the area of the inlet and outlet ports. The Aluminum plate has an initial temperature of 40 °C, and its temperature decreases during the charging process because of the heat transfer to the entering flow at the inlet. The Fluid domain has been simulated in a 2-D axisymmetric space, which represents the cylindrical geometry of the thermal storage tank.

Solution methods used for the simulation have been presented in table 5.1.

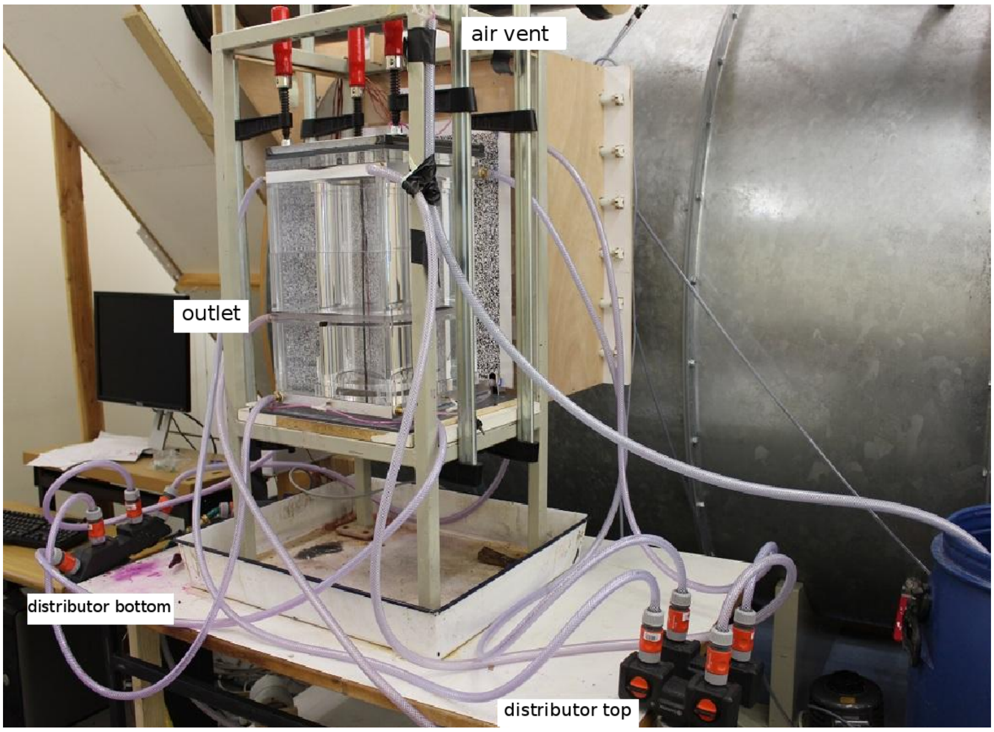

Figure 5.24: Experimental setup for charging process of the storage tank [66]

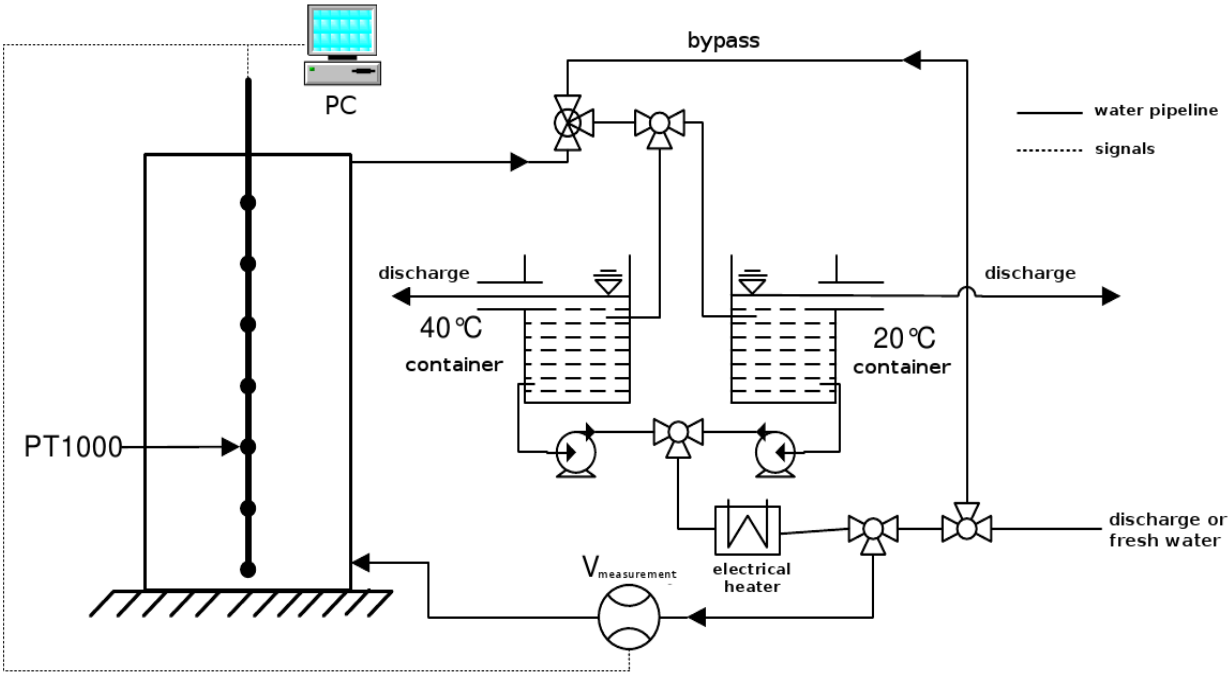

Figure 5.25: Schematic representation of experimental setup for charging process of the storage tank [66]

In different transient simulations, the water in the tank has been initially set to 40 °C and flow with 3 lpm volume flow rate enters from the inlet port at the bottom of the tank. In order to investigate the influence of the temperature difference between inlet flow temperature and water temperature inside the tank (ΔT) – as a representative parameter of the buoyancy forces and thereby Richardson number- two simulations have been performed with inlet flow temperature of 20 °C and 35 °C.

Figure 5.26 depicts the schematic illustration of storage tank CFD model with inlet and outlet ports and the aluminum plates. The tank has a height of 38 cm and a diameter of 18 cm. The extended part of the inlet channel has been considered with 10 cm in radial direction. The charging inflow in the storage tank is in radial direction, so the influence on the mixing process and destratification is relatively less than inflow in axial direction.

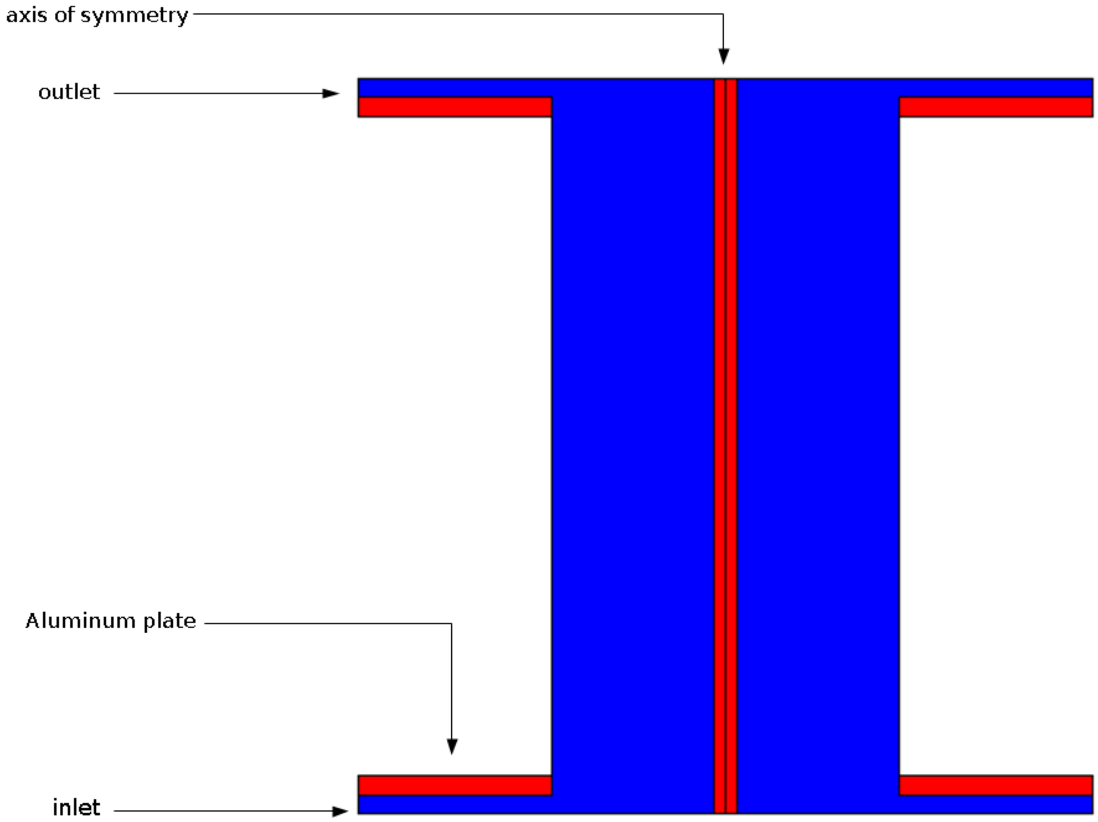

Figure 5.26: Schematic illustration of the storage tank CFD model with aluminum plates at the inlet and outlet ports

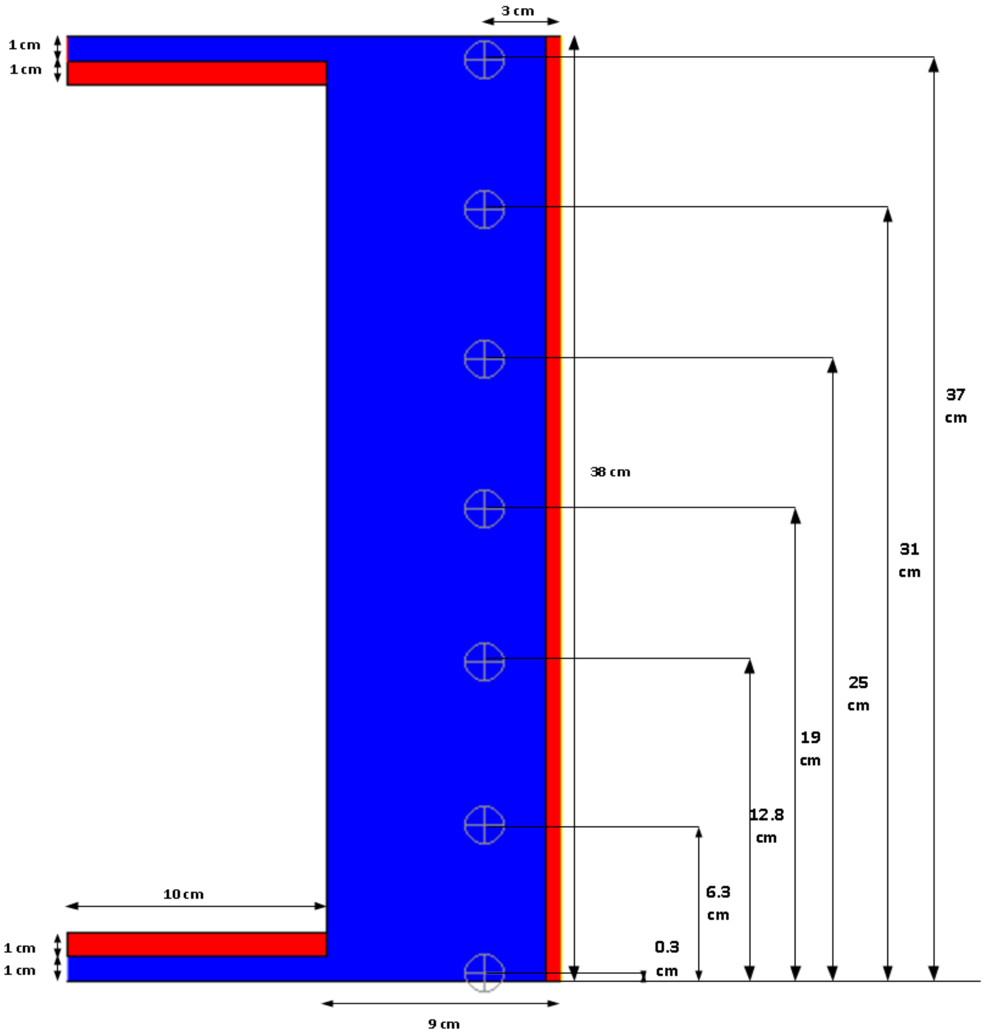

Figure 5.27: Schematic view of the storage tank with dimensions and temperature sensors position

Table 5.1: Applied solution and discretization methods for simulation case setup

Pressure-Velocity Coupling algorithm	Coupled
Spatial discretization for pressure	Body force weighted
Spatial discretization for momentum	Second order upwind
Spatial discretization for turbulent kinetic energy	Second order upwind
Spatial discretization for turbulent dissipation rate	Second order upwind
Transient formulation	Second order implicit
Time step size (s)	0.1
Fluid material	Water

In this part, it has been tried to compare the obtained temperature values from experiment at temperature sensors with the numerical simulation outcomes for different charging conditions.

The experimental part of the study has been performed in a parallel work from Chirag Joshi in institute of fluid machinery in Karlsruhe institute of technology.

Modeling of Aluminum Plate

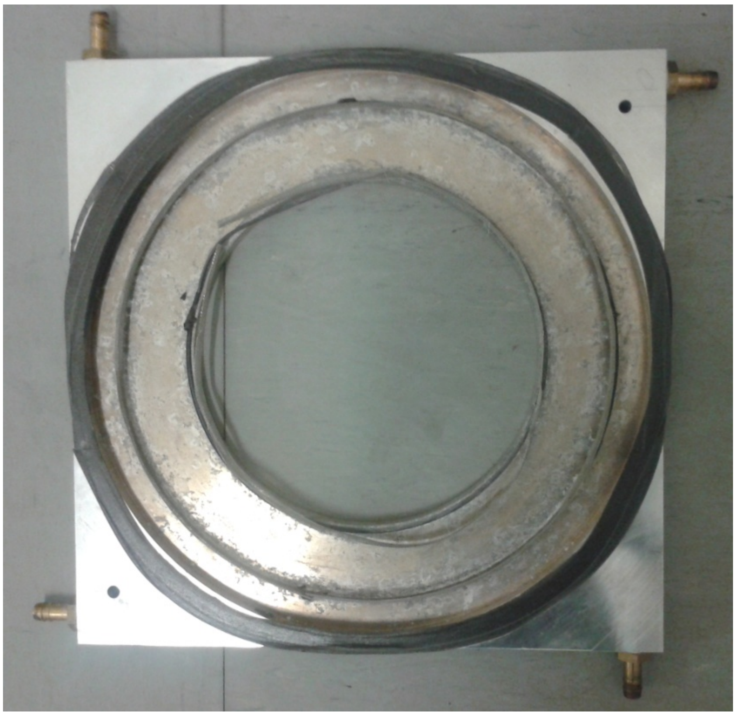

Figure 5.28: Aluminum plate used in experimental setup

Thermal mass of the aluminum plate has been modeled by means of the disk with equal volume around of tank entrance channel. The disk volume has been calculated as follows

$$(300 \cdot 300 \cdot 20) - \left(\pi \cdot \frac{180^2}{4} \cdot 20\right) - \left(\pi \cdot \frac{(290^2 - 180^2)}{4} \cdot 10\right) = \left(\frac{\pi}{4}\right) \cdot 10 \cdot (d^2 - 180^2)$$

$$d = 380\,mm \rightarrow Extension\ Length = (380 - 180)/2 = 100\,mm$$

As it can be seen in figure 5.27, a 100 mm extension of aluminum plate model on the inlet channel with the height of 10mm has been considered in CFD model. The conductive heat transfer between the aluminum plate model and the inlet channel wall results in temperature rise of the inflow in the wall region of the entrance channel.

5.4.2 Charging Flow with ΔT: 20 K

Reynolds Number Analysis in the Storage Tank

Figure 5.29 demonstrates the contours of Reynolds number in the storage tank after 30s charging with charging volume flow rate of 3 lpm. It should be mentioned that the characteristic length applied in this analysis is diameter of the storage tank. Evaluation shows that the Reynolds number in some regions of TES can rise up to 4700. Reynolds number increases in the inlet channel from inlet port until the entrance of the storage tank due to the velocity increasing in the channel. The charging mass flow rate in the channel remains constant, while the cross section of charging flow reduces. It is because of the ring- shape inlet cross section in 2D-axisymmetric flow. By decreasing of radius through the entrance channel, the flow cross section, which includes a ring in perimeter of the tank, decreases in a higher scale leading to a considerable increase in radial velocity magnitude towards the entrance of the tank. Furthermore, the maximum Reynolds number at the inlet port based on the outer perimeter of the tank as characteristic length is about 2800. Simulation with turbulence models, therefore, seems meaningful to obtain more reasonable and accurate results.

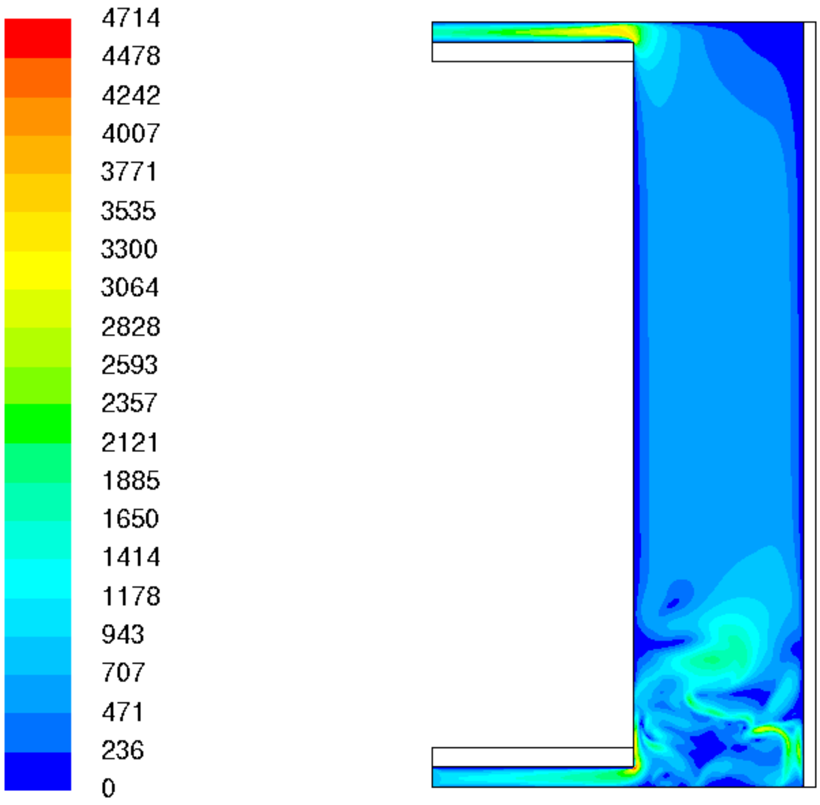

Figure 5.29: Reynolds number evaluation in storage tank based on tank diameter as characteristic length with 3 lpm charging volume flow rate after 30 s charging time in laminar simulation for $\Delta T = 20\ K$

Laminar Simulation

In laminar simulation, the charging process of TES with different charging temperatures has been studied.

Regarding the streamline contours, it can be concluded that eddies start to be created at the region where flow enters the storage tank. The analysis of the vorticity in the tank in a transient simulation illustrates that in the course of time during the charging process, the Vorticity values rise and the affected regions extend. Higher number of eddies in streamline contours by charging time progress confirms the extending of the regions with higher vorticity, and therefore, more mixing during the charging. Higher value of vorticity and eddies with different length scales at the lower part of the tank increases the possible turbulent flow in the near of the inlet channel. The calculated temperature contours for laminar simulation also shows some sharp edges of the temperature layers, which seems to be due to the inappropriate reproduction of the flow structure with laminar calculation.

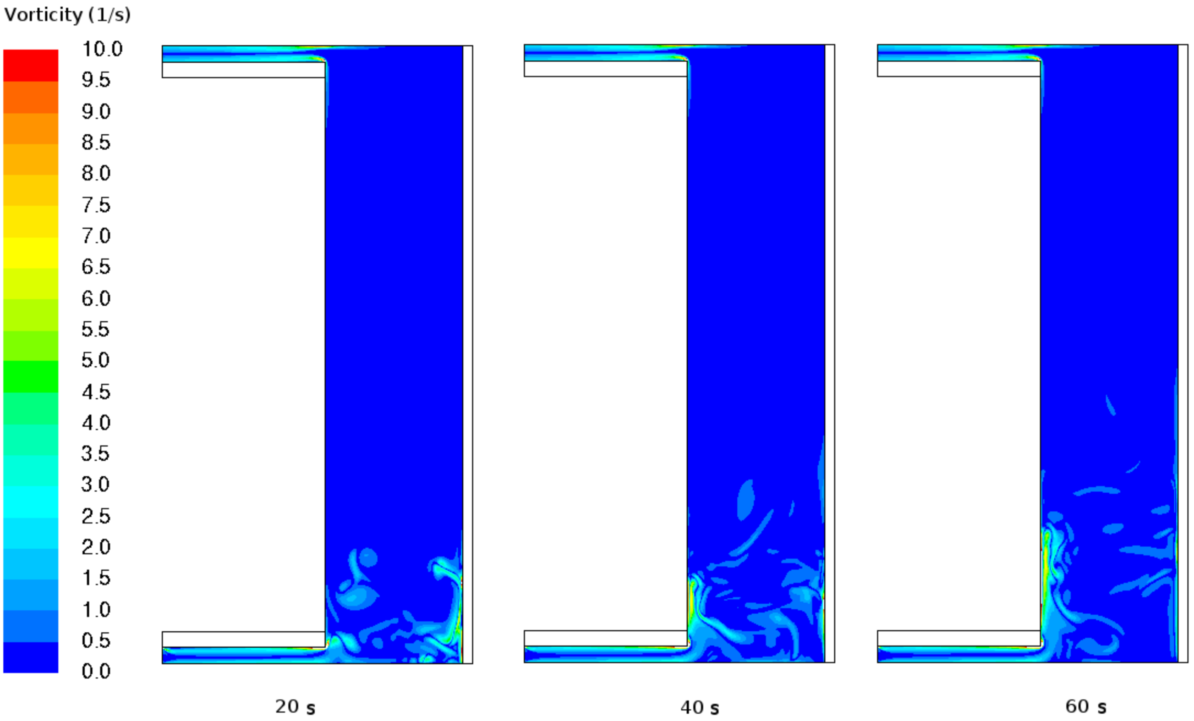

Figure 5.30: Vorticity contours for charging with 3 lpm in laminar simulation for $\Delta T = 20\ K$

High values of vorticity are observed at the wall region, which is because of higher velocity gradient. The vorticity value at this region increases by higher charging time. Streamline visualization at different charging time shows flow rising at the wall region after leaving the entrance channel. Due to higher temperature of aluminum plate, flows close to the wall become warmer than the flows in lower layers. Due to this effect, lower layers of fluid leaving the entrance channel are colder and tend to flow in radial direction owing to buoyancy force. On the other hand, upper flow layer in the entrance channel are warmer than the fluid in the lower layers and tend to rise after entering to the tank. This causes a higher temperature gradient in the radial direction and more non-homogeneous temperature of fluid layers in radial direction. Temperature contours at different charging time also represents the building of this thermal boundary layer at the wall region which works as a destratification factor.

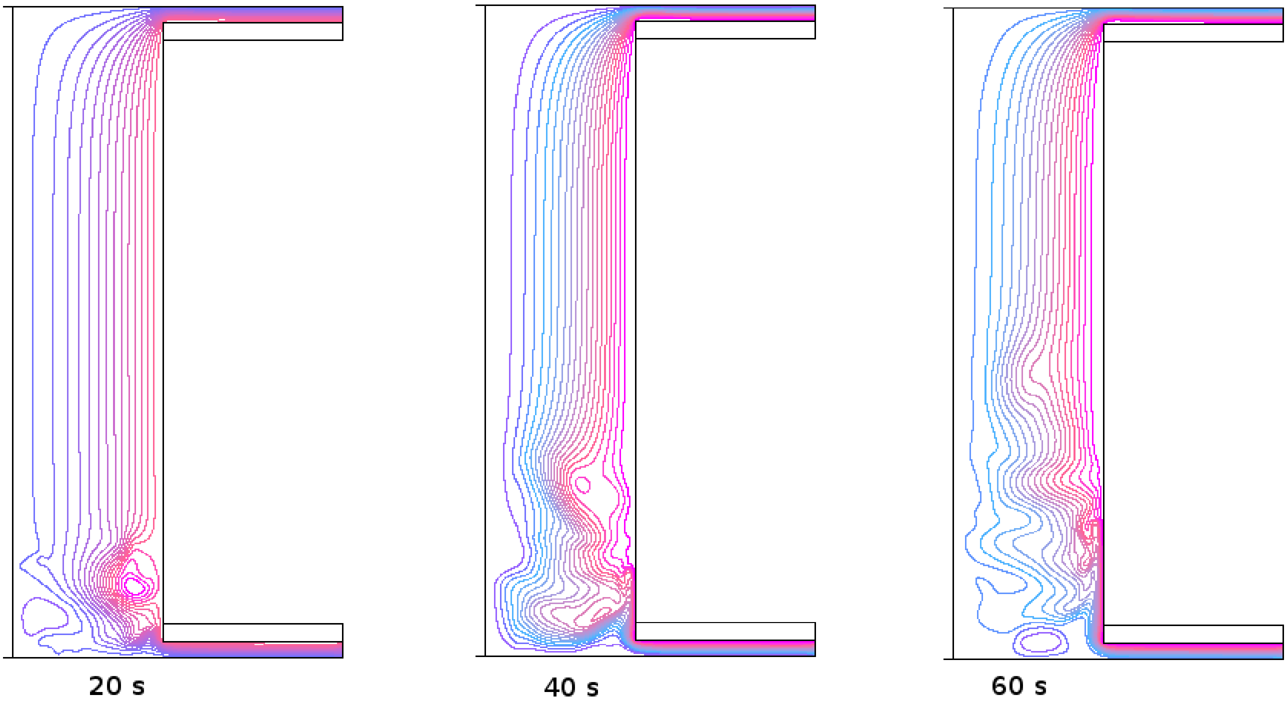

Figure 5.31: Streamlines for charging flow of 3 lpm in laminar simulation at different charging time for $\Delta T = 20\ K$

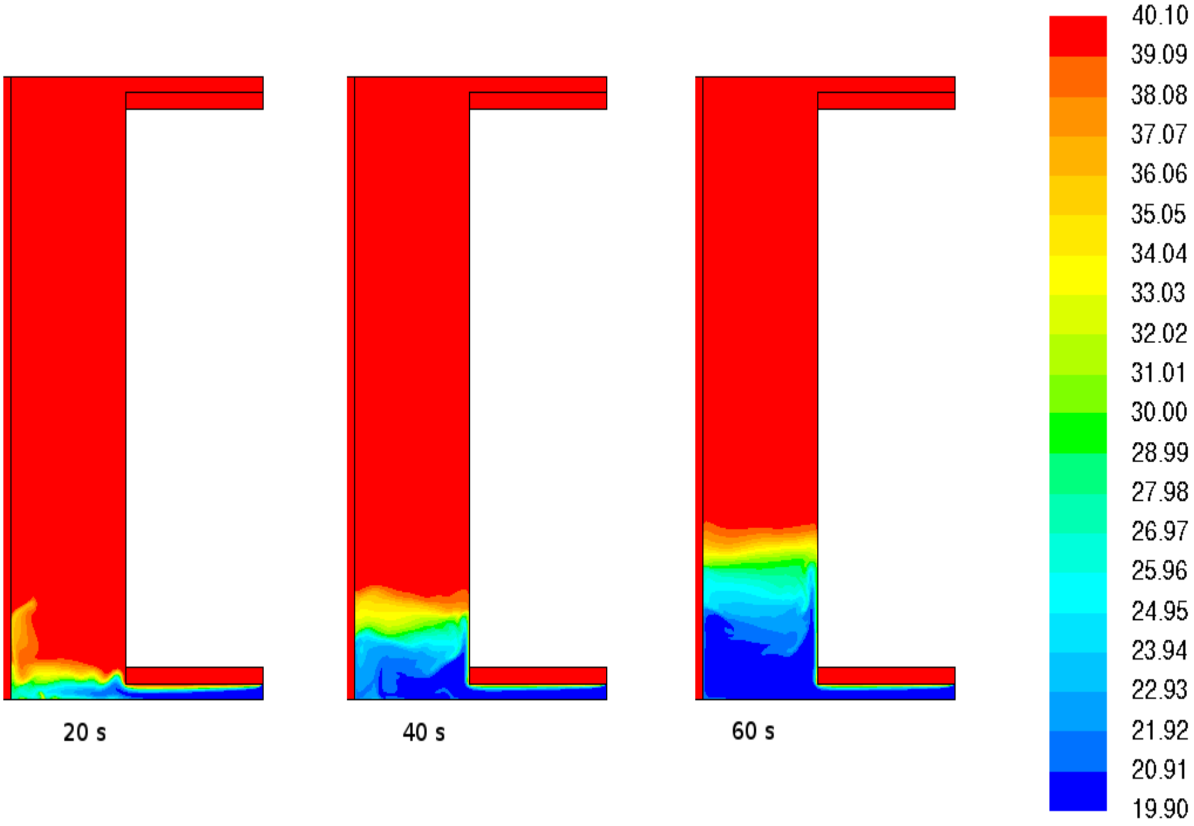

Figure 5.32: Temperature contours at different charging time for laminar simulation with $\Delta T\ =\ 20\ K$

Turbulent Simulation with Realizable $k-\varepsilon$ Model

High Reynolds number and value of vorticity at the lower part of the tank make the additional turbulent simulation reasonable. Realizable $k-\varepsilon$ model has been applied for the first turbulent simulation. Enhanced wall treatment has been used for near wall treatment in turbulence model.

The obtained results with this turbulence model have shown a good agreement with the experimental results in the previous studies in buoyancy- driven flow in TES [5]. Figure 5.33 shows the turbulent viscosity ratio contour for simulation with realizable $k-\varepsilon$ model. Turbulent viscosity ratio represents the importance of the turbulent fluctuations to the molecular viscosity of the fluid. Based on Figure 5.33, it can be concluded that turbulent viscosity ratio at the lower part of the tank raises to values more than 7 with charging flow rate of 3 lpm. As a result, the possibility of turbulent flow in this region is higher and turbulent simulation results of this region can be more accurate than the laminar simulation. Because in turbulent simulation, the viscosity of fluid has been calculated in an effective value which is the summation of molecular viscosity and the turbulent eddy viscosity.

Vorticity contour at smaller charging time shows high values close to the central axis. When charging time increases, vorticity values near the central axis decrease, but higher values show up at the wall region.

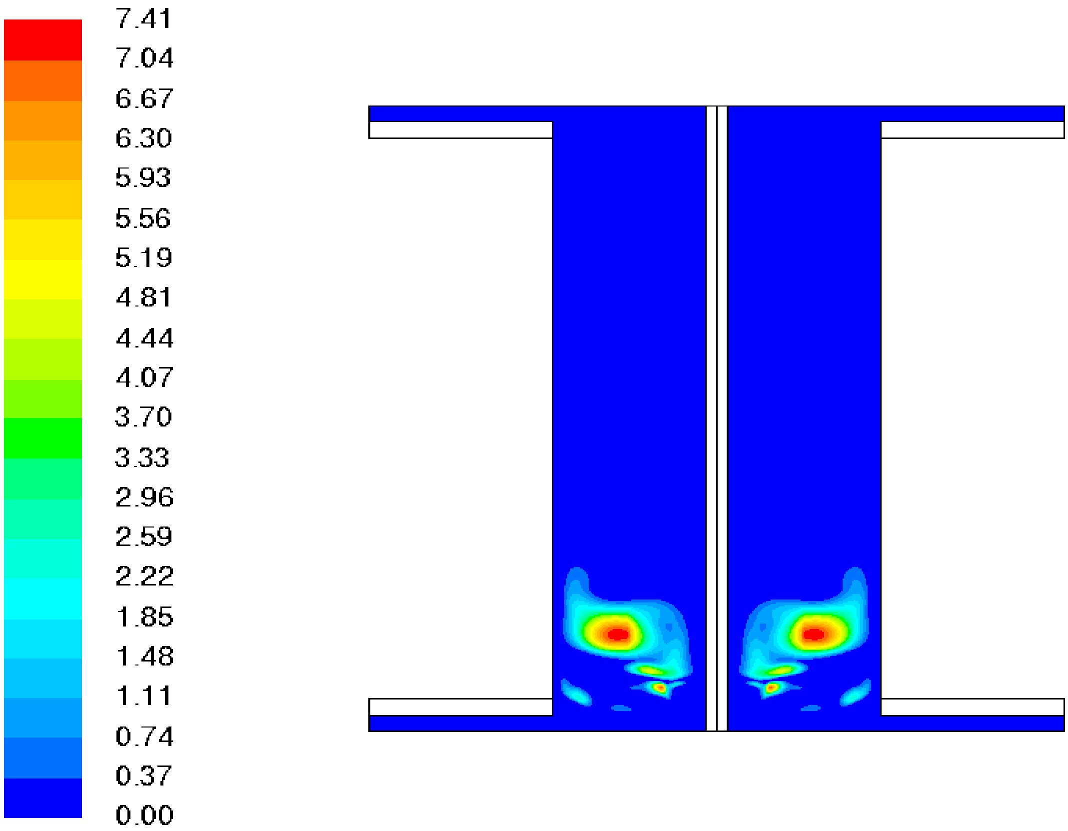

Figure 5.33: Turbulent viscosity ratio after 30 s charging for turbulent simulation with realizable $k-\varepsilon$ model and ΔT = 20 K

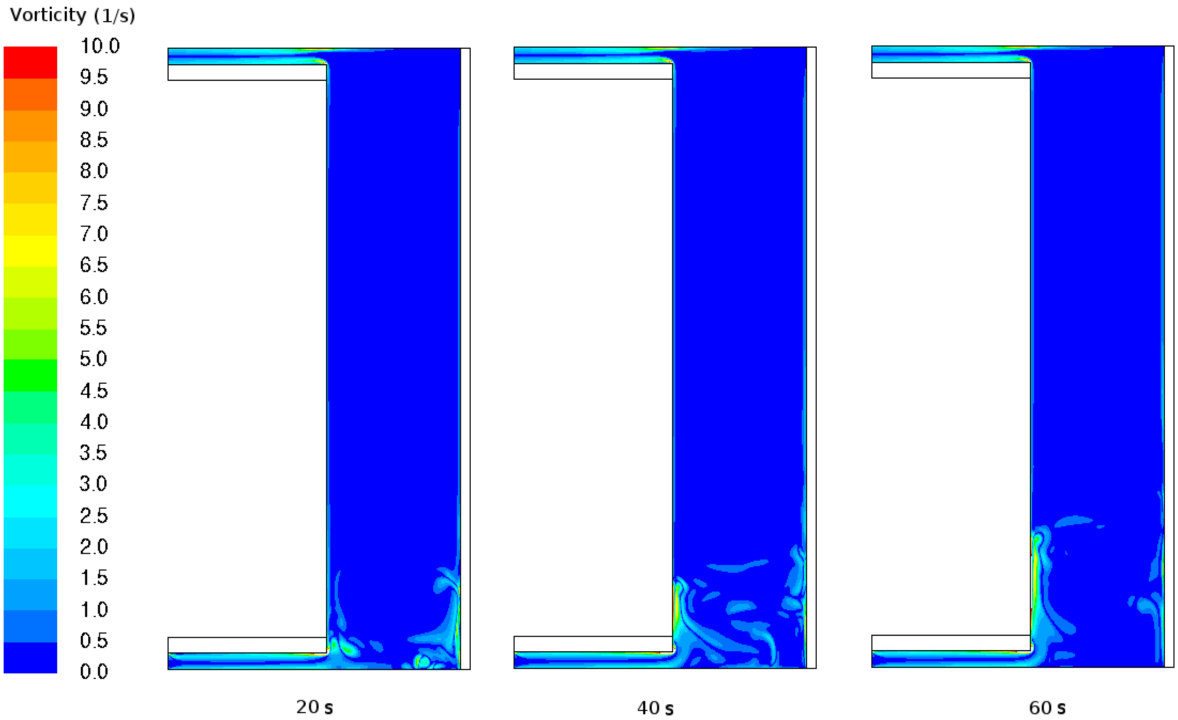

Figure 5.34: Vorticity contours for charging with 3 lpm in turbulent simulation with realizable $k-\varepsilon$ model for ΔT = 20 K

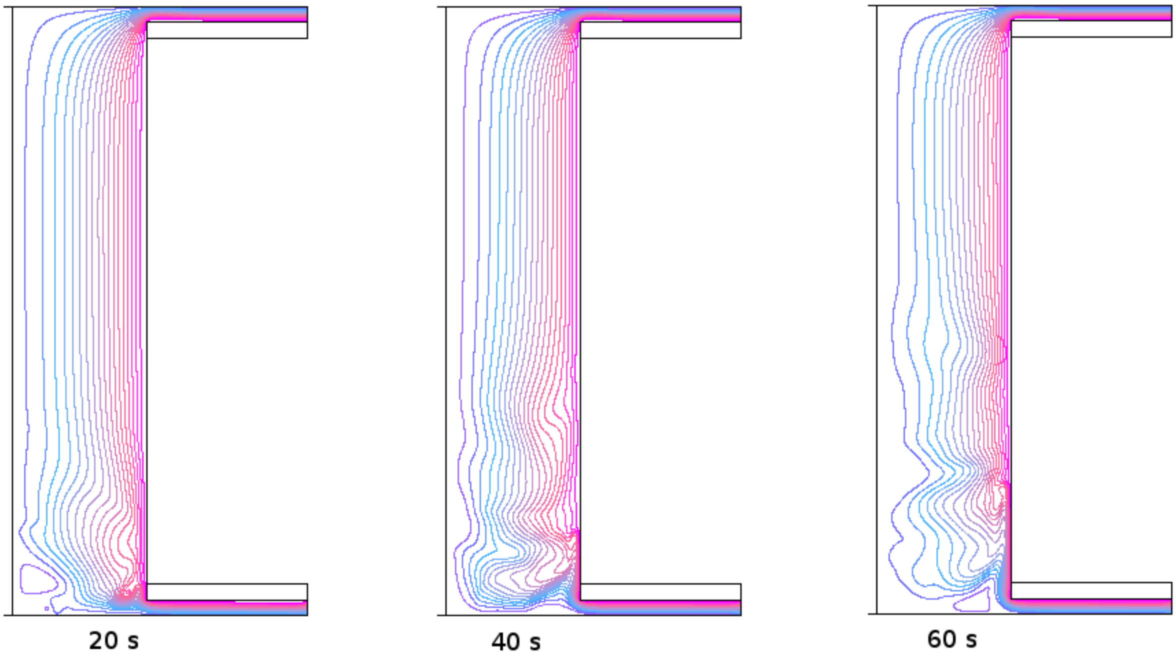

Figure 5.35: Streamline for charging flow of 3 lpm in turbulent simulation with realizable $k-\varepsilon$ model at different charging time for ΔT = 20 K

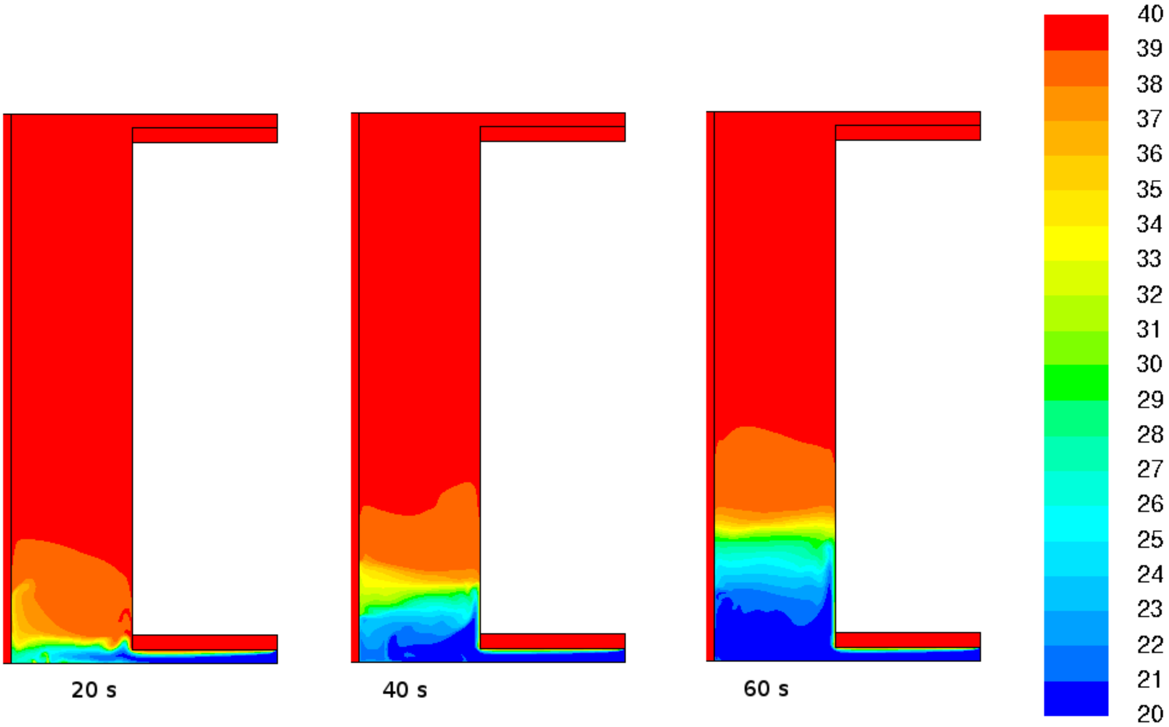

Figure 5.36: Temperature contours at different charging time for turbulent simulation with realizable $k - \varepsilon$ model and $\Delta T = 20\ K$

The Comparison of turbulent calculation results with laminar calculation illustrates that in turbulent simulation, recirculation regions are smaller, and less number of eddies appear in the region close to inlet channel.

Because of the relative small ratio of the eddy viscosity to molecular viscosity, the influence of the selected viscous model on the fluid variables becomes less important. Thus, the deviation between laminar and turbulent simulation results becomes less remarkable especially for the average values over horizontal surfaces.

5.4.3 Charging Flow with ΔT: 5 K

The new simulations have been performed in order to investigate the effect of buoyancy forces that is caused due to the temperature difference between the charging flow and the fluid inside the tank. In this study, the buoyancy forces work in the opposite direction to the inertial forces owing to the charging inflow. The same simulation setup as ΔT=20 K has been used for this simulation.

Turbulent Simulation with Realizable $k - \varepsilon$ Model

Also For ΔT = 5 K, the turbulent calculation with realizable $k - \varepsilon$ model has been performed.

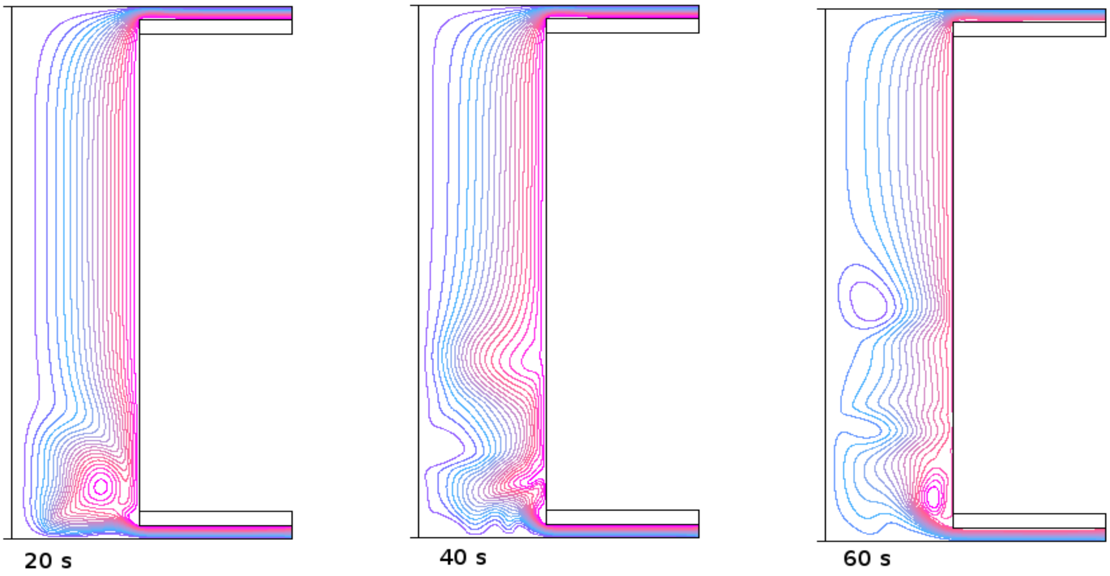

Figure 5.37: Streamline for charging flow of 3 lpm in turbulent simulation with realizable $k - \varepsilon$ model at different charging time and $\Delta T = 5\ K$

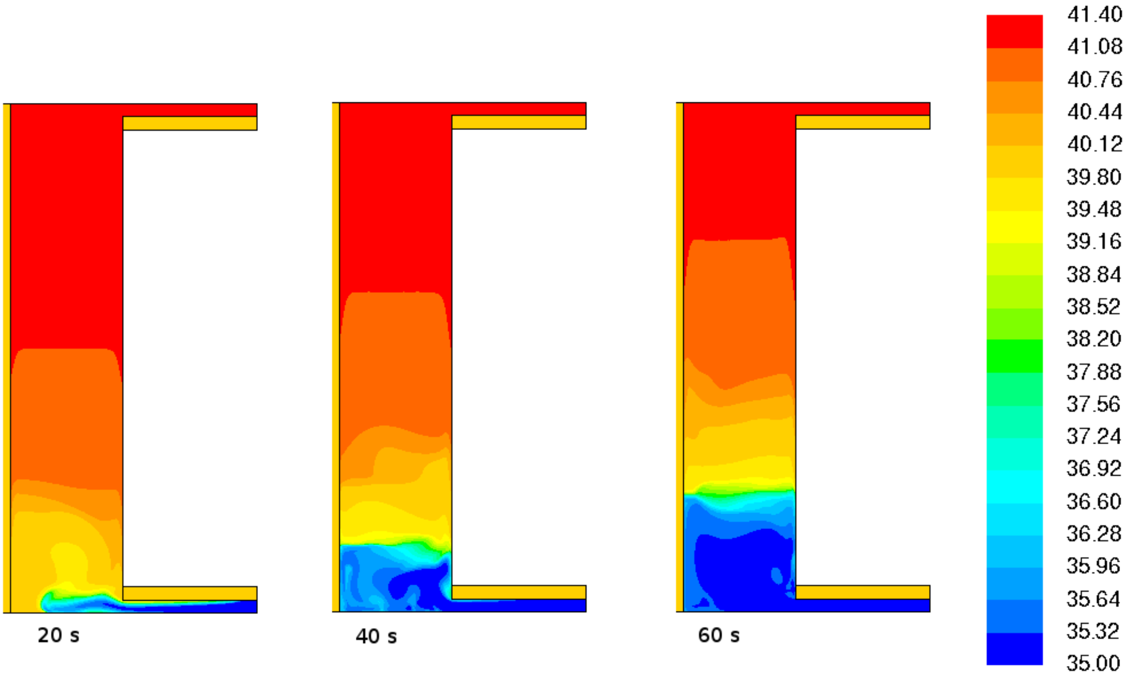

Figure 5.38: Temperature contours (°C) for charging flow of 3 lpm in turbulent simulation with realizable $k - \varepsilon$ model at different charging time and $\Delta T = 5\ K$

The influence of buoyancy forces in damping of turbulent motions at the region of inflow from channel to the tank is smaller in the case of ΔT = 5 K. Higher thermal diffusion observed in temperature contours, therefore, seems to be an outcome of stronger turbulent diffusion in comparison with case of ΔT = 20 K.

The temperature contour in the inlet channel shows that after 20 seconds charging, a larger thermal boundary layer has been built in the entrance channel next to the aluminum plate. This thermal boundary layer becomes smaller by the charging time progress due to the heat transfer from plate to the inflow, and therefore, less temperature difference between plate and inflow. For this reason, the influence of thermal boundary layer at the wall for lower ΔT is relatively smaller, which results in small value of vorticity at the wall region and less mixing at this region.

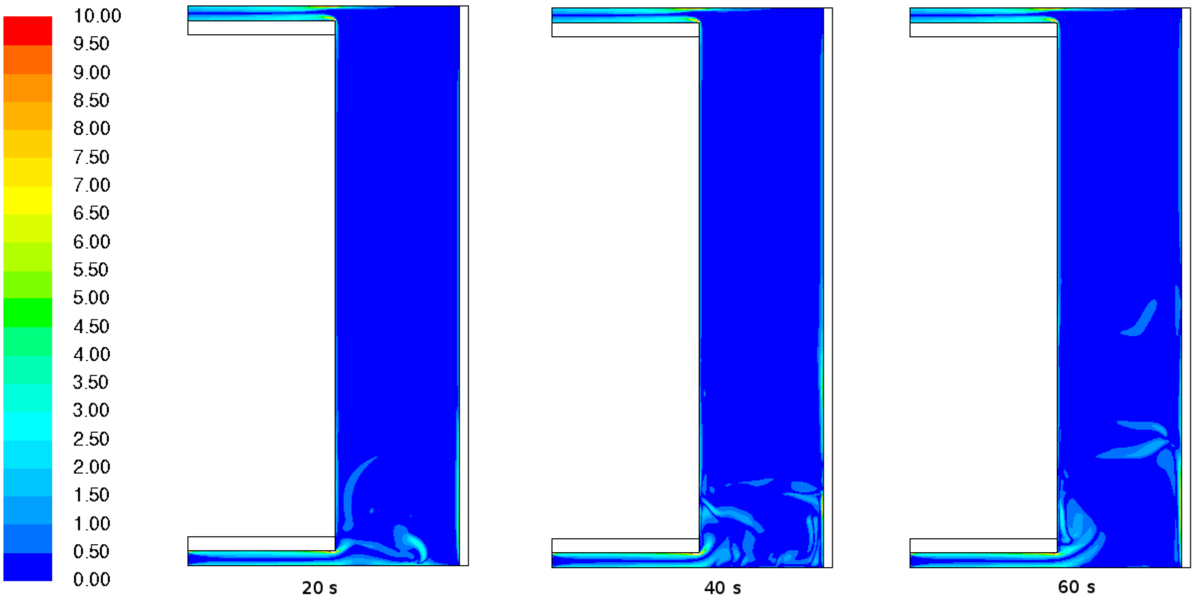

Figure 5.39: Vorticity contours (1/s) for charging with 3 lpm in turbulent simulation with realizable $k-\varepsilon$ model for $\Delta T = 5\ K$

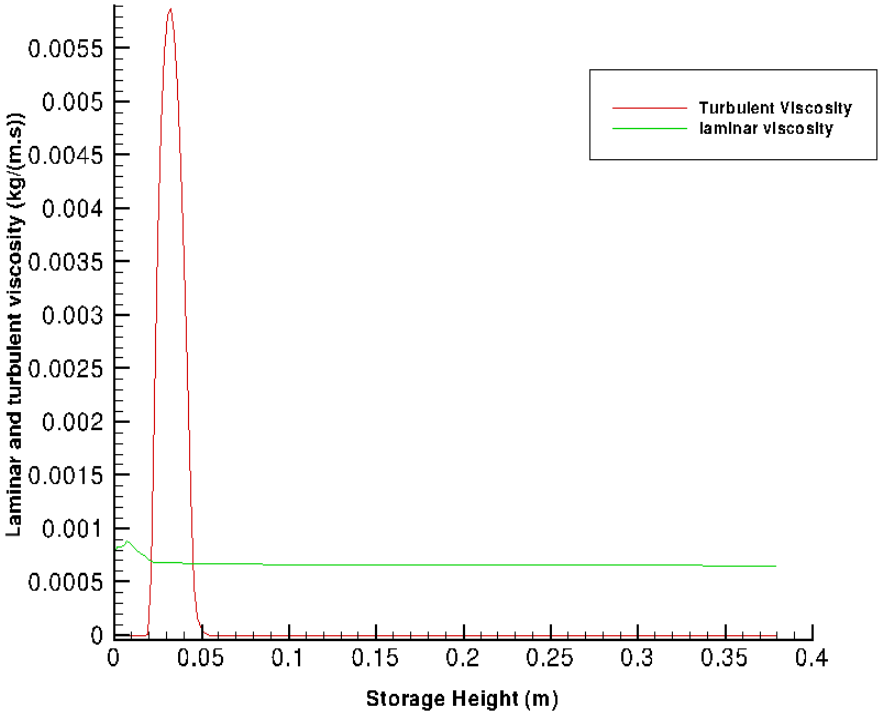

Figure 5.40: Laminar and turbulent viscosity for calculation with realizable $k-\varepsilon$ model in vertical direction with 3 cm distance from central axis of the storage tank after 20 s charging time for $\Delta T = 5\ K$

Turbulent and laminar viscosity plot after 20 seconds of charging shows that turbulent viscosity can rise up to 8 times larger than laminar viscosity at the lower part of the tank. This confirms the importance of the Reynolds stresses and turbulent fluctuations at the bottom of the tank. For this reason, any parameter that works as a damping parameter against the turbulent diffusion like buoyancy forces in the current simulation can be more influential in the mixing process.

5.4.4 Richardson Number Calculation in Simulations with Different ΔT

According to equation 3.3(see chapter 3), Richardson number for the cases with different charging temperatures has been calculated. Table 5.2 represents the Richardson number value at the storage tank inlet for ΔT = 20 K and ΔT = 5 K.

Richardson number calculation for ΔT = 20 K is as follows:

$$u_{av} = \frac{4Q}{\pi d^2} = \frac{4 \cdot 0.00005}{\pi \cdot 0.18^2} = 1.964 \cdot 10^{-3}$$

$$Ri = \frac{(\rho - \rho_m) g H}{\rho_m {u_{av}}^2} = \frac{(998.3 - 992.3) \cdot 9.81 \cdot 0.38}{992.3 \cdot (1.964 \cdot 10^{-3})^2} = 5843.56$$

Richardson number calculation for ΔT = 5 K as follows:

$$Ri = \frac{(\rho - \rho_m) g H}{\rho_m {u_{av}}^2} = \frac{(994.1 - 992.3) \cdot 9.81 \cdot 0.38}{992.3 \cdot (1.964 \cdot 10^{-3})^2} = 1753.06$$

Table 5.2: Richardson number at the inlet port

Temperature difference	Richardson number at the inlet port
ΔT = 20 K	5843.56
ΔT = 5 K	1753.06

5.5 Experimental Analysis of TES Charging Process

Experimental study of the corresponding charging process has been widely performed in diploma thesis of Florian Feuerstein [66]. Additionally, the experimental investigation of the model storage tank with a perforated pipe covered with polyurethane foam as charging device has been performed by supervising the master thesis of Anders Berg [67]. Background Oriented Schlieren (BOS), which belongs to new flow analysis methods, has been applied for flow visualization. The BOS method combined with PIV(Particle Image Velocimetry) is used to observe the density and temperature field [66].

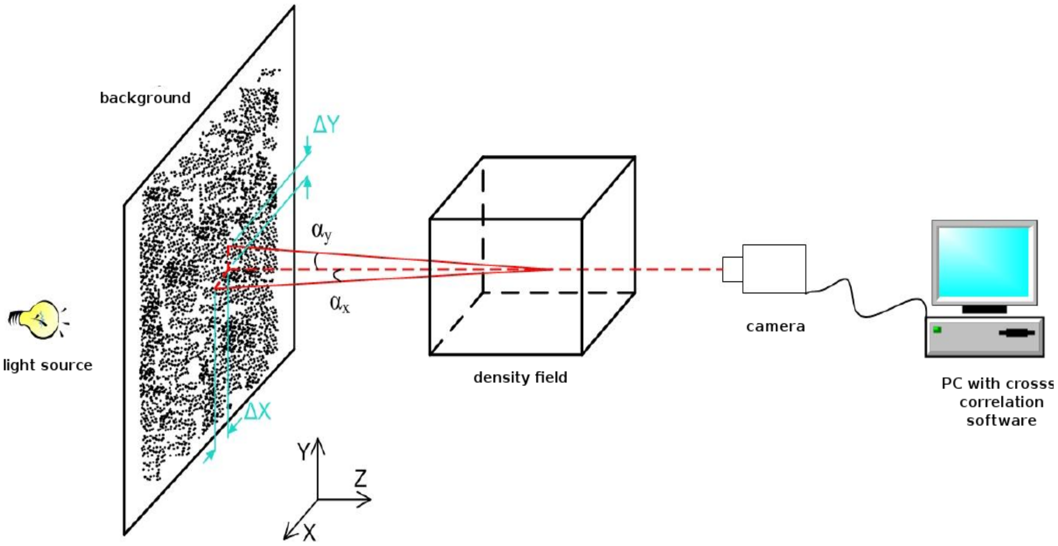

Figure 5.41: Schematic illustration of BOS method [66]

The PT1000 sensors have been also used to measure the temperature at the specified vertical position in the tank.

Figure 5.42 demonstrates how the temperature sensors positioned in the tank start to change when thermocline reaches to their vertical position.

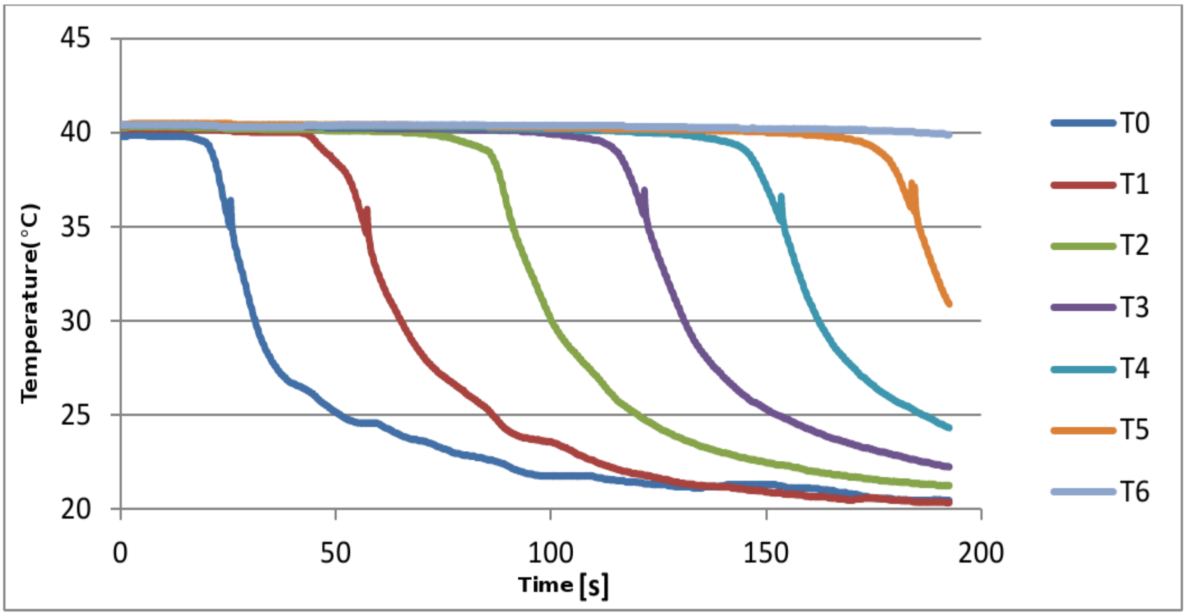

Figure 5.42: Temperature sensors time progress in charging process with $\Delta T = 20\ K$ [66]

The thermocline development in the charging process with $\Delta T = 20\ K$ has been observed by means of video capturing. In order to compare the tank situation in a specified moment with a reference situation, a reference image has been taken from the tank with 40°C filled water. Figure 5.43 represents the reference image and the image in a later time.

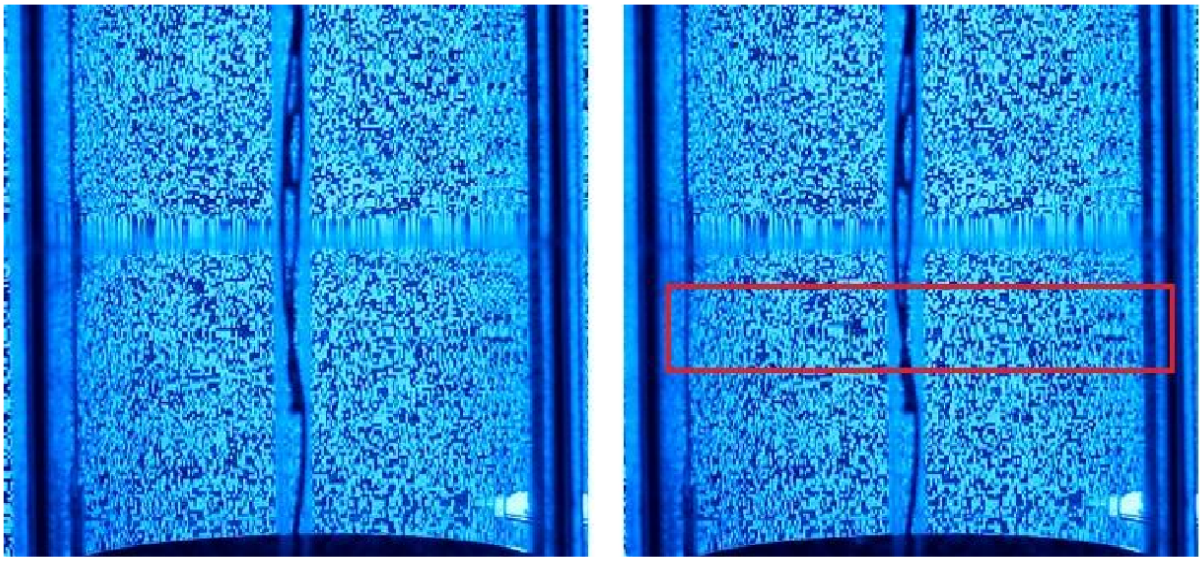

Figure 5.43: Comparison of reference image for the tank with 40 °C water(left) and image for the charging with 20 °C in a later time(right) [66]

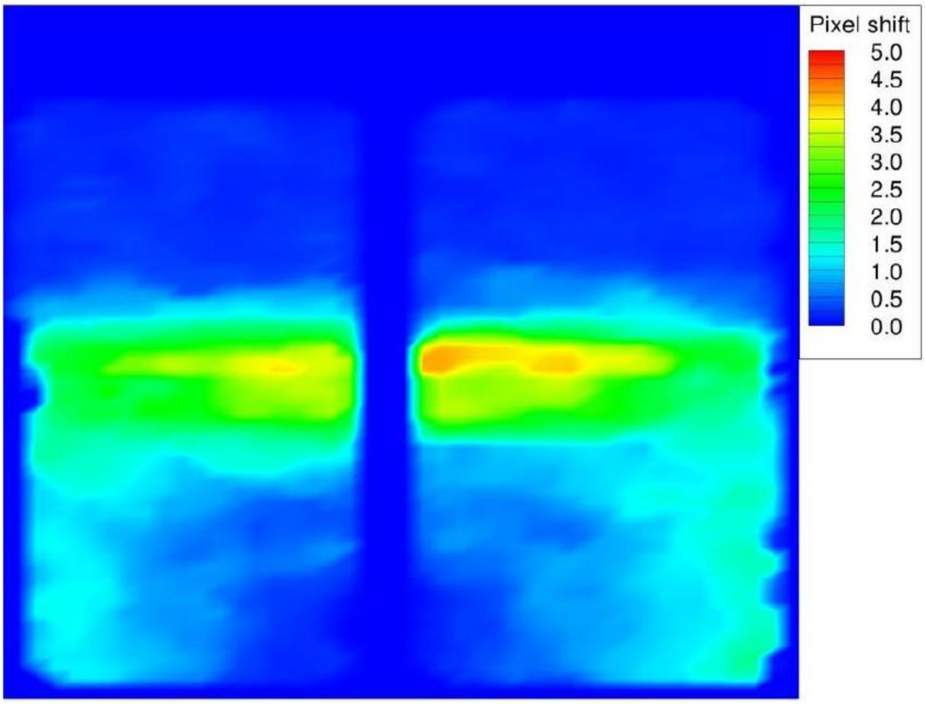

Figure 5.44: Pixel shift field for the captured moment in Figure 5.43 for charging with $\Delta T = 20\ K$ [66]

According to the mentioned master thesis, it has been concluded that BOS method can investigate the position and qualitative constitution of temperature gradient. This method is a reliable and cost-efficient method to be applied for the flow analysis of the charging process in thermal storage tank [66]. In the following, the pixel shift field obtained from BOS method has been used in order to make a qualitative comparison with temperature gradient field resulting from CFD simulation.

5.6 Comparison of Numerical Results with Experimental Results

5.6.1 Comparison of Temperature Values

In order to compare the obtained numerical results with experimental results, the temperature value of specified positions in storage tank has been exported. These positions correspond to temperature sensors located in different vertical positions of the tank in experimental work. Figure 5.45 represents the comparison between turbulent numerical simulation and experimental values in charging with ΔT = 20 K.

The comparison shows a good agreement between numerical and experimental results after 20 seconds of charging. The first temperature sensor at the bottom, after 40 seconds, shows a deviation from experimental value about 2 °C. This deviation has been repeated after 60 seconds of charging for the first sensor. The highest deviation from experimental results can be seen in the second sensor at the bottom after 60 seconds of charging.

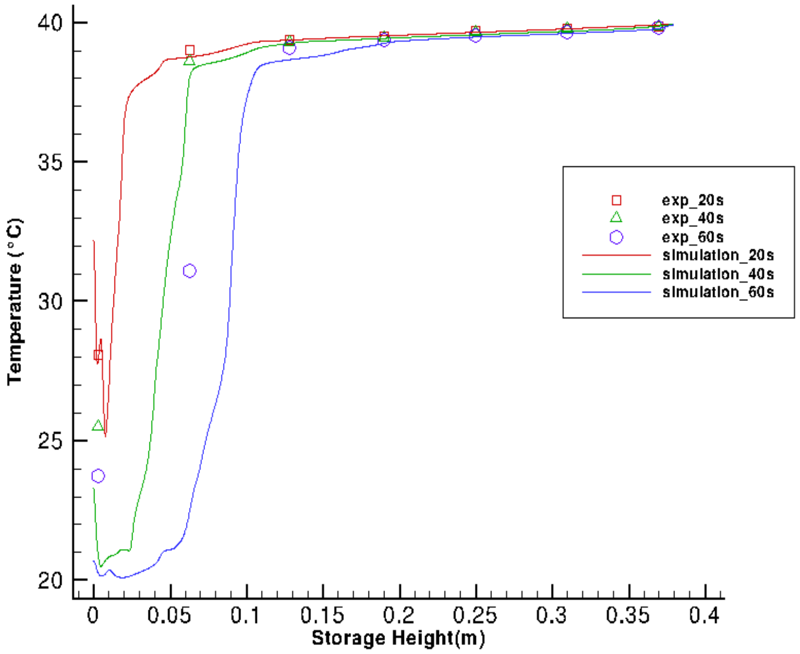

Figure 5.45: Comparison of experimental results with numerical results with realizable $k - \varepsilon$ turbulence model for charging with $\Delta T = 20\ K$ and 3 lpm charging volume flow rate

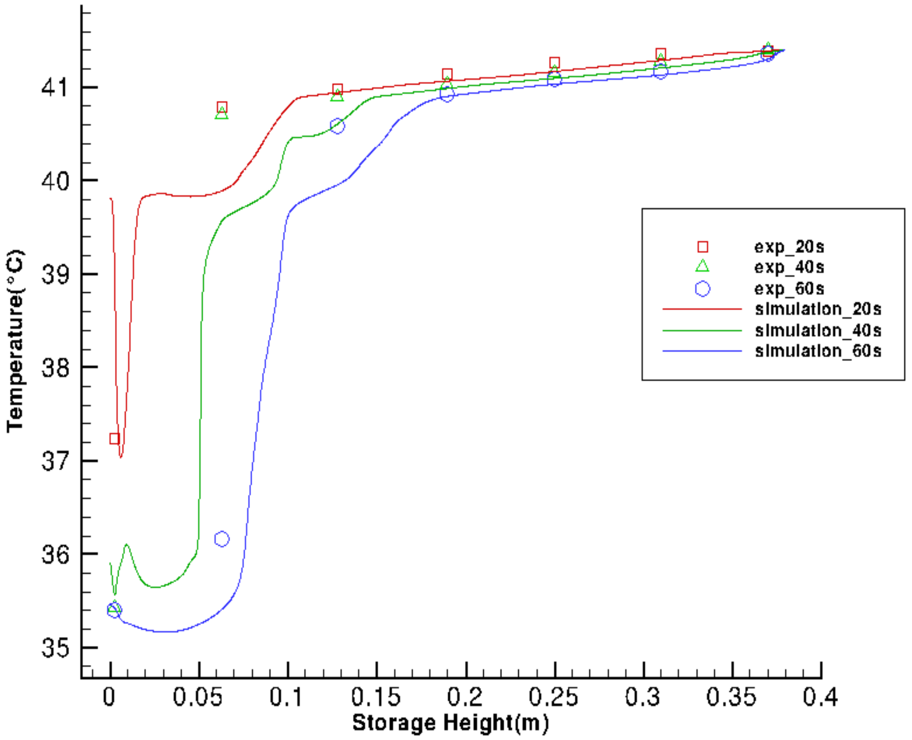

Figure 5.46: Comparison of experimental results with numerical results with realizable $k - \varepsilon$ turbulence model for charging with $\Delta T = 5\ K$ and 3 lpm charging volume flow rate

The numerical results for ΔT = 5 K also represents a good agreement with experimental results after 20 and 40 seconds of charging. The deviation of the second and the third sensor at the bottom are also about 1 °C. This could be due to the mismatching of the initial conditions in numerical and experimental setup.

5.6.2 Comparison of Temperature Gradient Field with Pixel Shift Field

In experimental investigation of temperature gradient in thermal storage tank, different qualitative methods can be applied. Background Oriented Schlieren (BOS) is one of these qualitative non-invasive methods. A high resolution digital camera is required for the experiment.

In this method, two pictures are taken from the flow field at two different moments. The first picture from an undisturbed flow field and the second one from the field containing density gradients. Cross correlation algorithms are applied to compare the pictures with each other. Pixel displacements of the background pictures obtained from the comparison can be used as a quantity representing density gradient. Pixel displacement vectors are produced because of the change in refractive index of the flow. In principle, density gradient of the flow causes the change in refractive index of the flow. BOS method provides qualitative information regarding density gradient perpendicular to the direction of viewing. One of the main advantages of the BOS method lies at its whole field visualization ability.

In another part of the comparison between simulation and experimental results, it has been tried to compare temperature gradient field from simulation with pixel shift field from the experiment. Pixel shift field represents a variable depending on density difference in the flow field. Therefore, the comparison of two variables has been performed in a qualitative manner. The flow close to the wall in thermocline region indicates high values in comparison with the central region of the thermocline. As discussed earlier, flow in vicinity of aluminum plate becomes warmer and rises due to the buoyancy forces in the region close to the tank wall. On the other hand, the charging flow with lower temperature flows in the region farther than the tank wall. This high temperature difference in a small region causes the high value of temperature gradient close to the wall. The pixel shift in this region cannot be captured in experimental investigation.

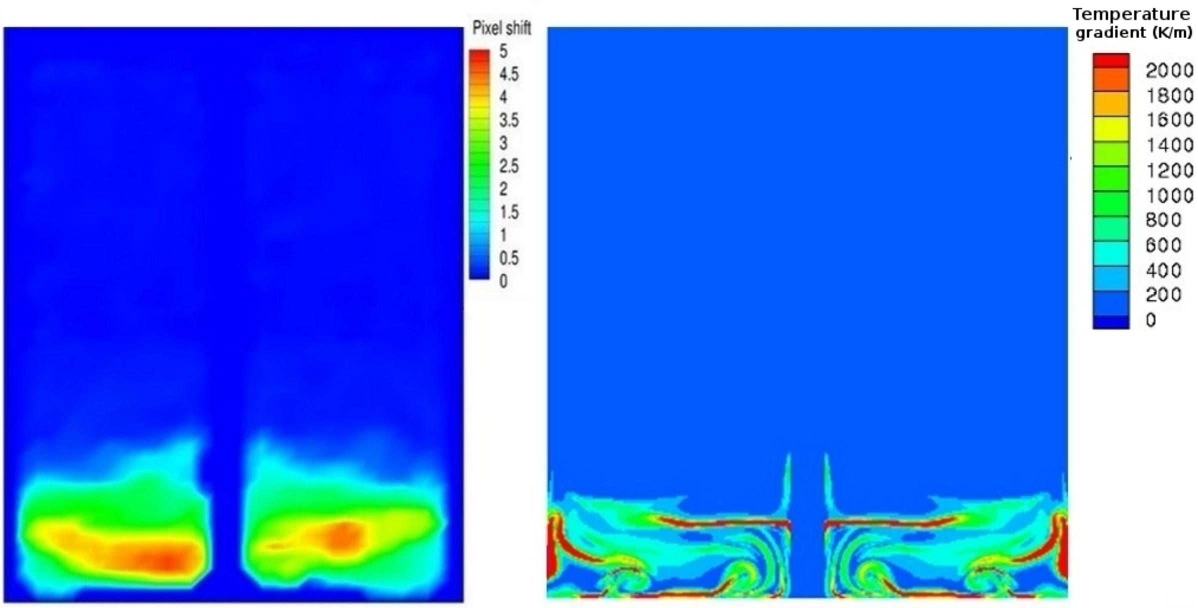

Figure 5.47: Qualitative comparison of temperature gradient field(right) with pixel shift field (left) after 20 s charging with $\Delta T = 20\,K$, Simulation results with realizable $k-\varepsilon$ model and 3 lpm charging volume flow rate, experimental results from [66]

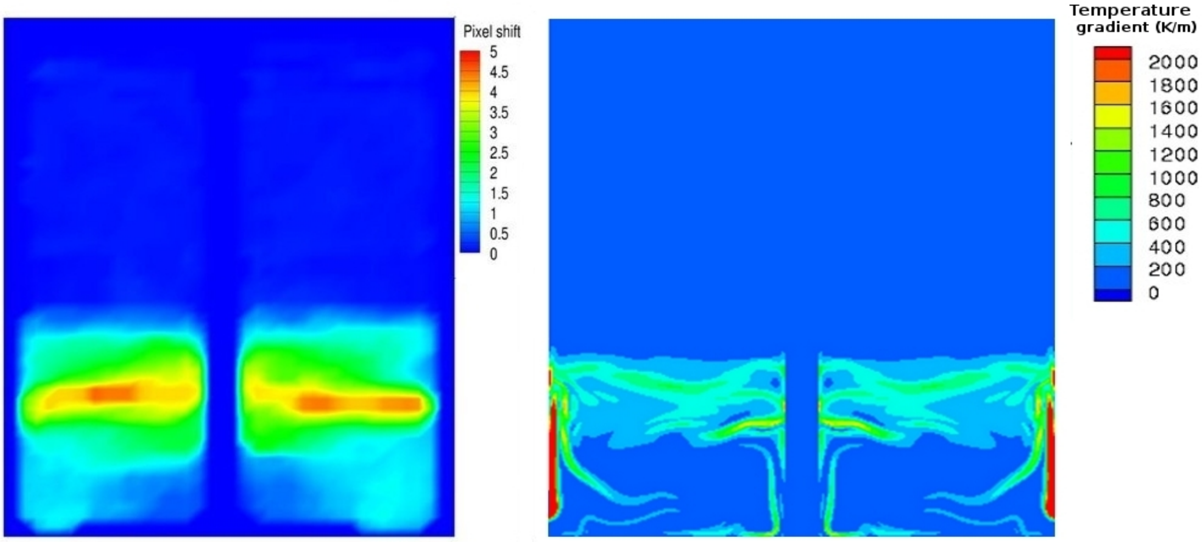

Figure 5.48: Qualitative comparison of temperature gradient field (right) with pixel shift field (left) after 40 s charging with $\Delta T = 20\,K$, Simulation results with realizable $k-\varepsilon$ model and 3 lpm charging volume flow rate, experimental results from [66]

5.7 Conclusion

Charging process of a thermal storage tank with radial charging flow has been investigated numerically and the obtained results have been compared with the relevant available findings from experimental investigation. Numerical studies are conducted under different initial and boundary conditions. Simulation results demonstrate a wide range of Reynolds number in the charging process. Hence, both Laminar and turbulent simulations have been performed to investigate the flow variables in storage tank. RANS turbulence models have been applied for the simulation. Among the RANS models, Realizable $k-\varepsilon$ RNG $k-\varepsilon$ and SST $k-\omega$ models have been applied in this study, which have shown promising results in the previous study of cases with similar problems. Higher values of turbulent eddy viscosity can be identified in the lower part of the tank. Turbulent simulation predicts the flow structure in this region better than laminar simulation. $k-\varepsilon$ models including realizable and RNG predict a thinner thermocline in comparison to SST $k-\omega$ model. Charging with higher charging flow rate causes a thicker thermocline, and therefore, more mixing because of the higher inertial forces.

The comparison of numerically obtained results with available experimental results also shows a good agreement, and therefore, the applied CFD model can predict the flow variables in a satisfying manner.

6 Numerical Study of the TES Charging Process with Stratification Pipe

6.1 Simulation of TES with Inlet Stratification Pipe

6.1.1 Inlet Stratification Pipe

The loss or degradation of thermal stratification in solar storage tanks is caused mainly by the mixing that occurs during the charge and discharge processes [68].

As it has been discussed in section 2.2, the thermally stratified storage tank integrated with adsorption heat pump works as a kind of heat storage during the adsorption phase, when the released heat in the system needs to be stored. Consequently, the stored heat in storage tank will be utilized in system during the desorption.

The ideal plug flow charging model for stratified storage tank coupled with Adsorption heat pump cycle has been discussed in section 2.2, comprehensively. In the reality, by insertion of fluid at each level the inertial forces cause some local mixing of fluid layers with some surrounding layers. The intensity of mixing process and the extent of the affected area depends on the velocity of the charging flow at the charging region and fluid viscosity. Other parameters which influence local mixing at the inlet region are inflow characteristic and geometrical design of the charging location.

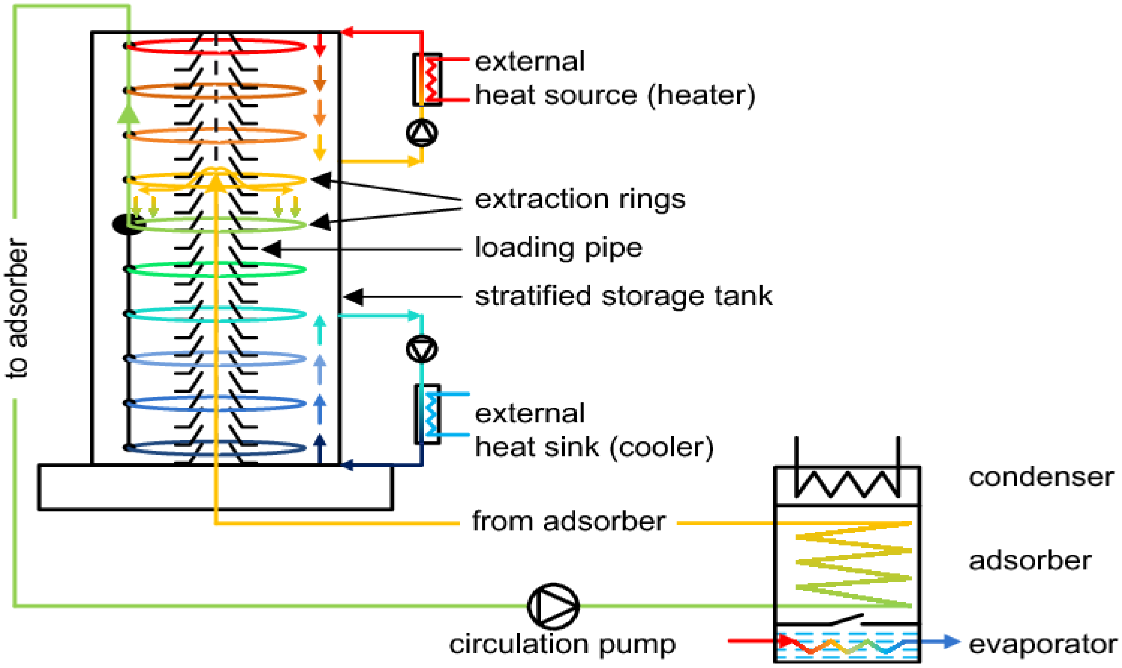

Figure 6.1: Storage tank with inlet stratification pipe and heating and cooling cycles coupled with adsorption module [69]

In the case that the fluid insertion in the tank is not performed at the proper position with similar density, buoyancy forces due to the temperature difference between the charging flow and the fluid layer in surrounding work as another mechanism that enforces mixing process in such an application. One solution for this problem could be restriction of the inlet region from the fluid layers in storage tank. Many of charging devices implemented to achieve better stratification in TES follow the same principle.

Different patented charging devices for thermal storage tank have been already presented and studied numerically and experimentally by numerous researchers. Most of them are vertically arranged outlets like charge systems of the ConSens GmbH, Solvis KG and Sailer GmbH [55]. These charging devices have been designed for solar thermal application. The capability of these devices in restriction of the inlet mixing have increased their relevance in the current application related to the stratified storage tank coupled with adsorption heat pump cycle. Shah et. al. have examined a rigid stratifier with three circular openings theoretically using CFD and experimentally through PIV and temperature measurements [19]. The investigation has shown that the entrainment of cold water into the stratifier occurs through the lowest opening, and mixed fluid enters the tank via the top opening.

Another main CFD analysis of the stratification devices implemented in thermal storage tank has been presented by Andersen et. al. [70]. Marketed thermal stratification devices have been explored experimentally and theoretically in this study. The rigid stratification pipe with circular openings implemented in TES has been studied by means of numerical simulation and non-invasive field measuring methods like particle image velocimetry (PIV), and laser-induced fluorescence (LIF). The second type of stratification device has been also examined in this work. This stratification pipe is a two-layer fabric stratification pipe. The CFD results have been compared with experimental findings by thermo-couples and also PIV and LIF. The investigation has focused on limited number of operating conditions in solar collector loops. Furthermore, two stratification devices have been applied in the charging process including forced volume flow rates and natural buoyancy flow. Figure 6.2 depicts the sketch of rigid stratification pipe with circular openings and fabric stratification pipe investigated in the corresponding study. The investigation revealed some advantages and disadvantages of the stratification pipe under applied operating conditions.

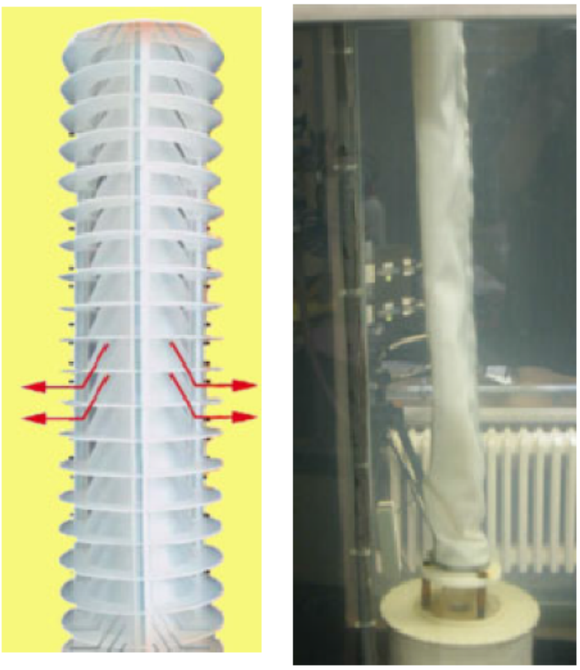

Figure 6.2: Rigid stratification pipe with circular openings (left) and fabric stratification pipe(right) [70]

One of the prevalent stratifier systems consists of pipes with vertically arranged outlets. This charging system is patented and marketed by German company Sailer GmbH [71]. According to the fluid density, it can stratify and leave the stratifier in the right height to the tank. In the present work, the same construction of stratification pipe with vertical openings have been adjusted and implemented for the charging of the storage tank system coupled with adsorption heat pump module. There are different reasons that diminish the thermal stratification in the storage tank. These reasons are as follows:

- Plume Entrainment

In the near of the inlet region from adsorber into stratification pipe, momentum effects of the fluid entering the storage are more important than buoyancy effects. In such situations, fluid plume can be defined as fluid jet. Because of the velocity gradient and shear effect, the surrounding fluid will be entrained and leads to more mixing effects [72]. In the present work, the entrainment of the fluid from the tank to stratification pipe through the openings has been described as suction effect.

- Inlet Jet Mixing

Because of the kinetic energy of the entering fluid, turbulent mixing in the near of the inlet leads to a locally increased mixing. One of the advantages of the stratification pipe for the charging process is that turbulent kinetic energy can be partly bounded inside of the stratification pipe. Therefore, the mixing effect influences have been more restricted. Turbulent kinetic energy developed from turbulence has been restricted in the region inside of the stratification pipe and does not impact fluids inside of the storage tank.

6.1.2 Storage Tank Geometry Description

Geometry of the cylindrical tank used for the implementation of stratification device is described as follows:

- Height: 1.9 m
- Diameter: 19 cm
- Inner diameter of stratification pipe: 3.4 cm
- Outer diameter of stratification pipe: 8.94 cm
- Heater outlet position: 57% of the storage height from the bottom(1.08 m)
- Heater inlet position: at the top of the storage tank
- Cooler outlet position: 25% of the storage height from the bottom(0.47 m)
- Cooler inlet position: at the bottom of the storage tank

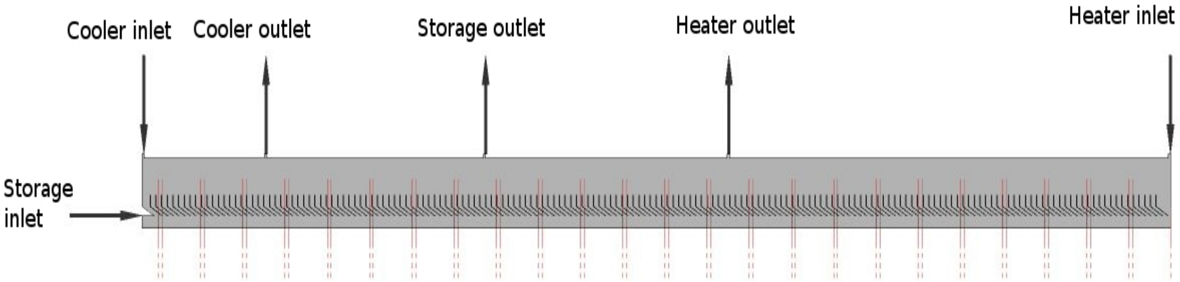

Figure 6.3: Storage tank 2-D axisymmetric domain with implemented stratification pipe and its boundary conditions

Storage Material

The heat transfer fluid selected for this application is Marlotherm LH, which is the product of the Sasol company [73]. Marlotherm LH is a high-performance synthetic, organic heat transfer medium for use in the liquid phase in closed heat transfer systems. The Marlotherm properties such as density, specific heat, thermal conductivity and viscosity has been defined in a piecewise linear manner in Ansys Fluent.

6.1.3 Grid Generation for CFD Model

ANSYS Gambit 2.4.6 has been applied for geometry creation and meshing of TES model. A combination of structured and unstructured mesh with about 400,000 quadrilateral and triangle cells has been generated. The quality of the mesh in Gambit has been verified successfully with skewed element criterion and with maximum value of 0.6667. The mesh quality has also been checked by other mesh quality criteria like determinant and aspect ratio.

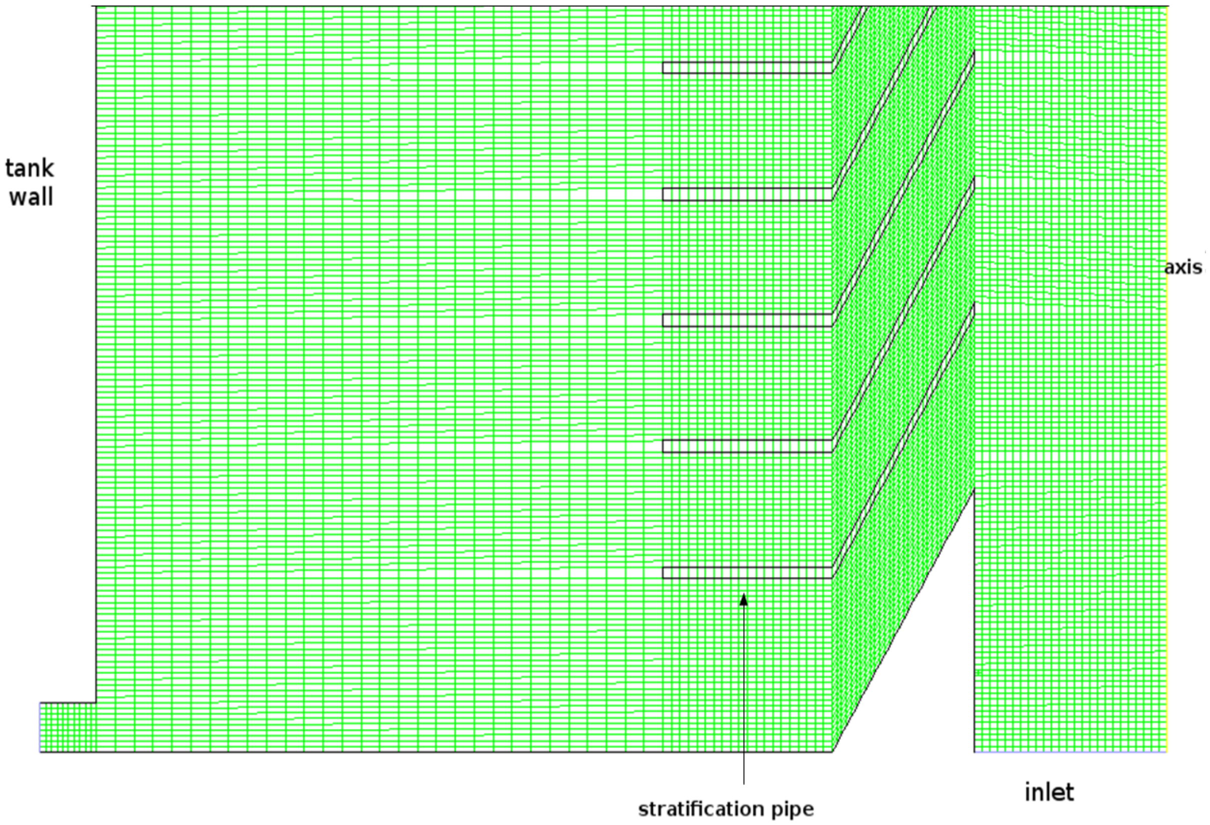

Figure 6.4: Outlook of the computational grid at lower part of the tank

Physical Process

As a representative example case for the simulation [4], the storage tank fluid domain has been initialized with 38°C at the bottom of the tank to 200 °C at the top of the tank. The linear stratification between this temperature ranges has been defined. The storage has been charged from the bottom with thermal oil with 119 °C and four different mass flow rates including 0.05, 0.1 , 0.2 and 0.4 kg/s. Simultaneously, the heater and cooler extract and reinsert the fluid with 20 percent of the storage charging mass flow rate.

Case Introduction

The simulation includes a turbulent buoyant plume which has been introduced at the bottom of the tank. In order to achieve a relevant stratification in the tank, an inlet stratification pipe has been used. Inlet stratification pipe has at different level circular openings where fluid can leave the pipe. Vertical distance between each 2 openings is about 9.5 mm. The whole idea of using inlet stratification pipe can be concluded as follows:

The fluid that has been injected at the bottom of the storage is warmer than the lower layers of the fluid in the storage tank, and thus, with lower Density. Regarding to density difference , it is expected that injected fluid raises and leaves the stratification pipe at the levels that fluid has the same density in the storage. Obviously, this is an ideal assumption. As it has been revealed from the previous studies [74], the injected fluid will be mixed with lower layer fluid in the storage and cannot reach the relevant fluid density level in the storage. If this turbulent mixing in the near of the inlet port is reduced, the insertion level of the fluid from pipe to the storage can be closer to the relevant density level in the storage.

Solver Setting and Simulation Space

Pressure-based solver has been used for CFD simulation. Simulation space is 2-D axisymmetric, and transient situation has been considered for temporal discretization. According to the appropriateness comparison for different turbulence models in 3.9, the realizable $k-\varepsilon$ and SST $k-\omega$ model seem to be relevant choices for the simulation. Additionally, pressure-velocity coupled scheme has been applied for iterative calculation. Table 6.1 represents different discretization methods applied in current simulation.

Table 6.1: Discretization methods applied in simulation

Pressure spatial discretization	Second order
Momentum spatial discretization	Second order upwind
Turbulent kinetic energy spatial discretization	Second order upwind
Turbulent dissipation rate spatial discretization	Second order upwind
Energy spatial discretization	Second order upwind
Transient formulation	Second order implicit
Time step size (s)	0.2
Fluid material	Marlotherm LH

Boundary Condition Definition

Solution domain contains five different boundary conditions for inflow and outflow, wall and symmetry axis. The inflow boundary conditions will be explained in the following section in detail,

Storage Inlet

Velocity inlet boundary condition type has been used for the storage inlet. First, in a separate simulation, flow in a pipe with the same diameter as inner diameter of the stratification pipe and different charging mass flow rates has been simulated, and after calculation, profile of velocity and turbulent variable like turbulent kinetic energy and dissipation rate in fully developed flow situation in pipe has been exported, and variable distribution has been applied as inlet boundary condition. The polynomial fitting of 8th order has been used for the velocity and turbulent kinetic energy profile and polynomial fitting of 9th order for turbulent energy dissipation rate profile. The Reynolds number for this simulation at the inlet boundary has been calculated, which shows a value about 3500 for the case with lowest charging mass flow rate representing a fully turbulent flow regime for pipe flow. Thus, turbulent simulation with realizable $k-\varepsilon$ model has been performed for all cases. Charging temperature at the inlet boundary has been set to 119 °C, which is an average temperature between the highest and the lowest temperature in the storage tank fluid domain.

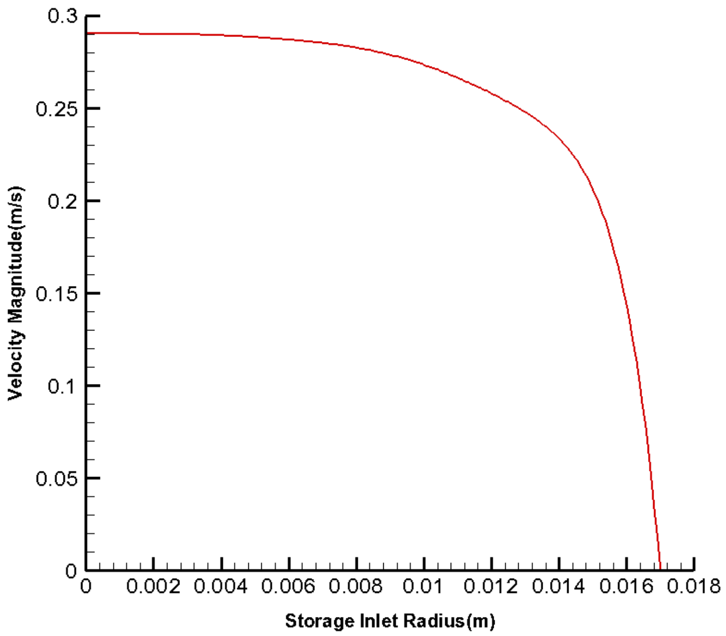

Figure 6.5: Storage Inlet velocity profile calculated in a fully developed flow situation for charging mass flow rate of 0.2 kg/s

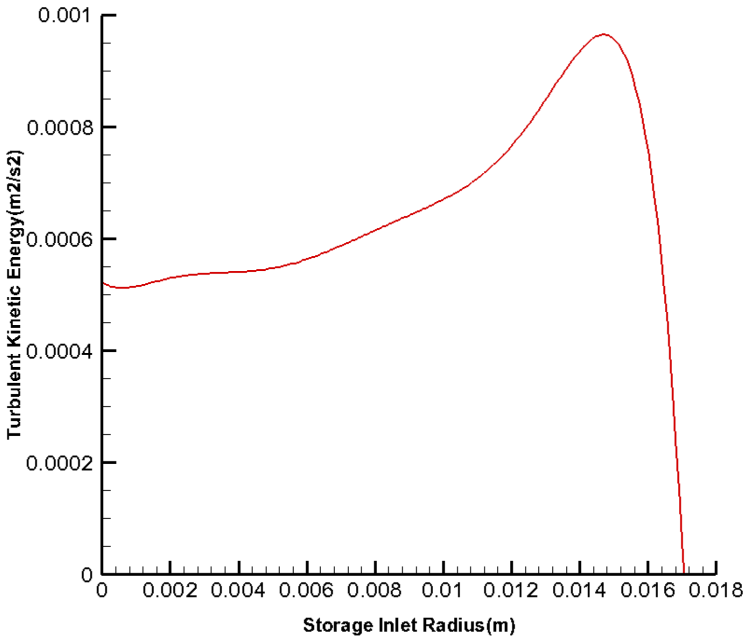

Figure 6.6: Storage Inlet turbulent kinetic energy profile calculated in a fully developed flow situation for charging mass flow rate of 0.2 kg/s

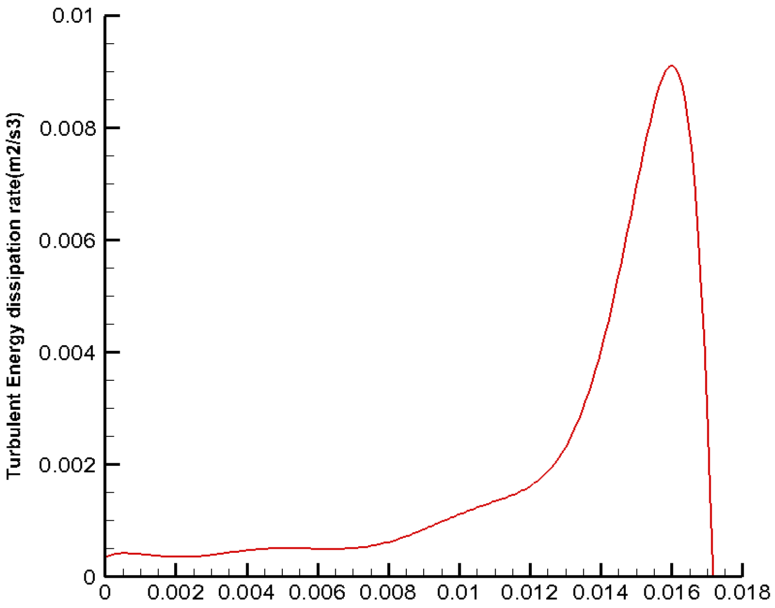

Figure 6.7: Storage Inlet turbulent energy dissipation rate profile calculated in a fully developed flow situation for charging mass flow rate of 0.2 kg/s

Heater Inlet

The TES coupled with adsorption module has additional heater cycle at upper part of the tank. In simulation domain, this cycle has been modeled by means of one outlet, where fluid with 20 percent of the storage charging mass flow rate will be extracted, and one inlet, where fluid with higher temperature will be introduced into the tank. Mass flow rate boundary condition type has been used for the heater inlet. The value of the mass flow rate through the heater is 20 percent of the storage charging mass flow rate and is 0.04 kg/s with inlet temperature of 200 °C, which is the initial temperature at the top of the storage.

Cooler Inlet

An additional cooler cycle has been implemented at the lower part of the tank. This cycle contains an inlet and outlet in solution domain. Mass flow rate boundary condition type has been also used for the cooler inlet with temperature of 38 °C which suits the initial temperature at the bottom of the tank. The value of the mass flow rate through the cooler is 20 percent of the storage charging mass flow rate and is 0.04 kg/s.

Heater and Cooler Outlet

As it has been mentioned earlier, fluid in cooler cycle has been extracted from the tank and after cooling down will be injected to the tank again. Fluid extraction from the tank has been simulated by means of cooler outlet in CFD model. In a similar manner, fluid extraction in heater cycle has been simulated by means of heater outlet in CFD model. Therefore, three outlet boundary conditions have been employed in numerical model and for all of them the outflow boundary condition has been applied. In ANSYS FLUENT, it is possible to use multiple outflow boundaries and specify the fractional flow rate through each boundary [27]. It will be realized by use of Flow Rate Weighting in outflow boundary condition. Flow Rate Weighting is a weighting factor that is defined as follows [27]

$$percentage\ flow\ through\ boundary = \frac{flow\ rate\ weighting\ specified\ on\ boundary}{sum\ of\ all\ flow\ rate\ weightings}$$

If the mass flow rate through all different outlet boundaries is the same, no flow rate weighting should be set because ANSYS FLUENT will scale the flow rate fractions to obtain equal fractions through all outflow boundaries by default [27]. In the case of different mass flow rates through boundaries, the Flow Rate Weighting should be set for every boundaries. Ansys Fluent treats the Outflow boundaries so that a zero diffusion flux is set for all flow variables, and an overall mass balance correction is done [27]. In other words, the flow condition at the outflow boundary is extrapolated from domain inside. Therefore, outflow conditions don’t influence the upstream flow. Additionally, zero diffusion flux implies no gradient in the direction normal to the exit plane but not in the cross-stream direction.

Wall Boundary Condition
With the assumption of no heat loss to the environment, the storage wall in the simulation has been defined as adiabatic wall. Shear condition in wall boundary condition has been considered as no slip condition.

Initial Condition
Initial temperature in the storage has been defined in a linear function from the bottom of the storage with 38 °C to the top of the storage with 200 °C. Figure 6.8 represents the initial temperature distribution used for the transient simulation.

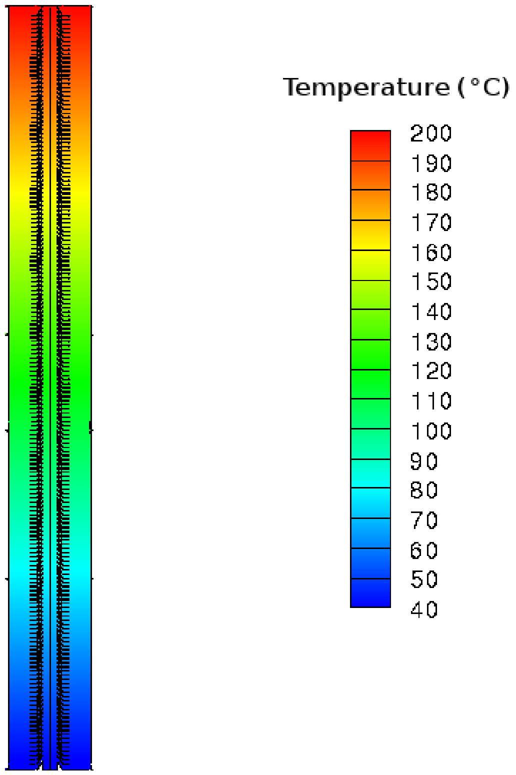

Figure 6.8: Initial temperature distribution in TES

6.2 Mesh Independency Study

In order to make sure that the calculated results are independent of the grid size, mesh independency has been controlled by comparison of simulation results with the same case setup in two different grid numbers one with about 400,000 and another with about 744,000 cells . Figure 6.9 and 6.10 show the average temperature distribution inside of the storage tank in charging time of 20 seconds and 60 seconds, respectively. Temperature values at different vertical position have been averaged between stratification pipe outer diameter and tank wall over the horizontal surface. The comparison of results shows that the simulation results are the same with very small tolerance, and therefore, the grid size with 400,000 cells is relevant to resolve the flow structures.

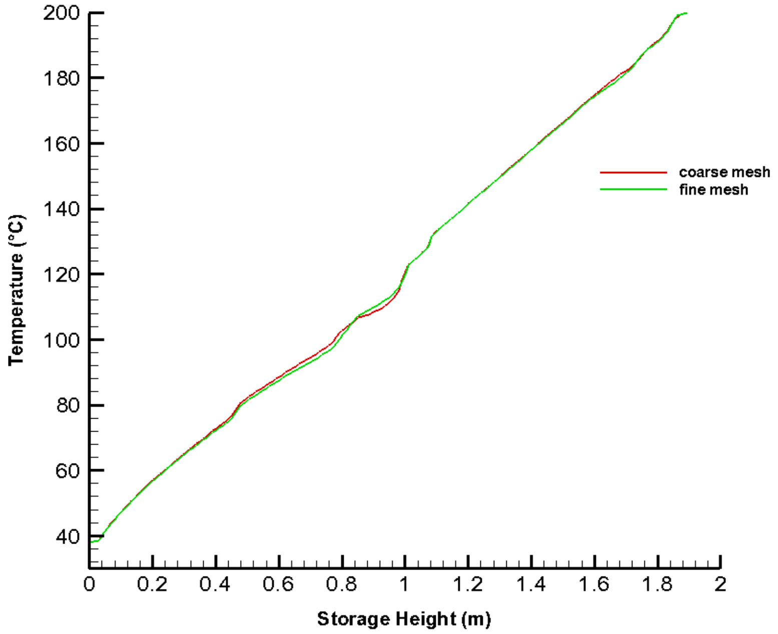

Figure 6.9: Average temperature distribution inside of the storage tank after 20 s of charging with 0.2 kg/s mass flow rate for coarse mesh (about 400,000) and fine mesh (744,000)

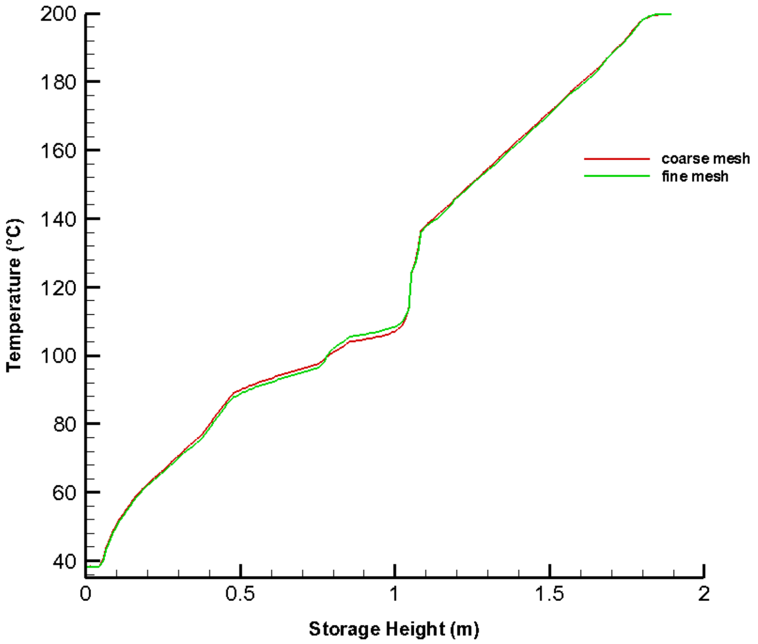

Figure 6.10: Average temperature distribution inside of the storage tank after 60 s of charging with 0.2 kg/s mass flow rate for coarse mesh (about 400,000) and fine mesh (about 744,000)

6.3 Simulation Results with Realizable $k-\varepsilon$ Model

6.3.1 Analysis of Turbulent Mixing in TES by means of Eddy Viscosity

Reynolds stresses proportionality to mean rates of deformation can be represented by turbulent eddy viscosity. It is an artificial variable that describes the intensity of turbulent motion and appears in form of an additional viscosity. Figure 6.11 shows the evolution process of turbulent viscosity at different charging time. Higher turbulent viscosity can be observed in the inlet region in stratification pipe, and it shows high value between main insertion level and storage outlet after propagation inside the pipe until the level of main insertion to the tank. The regions with higher turbulent viscosity indicate higher transport of momentum because of the effect of turbulent eddies. Therefore, in these regions more mixing of the fluid in storage is expected.

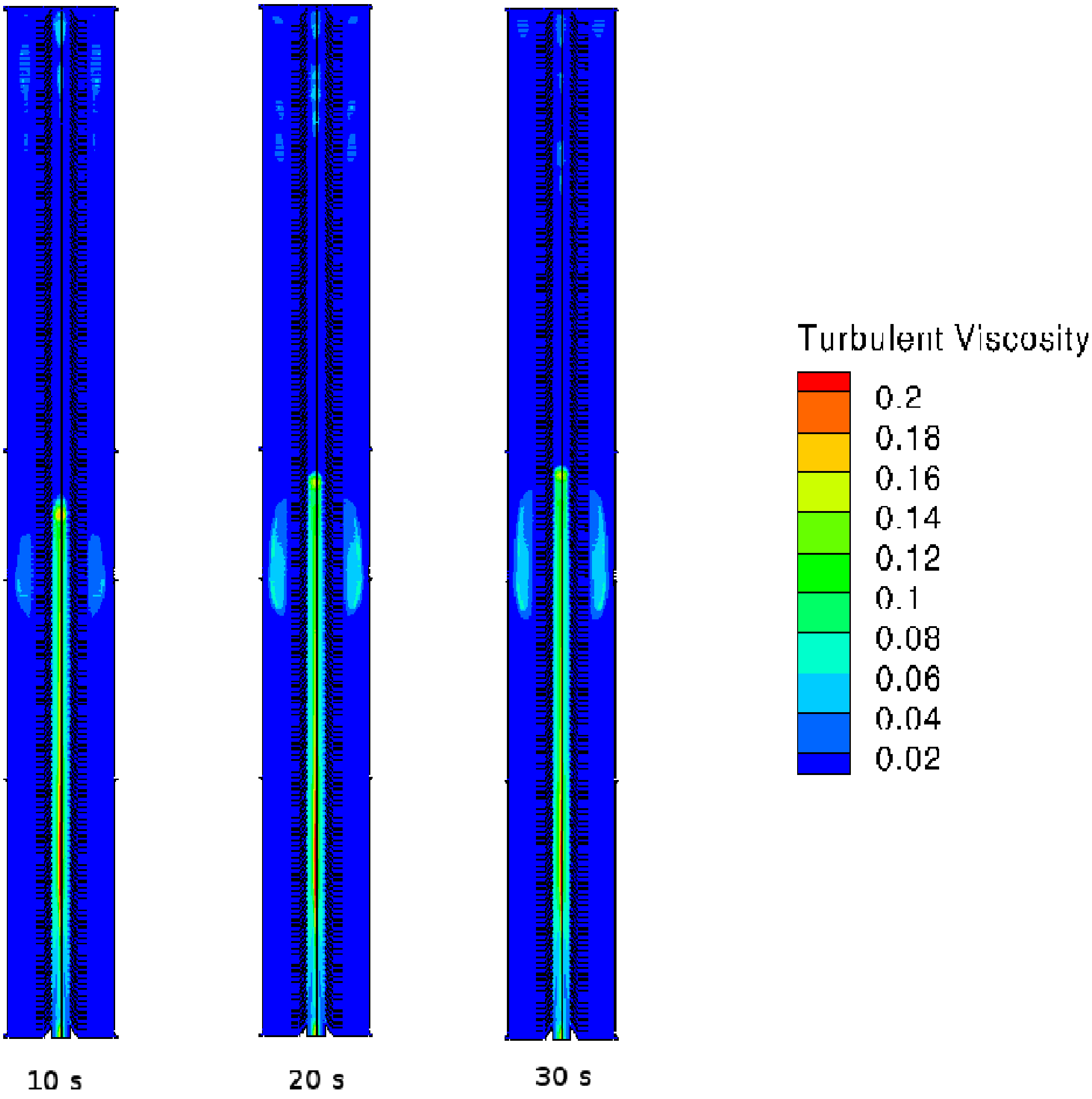

Figure 6.11: Turbulent eddy viscosity contours (kg/(m.s)) in charging process with 0.2 kg/s charging mass flow rate (simulation with realizable $k-\varepsilon$ model)

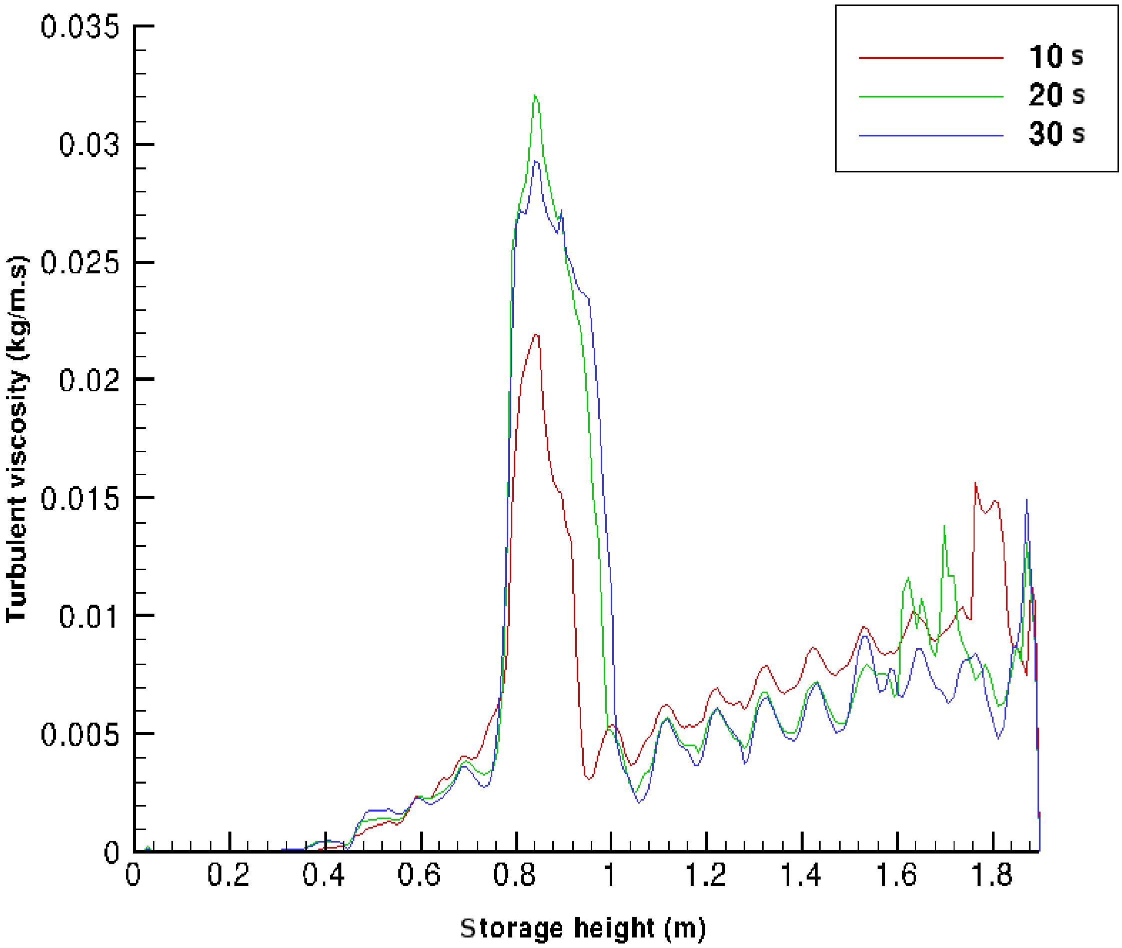

Figure 6.12: Average turbulent viscosity in storage tank in transient simulation with realizable $k - \varepsilon$ model and 0.2 kg/s charging mass flow rate

Average values of the turbulent viscosity in horizontal direction at the region between outer diameter of the pipe and storage tank wall are depicted in figure 6.12. From this figure it can be seen that turbulent viscosity value in the region of main flow insertion from stratification pipe into the tank show the maximum values inside of the tank. In addition, observation of turbulent viscosity curve at different charging time indicates an increasing in the maximum value at the beginning of charging, and after certain charging time, the maximum values decreases. After reaching the charging flow jet to the insertion point, eddy viscosity starts to increase due to turbulent kinetic energy of the flow jet leaving the pipe to the tank. The dissipation of turbulent kinetic energy is a consequence of working of small eddies against viscous stresses which leads to turbulent energy dissipation and eddy viscosity reduction. Figure 6.13 demonstrates the streamlines in the region of main insertion from pipe to storage tank. From the streamline evolution at different charging time it can be concluded that between 10 and 20 seconds by increasing of the reaching point inside of stratification pipe and higher kinetic energy after leaving the pipe until storage outlet, larger recirculation area builds up. As a result, the eddy turbulent viscosity increases to its maximum value in this time period. Between 20 seconds and 30 seconds, turbulent kinetic energy dissipation causes small reduction in the maximum value.

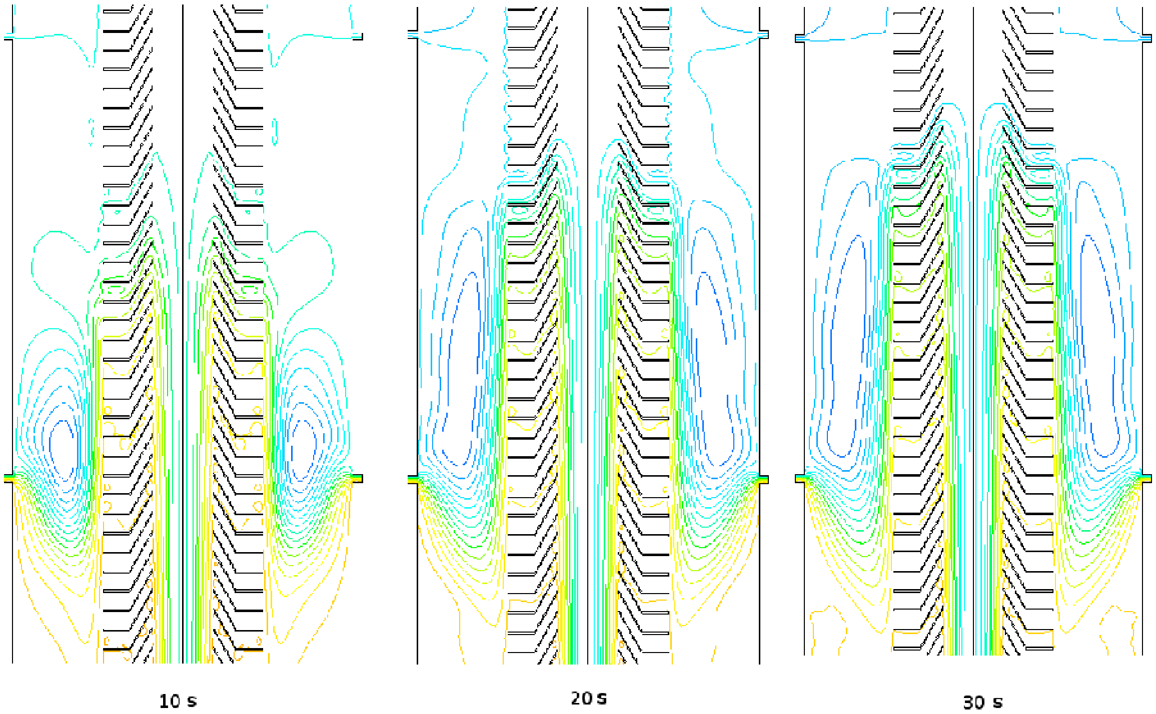

Figure 6.13: Streamline illustration at different charging time at the region of main outflow from stratification pipe to storage tank (transient simulation with realizable $k - \varepsilon$ model and 0.2 kg/s charging mass flow rate)

6.3.2 Analysis of the Entrainment Effect

Entrainment is generally moving of fluid layers by means of other fluid layers in the neighborhood due to shear forces or turbulent diffusion. In charging process of the TES from the bottom, fluid jet with higher velocity compared to the fluid layers in the environment influence the fluid layers in lower part of the TES. During this entrainment, colder fluid in TES is mixed up with warmer charging fluid jet, and mixed fluid with lower temperature than charging flow can rise less than warmer charging flow without mixing. Figure 6.14 shows streamlines at the bottom of TES in the charging process. In the simulation with cooler cycle at the lower part of the tank, the horizontal flow jet through the cooler inlet can enhance the entrainment effect at the lower fluid layers. The cooler cycle in stratisorp cycle causes the same suction effect at the bottom, which is completely unacceptable. Therefore, the corresponding stratification pipe has not been considered for further experimental investigations.

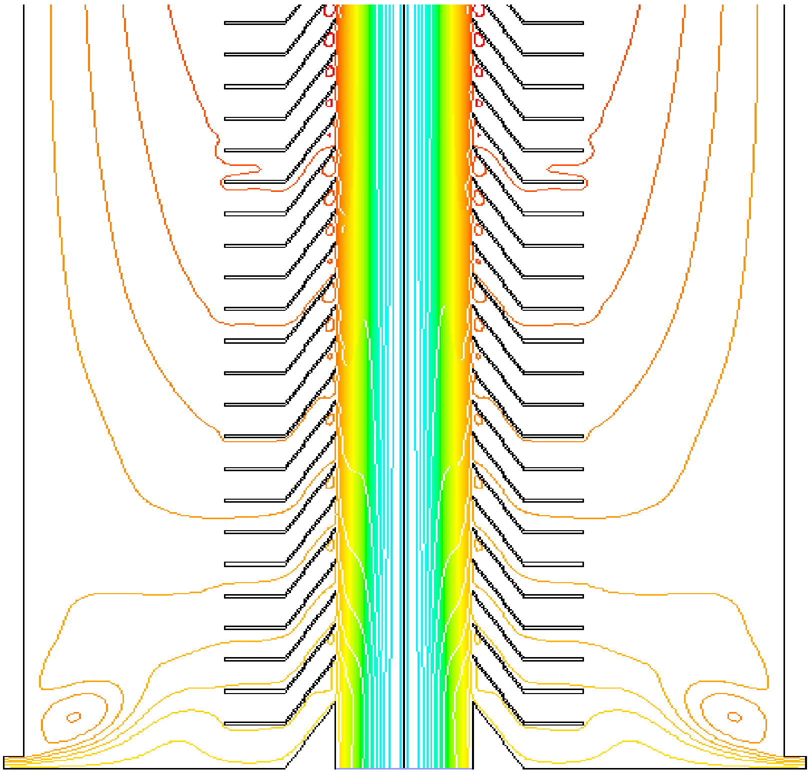

Figure 6.14: Streamlines showing the entrainment effect at the bottom of the tank in simulation with 0.2 kg/s charging mass flow rate for transient simulation with realizable $k - \varepsilon$ model

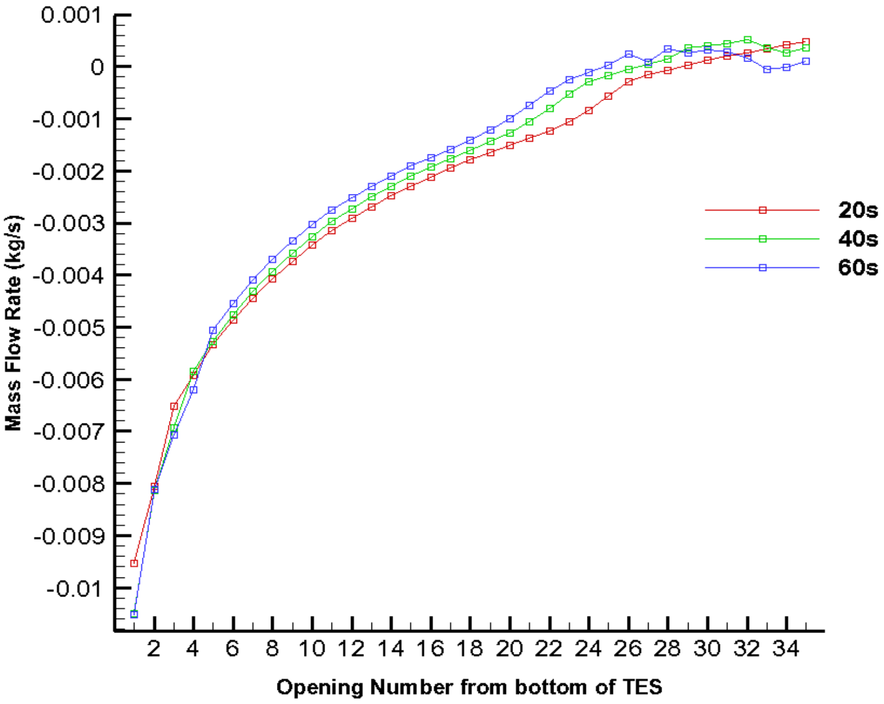

Figure 6.15: Mass flow rate through the lower openings of the stratification pipe in simulation with charging mass flow of 0.2 kg/s for transient simulation with realizable $k - \varepsilon$ model

Diagram depicted in figure 6.15 represents the mass flow rate through the openings of the stratification pipe in 35 openings numbered from bottom of the tank. A negative mass flow rate shows a mass flow rate from storage tank into stratification pipe which is described as entrainment effect. From diagram 6.15 it can be concluded that entrainment effect at the lower openings of the TES reduces slightly with charging time, but remains at unacceptable level for the practical application.

6.3.3 Study of Temperature Profile Development

The main mechanisms influencing the transient development of the temperature profile in a TES are heat transport process, mixing of the charging fluid with stored fluid, and local turbulence because of stratification [75]. From the temperature distribution inside of the storage it can be seen that the region above to the heater outlet doesn’t show a significant mixing. The fluid at the extraction level of heater cycle has been extracted (heater outlet in CFD model) and the fluid with the same temperature as the upper layer in tank has been introduced at the upper part. For this reason, no buoyancy forces can be produced by introducing at the heater inlet. The forced convection due to flow introducing at the heater inlet, further fluid layers to the bottom. The only parameter which can cause some mixing effect is inertial forces in axial direction. This parameter has been reduced by radial charging through heater inlet. Streamlines in the region between heater inlet and heater outlet also show no recirculation area with exception of a small area close to heater inlet port.

Because of the insertion at the heater inlet and extraction at the heater outlet, temperature profile has been shifted to the left and with the time progress, this shifting increases. This behavior can also be observed by ideal plug flow charging model. The average values of the temperature between outer diameter of the stratification pipe and storage tank wall are demonstrated in figure 6.16. It shows that the fluid insertion level from stratification pipe to storage tank is about 1.1m from the bottom of the tank which is in the near of the heater outlet position. At this height, the initial linear stratified temperature profile starts to break. At lower levels especially until cooler outlet, mixing leads to destroy the linear stratification with higher intensity.

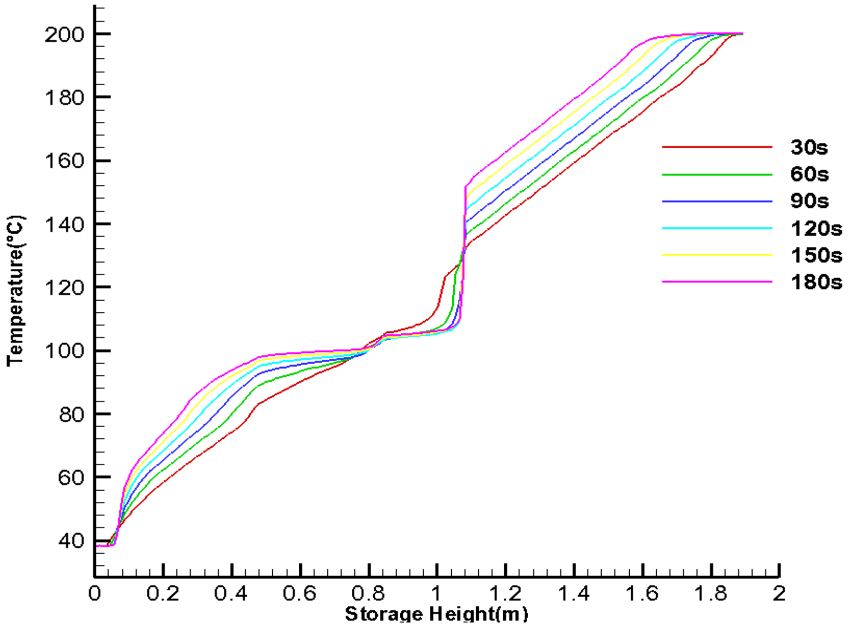

Figure 6.16: Average temperature distribution in storage tank for different charging time in transient simulation with realizable $k - \varepsilon$ model

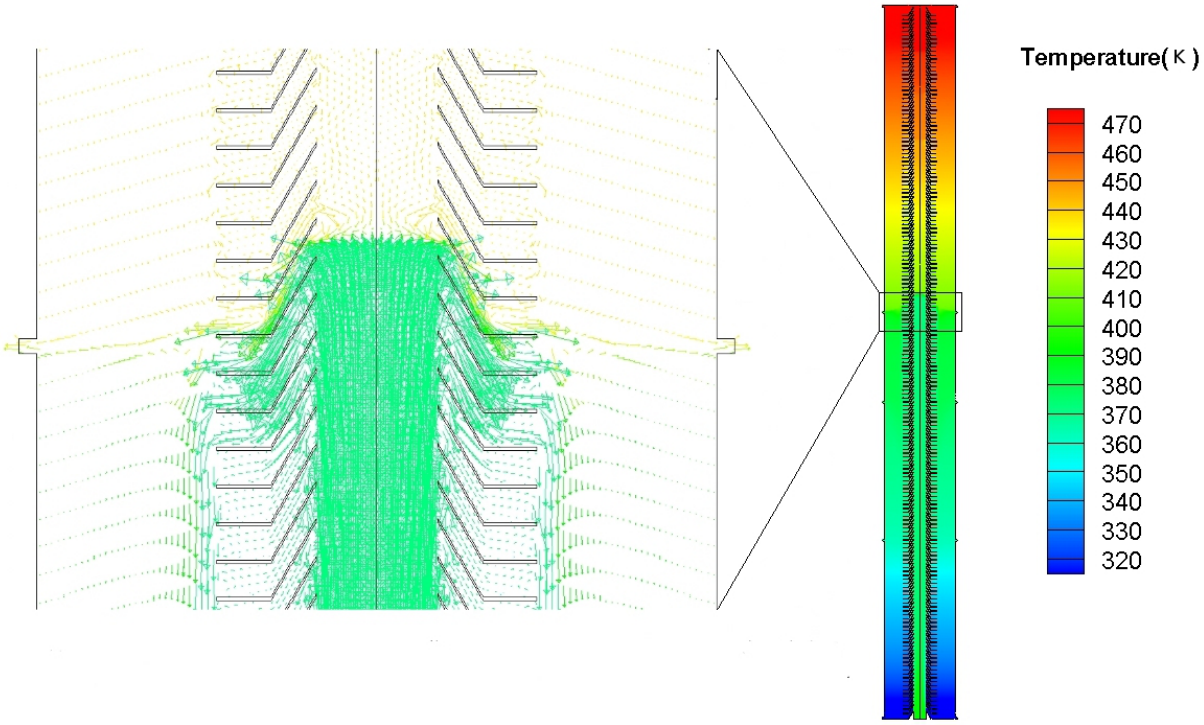

Figure 6.17: Temperature contour and velocity vector with the magnification of the insertion region from stratification pipe to the storage tank after 60 s of charging with 0.2 kg/s charging mass flow rate (simulation with realizable $k - \varepsilon$ model)

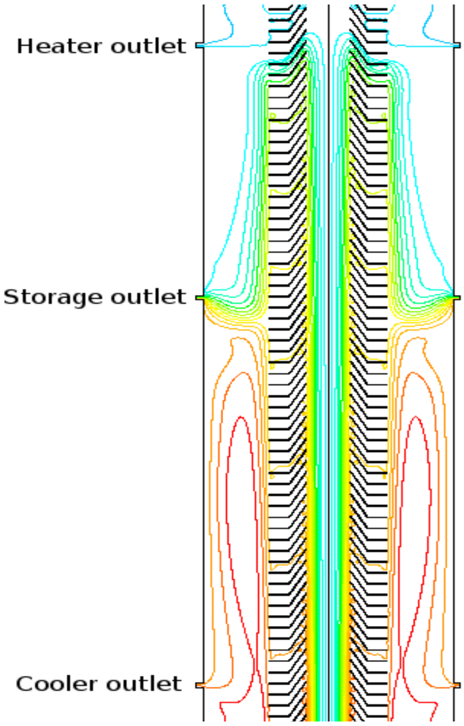

Figure 6.18: Isovalue of stream function in the middle part of storage after 3 minutes of charging with 0.2 kg/s charging mass flow rate (simulation with realizable $k - \varepsilon$ model)

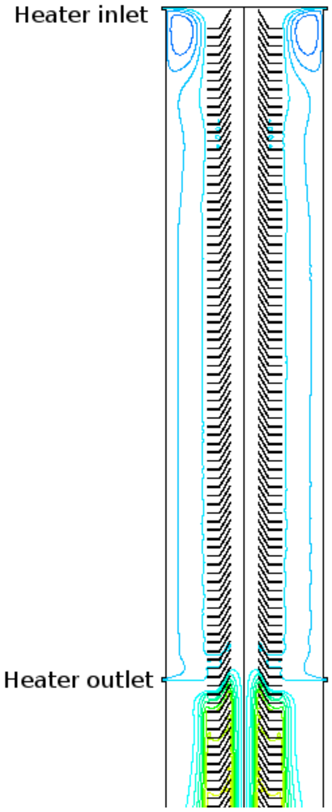

Figure 6.19: Isovalue of stream function in the upper part of storage after 3 minutes of charging with 0.2 kg/s charging mass flow rate (simulation with realizable $k - \varepsilon$ model)

Streamline in the lower part of storage, where the storage outlet and cooler outlet are located, shows more mixing. The fluid in the near of the heater outlet level leaves considerably the stratification pipe. Afterwards, it falls down until a level less than storage outlet and then rises up again until it leaves the storage at the storage outlet. In this region the flow has considerably higher axial velocity in the near of the pipe which causes a higher horizontal temperature gradient at this storage height. This flow behavior also contradicts the ideal plug flow model. Regarding to the initial temperature distribution, there is density distribution of the fluid in the storage. The insertion level from the pipe to the storage is very close to the region with the same density as the injecting fluid. It means the aim and idea of the insertion at the relevant density level for avoiding the mixing in the storage has been relatively achieved.

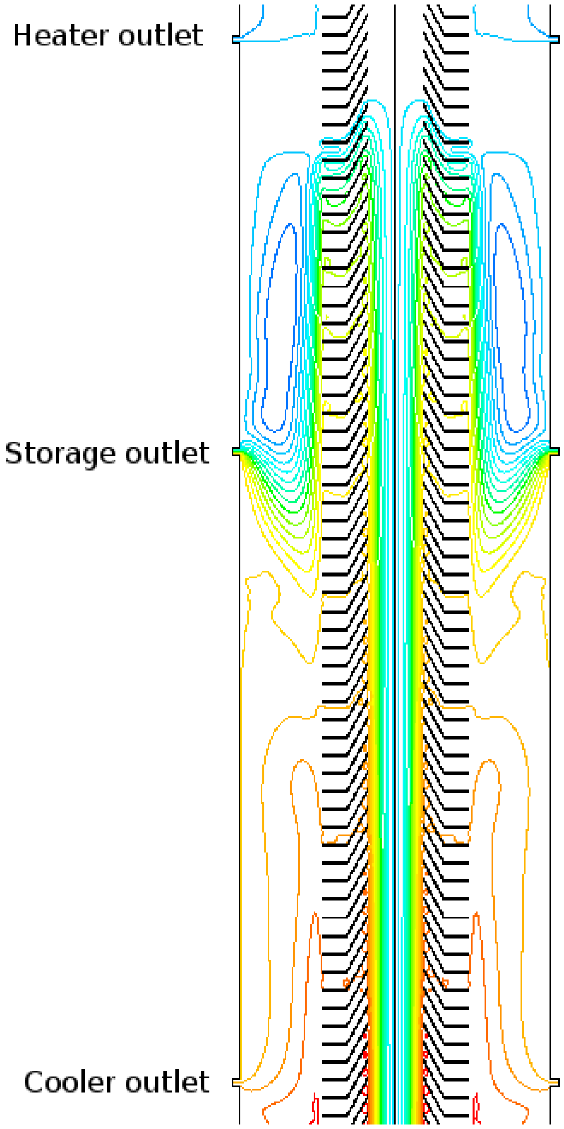

Figure 6.20: Isovalue of stream function in the middle part of the storage tank after 30 s of charging with 0.2 kg/s charging mass flow rate (simulation with realizable $k-\varepsilon$ model)

Figure 6.20 shows the stream function isovalues after 30 seconds of charging in the middle part of the tank. From contours it can be observed how larger eddies in the region between storage outlet and heater outlet appear and increase the mixing rate in this region at the beginning of charging. By higher charging time, these eddies become smaller, and the mixing effect reduces.

Dimensionless Numbers Analysis at the Storage Boundaries

In order to have a general view of the Reynolds number at the solution boundaries, the facet average values of the Reynolds number at the solution domain boundaries for different charging mass flow rates have been represented in table 6.2. The Reynolds number over these boundaries has been calculated with respect to average value of velocity over the boundaries. This table shows that for charging mass flow rate of 0.05 kg/s, Reynolds number at the inlet port lies in transition range of the pipe flow, and for charging mass flow rate more than 0.1

kg/s, Reynolds number at the inlet port exceeds the fully turbulent flow Reynolds number limit for the pipe flow (about 4000). For this reason, implementing of turbulence model for these parts of simulations seems to be reasonable.

Table 6.2: Average of facet values of Reynolds number for different charging mass flow rates at different boundaries of the storage tank

	Mass flow rate=0.05 kg/s	Mass flow rate=0.1 kg/s	Mass flow rate=0.2 kg/s	Mass flow rate=0.4 kg/s
Storage inlet	2626.30	5043.87	10051.8	19696.63
Heater inlet	39.78	79.57	159.15	318.31
Heater outlet	25.65	47.83	102.45	176.57
Cooler inlet	5.92	11.85	23.71	47.43
Cooler outlet	14.89	26.21	58.21	88.35
Outlet	73.41	128.75	322.48	799.50

Temperature Distribution Analysis for Different Charging Mass Flow Rate

Temperature difference with initial temperature distribution for different charging mass flow rates has been represented in a diagram in Figure 6.22. This diagram demonstrates that in lower charging mass flow rates like 0.1 kg/s higher mixing at the lower part of the tank leads to higher deviation from initial temperature distribution. Due to less mixing of charging flow with fluid inside of the tank for higher charging mass flow rates, temperature deviation represents lower value in the region of main flow insertion from stratification pipe to storage tank.

Table 6.3: Integral of temperature deviation from initial temperature over storage height

Charging mass flow rate (kg/s)	Integral of temperature deviation from initial temperature over storage height
0.1	17.54
0.2	11.71
0.4	10.03

Higher charging mass flow rates tend to less mixing process in the tank. For higher charging mass flow rates, the inlet Richardson number has a smaller value. Therefore, the mixing forces are more important than the buoyancy forces. For a storage tank without stratifier, it results to more mixing and less stratification. In the case of storage tank with stratification pipe, the mixing process will be restricted mainly inside of the stratification pipe. Therefore, the mixing effect due to high charging flow rate doesn't result in considerable destratification inside of the storage tank.

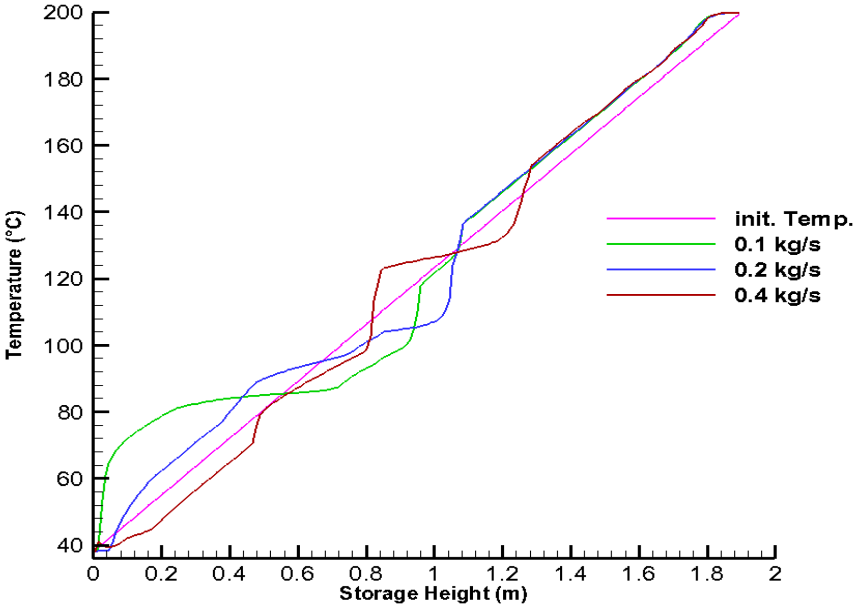

Figure 6.21: Average temperature distribution in TES in transient simulation with realizable $k-\varepsilon$ model for different charging mass flow rates (0.1 kg/s after 120 s, 0.2 kg/s after 60 s and 0.4 kg/s after 30 s)

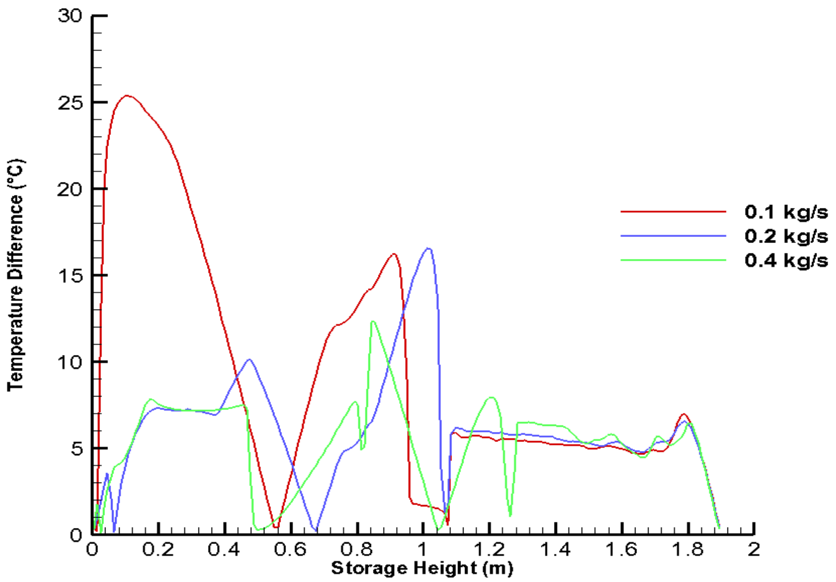

Figure 6.22: Temperature difference between initial linear temperature distribution and average temperature distribution in TES in transient simulation with realizable $k-\varepsilon$ model for different charging mass flow rates (0.1 kg/s after 120 s, 0.2 kg/s after 60 s and 0.4 kg/s after 30 s)

Integral of the temperature deviation in figure 6.22 has been demonstrated in table 6.3. Charging mass flow rate of 0.4 kg/s shows the lowest value in this table. It means that the charging with higher mass flow rate leads to less temperature deviation from initial temperature distribution, and therefore, less destratification totally. The comparison of the cases with different charging mass flow rates has been done at different charging time, so the mass weighted Enthalpy of the fluid inside of the storage tank solution domain is equal for three cases.

6.3.4 Pressure Difference Analysis

Simulation results of the case with charging flow of 0.05 kg/s has been used for this part of analysis. As it has been already discussed in 3.15, according to Bernoulli equation and by small friction forces in this simulation, the pressure difference between charging pipe and storage tank causes the mass flow out of or in the storage tank. Figure 6.23 depicts the pressure difference between stratification pipe and storage tank. A negative pressure difference causes a mass flow rate from storage tank to stratification pipe that has been already introduced as entrainment effect. This region is shown as sucking region in figure 6.23. A positive pressure difference leads to a complete or partly outflow from stratification pipe to the storage tank.

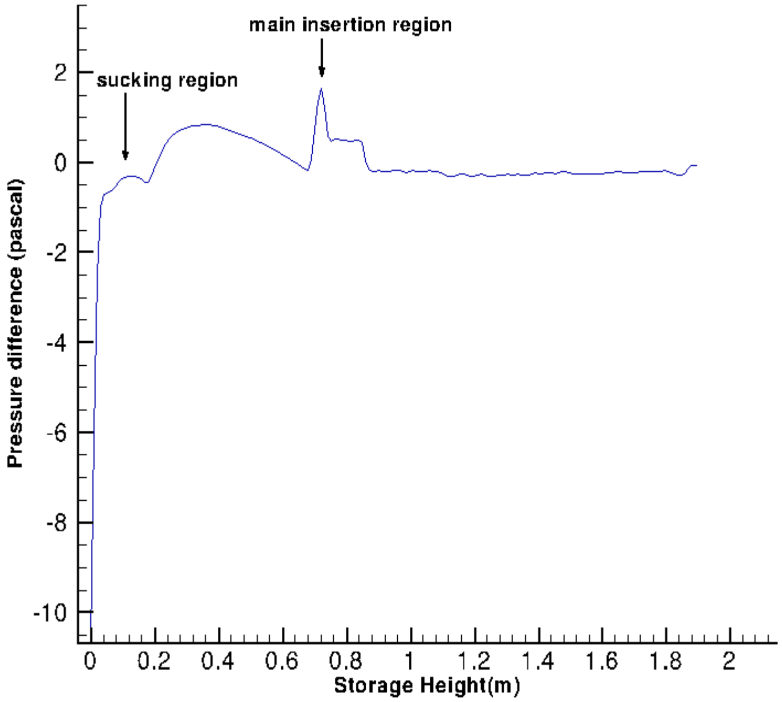

Figure 6.23: Pressure difference between stratification pipe and storage tank along the tank height

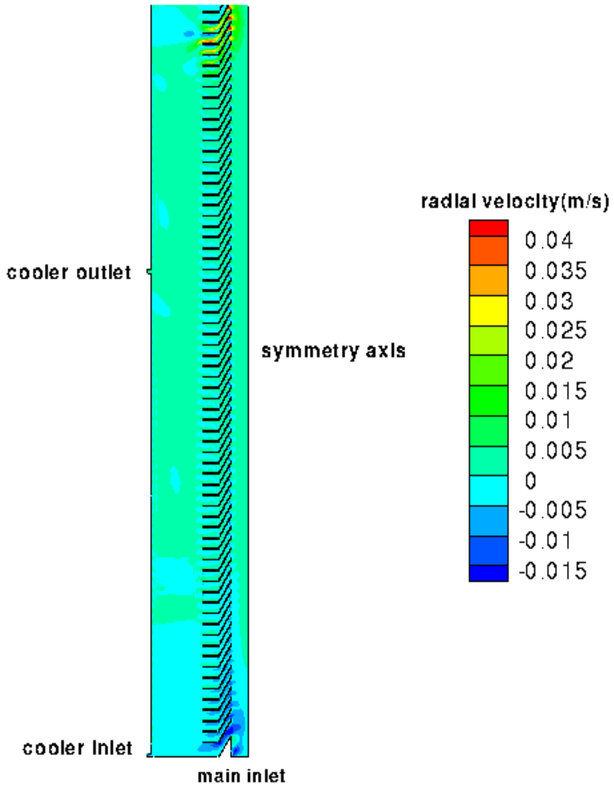

Figure 6.24: Radial velocity representing the suction effect at the bottom and main insertion region in the middle of the tank

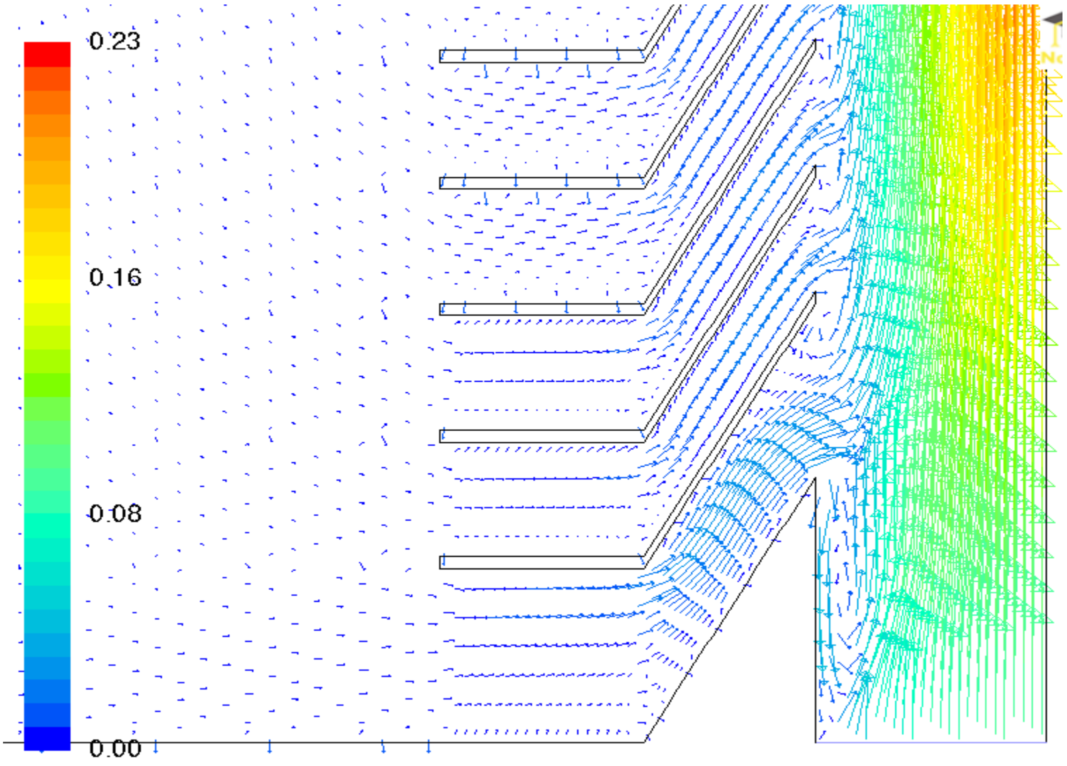

Figure 6.25: Velocity vector colored by velocity magnitude (m/s) at the sucking region

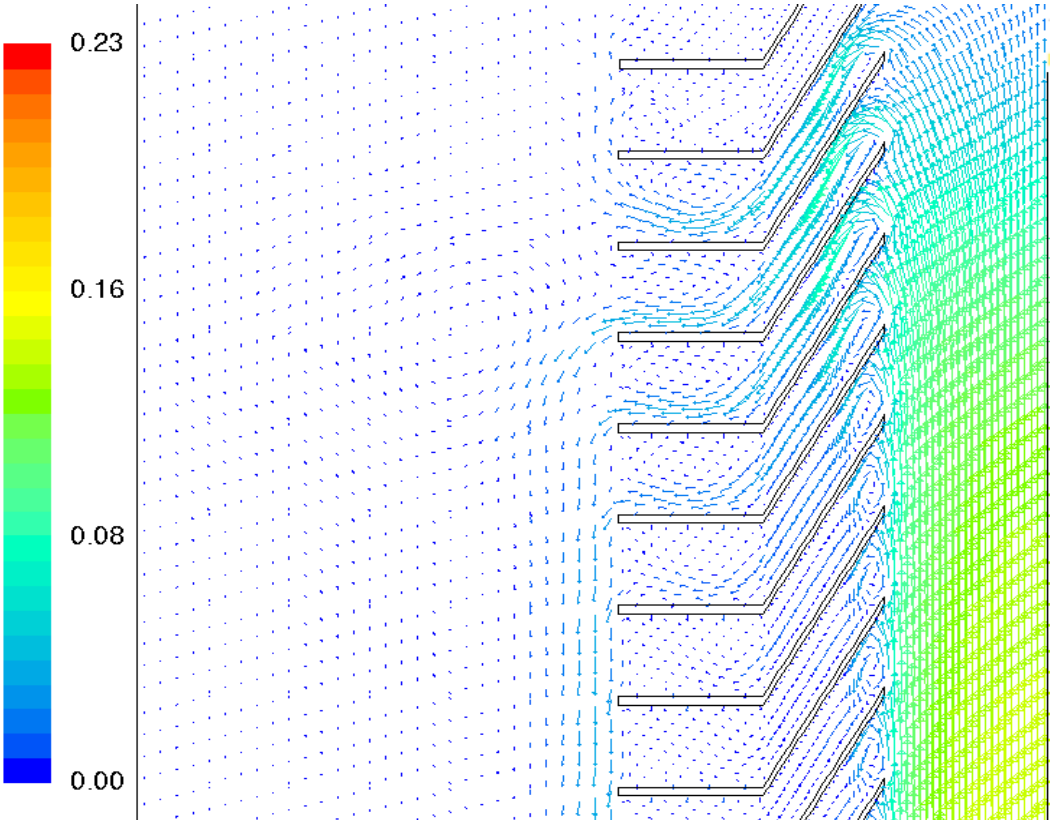

Figure 6.26: Velocity vector colored by velocity magnitude (m/s) at the main insertion region

The highest outflow mass flow rate from stratification pipe to the storage tank occurs at the region shown as main insertion region in figure 6.23, which represents the highest positive pressure difference. The sucking region and main insertion region can be seen as region with the highest and the lowest radial velocity in figure 6.24.

Charging from the Top of the Storage Tank

In a new simulation with the same geometry and boundary conditions and replacement of heater and cooler cycle position, the charging flow is introduced from the top of the storage through the stratification pipe. In the new simulation setup, Heater inlet is located in the same height as storage inlet. It means that the flow in the tank in the region of storage inlet is warmer than the charging flow temperature. Charging mass flow rate of 0.05 kg/s has been set for new simulation setup. The entrainment effect through the first five openings next to the charging pipe inlet (the first five upper openings) has been compared with the entrainment effect at the bottom of the tank in the simulation case with charging from the bottom.

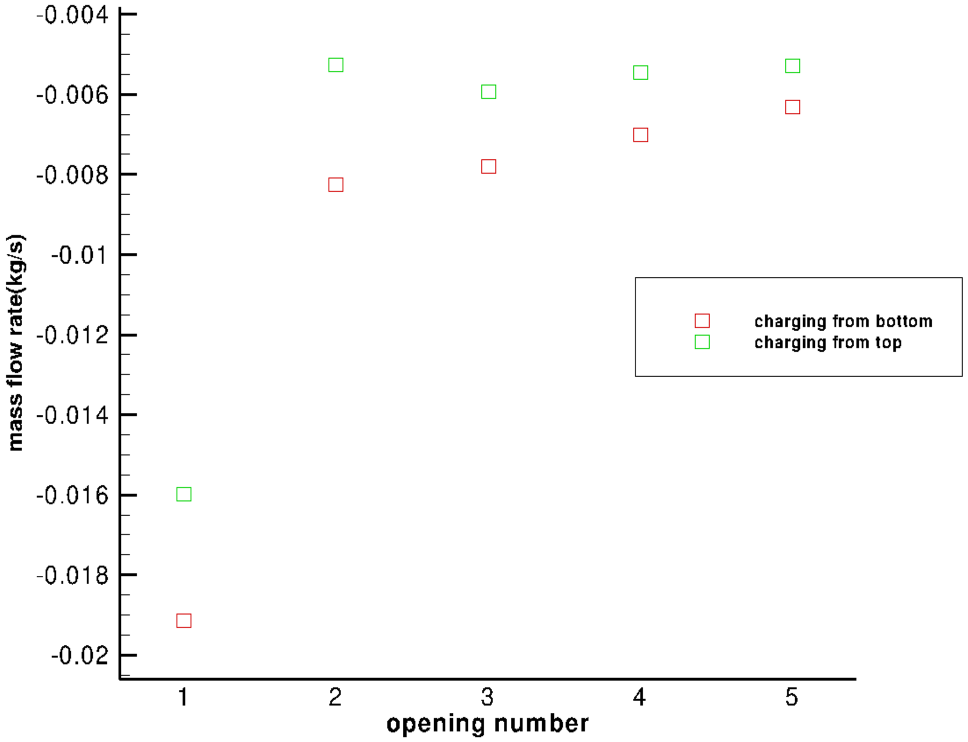

Figure 6.27: Mass flow rate through the first openings in the region of storage inlet for cases of charging from top and bottom (simulation with realizable $k - \varepsilon$ model)

A relative lower entrainment effect is observed in case for charging from top of the storage tank. It lies on the intensified axial momentum and higher deviation of the flow through the heater inlet in the case of charging from the top of the storage tank.

6.4 Analysis of Effective Thermal Conductivity

6.4.1 Effective Thermal Conductivity due to Advection

In 1-D plug flow model of TES the heat transfer process has been simulated by considering the heat conduction. In charging process of the TES, advection due to the bulk fluid flow can be another heat transfer mechanism, which leads to stronger mixing in the tank. In order to calculate the advection part of effective thermal conductivity, a user defined function (UDF) has been written and loaded with ANSYS Fluent case file. UDF files are written in C programming language and can be executed as interpreted or compiled functions. The UDF after loading in Ansys Fluent case file has been interpreted and executed to calculate the desired variable in equation 3.36. Convective heat transfer part has been summed over horizontal surfaces at different heights of the tank. In addition, the production of horizontal surface and average value of temperature gradient in axial direction has been exported over different horizontal surfaces at different heights of the tank. By means of these parameters, the effective thermal conductivity due to advection has been calculated at different charging time. The analysis of the diagram after 30 seconds shows that, the effective thermal conductivity reaches its highest values in the region, where flow leaves the pipe to storage tank mainly. The highest value in this region tends to reduce by higher charging time and be distributed over a more extended area in axial direction.

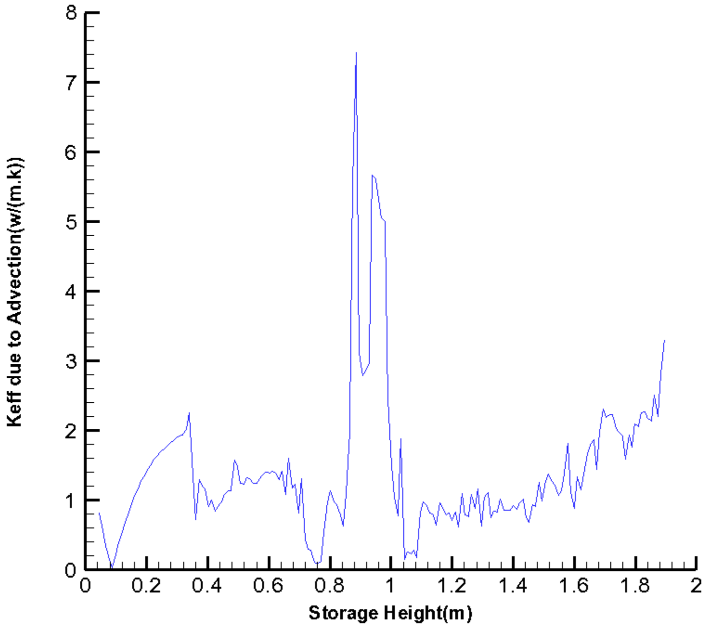

Figure 6.28: Effective thermal conductivity due to advection after 30 s of charging with 0.2 kg/s (simulation with realizable $k - \varepsilon$ model)

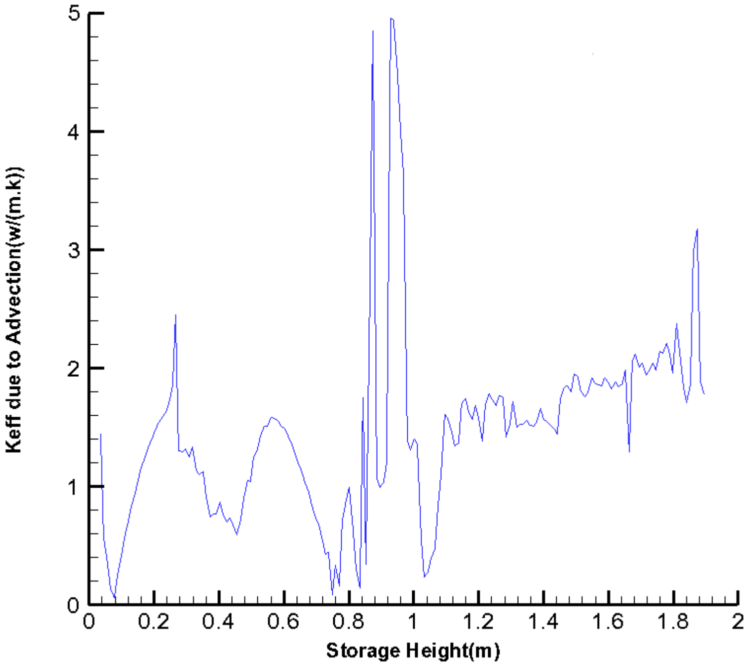

Figure 6.29: Effective thermal conductivity due to advection after 60 s of charging with 0.2 kg/s (simulation with realizable $k - \varepsilon$ model)

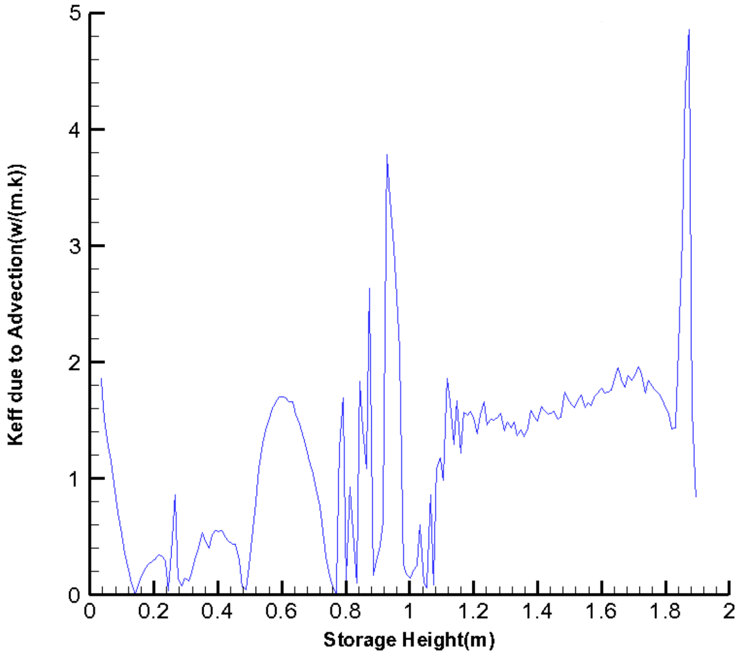

Figure 6.30: Effective thermal conductivity due to advection after 90 s of charging with 0.2 kg/s (simulation with realizable $k - \varepsilon$ model)

6.4.2 Effective Thermal Conductivity due to Turbulence

Turbulent diffusion in fluid flow in TES enhances the mixing due to increasing the transport rate of momentum, which leads to homogenization. On the other hand, enhanced energy transport rate due to turbulence causes an intensified heat transfer process. This enhancement can be considered on the basis of additional thermal conductivity called effective thermal conductivity due to turbulent motions. The effective thermal conductivity due to turbulence and advection along the vertical axis of the storage tank is an important parameter influencing the COP of the whole system. It accounts for convection effect and turbulent mixing in the storage tank. Therefore, it can only be determined for a specific geometry of tank, inlet and outlet ports, initial and boundary conditions. For any given geometry, it depends on the fluid charging volume flow rate, storage material, and the temperature profile in the storage tank. In transient simulation, effective thermal conductivity in the storage with realizable k-epsilon turbulence model has been calculated and the average values over the whole horizontal area at different storage heights have been plotted. The results demonstrate also the maximum value in the region of main flow insertion from stratification pipe to the storage. Turbulent viscosity contour depicted in figure 6.31 demonstrates the highest value of turbulent viscosity, and consequently, effective thermal conductivity due to turbulence. The comparison of two parts of the effective thermal conductivity reveals that the effective thermal conductivity due to turbulence is considerably higher than effective thermal conductivity part due to advection except for a small region at the lower part of the storage tank.

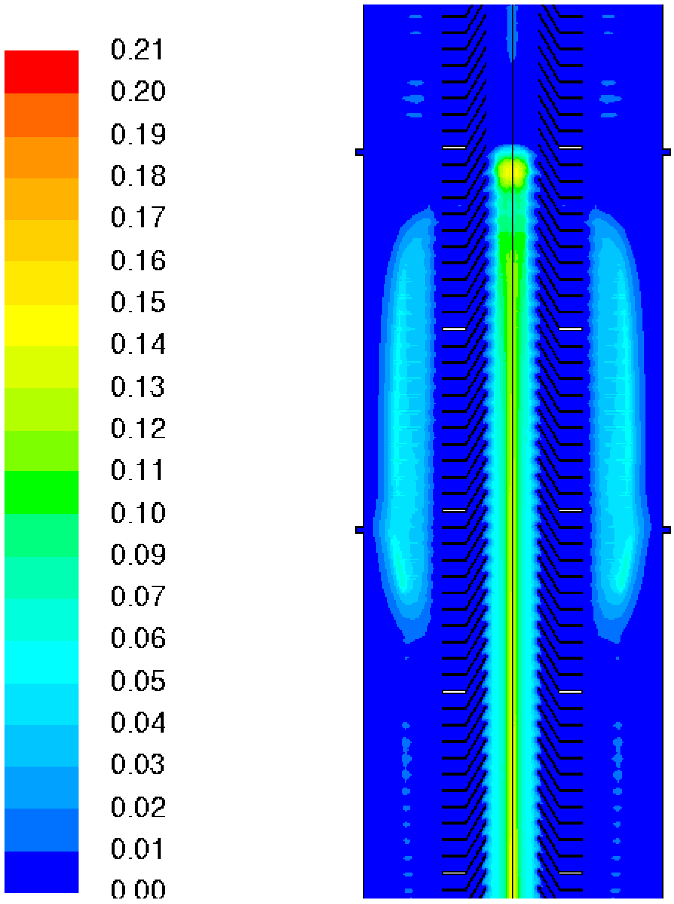

Figure 6.31: Turbulent viscosity contour (kg/(m.s)) in the storage outlet region after 60 s of charging with 0.2 kg/s charging mass flow rate (simulation with realizable $k-\varepsilon$ model)

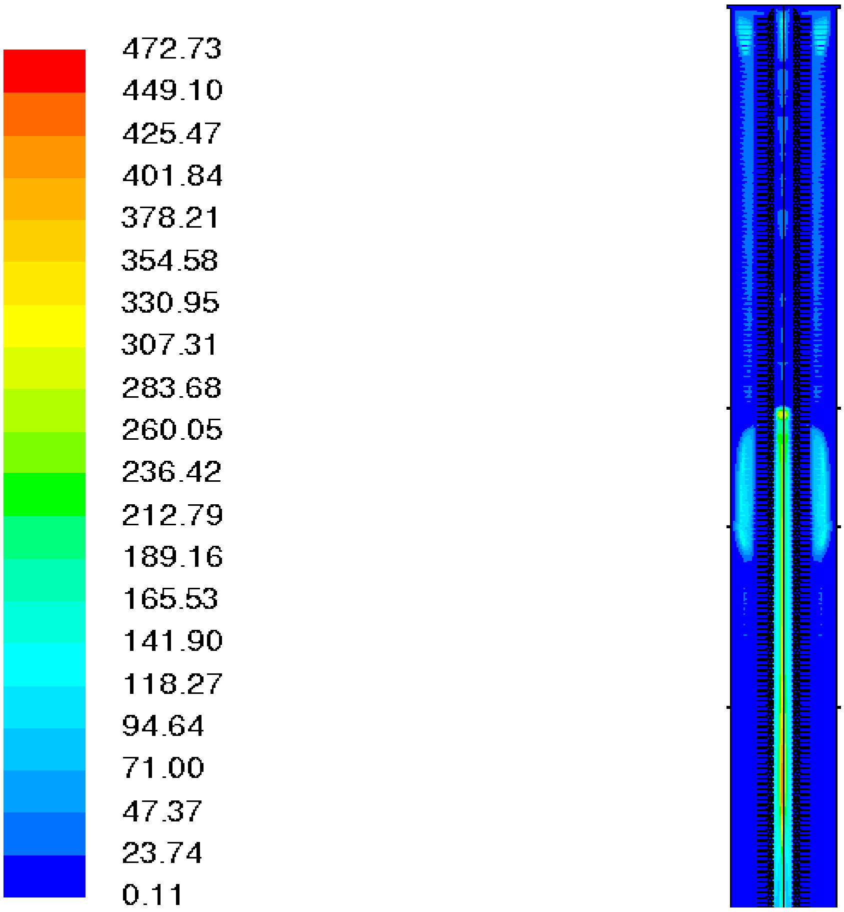

Figure 6.32: Contour of effective thermal conductivity (W/(m.K)) due to turbulence after 60 s of charging with 0.2 kg/s charging mass flow rate (simulation with realizable $k - \varepsilon$ model)

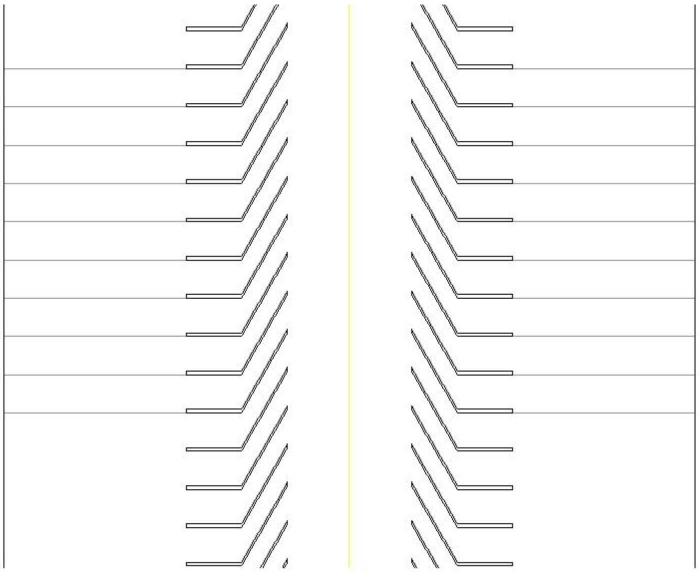

Figure 6.33: Horizontal surfaces between outer diameter of the stratification pipe and storage tank wall for averaging of values

Average effective thermal conductivity at different horizontal surfaces along the storage height shows that effective thermal conductivity in the region of flow insertion from stratification pipe to the storage reduces by increasing of charging time. This region represents the maximum value of the effective thermal conductivity in the tank. The effective thermal conductivity due to turbulence is determined by turbulent eddy viscosity which is a function of turbulent kinetic energy and its dissipation rate. Due to dissipation of the turbulent kinetic energy by increasing of charging time, the turbulent kinetic energy of the flow, and consequently, the turbulent viscosity starts to reduce and so the effective thermal conductivity shows lower values by time progress. On the other hand, in the region of heater inlet, the average effective thermal conductivity shows a small increase during the charging time. Because of kinetic energy of the charging flow of the heater inlet, the turbulent kinetic energy production term is influenced by the mean flow during the charging process, and therefore, turbulent viscosity shows a small increment by higher charging time.

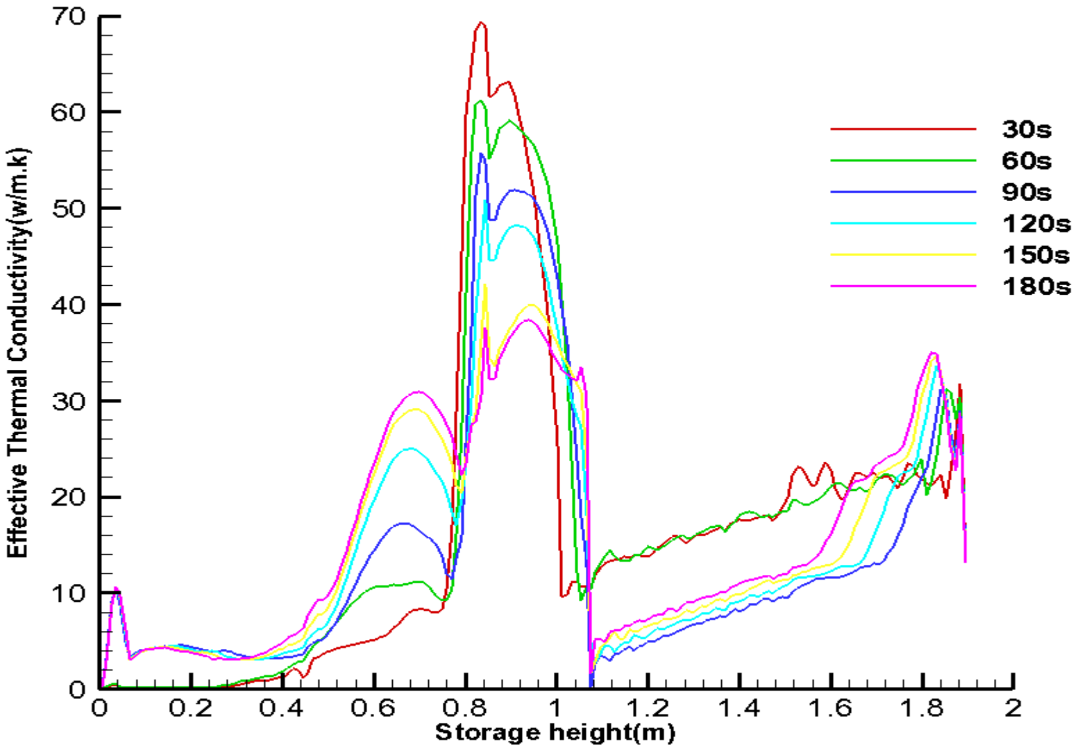

Figure 6.34: Average effective thermal conductivity due to turbulence versus storage height at different charging time in transient calculation with realizable k-epsilon turbulence model

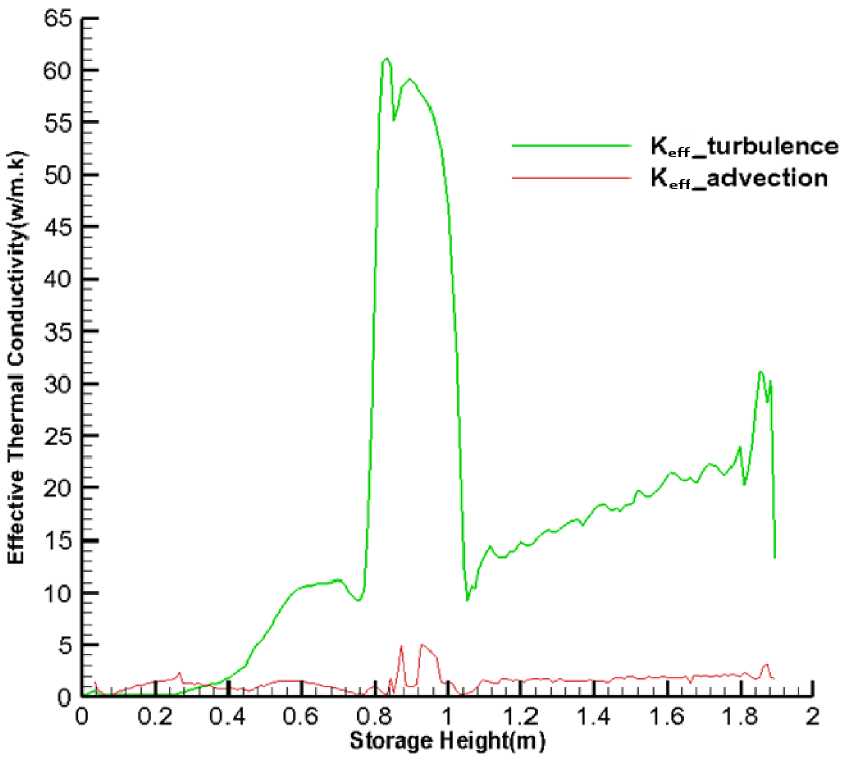

Figure 6.35: Comparison of effective thermal conductivity due to turbulence and advection after 60 s of charging with 0.2 kg/s mass flow rate (simulation with realizable $k-\varepsilon$ model)

6.5 Simulation Results with SST $k-\omega$ Model

Simulation with the same setup has been repeated with SST $k-\omega$ turbulence model. Figure 6.36 demonstrate the contours of turbulent viscosity calculated with realizable $k-\varepsilon$ and SST $k-\omega$ model. Both models forecast the high value of turbulent viscosity in the same region of the storage tank. But realizable $k-\varepsilon$ model predicts relative higher values in this region as well as in stratification pipe. Furthermore, the region with higher values in storage tank for SST $k-\omega$ model shows a more extended region. Modification of turbulent viscosity to account for turbulent shear stress transport in SST $k-\omega$ model can be a reason of extended area with higher turbulent viscosity. Also at the upper part of the tank close to the heater inlet, realizable $k-\varepsilon$ model predicts higher values of turbulent viscosity than SST $k-\omega$ model.

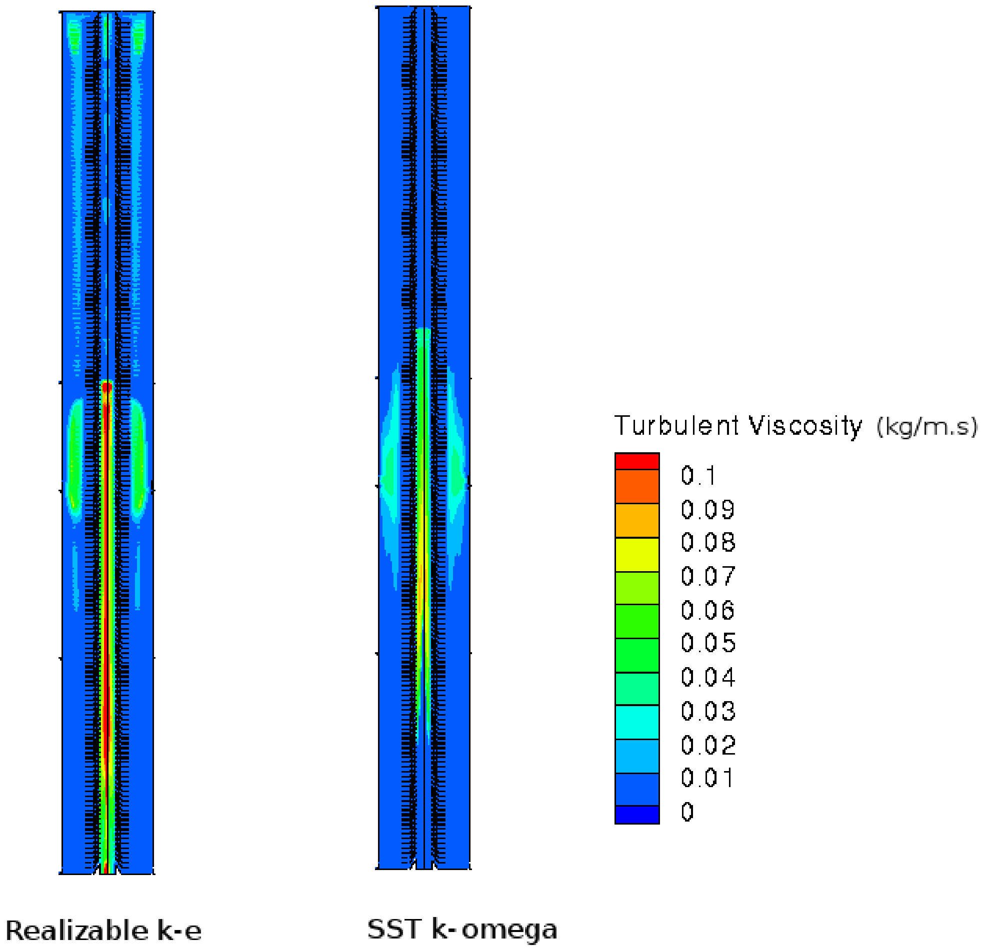

Figure 6.36: Turbulent viscosity comparison between realizable $k-\varepsilon$ and SST $k-\omega$ model after 60 s of charging with 0.2 kg/s mass flow rate

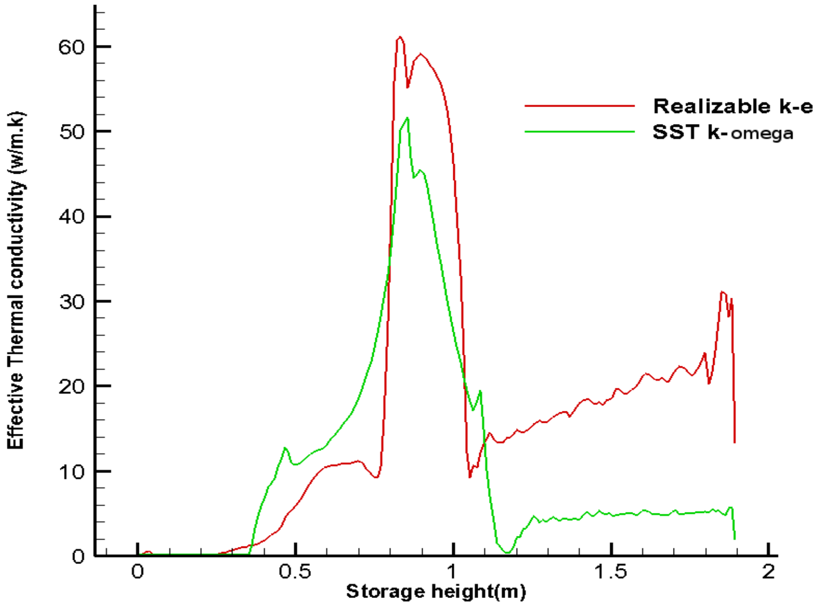

Figure 6.37: Average effective thermal conductivity due to turbulence after 60 s of charging with 0.2 kg/s mass flow rate for realizable $k-\varepsilon$ and SST $k-\omega$ model

Average value of effective thermal conductivity for realizable $k-\varepsilon$ model also demonstrates higher value in the region of flow insertion from pipe to storage and between heater outlet and heater inlet. Because of the extended region with higher turbulent viscosity in SST $k-\omega$ model, the region at the bottom of main insertion region from pipe to storage predicts higher value in comparison to realizable $k-\varepsilon$ model.

6.6 Modified Geometry of Inlet Stratification Pipe

6.6.1 Inlet Stratification Pipe Channel Geometry

Simulation results from the last sections exhibit the high degree of mixing during the charging process especially between the cooler cycle inlet and outlet at lower part of the TES. Cooler inlet at the bottom, which results in a charging flow with radial velocity, increases the mixing between warmer charging flow from the main inlet at the bottom of the tank and colder flow from the cooler inlet. The mixed fluid leaves the stratification pipe from the upper openings and mixes again with the water inside of the tank. From the figure 6.15 it can be seen that the entering volume flow rate from the tank into stratification pipe at the lower openings of the pipe is higher and reduces at the higher openings. This plot also shows how the entrainment effect reduces during the charging time. For the mixing at the lower part of the tank, entrainment effect at the lower openings is therefore very significant. The original opening geometry of stratification pipe is similar to the patented and marketed product of German company Sailer GmbH. In this section, the opening geometry of the stratification pipe has been modified in order to reduce the entrainment effect in TES. For determination of opening geometry, three parameters have been considered to be varied in different simulations and their influence on the entrainment has been investigated by means of CFD results post processing. Three geometrical parameters for the openings are as follows:

1- Slope at the entrance of the opening channel(a)
2- Slope in the middle of the opening channel(b)
3- Vertical distance between opening channel plates at the outlet of stratification pipe to the storage tank(c)

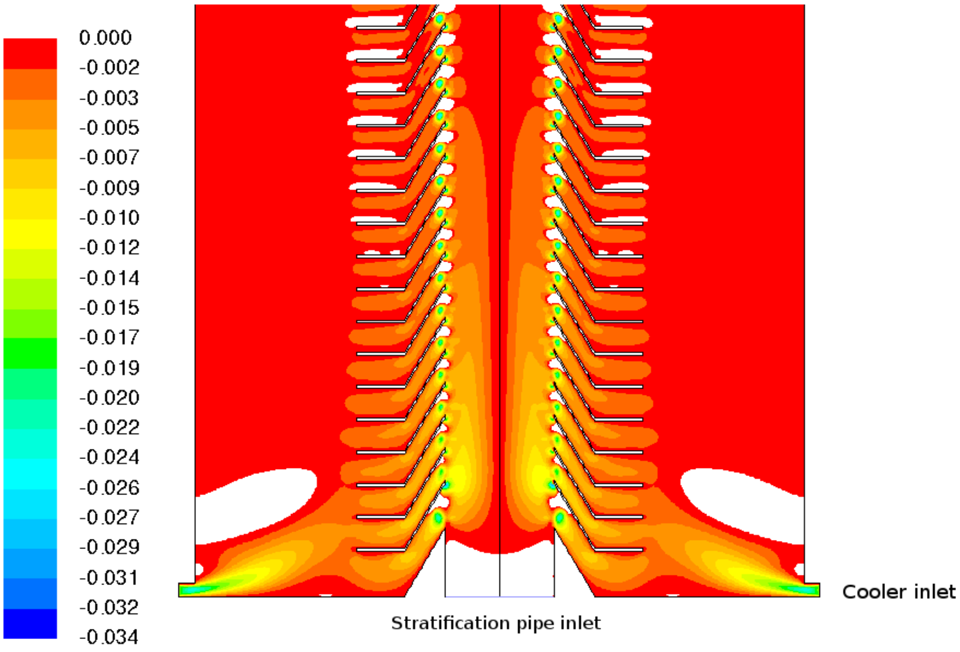

Figure 6.38: Radial velocity contour (m/s) at the lower part of TES after 30 s of charging with 0.2 kg/s mass flow rate for realizable $k-\varepsilon$ model

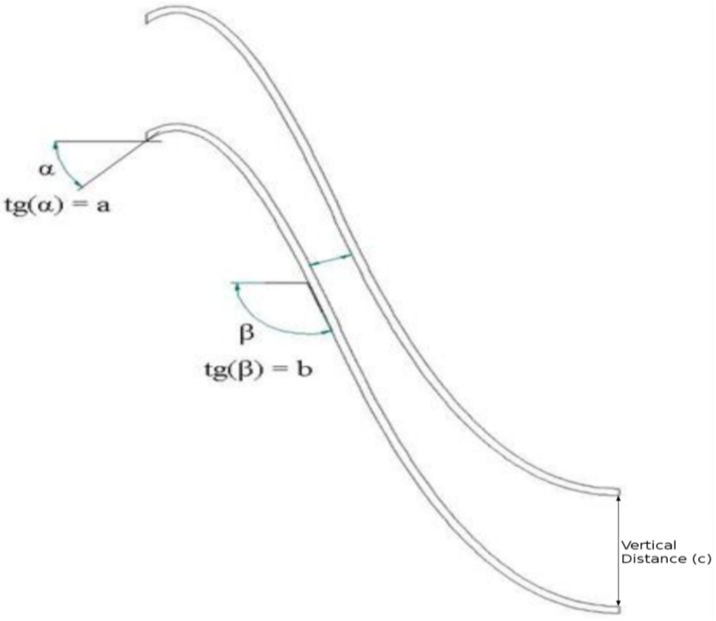

Figure 6.39: Geometrical parameters for stratification pipe opening channel [76]

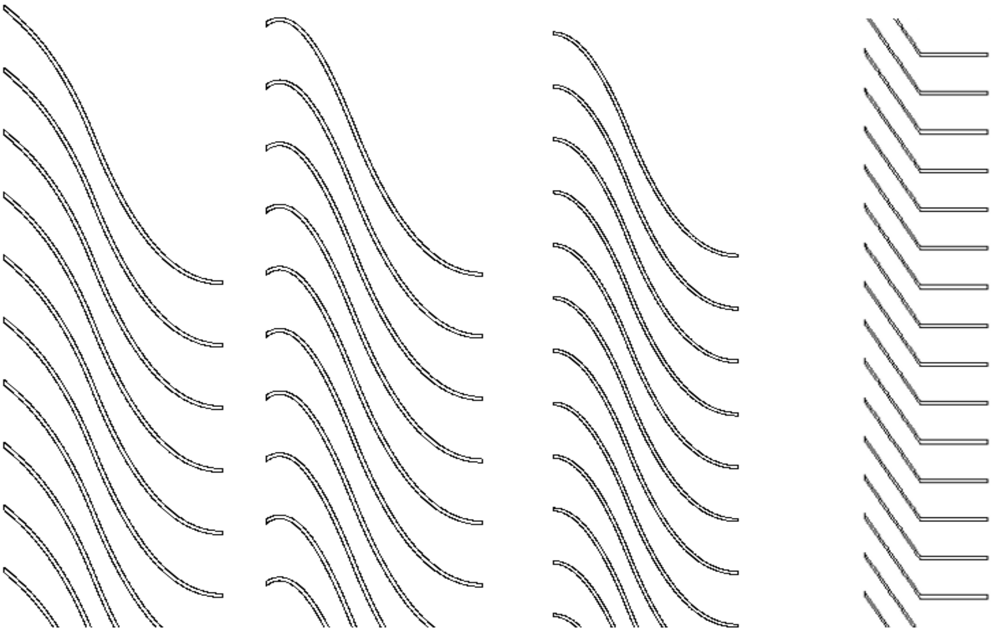

Figure 6.40: Stratification pipe original geometry (right) and new variations with different slope at the channel entrance from pipe to the storage tank (from left to right -1,1,0)

The new channel geometry profile has been created by combining of two polynomial profiles. The profile function has been presented in the appendix A.

6.6.2 Simulation with Different Charging Flow Temperatures

Different geometries of inlet stratification pipe with different parameters have been installed in the applied geometry of storage tank which is introduced in figure 6.41. The applied geometry includes three Plexiglas blocks in the practice with four 1 mm gaps. The total height of the tank is 38 cm with 18 cm diameter. The stratification pipe channels are located in the middle of the tank with inner diameter of 3.4 cm and outer diameter of 13.4 cm. About 1 Million unstructured cells have been used to discretize the fluid domain. It has been tried to investigate the mixing process of the flow in a steady state simulation with three inlets and different temperatures in the storage tank. The upper inlet has been defined with charging volume flow rate of 1 liter/min and 40 °C temperature. The lower inlet has the same charging volume flow rate but with 20 °C temperature. The main charging flow of the storage is 3 lit/min with different temperatures between 20 and 40 °C. The storage outlet has been defined at the second gap from the bottom of the tank. By keeping the geometrical parameters of the stratification pipe constant and varying the charging temperature with constant charging mass flow rate, the effect of buoyancy forces on the mixing of flows with different temperatures in correspondent geometry has been studied.

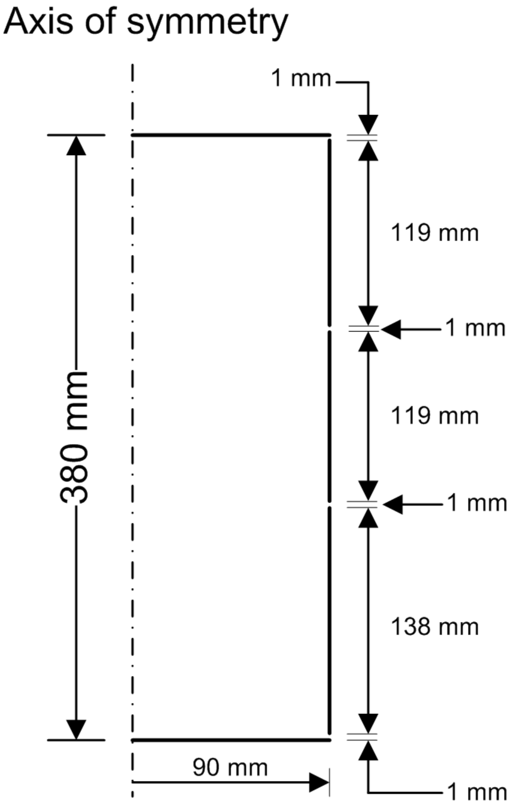

Figure 6.41: Geometrical information of the applied storage tank for simulation

For this section of simulations, the geometrical parameters are set to (a=0, b= -3, c=15). Thus, the inner slope of the stratification pipe is 0 and the middle slope -3, and the distance between channels is 15 mm. Three simulations have been performed with charging temperatures of 24, 30 and 36 °C.

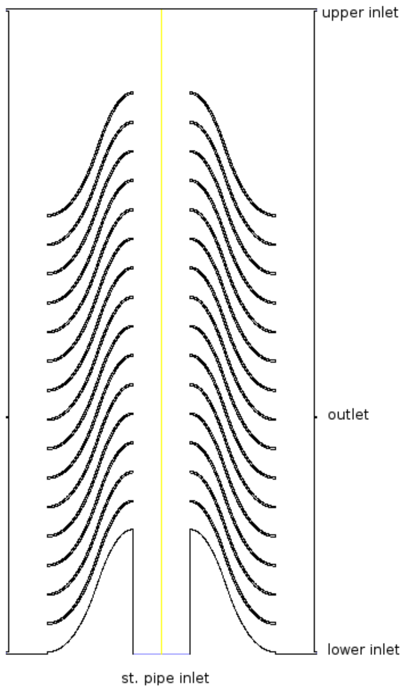

Figure 6.42: Boundary conditions in CFD model of storage tank with stratification pipe

Simulation with Charging Flow of 24 °C

In the charging process with intermediate temperature between upper inlet temperature and lower inlet temperature, four factors can influence the position of flow insertion from stratification pipe to storage tank. These factors are

1- The inertial forces due to charging flow rate
2- Buoyancy forces due to temperature differences between incoming flows
3- Geometrical parameters of the stratification pipe
4- Outlet position

In the simulation with different charging flow temperature, the only factor which changes in simulations is buoyancy forces and other three factors have been kept constant. Solution methods and other simulation setup for the calculation have been presented in table 6.4.

Table 6.4: Solution methods for the simulation case setup for modified geometry of stratification pipe

Pressure-Velocity Coupling algorithm	Coupled
Spatial discretization for pressure	Body force weighted
Spatial discretization for momentum	Second order upwind
Spatial discretization for Energy	Second order upwind
Time discretization	Steady state
Viscous model	Laminar and turbulent
Fluid material	Water

Analysis of Reynolds Number in the Storage Tank

Before starting the simulation with convenient viscous model, a Reynolds number analysis in TES based on the inner diameter of the stratification pipe as characteristic length has been performed. The steady state calculation has been done with 3lpm main charging flow and 24 °C charging temperature and two additional inlets, one at the top with 1 lpm volume flow rate and 40 °C temperature and another at the bottom of the tank with 1 lpm volume flow rate and 20 °C temperature.

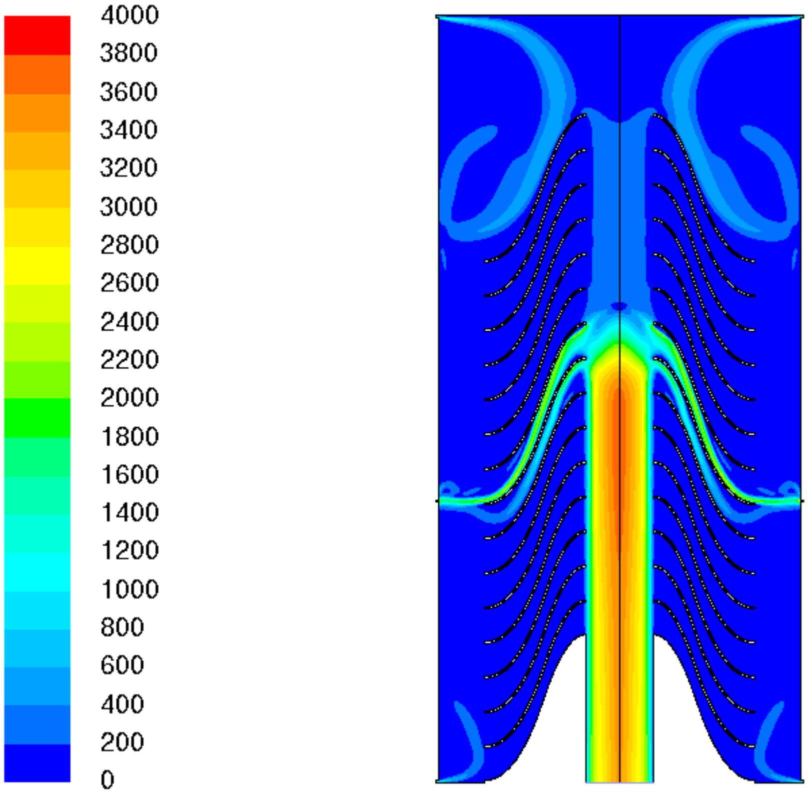

Figure 6.43: Reynolds number in storage tank with 3 lpm charging volume flow rate and 24 °C temperature and characteristic length based on inner diameter of stratification pipe in steady state laminar simulation

This analysis reveals that, the region inside of the stratification pipe from main inlet till the level of main flow insertion from pipe to storage has a larger Reynolds number between 2500 and 4000 which is in transient or turbulent flow regime of the pipe flow. On the other hand, the large part of the regions in the TES except the small area of flow insertion from pipe to the tank, has a small Reynolds number less than 1000, which is in laminar regime of the pipe flow. For these different Reynolds number values in the tank, both laminar and turbulent simulations have been performed to resolve the flow structures in more accurate and proper way.

Laminar Simulation

Steady state Simulation results show that higher temperature difference between charging flow through stratification pipe and flow through lower inlet leads to higher rising of charging flow stream in stratification pipe until the level of main outflow from the stratification pipe to the storage tank . In the corresponding case, with higher buoyancy force the reaching point of the charging flow in the pipe increases and causes higher falling down of the flow in storage tank until leaving through outlet. The falling down of the flow jet in the storage tank intensifies the mixing in the region between jet outflow from the pipe and outlet. As from the streamline visualization in Figure 6.44 can be seen, the flow jet in simulation with 24 °C leaves the stratification pipe at the level of outlet position, while in charging with 30 °C flow jet raises up to the higher channel in pipe and after falling down until a lower level than outlet position, leaves the storage tank through outlet. The fluid jet with higher temperature on the way to the outlet mixes up with fluid in the tank.

Furthermore, higher level of the fluid jet leaving the pipe to the tank causes eddy formation at different regions in the storage tank, especially close to the outlet position and leads to more mixing.

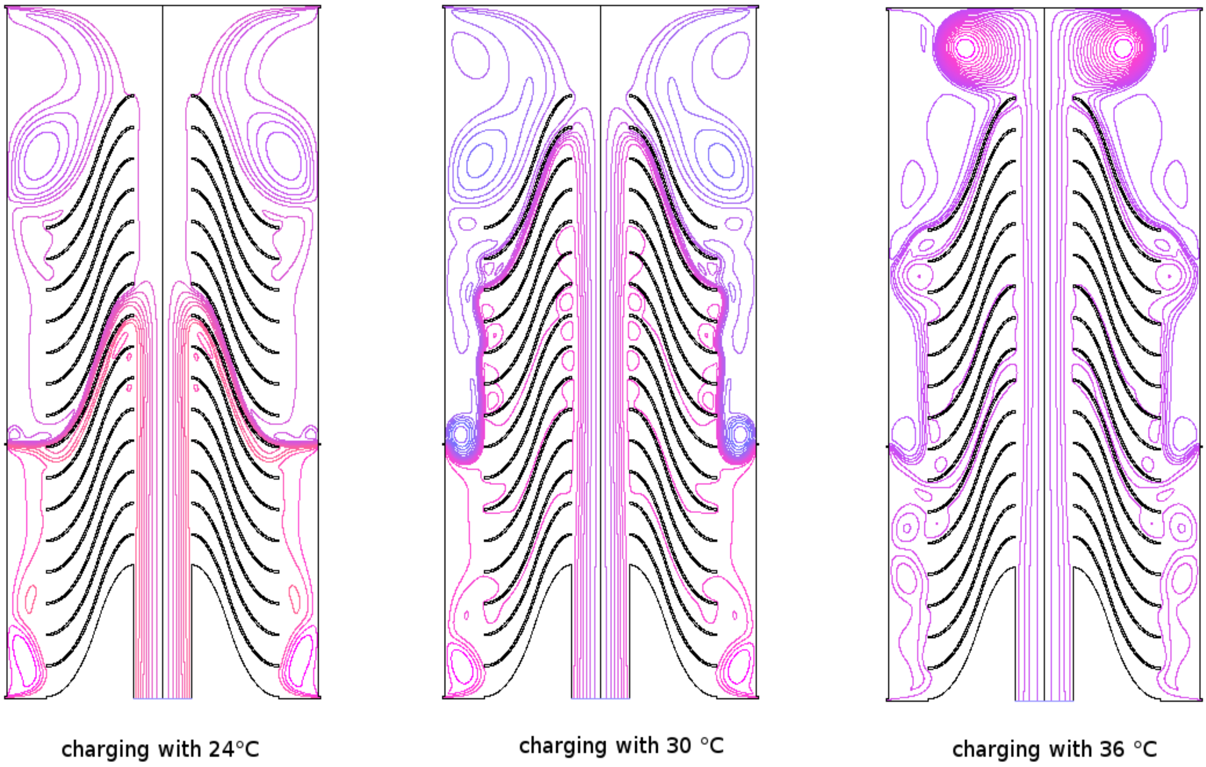
charging with 24°C

charging with 30 °C

charging with 36 °C

Figure 6.44: Streamline for different charging flow temperatures in laminar simulation

From the streamlines in laminar simulation it can be investigated that charging flow inside of the stratification pipe rises up to higher level when charging with higher charging flow temperature which causes higher buoyancy forces. In the case with charging flow temperature of 36 °C, charging flow rises till the upper shell of the tank and as a result, a region of eddies starts to build up.

Turbulent Simulation

As from the Reynolds number analysis can be investigated, the region inside of the pipe between storage inlet and main flow from pipe to storage and the region inside of the storage tank between the flow insertion from pipe to the storage and outlet experience higher Reynolds number and possibly turbulent flow. Increased momentum transfer due to the fluctuating motion represents the turbulence contribution to increased momentum diffusion. On the other hand, increased thermal diffusion due to turbulent fluctuation enhances the heat transfer in turbulent flow region. Therefore, it is expected that temperature profile shows more mixed and continuous regions in turbulent simulation. In addition, the reaching point of the charging flow in pipe for higher charging flow temperature is less than laminar simulation.

The reason of this smaller reaching point can lie on higher losses due to viscous dissipation in turbulent flow.

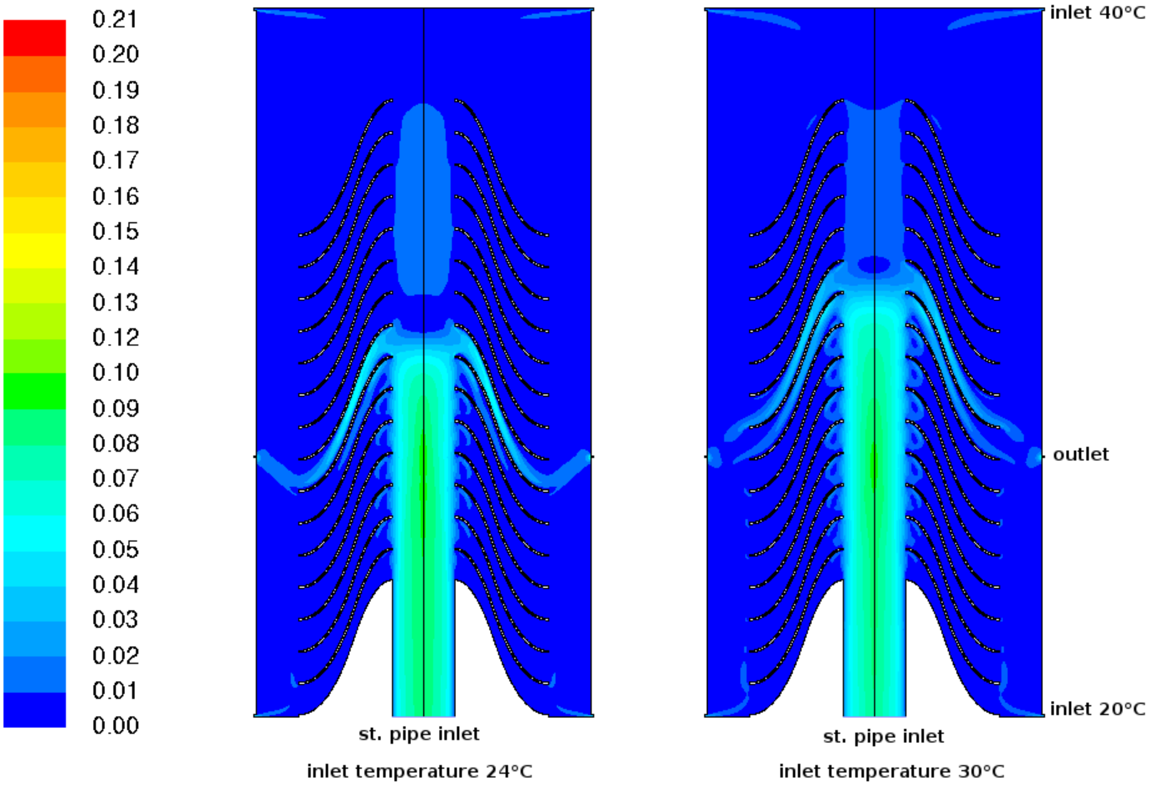

Figure 6.45: Velocity contour (m/s) comparison in steady state simulations with charging temperature of 24 and 30 °C in turbulent simulation with realizable $k-\varepsilon$ model

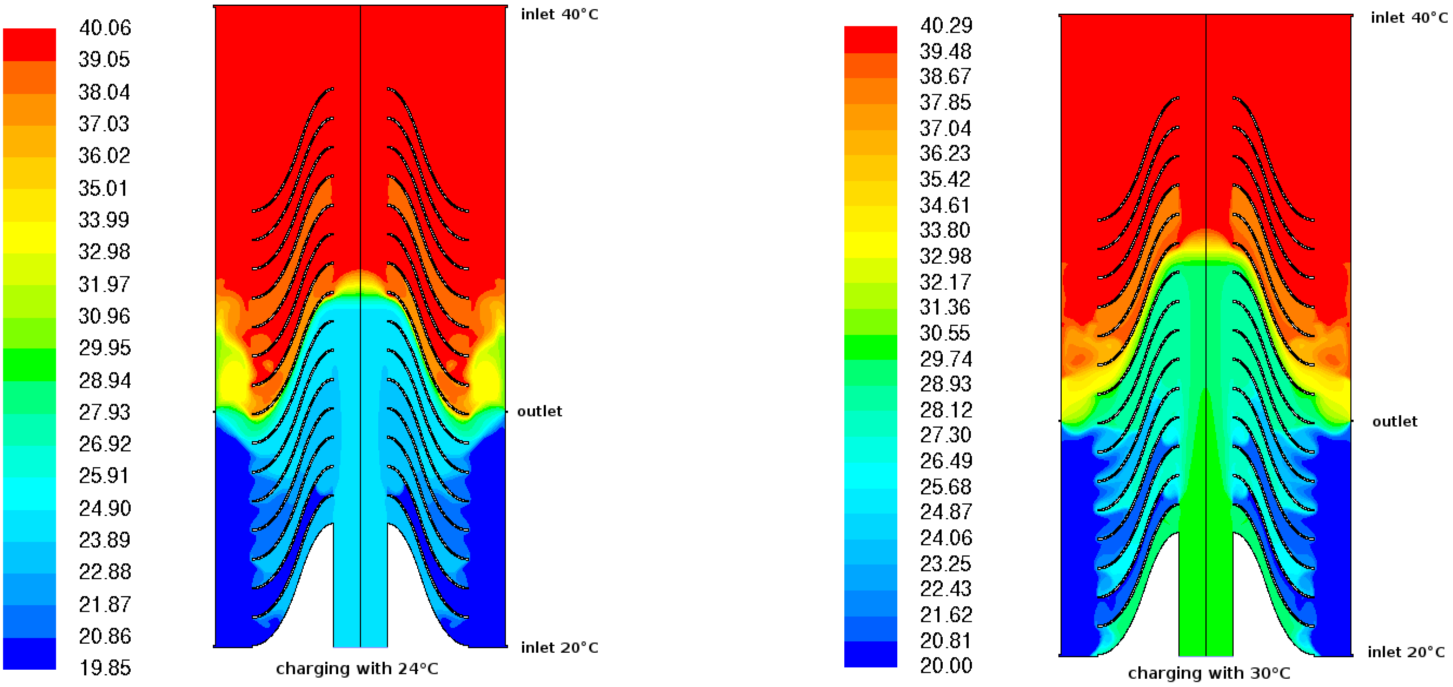

Figure 6.46: Temperature contour (°C) comparison in steady state simulation for charging with 24 and 30 °C in turbulent simulation with realizable $k-\varepsilon$ model

Higher Reynolds number in the region of main outflow from stratification pipe to the storage, and consequently, higher turbulent viscosity leads to higher rate of momentum and thermal diffusion in this region. This region with more mixing and thicker thermocline is recognizable from the temperature contours.

Backflow at the Outlet Boundary

One challenging problem in simulation includes the backflow at the outlet boundary condition. If the velocity and pressure detail at flow exit boundary are not known, outflow boundary condition in Ansys Fluent can be a relevant choice. Ansys Fluent uses a zero diffusion flux for all flow variables for outflow boundary condition. Furthermore, an overall mass balance correction in fluid domain has been undertaken. Thus, the outflow plane condition is provided from the domain by extrapolation and doesn’t impact the upstream flow. Therefore, the pressure and velocity at the outflow boundary are updated by extrapolation from fluid domain. Building a recirculation area at the outflow boundary causes some backflow to the fluid domain that leads to convergence difficulty and invalidity of the results. Figure 6.47 demonstrates the recirculation region at outflow boundary. Streamlines at the outlet show how the sharp edge of the storage tank geometry at the beginning of outlet channel causes recirculation region at outlet boundary. This situation appears in some simulation cases that by means of outlet channel prolongation have been tried to avoid backflow condition at the outlet. Figure 6.48 illustrates how the outlet channel prolongation avoids recirculation region at outlet boundary. When the outlet channel has been prolonged, as it has been outlined in figure 6.48, then recirculation region starts to be built before the outlet boundary and doesn’t reach it.

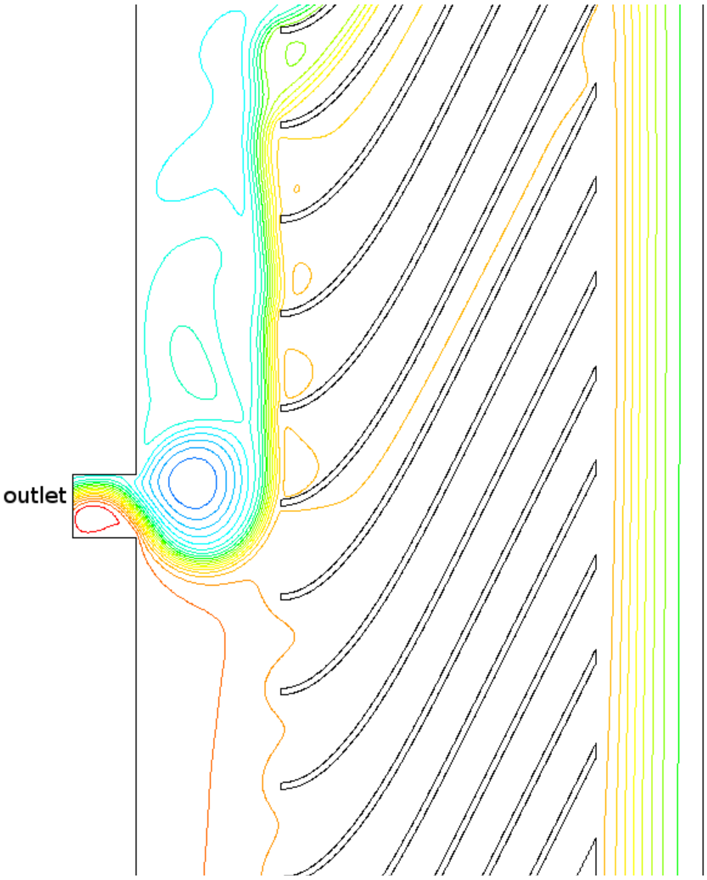

Figure 6.47: Backflow condition at outlet boundary condition

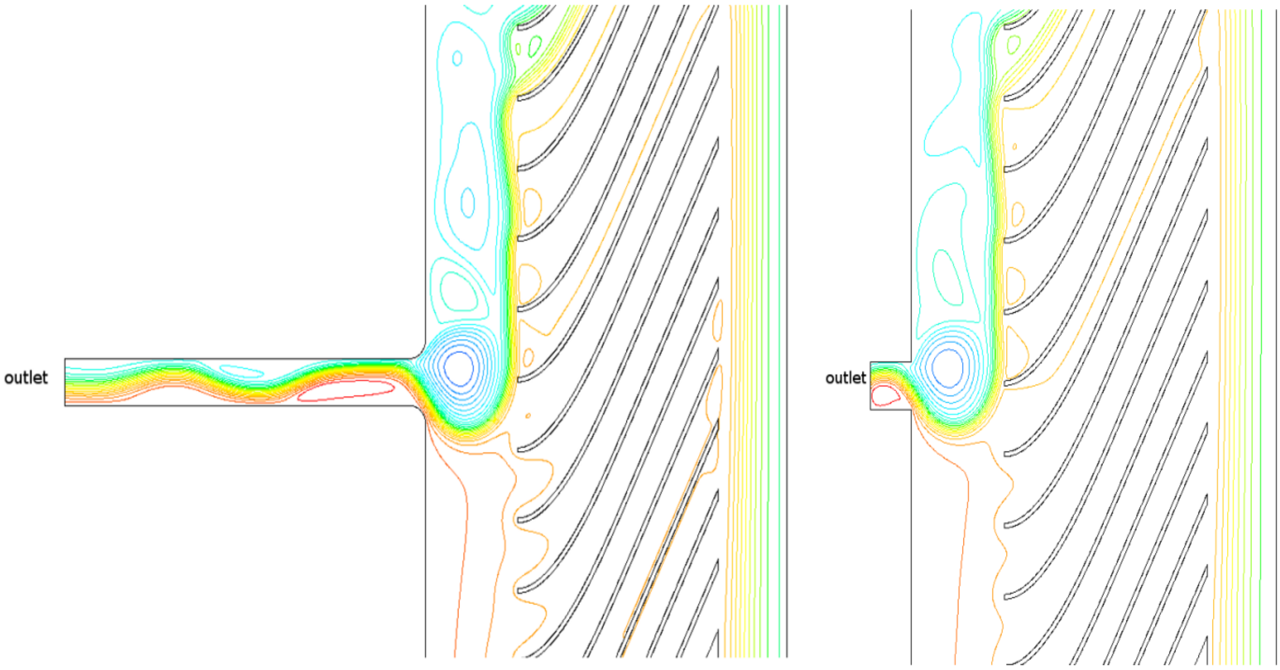

Figure 6.48: Streamlines at the outlet boundary condition after extension of the outlet channel

Stratification Pipe Geometry Modification in Diploma Thesis

By supervising the diploma thesis of Carles Ribas Tugores, the geometry of the stratification pipe has been modified based on two criterions [76]. One describes temperature profile deviation from an ideal stratified tank temperature profile which is defined as reference case. Another parameter is defined based on the channel mass flow rate deviation from the reference case. Mass flow rate through channels multiplied by distance between channel center and outlet center and have been summarized over the channels. The result value is normalized by division by theoretic worst case, where the total mass flow rate reaches the top of the tank. The stratification pipe geometry has been optimized based on these two parameters in a series of steady state simulation with charging temperature of 30 °C and 25 °C. Two additional inlets have been used to inject water with 20 °C and 40 °C from the bottom and top of the tank, respectively. Figure 6.49 demonstrates the model geometry of the tank with the corresponding boundary conditions.

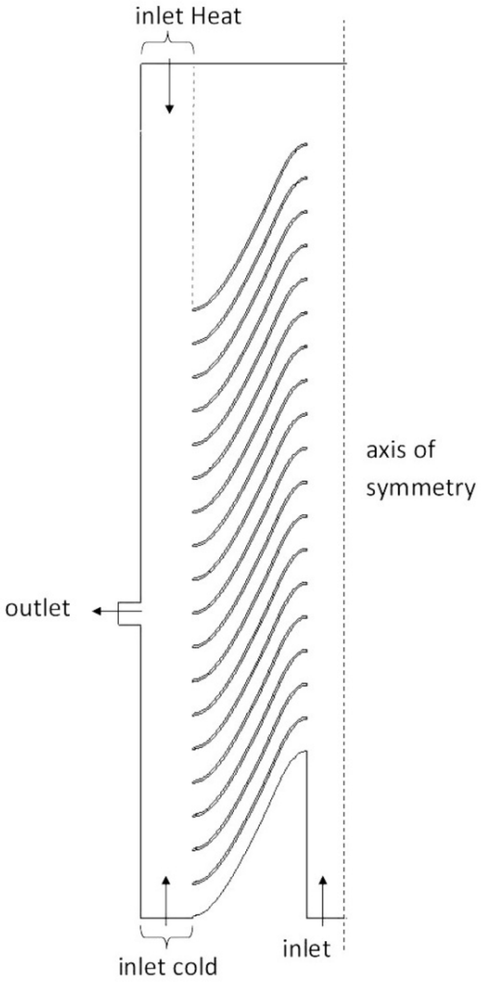

Figure 6.49: Model geometry used for the optimization simulations [76]

The results show the charging temperature influences the optimized geometry of the stratification pipe. Additionally, the optimum shape depends on two main parameters. These two parameters are influenced by geometrical coefficients determining the shape of the inlet stratification pipe. One parameter is defined as maximum height that flow can reach inside of the stratification pipe (H_{max}). The second parameter is the vertical distance of the channel profile (H_p). These two parameters influence the optimized geometry in a combined manner. For example, if the reached height in the stratification pipe is farther from outlet height, higher value of the profile vertical distance results in better stratification. It has been concluded, that inner slope of stratification pipe(a), vertical distance between the channels(c) and charging temperature can influence the flow maximum reached height in stratification pipe (H_{max}). On the other hand, profile vertical distance (H_p) is influenced by geometrical parameters of channel profiles a and b.

6.7 Entrainment Effect Analysis in Different Geometries of Pipe

In order to investigate the effect of the inner slope on the fluid flow through the stratification pipe openings, a special case with the same charging temperature as the storage fluid temperature with the outlet position at the top of the storage has been simulated. Figure 6.50 represents streamlines in charging of this special case and the corresponded boundary conditions.

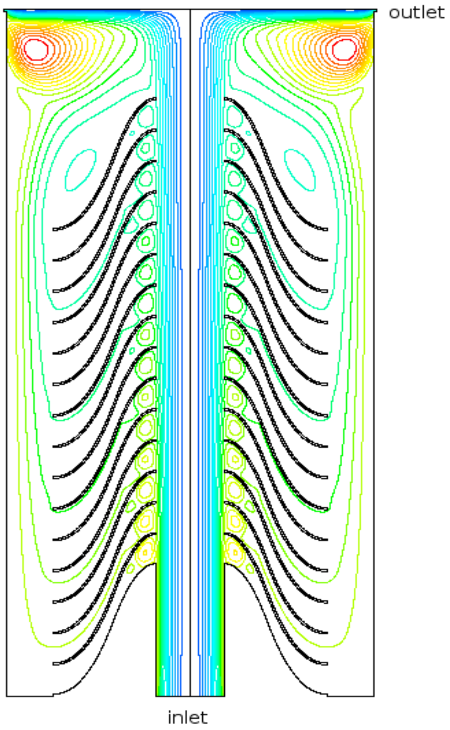

Figure 6.50: Streamlines in charging process of the storage tank with outlet at the top and one main inlet at the bottom for steady state simulation

In this simulation, there is no buoyancy force and the outlet position is at the top of the storage. Therefore, less mass flow rate through the openings is favored.

By means of mass flow rate illustration through the stratification pipe openings, the influence of the inner slope on the fluid flow insertion to the storage has been studied.

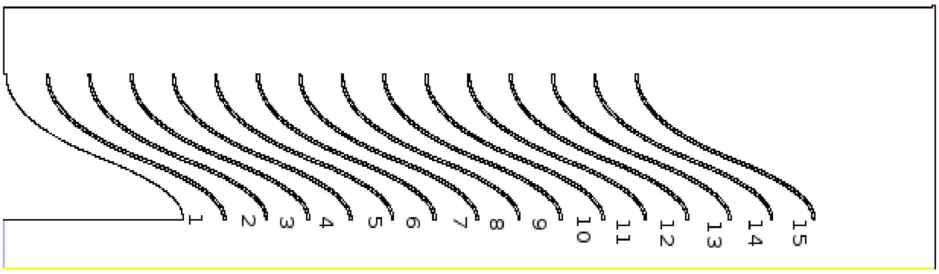

Figure 6.51: Opening number of the inlet stratification pipe

The figures 6.52 and 6.53 demonstrate the mass flow rate through the openings number in simulations with 0.1 kg/s and 0.2 kg/s charging mass flow rate. In both cases, the stratification pipe geometry with zero inner slope shows a higher mass flow rate through the openings with exception of the first opening. Also with lower absolute value of the inner slope, the mass flow rate through the openings shows bigger values in comparison to the geometry with higher absolute value of the inner slope. As in this case study, the same charging temperature as the fluid temperature in the storage tank has been used and the outlet position is at the top of the tank, less mass flow rate through the openings is favored, and for this reason, higher absolute value of inner slope of stratification pipe works as a more optimal design for avoiding the undesirable mass flow rate through the openings. It can be concluded that, by considering of suction effect from storage tank to stratification pipe, higher absolute value of stratification pipe inner slope can avoid the undesirable mass flow rate through channels better than lower absolute values of the inner slope, and therefore, provide better results. The higher absolute values of inner slope still show entrainment effect over the opening channels and for the corresponding application in stratisorp cycle are not the best geometrical choices.

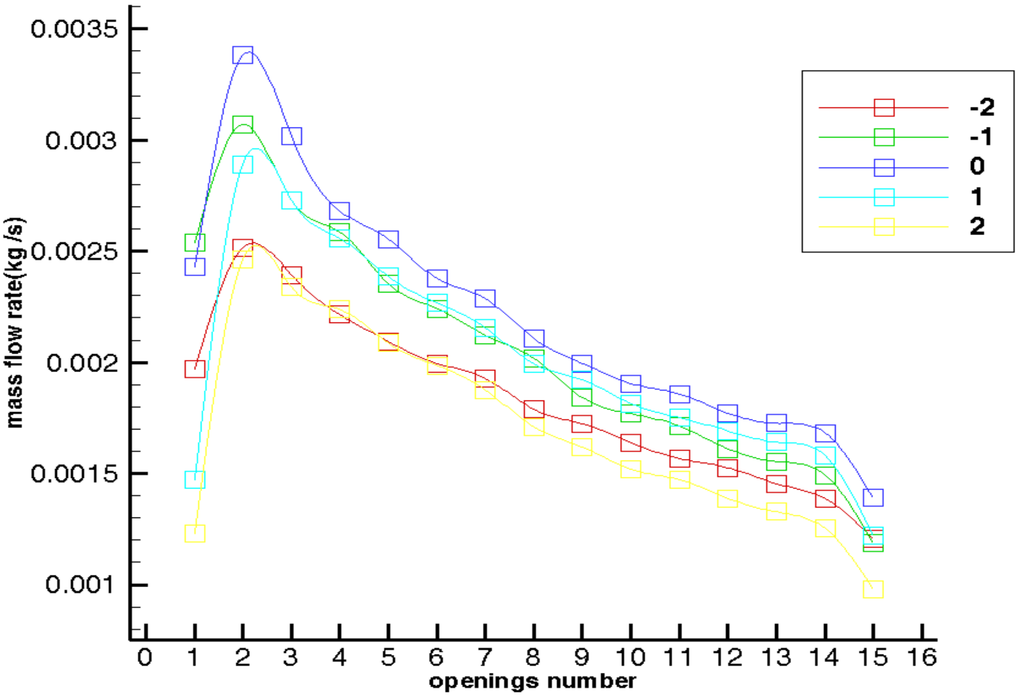

Figure 6.52: Mass flow rate through stratification pipe openings for charging mass flow rate of 0.1 kg/s (steady state simulation)

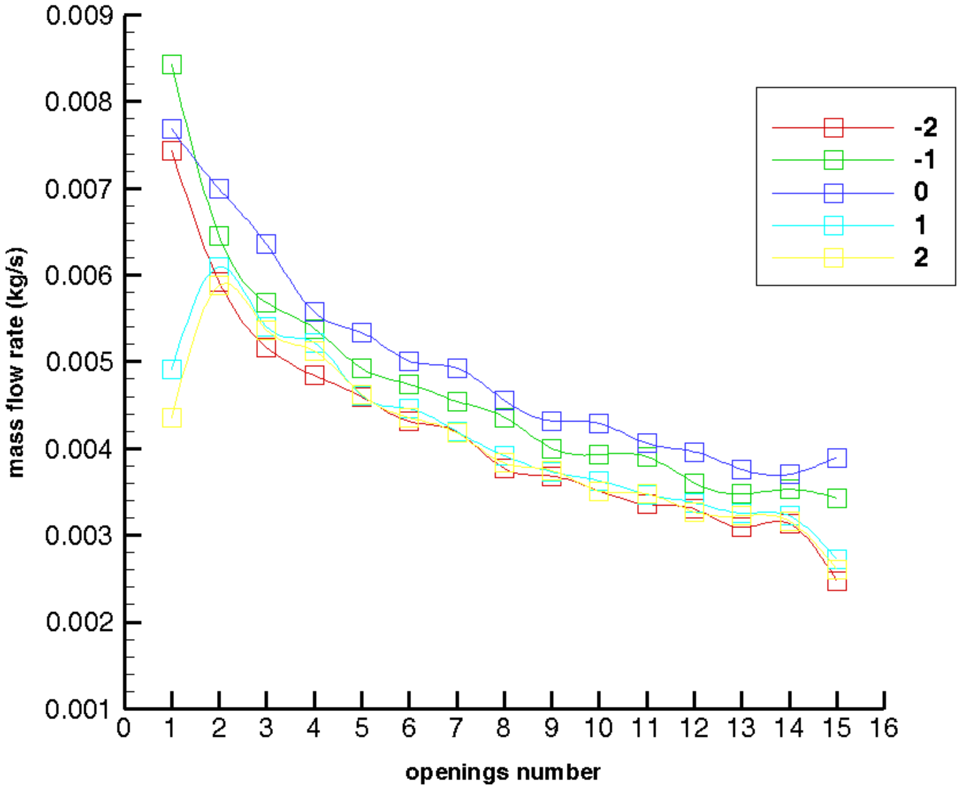

Figure 6.53: Mass flow rate through stratification pipe openings for charging mass flow rate of 0.2 kg/s (steady state simulation)

6.8 Conclusion

An adapted geometry of a marketed stratification pipe has been simulated in order to reduce the mixing mechanism in charging process. The simulation results revealed, that the entrainment effect due to mixing of the storage charging flow and the inflow from the cooler cycle demonstrates a significant mixing mechanism.

The advection and turbulence contribution to the effective thermal conductivity of the fluid flow in charging process of the thermal storage tank with inlet stratification pipe have been investigated by means of numerical simulation. The storage medium used in the simulation is Marlotherm LH, a synthetic thermal oil. The simulation results demonstrate the significance of the turbulence part of effective thermal conductivity in comparison to advection counterpart.

In one part of optimization process the focus was directed to the entrainment effect as a main issue resulting in mixing in the charging process of the storage tank. Water has been used as storage medium in simulations with modified geometry of stratification pipe. The simulation results of the storage tank charging process with modified geometry of stratification pipe show less mass flow rate through the stratification pipe channels for higher absolute values of the inner slope. Therefore, these values can reduce the entrainment effect at the bottom of the storage tank, but still for the corresponding application in stratisorp cycle they are not the best geometrical choices.

In another part of optimization process with focus on stratified tank, it can be concluded, that two main parameters including maximum reaching point of flow in the pipe (H_{max}) and vertical distance of the channel profile (H_p) determine the optimum geometry of the stratification pipe in a combined manner. (H_{max}) is influenced by inner slope of stratification pipe(a), vertical distance between the channels(c), and charging temperature . On the other hand, (H_p) is a function of geometrical parameters of channel profile (a) and (b). According the obtained simulation results from this chapter, the designed stratification pipe has been rejected for further investigation in this application. Instead of that, the charging process of thermal storage tank through ring charging system has been investigated numerically in the following chapter.

7 Numerical Study of the TES Charging Process with Porous Medium CFD Model

7.1 Simulation of Charging Process with Ring Charging Device

7.1.1 Ring Charging System

In this part of the thesis, it has been tried to simulate and study the charging process of a TES model with ring shape charging device. Figure 7.1 represents the idea of TES with ring charging device. According to idea of this charging system, the charging flow will be injected to the tank through different holes located on the perimeter of the charging ring. In the current study, a test example of such a TES with 2 rings, one as a charging port and another as a discharging port have been simulated. The charging ring includes different row of the holes, that are distributed around the ring. These holes are modeled as a continuous line with inlet boundary condition in CFD model. The main aim of the investigation in this part is to inquire the impact of the porous zone on the charging flow in charging process of the TES with ring charging system.

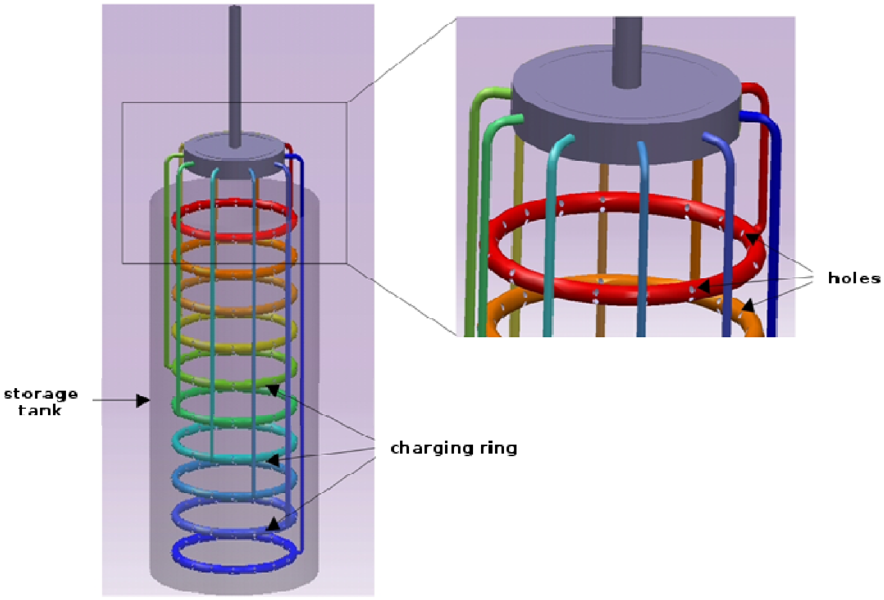

Figure 7.1: Schematic model of storage tank with a ring charging device

7.1.2 Simulation Setup and Boundary Conditions

As it has been mentioned earlier, the charging holes on the charging ring have been modeled by two continuous splines as inlet boundary condition, one in the inner side of the ring and another at the outer side of the ring. The number of cells used for the domain discretization is about 500,000 cells, which include the O-Grid around the ring geometry and H-grid in the farther regions. As these inlets have been modeled in a 2-D axisymmetric domain, they build the strap-shape area around the whole ring in complete fluid domain. Thus, the charging through them can be realized in radial direction. The radial charging through these rings causes less mixing of surrounding fluid due to the inertial impact of charging flow. The outflow boundary condition has been set for the discharging of flow through the upper ring. Adiabatic wall has been considered for thermal condition of wall boundaries. Mass flow boundary condition has been used for the inlet boundaries. Each inlet boundaries from the inner side of the ring and the outer side of the ring has a uniformly distributed velocity that corresponds the 0.1 kg/s mass flow rate. In other words, 0.2 kg/s mass flow rate flows into the domain through two inlet boundaries in the lower ring, and the same mass flow rate flows out of the domain through two outlet boundaries in the upper ring. The flow enters the tank with 20 °C and the storage tank has been initialized with 20 °C at the lower half and 40°C at the upper half. Therefore, no buoyancy forces influence the inflow in the inlet region. Turbulent viscosity ratio in turbulent simulation with realizable $k-\varepsilon$ model shows a ratio about 160, which confirms the calculation with turbulence model. Table 7.1 represents the discretization methods and simulation setup applied for the both simulations.

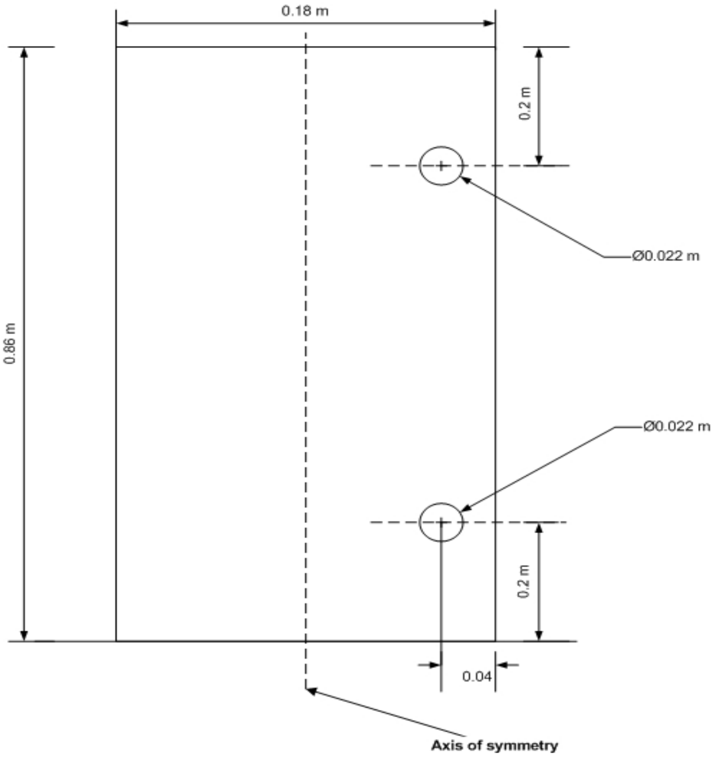

Figure 7.2: Geometrical sketch of the TES model applied for porous media model implementation

Table 7.1: Solution methods for the case setup of the simulation with porous zone

Pressure-Velocity Coupling algorithm	Coupled
Spatial discretization for pressure	Body force weighted
Spatial discretization for momentum	Second order upwind
Spatial discretization for Energy	Second order upwind
Spatial discretization for turbulent kinetic Energy	Second order upwind
Spatial discretization for turbulent Energy dissipation rate	Second order upwind
Transient formulation	Second order implicit
Time step size (s)	0.1
Viscous model	Turbulent
Fluid material	Water

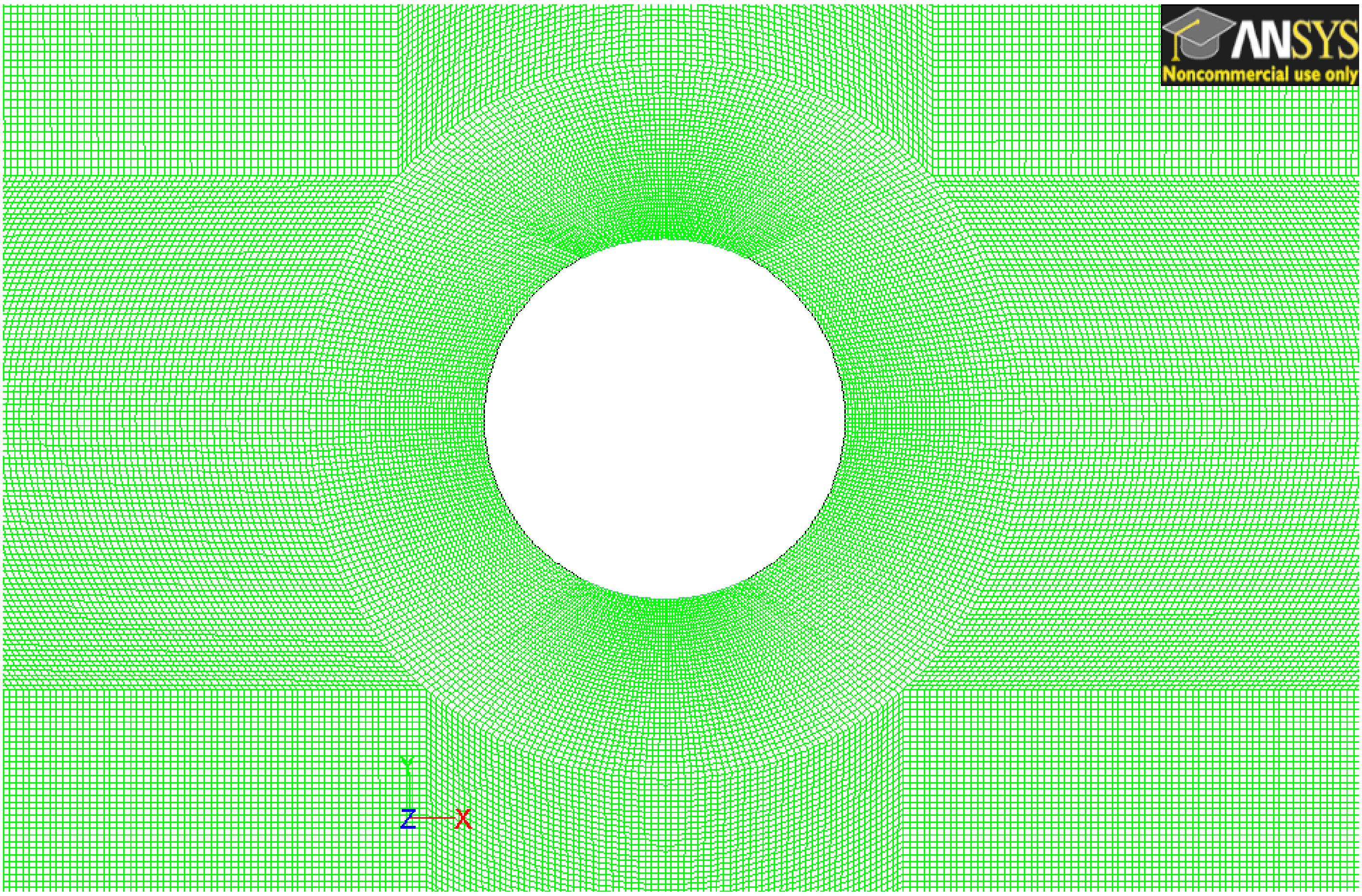

Figure 7.3: O-grid and H-grid around the charging ring of TES model

7.1.3 Porous Media Turbulence Model

The porous material used in engineering application demonstrates a small permeability and high resistance against the fluid flow. For this reason, the laminar flow is the usual regime in many cases. However, high Reynolds number flow through porous media can lead to turbulent flow within the pores [77]. Different researchers have followed a macroscopic approach for low Reynolds number flows in porous media in order to treat turbulence. Almost all of the models derived to simulate turbulence in porous media are based on the clear fluid $k - \varepsilon$ model being modified to consider the effect of the solid matrix [78].

In a research by Nakayama and Kuwahara, the influence of porous medium on the turbulent flow has been considered by a two-equation macroscopic turbulence model which is provided by spatially averaging of the Reynolds-averaged Navier-Stokes equations [79].

They presented a macroscopic turbulence model describing the flow behavior in a porous medium. In a separate study, they tried to compare the macroscopic results from RANS with a large eddy simulation of turbulent flow in porous media [80]. Based on this LES study, they concluded that Ergun equation may describe the drag relationship for the turbulent flow in porous media in a relevant manner. For the current simulation, the Ansys Fluent porous media model with realizable $k - \varepsilon$ model has been used for the calculation. Ansys Fluent modifies the realizable $k - \varepsilon$ model transport equations in order to account for the porous medium impact on the turbulent flow.

7.1.4 Calculation of Inertial and Viscous Resistance Coefficients

As it is described in section 4.3, there are two characteristic parameters for definition of porous media model in CFD solver. For the selected porous medium, the inertial and viscous resistance coefficient can be calculated as follows:

The Appendix C represents a data sheet related to the Polyurethane foam that is applied for the simulation. The required properties for the calculation of inertial and viscous resistance coefficient have been illustrated in table 7.2.

Table 7.2: Density and pores per inch (PPI) of the polyurethane foam

Apparent density $\left[{}^{kg}/_{m^3}\right]$	Pores per unit length $\left[{}^{1}/_{linear\ inch}\right]$
25	20

The number of cylindrical shaped pores per cubic centimeter can be calculated as follows:

$$\xi_c = \left(\frac{20\left[{}^{1}/_{linear\ inch}\right]}{2.54\left[{}^{cm}/_{inch}\right]}\right)^2 \cdot 1\left[\frac{1}{cm}\right] = 62\left[\frac{1}{cm^3}\right] \tag{7.1}$$

The foam material is polyurethane which has a density of 1050 ${}^{kg}/_{m^3}$

Using the material density, the foam porosity can be calculated as follows:

$$\eta = 1 - \frac{\rho_p}{\rho_s} = 1 - \frac{25}{1050} = 0.9762 \tag{7.2}$$

As it has been described in section 4.3, average pore volume and average pore diameter can be obtained as follows:

$$V_c = \frac{\eta}{\xi_c} = \frac{0.9762}{62} = 0.0157\ cm^3 \tag{7.3}$$

$$d_c = \sqrt{\frac{4V_c}{\pi}} = \sqrt{\frac{4 \cdot 0.0157}{\pi}} = 0.141\ cm \tag{7.4}$$

Equivalent particle diameter has been calculated as follows:

$$d_e = 1.5 \cdot \frac{(1-\eta)}{\eta} \cdot d_c = 1.5 \cdot \frac{1-0.9762}{0.9762} \cdot 0.141 = 0.00515\ cm \tag{7.5}$$

So the viscous and inertial resistance coefficients can be calculated with following equations:

$$\alpha = \frac{(d_e)^2}{150} \cdot \frac{\eta^3}{(1-\eta)^2} = \frac{(0.00515 \cdot 10^{-2})^2}{150} \cdot \frac{0.9762^3}{(1-0.9762)^2} = 2.904 \cdot 10^{-8}\ m^2 \tag{7.6}$$

$$C_i = \frac{3.5}{d_e} \cdot \frac{1-\eta}{\eta^3} \frac{3.5}{0{,}00515 \cdot 10^{-2}} \cdot \frac{(1-0.9762)}{0.9762^3} = 1{,}738 \cdot 10^3\ \frac{1}{m} \tag{7.7}$$

The porous zone with correspondent porosity and resistance coefficients has been applied in domain between inlet and outlet ports.

7.2 Simulation with Implemented Porous Media Model

The porous zone model has been applied for the highlighted region in Figure 7.4. This region includes the flow route from inlet to outlet.

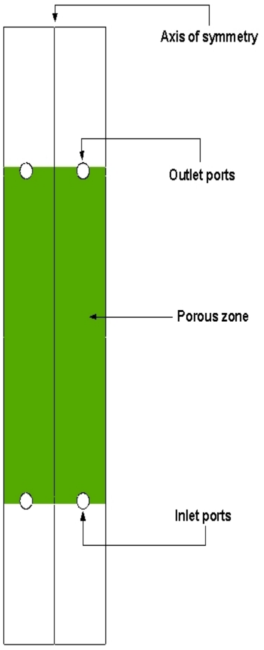

Figure 7.4: Implemented porous zone inside of the test storage tank

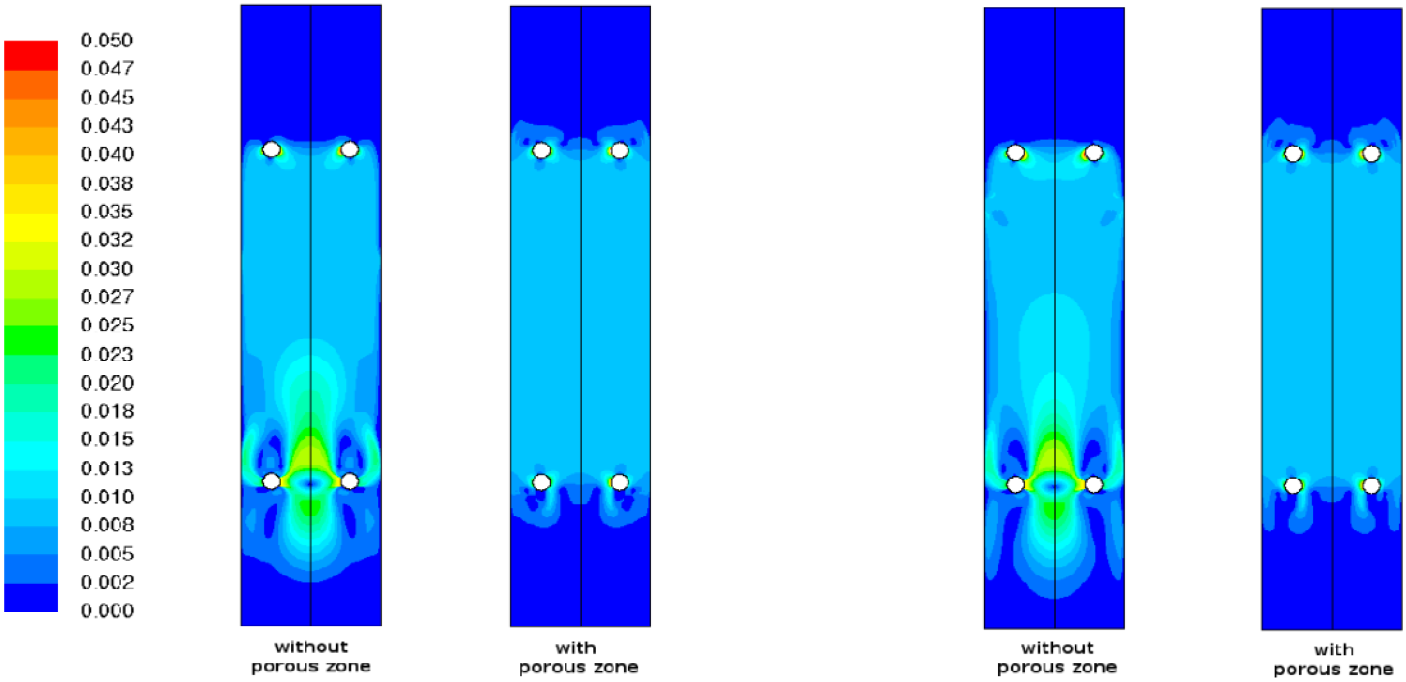

Figure 7.5: Velocity contours (m/s) in charging process of the TES with implemented porous zone and without porous zone after 10 s of charging (left) and after 20 s of charging (right) in simulation with realizable $k - \varepsilon$ model

Two separate simulations have been performed with the same charging volume flow rate, charging temperature, initial condition and boundary condition, but one with implemented porous zone and another without porous zone. With analysis of the velocity field and streamlines in two simulation results, the impact of the porous zone on the charging flow can be investigated. In a transient simulation, the velocity field in the tank after 10 and 20 seconds of charging has been compared. As it can be seen in streamlines of two cases, small recirculation regions are built in the region of inlet port for simulation without porous zone. This region doesn't appear in the simulation with porous zone. Velocity contour after 10 and 20 seconds of charging also shows more uniform velocity distribution in the case with implemented porous zone. The role of the porous zone in pressure drop of the charging flow causes a reduction of inertial forces in the near of inlet region.

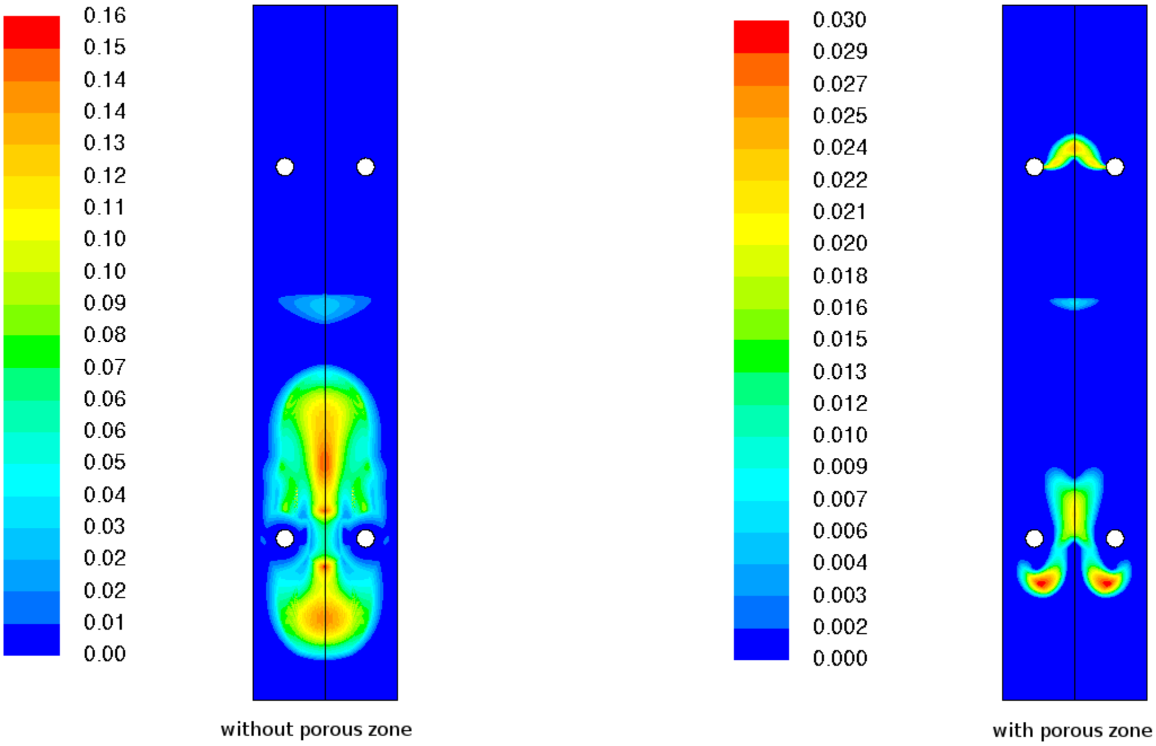

Figure 7.6: Turbulent viscosity (kg/(m.s)) comparison between TES with implemented porous zone and without porous zone after 10 s of charging (simulation with realizable $k-\varepsilon$ model)

7.3 Porous Media Influence on the Charging Process

From the computed velocity contour in both cases can be investigated that porous zone influences the inflow to the tank with providing more uniformly distributed flow over the tank radial cross section. Uniform velocity distribution in radial direction decreases the possibility of building a recirculation region through a velocity gradient in radial direction. The Reynolds number at the inlet port based on the perimeter of the inlet port is about 7935 and the maximum Reynolds number over the storage tank cross section based on the tank diameter shows a value of 1563. With assumption of plug flow charging model, the Reynolds number over the cross section based on the tank diameter is about 1462. Therefore, the influence of the porous zone on the stratification shows its significance in the inlet port region and the implementation of the porous zone can be restricted to the inlet region, which reduces the expense of porous zone implementation in practice. This influence can be concluded as damping effect of the porous zone on the turbulent diffusion in the inlet region. On the other hand, while the mean velocity gradient in turbulent flow works as a turbulent kinetic energy production parameter, the low velocity gradient in the porous zone reduces the mixing due to the turbulent diffusion. The turbulent eddy viscosity computed by realizable $k - \varepsilon$ model also predicts about five times smaller value in the case of simulation with porous zone.

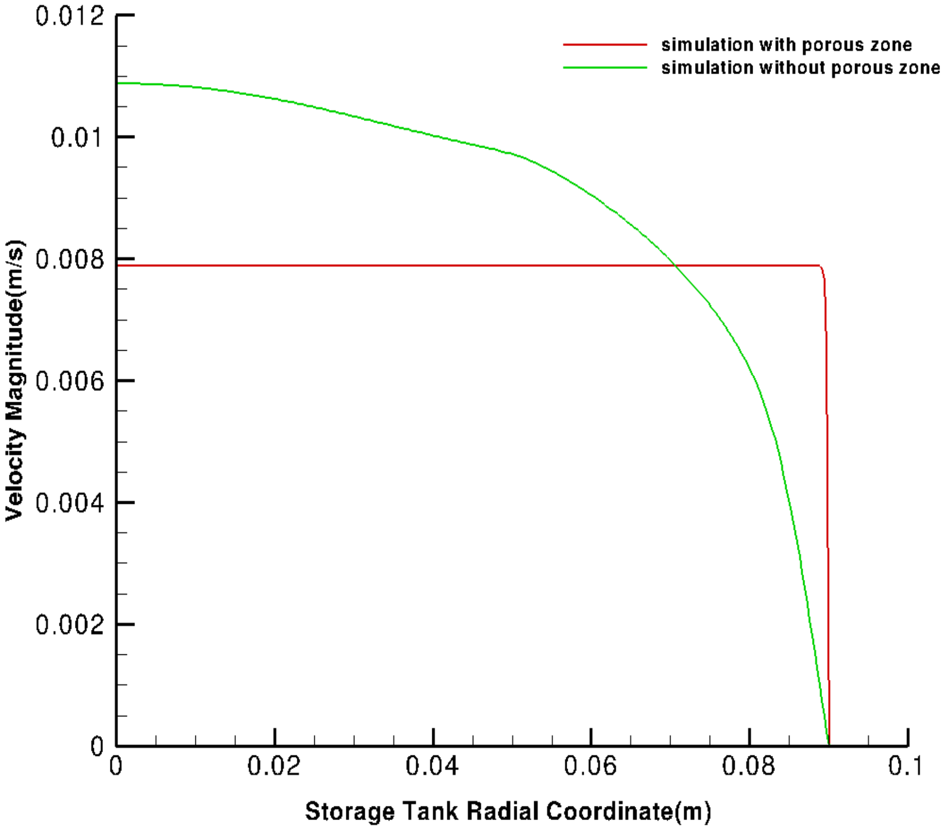

Figure 7.7: Velocity distribution over the radial direction at the center of the storage tank after 20 s of charging

7.4 Simulation with Free Jet Charging through the Inlet Pipe

7.4.1 Geometry and Simulation Setup

Free jet problem is one of the most studied engineering problems. In this part of the thesis, free jet charging flow through a thermal storage tank has been investigated. The pipe installed at the bottom of the tank is used as a tool to charge the storage tank with free jet. The charging flow temperature is higher than the fluid temperature in the tank, which allows for a buoyancy forces towards the top. Intensified molecular thermal diffusivity due to turbulence in the inlet region of the tank magnifies the mixing procedure in this region leading to destratification in TES. This mixing parameter plays more important role in the TES with direct charging system. In order to avoid the turbulence generated from the mixing procedure of the hot and cold water in direct charging system, different tools can be installed in the inlet region. Two of them including baffle plate and porous structure have been presented by Han et al. [2]. These two systems have been shown in figure 7.8. in this section, the free jet charging without any turbulence damping obstacle in the inlet region is numerically simulated, and relevant flow variables has been studied. In the following section of this chapter, a porous medium foam has been simulated in the fluid domain. The effect of the porous zone as a reducer of turbulence mixing in the inlet region has been investigated through post processing of calculated turbulence variables.

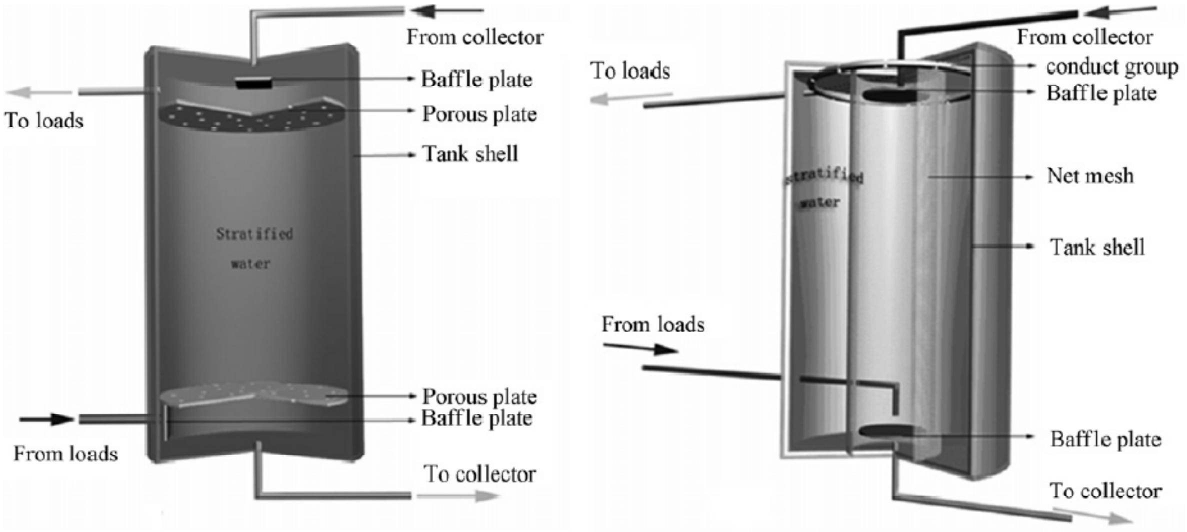

Figure 7.8: Baffle plate and porous structure set to the inlet region in solar TES system [2]

In the current section of thesis, the direct charging of the storage tank through a charging pipe has been numerically studied. Since the turbulent mixing in the inlet region for the direct charging to the storage tank is an influential parameter of destratification, the main focus of the simulation is on the investigation of turbulent variables like turbulent kinetic energy and turbulent eddy viscosity in the direct charging of the storage tank without any obstacle in front of the charging pipe. The inlet flow has higher temperature than the fluid in the tank, so the buoyancy forces support the inertial forces of fluid flow and intensify the turbulent fluctuations.

The CFD simulation of the free jet charging of the storage tank has been performed according to an available experimental setup of the storage tank with the installed inlet pipe.

Cylindrical tank with installed pipe has been simulated in a 2-D axisymmetric CFD model. Fluid domain has been discretized with about 725000 quadrilateral cells in a block structured grid. The fluid domain of the CFD model extends to 1.46 m as height and 0.35m as radius of the tank. The inlet pipe with 415mm length and 23mm inner diameter has been positioned at the center of the tank. The inlet of the pipe has been simulated as mass flow rate boundary condition with 0.055 kg/s (about 3.36 lpm volume flow rate) and 40 °C charging temperature. The storage tank has been initialized with uniform temperature of 20 °C. The upper edge of the domain boundary has been used for the domain outlet as outflow boundary condition. Reynolds number analysis in the tank confirms a turbulent flow regime inside of the pipe and the inlet region from pipe to the storage tank. For this reason, turbulent simulation has been performed for the current section.

Figure 7.9: Picture of the tank with inlet pipe

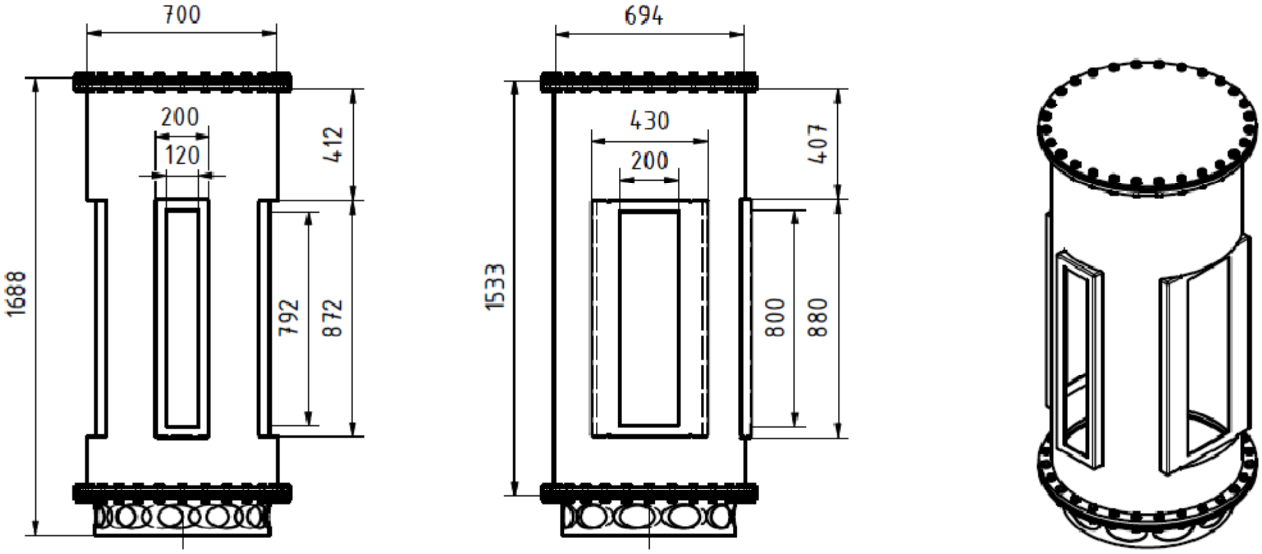

Figure 7.10: Geometrical dimension of the storage tank applied in simulation

Table 7.3: Solution methods for the simulation of free jet charging trough inlet pipe

Pressure-Velocity Coupling algorithm	Coupled
Spatial discretization for pressure	Body force weighted
Spatial discretization for momentum	Second order upwind
Spatial discretization for energy	Second order upwind
Spatial discretization for turbulent kinetic Energy	Second order upwind
Spatial discretization for turbulent energy dissipation rate	Second order upwind
Transient formulation	Second order implicit
Time step size (s)	0.5
Viscous model	Turbulent
Fluid material	Water

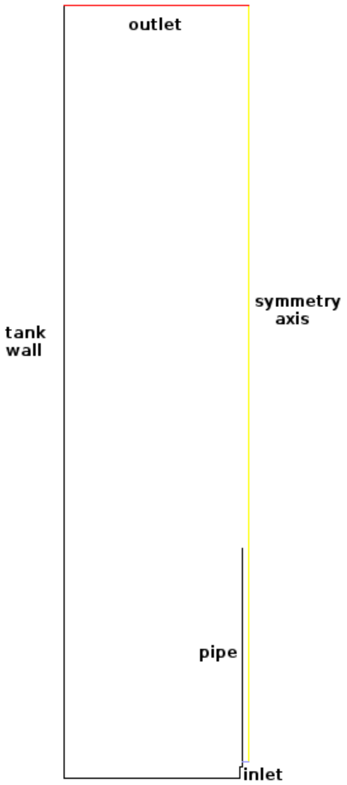

Figure 7.11: Tank and inlet pipe sketch with boundary conditions for CFD simulation

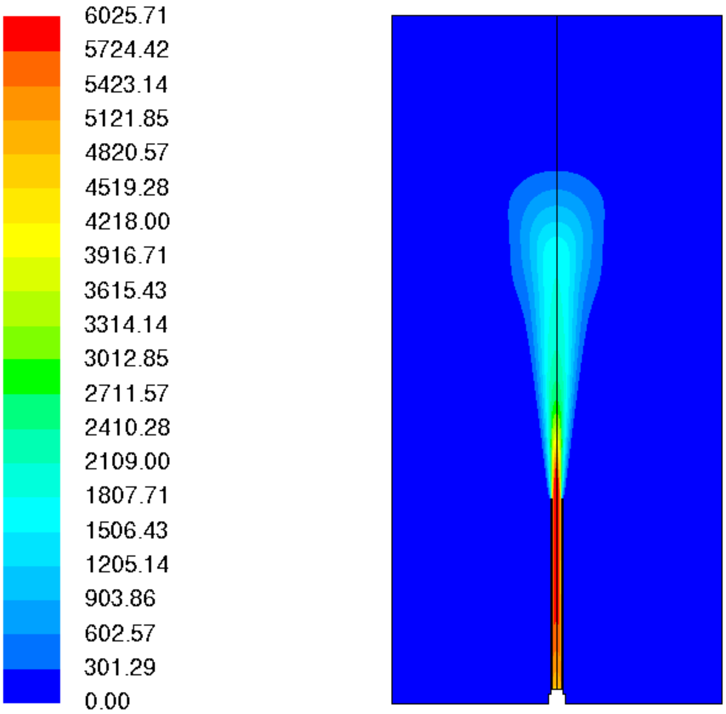

Figure 7.12: Reynolds number field based on the pipe diameter as characteristic length after 20 s of charging in simulation with realizable $k - \varepsilon$ model

7.4.2 Mesh Independency Study

Mesh independency study has been performed by means of two different cases with coarser and finer mesh. The coarser mesh includes about 725000 cells and finer mesh about 1 million cells, which has been created in a block-structured manner. After calculation with two cases with the similar simulation parameters, the results for temperature distribution along the central axis have been compared after 20 seconds and 60 seconds of charging time. It can be concluded, that no considerable deviation is observed between these two cases. Thus, the coarser mesh with about 725000 cells has been used for the further calculation.

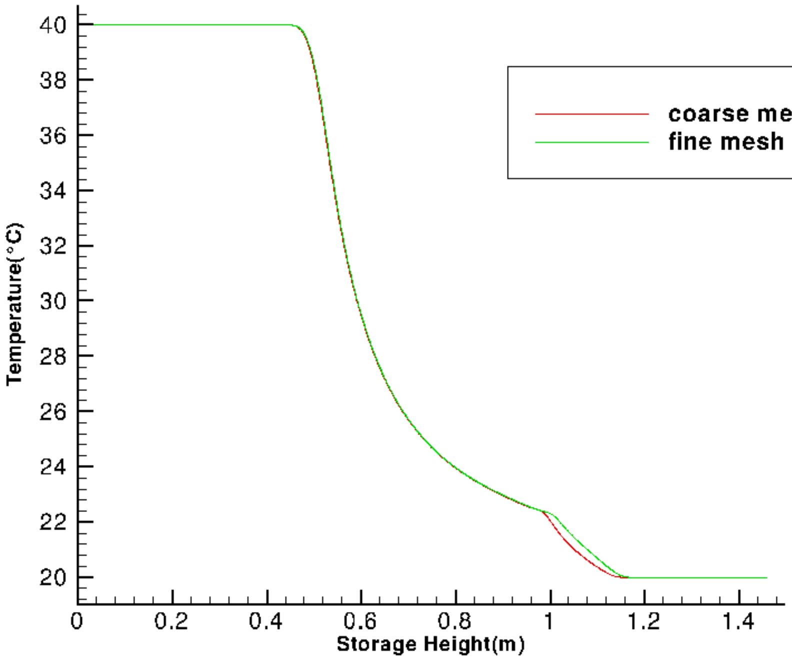

Figure 7.13: Temperature distribution along the central axis of the tank in simulation with realizable $k - \varepsilon$ for coarse mesh (about 725000 cells) and fine mesh (about 1 million cells) after 20 s of charging with 40 °C (storage tank initial temperature: 20 °C)

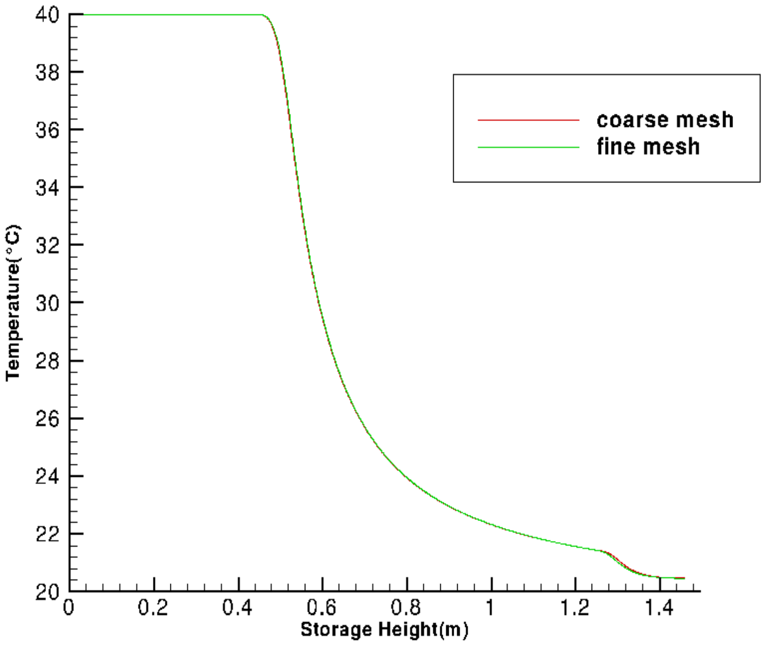

Figure 7.14: Temperature distribution along the central axis of the tank in simulation with realizable $k - \varepsilon$ model for coarse mesh (about 725000 cells) and fine mesh (about 1 million cells) after 60 s of charging with 40 °C (storage tank initial temperature:20 °C)

7.4.3 Simulation Results

High velocity gradient and shear rate in the pipe outlet to the storage increase the turbulence production, which contributes to higher thermal diffusion. In addition, advection heat transfer significantly increases with high velocity magnitude at the pipe outlet. Temperature contours in different charging time clearly reveal the high degree of mixing in the pipe inlet region along the central axis.

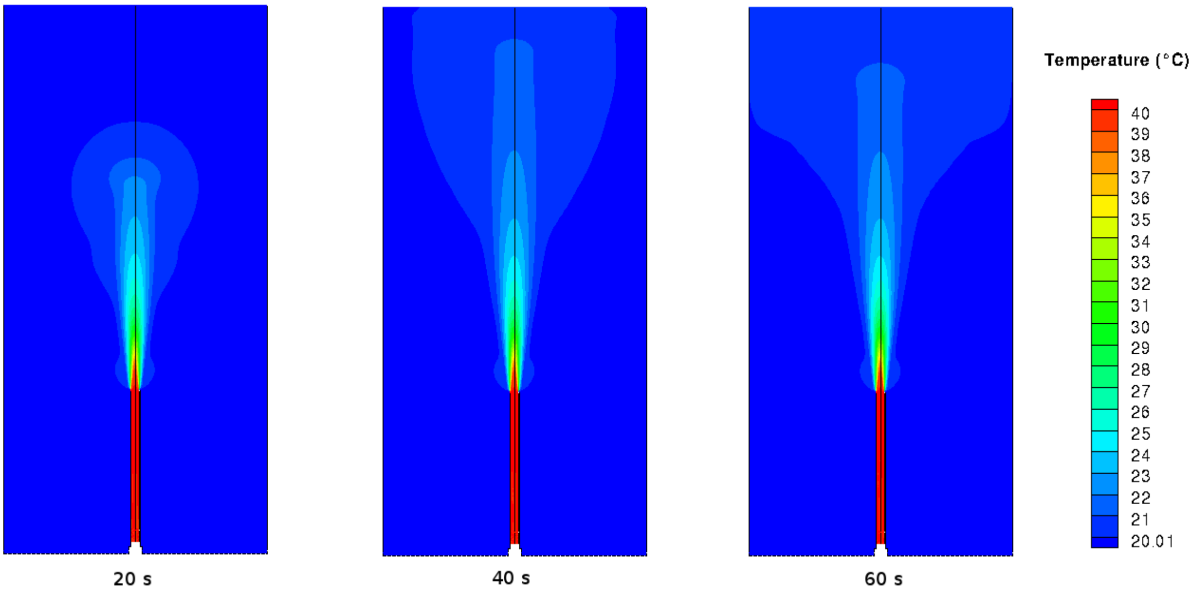

Figure 7.15: Temperature contours at different charging times in calculation with realizable $k - \varepsilon$ model

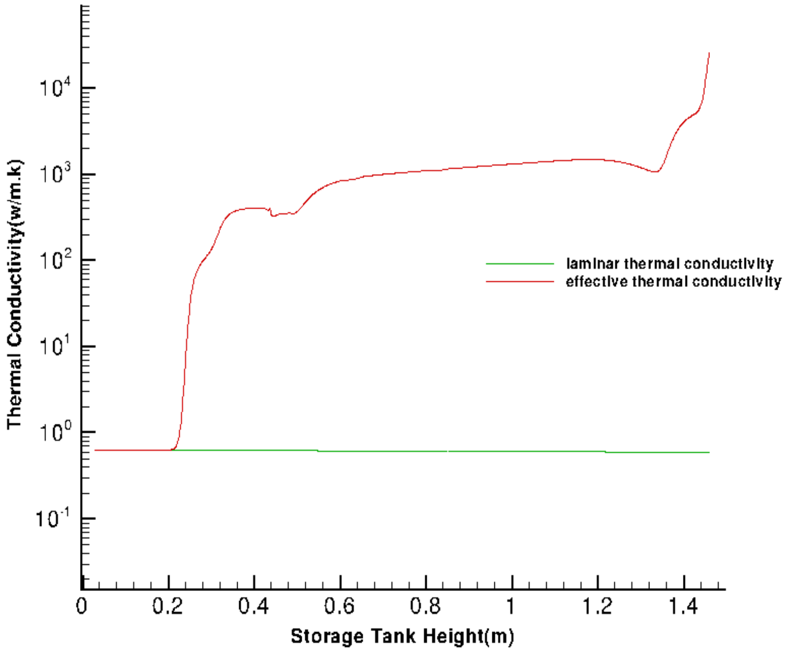

Figure 7.16: Effective thermal conductivity due to turbulent diffusion and laminar conductivity over the central axis of the storage tank in logarithmic scale after 40 s of charging in simulation with realizable $k - \varepsilon$ model

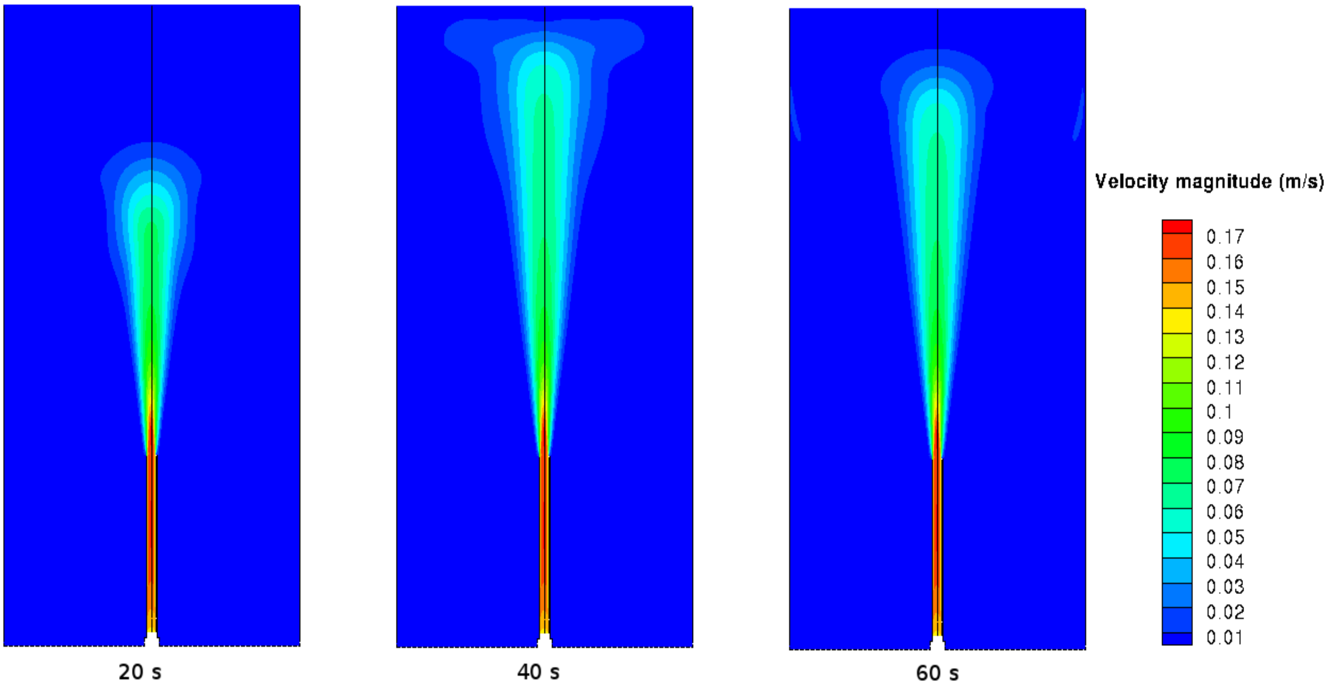

Figure 7.17: Velocity contours at different charging times in calculation with realizable $\boldsymbol{k-\varepsilon}$ model for free jet charging

7.5 Simulation of Free Jet Charging by Implementation of Foam

7.5.1 Simulation Setup

The discussion in this section will focus on the description of the foam influence on the charging flow. The foam disc with 50 mm height and 190 mm diameter has been modeled in the fluid domain as a porous zone. The foam disc center is located on the central axis of the tank at 625 mm above the bottom of the tank. Figure 7.18 displays the foam location inside of the tank. The calculated parameters for resistance coefficients and the porosity in section 7.1.4 are used for the foam porous zone in CFD model.

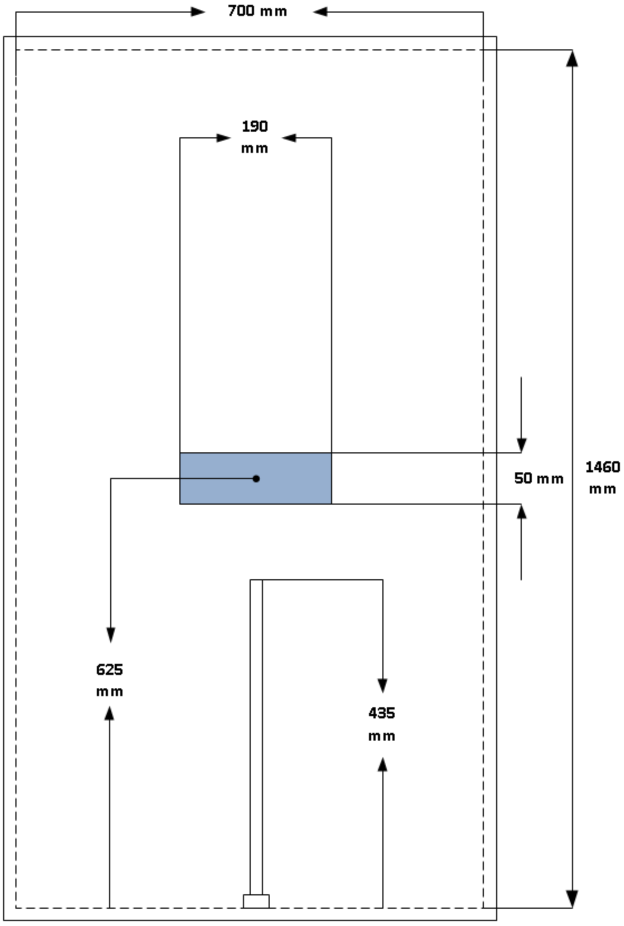

Figure 7.18: Geometry of the storage tank with the foam disc

The same solution methods and simulation parameters as the case of free jet direct charging have been used for the current simulation. Ansys Fluent treats the effect of the porous zone on the fluid flow through consideration of porosity in all scalar transport equations and the continuity equation for the transient porous media calculation. According to this treatment, the time-derivative term in transport equation of a scalar quantity like ϕ becomes $\frac{\partial}{\partial t}(\eta\rho\phi)$, where η is the porosity [27].
The influence of the porous zone as a solid medium on the thermal conductivity of the fluid is modeled by definition of an effective thermal conductivity as follows [27]:

$$k_{eff-p} = \eta k_f + (1-\eta)k_s \tag{7.8}$$

Where k_f is the fluid phase thermal conductivity, which includes the turbulent part of the thermal conductivity, and k_s is the solid medium conductivity of porous medium skeleton.

7.5.2 Simulation Results for Calculation with Realizable $k-\varepsilon$ Model

The impact of the disc foam on the turbulent motion can be interpreted as its viscous and inertial resistance against the flow momentum. The decline of the turbulent kinetic energy through the foam causes a gradual reduction of turbulent eddy viscosity, and thereby, reduction of the turbulent heat fluxes. Temperature field after different charging time demonstrates the reduction of thermal diffusion and mixing in flow stream-wise direction. Analysis of effective thermal conductivity due to turbulence over the central axis of the storage tank reveals the value decrement of until three orders of magnitude between the foam outlet and top of the storage tank. The value of effective thermal conductivity due to

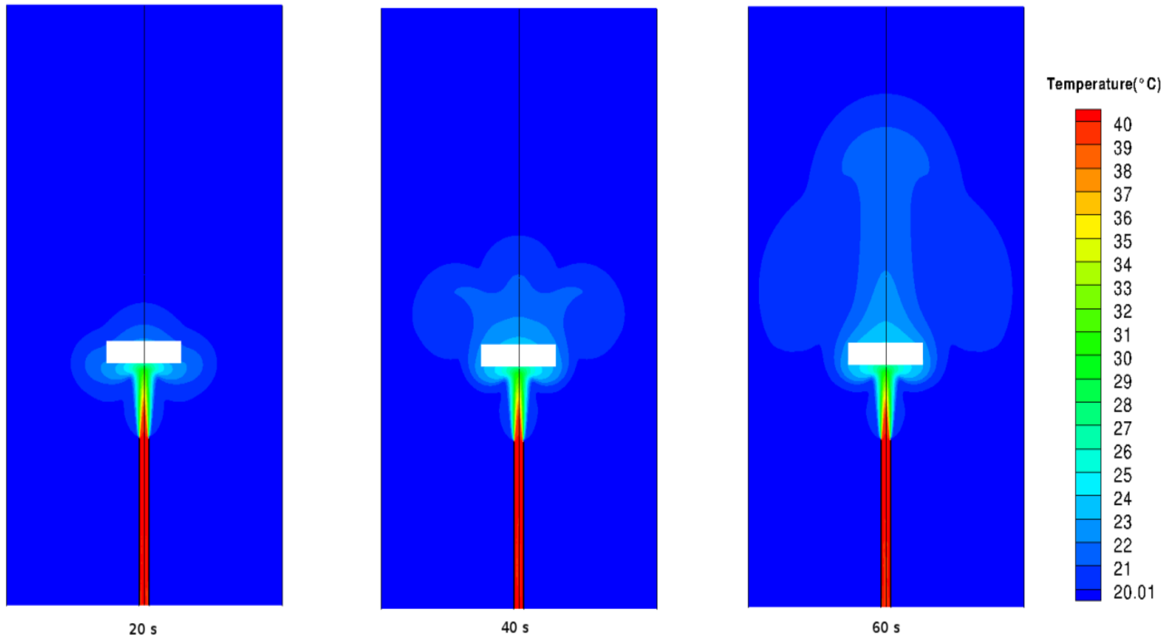

Figure 7.19: Temperature contours at different charging times in simulation with realizable $k-\varepsilon$ model

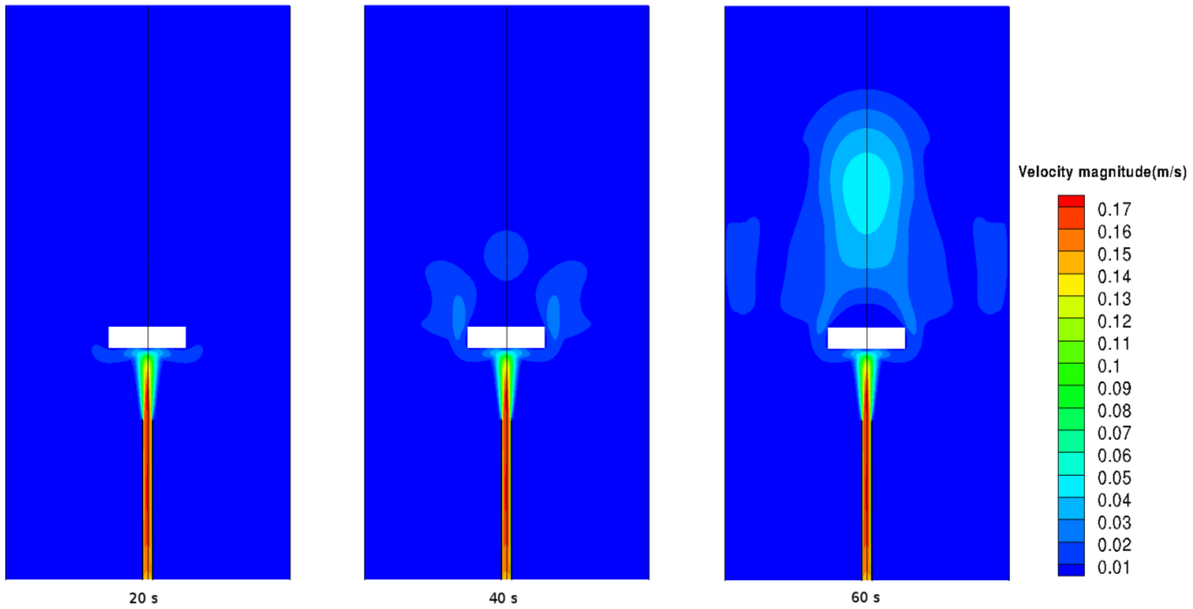

Figure 7.20: Velocity contours at different charging times in simulation with realizable $k-\varepsilon$ model

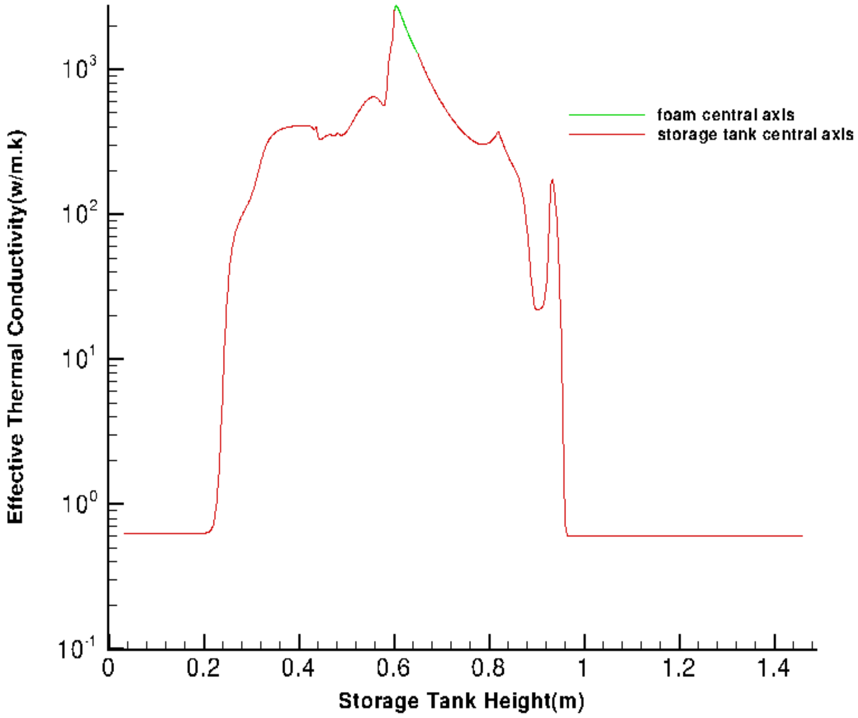

Figure 7.21: Effective thermal conductivity due to turbulent diffusion over the central axis of the storage tank in logarithmic scale after 40 s of charging time in simulation with realizable $k - \varepsilon$ model

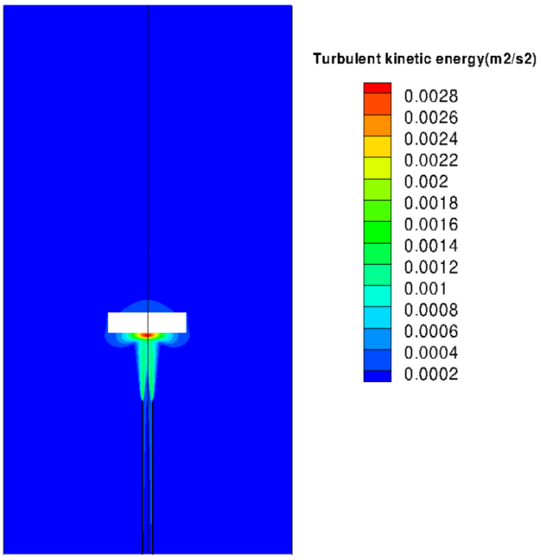

Figure 7.22: Turbulent kinetic energy contour after 60 s of charging in simulation with realizable $k - \varepsilon$ model

Turbulence through foam axis experiences a relatively high gradient. The Simulation results are provided for the porosity value of 0.97, which is a relatively high value. In the case of lower values for porosity in simulation, it is expected, that effective thermal conductivity through the foam axis experiences a steeper decrement.

7.6 Comparison of Numerical Results with Experimental Results

As discussed in section 5.6.2, temperature gradient field from numerical simulation and pixel shift field from BOS experiments [67] can provide a qualitative comparison of two methods.

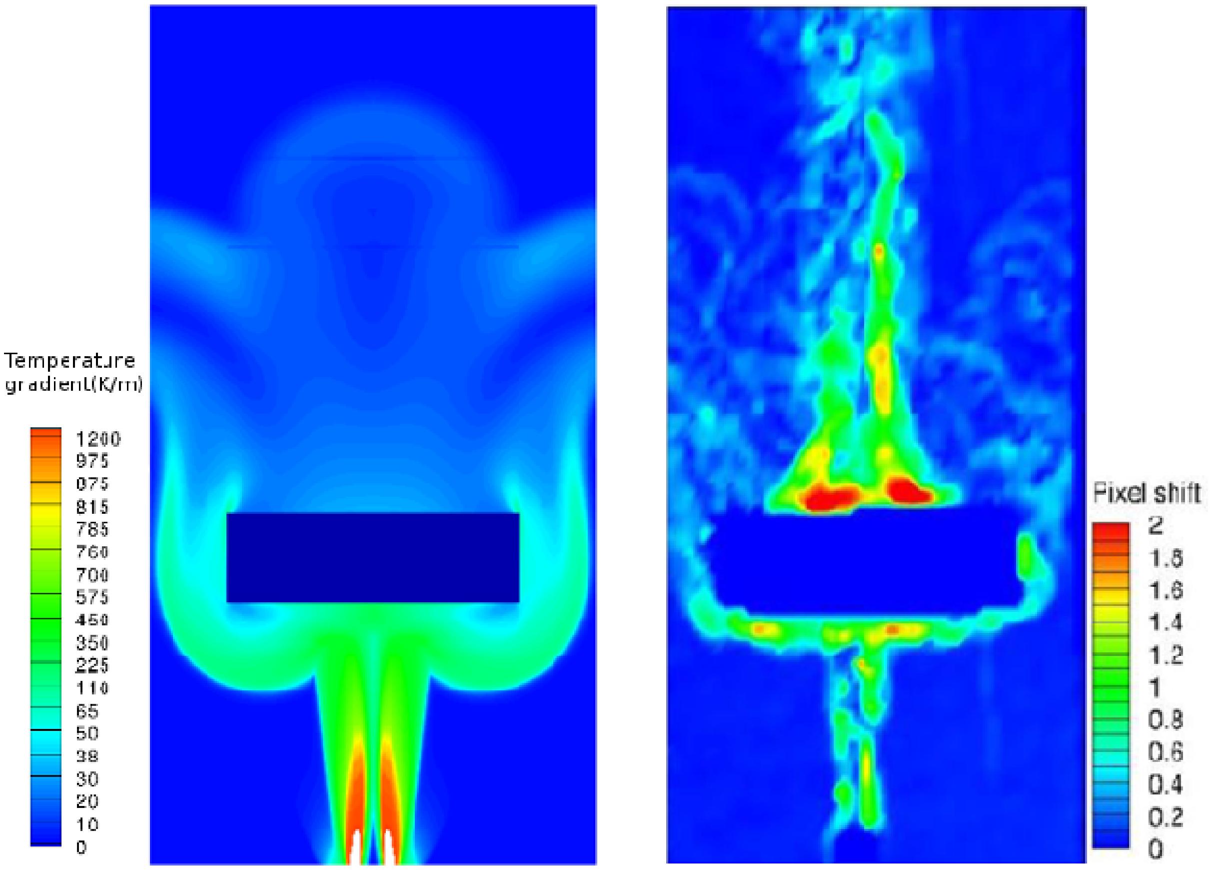

Figure 7.23: Qualitative comparison of temperature gradient from numerical simulation with realizable $k-\varepsilon$ model and pixel shift from BOS experimental results [67] after 40 s of charging time

The highest gradient occurs close to the foam region in the current simulation. For this reason, the temperature gradient contour in this region is compared with pixel shift contour. It should be mentioned that the numerical simulation predicts a thicker temperature gradient region around the foam. In addition, the region after the foam shows higher difference in gradient for the BOS experiment in comparison to numerical simulation.

7.7 Conclusion

The impact of the porous medium on the charging flow in TES has been investigated in detail in the current chapter. It is important to clarify the influence of the porous medium from two different points of view. In the first part of the chapter, which corresponds to the simulation with ring charging system, the porous medium influences the charging flow in the reduction of velocity gradient and therewith less recirculation region and less mixing of the fluid layers. Smaller velocity gradient, on the other hand, reduces the turbulent kinetic energy production.

Less turbulent kinetic energy production decreases the mixing due to the additional momentum and thermal diffusion induced by turbulence.

The other point of view deals with the effect of porous medium resistance on the charging flow momentum. Simulation results demonstrate a considerable reduction of fluctuation part of the charging velocity through porous zone.

The suppression effect of the porous zone on turbulent kinetic energy decreases the effective thermal conductivity due to turbulence.

8 Concluding Remarks and Outlook

The current thesis mainly investigates the flow structures in charging process of a thermal storage tank applied in adsorption heat pump cycle. The cycle includes the adsorption and desorption half cycles. The released heat during the adsorption half cycle can be stored in thermal storage tank and is utilized as the required heat during the desorption half cycle.
The potential of heat recovery between two half cycles highlights the significance of the efficient charging and discharging processes in a thermal storage tank.
The investigation deals with thermal storage tank charging and discharging processes with certain mass flow rate and different temperatures. Additionally, one heater cycle and one cooler cycle are integrated in the thermal storage tank charging process.
A model storage tank with one inlet and outlet has been constructed in order to compare the obtained numerical results with available experimental results from a parallel investigation. For this investigation, the charging process of a thermal energy storage with radial charging flow for different temperature difference between the charging flow and fluid in the storage tank and different charging mass flow rates has been simulated. The charging process has been performed through an inlet at the bottom of the storage tank, and an outlet at the top. Simulation results have shown a wide range of Reynolds numbers in the charging process and both laminar and turbulent simulations have been performed to investigate the flow variables in the storage tank. Among the RANS turbulence models, realizable $k-\varepsilon$, RNG $k-\varepsilon$ and SST $k-\omega$ models have been applied for this investigation. Simulations with $k-\varepsilon$ models predict a thinner thermocline in comparison to SST $k-\omega$ model. The simulation results of a charging process with higher charging flow rate predict a thicker thermocline, and therefore more mixing due to the higher inertial forces.
The comparison of numerically obtained results with available experimental results show a relative good agreement. It should be mentioned, that the numerical simulation predicts a relative faster mixing process than the experimental investigation. The same numerical schemes and turbulence model have been applied for further simulations of thermal storage tank with inlet stratification pipe.
The numerical investigation of thermal energy storage with inlet stratification pipe has been performed for a selected case of the storage tank charging process. This case represents the storage tank initially stratified with a linear temperature distribution between maximum and minimum value of the temperature over the whole cycle. The charging process has been simulated with an average temperature over the whole cycle. The main mixing mechanisms in the charging process have been investigated thoroughly. These main mixing processes include primarily the turbulent diffusion at the inlet region because of high momentum of the inlet flow and secondly the entrainment effect of the fluid from storage tank into stratification pipe. The influence of the entrainment on the stratification is intensified through the inlet of the cooler cycle at the bottom of the storage tank.
The effective thermal conductivity during the charging process as an important parameter in the system simulation has been calculated with regard to two points of view, including convection and turbulent diffusion. Simulation results illustrate the more considerable contribution of turbulent diffusion to the effective thermal conductivity. Simulation results for the selected configuration with stratification pipe reveal the high value of effective thermal conductivity due to turbulence and advection in storage tank. Therefore it is inappropriate for the application in stratisorp cycle.
The further simulation results of the storage tank charging process with modified geometry of stratification pipe exhibit, that higher absolute values for the inner slope of the stratification pipe permit lower undesirable mass flow through the stratification pipe channels, and

therewith, it causes a better stratification behavior during the charging process of thermal energy storage. However, these values still show entrainment effect, and for the corresponding application in stratisorp cycle, they are not the best geometrical choices.

In the simulation of the storage tank with ring charging system, no stratification device has been applied, and the charging flow has been injected at different vertical positions.

For a simple CFD model of TES with two rings for charging and discharging, the porous media CFD model has been applied for the flow simulation between inlet and outlet ports. The porous media model results in more uniform velocity distribution over the cross section of the storage tank. The contribution of porous zone in mixing reduction is described by more uniform velocity distribution, which means smaller velocity gradient and shear stresses.

On the other hand, a smaller velocity gradient reduces the turbulent kinetic energy production between charging and discharging regions.

The effect of the porous medium on the turbulent kinetic energy has been investigated in direct charging flow simulation. Simulation results demonstrate a strong turbulence damping effect through and after the porous zone. As a result, the effective thermal conductivity due to turbulence decreases, and mixing procedure because of turbulent diffusion at the inlet region is considerably restricted.

From the whole system point of view, adsorption heat pump cycle is a cyclic steady state process, and the flow in storage tank within a cycle cannot be represented by a stationary flow situation. During the complete cycle, the storage tank has been charged in an unsteady process, but the storage tank status is the same at the beginning and end of the cycle, and the process as a whole is steady state. The thermal storage tank is charged and discharged with different temperatures during the whole adsorption cycle.

From CFD side, the model boundary conditions are changed during a transient simulation. In the current study, the selected case of the whole cycle has been simulated in transient simulation.

For the purpose of a detailed investigation of transient process in the storage tank during the whole cycle, it is advantageous to simulate the coupled system. The CFD model with ring charging system is beneficial for this purpose. This aim has been pursued by supervision of a master thesis, which results to a successful coupling of system and CFD model in a model storage tank with ring charging system. In the coupled system, the boundary conditions in CFD model are determined from the system simulation in each time step. On the other hand, the CFD results in each time step are used as input in system model simulation.

References

1. Dickinson, R.M., C.A. Cruickshank, and S.J. Harrison, *Charge and discharge strategies for a multi-tank thermal energy storage.* Applied Energy, 2013. **109**(0): p. 366-373.
2. Han, Y.M., R.Z. Wang, and Y.J. Dai, *Thermal stratification within the water tank.* Renewable and Sustainable Energy Reviews, 2009. **13**(5): p. 1014-1026.
3. Nizami, D.J., et al., *Negative buoyant plume model for solar domestic hot water tank systems incorporating a vertical inlet.* Solar Energy, 2013. **87**(0): p. 53-63.
4. Joshi, C., Taheri, H., Schwamberger, V., Füldner, G., Schmidt, F.P. , *Performance enhancement of adsorption heat pump using stratified thermal storage: Simulation results*. 2010: 1st International Conference on Materials for Energy (EnMat2010), Karlsruhe, Germany.
5. Hampel, M., *Rechnerunterstützte Entwicklung von Warmwasser-Wärmespeichern für Solaranlagen*. Dissertation, 2008: Institut für Thermodynamik und Wärmetechnik (ITW), Fakultät Maschinenbau der Universität Stuttgart (http://elib.uni-stuttgart.de/opus/volltexte/2008/3569).
6. Henninger, S.K., et al., *Novel Sorption Materials for Solar Heating and Cooling.* Energy Procedia, 2012. **30**(0): p. 279-288.
7. Munz, G., Schmidt, F., Nunez, T., Schnabel, L., *Adsorptionswärmepumpe mit Wärmespeicher, Europ. Pat. WO/2008/034561*. 2008, Fraunhofer-Gesellschaft zur Förderung der angewandten Forschung e. V. 2007.
8. Schwamberger V. ; Joshi C. ; Taheri H. ; Schmidt, F.P., *Thermodynamische und numerische Untersuchung eines neuartigen Sorptionszyklus zur Anwendung in Adsorptionswärmepumpen und kältemaschinen*. 2013, Karlsruher Institut für Technologie (KIT): KIT Scientific Reports 7640,"Chancen der Energiewende".
9. Joshi, C., Schwamberger, V., Taheri, H., Schmidt, F., *Neuartiges Schichtspeichersystem zur Effizienzsteigerung von Adsorptionswärmepumpen und kältemaschinen*. 2010, Karlsruher Institut für Technologie (KIT), Fachgebiet Strömungsmaschinen, SRG Energie- und Gebäudetechnologie (http://www.fachdokumente.lubw.baden-wuerttemberg.de/servlet/is/101574/BWE27005_Forschungsberichtsblatt.pdf?command=downloadContent&filename=BWE27005_Forschungsberichtsblatt.pdf&FIS=203).
10. Zurigat, Y.H., P.R. Liche, and A.J. Ghajar, *Influence of inlet geometry on mixing in thermocline thermal energy storage.* International Journal of Heat and Mass Transfer, 1991. **34**(1): p. 115-125.
11. Abu-Hamdan, M.G., Y.H. Zurigat, and A.J. Ghajar, *An experimental study of a stratified thermal storage under variable inlet temperature for different inlet designs.* International Journal of Heat and Mass Transfer, 1992. **35**(8): p. 1927-1934.
12. Cai, L., W.E. Stewart Jr, and C.W. Sohn, *Turbulent buoyant flows into a two dimensional storage tank.* International Journal of Heat and Mass Transfer, 1993. **36**(17): p. 4247-4256.
13. Davidson, J.H., D.A. Adams, and J.A. Miller, *A Coefficient to Characterize Mixing in Solar Water Storage Tanks.* Journal of Solar Energy Engineering, 1994. **116**(2): p. 94-99.
14. Eames, P.C. and B. Norton, *The effect of tank geometry on thermally stratified sensible heat storage subject to low Reynolds number flows.* International Journal of Heat and Mass Transfer, 1998. **41**(14): p. 2131-2142.

15. Alizadeh, S., *An experimental and numerical study of thermal stratification in a horizontal cylindrical solar storage tank.* Solar Energy, 1999. **66**(6): p. 409-421.
16. Andersen, E., et al., *Thermal destratification in small standard solar tanks due to mixing during tapping*, in *Proceedings of ISES 1999 Solar World Congress*. 1999.
17. Shah, L.J. and S. Furbo, *Entrance effects in solar storage tanks.* Solar Energy, 2003. **75**(4): p. 337-348.
18. Altuntop, N., et al., *Effect of obstacles on thermal stratification in hot water storage tanks.* Applied Thermal Engineering, 2005. **25**(14–15): p. 2285-2298.
19. Shah, L.J., E. Andersen, and S. Furbo, *Theoretical and experimental investigations of inlet stratifiers for solar storage tanks.* Applied Thermal Engineering, 2005. **25**(14–15): p. 2086-2099.
20. Furbo, S., et al., *Performance improvement by discharge from different levels in solar storage tanks.* Solar Energy, 2005. **79**(5): p. 431-439.
21. Panthalookaran, V., W. Heidemann, and H. Müller-Steinhagen, *A new method of characterization for stratified thermal energy stores.* Solar Energy, 2007. **81**(8): p. 1043-1054.
22. Andersen, E., S. Furbo, and J. Fan, *Multilayer fabric stratification pipes for solar tanks.* Solar Energy, 2007. **81**(10): p. 1219-1226.
23. Ievers, S. and W. Lin, *Numerical simulation of three-dimensional flow dynamics in a hot water storage tank.* Applied Energy, 2009. **86**(12): p. 2604-2614.
24. Palacios, E., et al., *Experimental analysis of solar thermal storage in a water tank with open side inlets.* Applied Energy, 2012. **89**(1): p. 401-412.
25. Fan, J. and S. Furbo, *Buoyancy driven flow in a hot water tank due to standby heat loss.* Solar Energy, 2012. **86**(11): p. 3438-3449.
26. De Césaro Oliveski, R., A. Krenzinger, and H.A. Vielmo, *Comparison between models for the simulation of hot water storage tanks.* Solar Energy, 2003. **75**(2): p. 121-134.
27. *Ansys Fluent 14.0 User's Guide*. 2011, Ansys, Inc.
28. Yaïci, W., et al., *Three-dimensional unsteady CFD simulations of a thermal storage tank performance for optimum design.* Applied Thermal Engineering, 2013. **60**(1–2): p. 152-163.
29. Castell, A., et al., *Dimensionless numbers used to characterize stratification in water tanks for discharging at low flow rates.* Renewable Energy, 2010. **35**(10): p. 2192-2199.
30. Versteeg, H.K., Malalasekera, W., *An introduction to computational fluid dynamics, the finite volume method.* 2007.
31. Matos, A.d., F.A.A. Pinho, and A. Silveira-Neto, *Large-eddy simulation of turbulent flow over a two-dimensional cavity with temperature fluctuations.* International Journal of Heat and Mass Transfer, 1999. **42**(1): p. 49-59.
32. Hou, T.Y., X. Hu, and F. Hussain, *Multiscale modeling of incompressible turbulent flows.* Journal of Computational Physics, 2013. **232**(1): p. 383-396.
33. Sato, Y., E. Deutsch, and O. Simonin, *Direct numerical simulations of heat transfer by solid particles suspended in homogeneous isotropic turbulence.* International Journal of Heat and Fluid Flow, 1998. **19**(2): p. 187-192.
34. Rodi, W., *DNS and LES of some engineering flows.* Fluid Dynamics Research, 2006. **38**(2–3): p. 145-173.
35. Ould-Rouiss, M., L. Redjem-Saad, and G. Lauriat, *Direct numerical simulation of turbulent heat transfer in annuli: Effect of heat flux ratio.* International Journal of Heat and Fluid Flow, 2009. **30**(4): p. 579-589.

36. Ahn, J., et al., *Direct numerical simulations of fully developed turbulent pipe flows for Reτ=180, 544 and 934.* International Journal of Heat and Fluid Flow, 2013. **44**(0): p. 222-228.
37. Yahya, S.M., S.F. Anwer, and S. Sanghi, *Performance of Different SGS Models of LES for Low Mach Number Channel Flow.* Procedia Engineering, 2012. **38**(0): p. 1192-1208.
38. Wegner, B., Y. Huai, and A. Sadiki, *Comparative study of turbulent mixing in jet in cross-flow configurations using LES.* International Journal of Heat and Fluid Flow, 2004. **25**(5): p. 767-775.
39. Popiolek, T.L., A.M. Awruch, and P.R.F. Teixeira, *Finite element analysis of laminar and turbulent flows using LES and subgrid-scale models.* Applied Mathematical Modelling, 2006. **30**(2): p. 177-199.
40. Fröhlich, J. and D. von Terzi, *Hybrid LES/RANS methods for the simulation of turbulent flows.* Progress in Aerospace Sciences, 2008. **44**(5): p. 349-377.
41. Gopalan, H., S. Heinz, and M.K. Stöllinger, *A unified RANS–LES model: Computational development, accuracy and cost.* Journal of Computational Physics, 2013. **249**(0): p. 249-274.
42. Spalart, P.R. and S.R. Allmaras, *A one-equation turbulence model for aerodynamic flows.* AIAA-Paper 92-0439.
43. Jaramillo, J.E., et al., *DNS and RANS modelling of a turbulent plane impinging jet.* International Journal of Heat and Mass Transfer, 2012. **55**(4): p. 789-801.
44. Yakhot, V., et al., *Development of turbulence models for shear flows by a double expansion technique.* Physics of Fluids A: Fluid Dynamics (1989-1993), 1992. **4**(7): p. 1510-1520.
45. Shih, T.-H., et al., *A new k-ϵ eddy viscosity model for high reynolds number turbulent flows.* Computers & Fluids, 1995. **24**(3): p. 227-238.
46. Menter, F.R., *Zonal two equation kappa-omega turbulence models for aerodynamic flows*. 1993, Linthicum Heights, MD: NASA Center for AeroSpace Information.
47. Park, T.S., H.J. Sung, and K. Suzuki, *Development of a nonlinear near-wall turbulence model for turbulent flow and heat transfer.* International Journal of Heat and Fluid Flow, 2003. **24**(1): p. 29-40.
48. Utyuzhnikov, S.V., *Domain decomposition for near-wall turbulent flows.* Computers & Fluids, 2009. **38**(9): p. 1710-1717.
49. Casey, M., Wintergerste, T., *Quality and Trust in Industrial CFD- Best Ptactice Guidelines,* . 2000, ERCOFTAC.
50. Craft, T.J., et al., *Development and application of wall-function treatments for turbulent forced and mixed convection flows.* Fluid Dynamics Research, 2006. **38**(2–3): p. 127-144.
51. Bricteux, L., et al., *Direct and large eddy simulation of turbulent heat transfer at very low Prandtl number: Application to lead–bismuth flows.* Nuclear Engineering and Design, 2012. **246**(0): p. 91-97.
52. Chandra, L. and G. Grötzbach, *Analysis and modelling of the turbulent diffusion of turbulent heat fluxes in natural convection.* International Journal of Heat and Fluid Flow, 2008. **29**(3): p. 743-751.
53. Lohse, R., *Einfluss von Beladeeinrichtungen auf die thermische Schichtung in Warmwasserspeichern*. 2009: Institute für Mechanik und Thermodynamik, Fakultät für Maschinenbau, TU Chemnitz (http://www.shaker.de/Online-Gesamtkatalog-Download/2013.05.06-20.10.10-129.13.72.198-radA4D48.tmp/3-8322-9203-9_INH.PDF).

54. Lohse, R., et al., *Be- und Entladesysteme für thermische Schichtenspeicher: Teil 2 – Untersuchungen des Beladeverhaltens.* Chemie Ingenieur Technik, 2008. **80**(7): p. 935-943.
55. Göppert, S., et al., *New computation method for stratification pipes of solar storage tanks.* Solar Energy, 2009. **83**(9): p. 1578-1587.
56. Göppert, S., Lohse. R., Urbaneck, T., Schirmer, U., Platzer, B., Bühl, J., Nilius, A., *Weiterentwicklung und Optimierung von Be- und Entladesystemen für Tank- und Erdbeckenspeicher.* 2008: Technische Universität Chemnitz,Technische Universität Ilmenau.
57. Xu, W., et al., *Numerical investigation on the flow characteristics and permeability of three-dimensional reticulated foam materials.* Chemical Engineering Journal, 2008. **140**(1–3): p. 562-569.
58. Boomsma, K., D. Poulikakos, and Y. Ventikos, *Simulations of flow through open cell metal foams using an idealized periodic cell structure.* International Journal of Heat and Fluid Flow, 2003. **24**(6): p. 825-834.
59. Hasert, M., J. Bernsdorf, and S. Roller, *Lattice Boltzmann Simulation of non-Darcy Flow in Porous Media.* Procedia Computer Science, 2011. **4**(0): p. 1048-1057.
60. Zhong, W., et al., *Determination of flow rate characteristics of porous media using charge method.* Flow Measurement and Instrumentation, 2011. **22**(3): p. 201-207.
61. Gnielinski, V., *Heat Exchanger Design Handbook.* 1983, New York: Hemisphere Publishing Corporation.
62. Innocentini, M.D.M., et al., *Prediction of ceramic foams permeability using Ergun's equation.* Materials Research-ibero-american Journal of Materials, 1999. **2**(4).
63. Zurigat, Y.H., A.J. Ghajar, and P.M. Moretti, *Stratified thermal storage tank inlet mixing characterization.* Applied Energy, 1988. **30**(2): p. 99-111.
64. Chung, J.D., et al., *The effect of diffuser configuration on thermal stratification in a rectangular storage tank.* Renewable Energy, 2008. **33**(10): p. 2236-2245.
65. Zachár, A., I. Farkas, and F. Szlivka, *Numerical analyses of the impact of plates for thermal stratification inside a storage tank with upper and lower inlet flows.* Solar Energy, 2003. **74**(4): p. 287-302.
66. Feuerstein, F., *Experimentelle Untersuchung von thermischen Schichtspeichern mittels optischer Strömungsvisualisierungsverfahren, Bachground Oriented Schlieren (BOS).* Diplomarbeit, April 2013: Fachgebiet Strömungsmaschinen , Karlsruher Institut für Technologie (KIT), Karlsruhe, Germany.
67. Berg, A., *Numerical and experimental study of the fluid flow in porous medium in charging process of stratified thermal storage tank.* Master thesis, April 2013, Royal Institute of Technology (KTH): School of Industrial Engineering and Management, Division of Applied Thermodynamics and Refrigeration, Stockholm, Sweden.
68. García-Marí, E., et al., *A new inlet device that enhances thermal stratification during charging in a hot water storage tank.* Applied Thermal Engineering, 2013. **61**(2): p. 663-669.
69. Schmidt, F., *Entwicklungspotenzial thermisch angetriebener Wärmepumpen.* 2012, Jahrestagung KIT-Zentrum Energie.
70. Andersen, E., et al., *Investigations on stratification devices for hot water heat stores.* International Journal of Energy Research, 2008. **32**(3): p. 255-263.
71. *Firma Sailer, Sailer Einschichtvorrichtung, 2010*

72. Kaminski, E., S. Tait, and G. Carazzo, *Turbulent entrainment in jets with arbitrary buoyancy.* Journal of Fluid Mechanics, 2005. **526**(-1): p. 361-376.

73. *Produktinformationen zu Marlotherm SH, Marlotherm LH (Datenblatt)*. 2004, Firma Sasol: http://www.marlotherm.com/pdf/MARLOTHERM_SH_GB.pdf, http://www.marlotherm.com/pdf/MARLOTHERM_LH_GB.pdf
74. Göppert, S., et al., *Be- und Entladesysteme für thermische Schichtenspeicher: Teil 1 – Überblick.* Chemie Ingenieur Technik, 2008. **80**(3): p. 287-293.
75. Steinert, P., S. Göppert, and B. Platzer, *Transient calculation of charge and discharge cycles in thermally stratified energy storages.* Solar Energy, 2013. **97**(0): p. 505-516.
76. Ribas Tugores, C., *Analysis of design variations of an inlet stratification pipe for application in thermal storage tanks.* Master thesis, September 2012: Karlsruhe Institute of Technology (KIT), Department of Mechanical Engineering, Institute of Fluid Machinery.
77. Antohe, B.V. and J.L. Lage, *A general two-equation macroscopic turbulence model for incompressible flow in porous media.* International Journal of Heat and Mass Transfer, 1997. **40**(13): p. 3013-3024.
78. Nimvari, M.E., et al., *Numerical simulation of turbulent reacting flow in porous media using two macroscopic turbulence models.* Computers & Fluids, 2013. **88**(0): p. 232-240.
79. Nakayama, A. and F. Kuwahara, *A Macroscopic Turbulence Model for Flow in a Porous Medium.* Journal of Fluids Engineering, 1999. **121**(2): p. 427-433.
80. Kuwahara, F., T. Yamane, and A. Nakayama, *Large eddy simulation of turbulent flow in porous media.* International Communications in Heat and Mass Transfer, 2006. **33**(4): p. 411-418.

List of Figures

List of Tables

Appendix

Appendix A: Equations

$k-\varepsilon$ Turbulence Model

$$\frac{\partial}{\partial t}(\rho k)+\frac{\partial}{\partial x_j}(\rho k u_j)=\frac{\partial}{\partial x_j}\left[\left(\mu+\frac{\mu_t}{\sigma_k}\right)\frac{\partial k}{\partial x_j}\right]+G_k+G_b-\rho\varepsilon-\mathrm{Y}_k+S_k$$

$$\frac{\partial}{\partial t}(\rho \varepsilon)+\frac{\partial}{\partial x_j}(\rho \varepsilon u_j)=\frac{\partial}{\partial x_j}\left[\left(\mu+\frac{\mu_t}{\sigma_\varepsilon}\right)\frac{\partial \varepsilon}{\partial x_j}\right]+C_{1\varepsilon}\frac{\varepsilon}{k}(G_k+C_{3\varepsilon}G_b)-C_{2\varepsilon}\rho\frac{\varepsilon^2}{k}+S_\varepsilon$$

$k-\varepsilon$ Turbulence Model Constants

$C_{1\varepsilon}$	$C_{2\varepsilon}$	$C_{3\varepsilon}$	C_μ	σ_k	σ_ε	σ_t
1.44	1.92	2.89	0.09	1.00	1.3	0.9

$k-\omega$ Turbulence Model

$$\frac{\partial}{\partial t}(\rho k)+\frac{\partial}{\partial x_i}(\rho k u_i)=\frac{\partial}{\partial x_j}\left[\Gamma_k\frac{\partial k}{\partial x_j}\right]+G_k-\mathrm{Y}_k+S_k$$

$$\frac{\partial}{\partial t}(\rho \omega)+\frac{\partial}{\partial x_i}(\rho \omega u_i)=\frac{\partial}{\partial x_j}\left[\Gamma_\omega\frac{\partial \omega}{\partial x_j}\right]+G_\omega-\mathrm{Y}_\omega+S_\omega$$

$$\mu_t = \rho.\frac{k}{\omega}$$

$$\Gamma_k = \mu + \frac{\mu_t}{\sigma_k}$$

$$\Gamma_\omega = \mu + \frac{\mu_t}{\sigma_\omega}$$

$$\mu_t = a^*\frac{\rho k}{\omega}$$

The ω-equation in SST $k-\omega$ model

$$\frac{\partial}{\partial t}(\rho\omega)+\frac{\partial}{\partial x_i}(\rho\omega u_i)=\frac{\partial}{\partial x_j}\left[\Gamma_\omega\frac{\partial\omega}{\partial x_j}\right]+G_\omega-Y_\omega+D_w+S_\omega$$

Reynolds stress model (RSM)

$$\begin{aligned}&\underbrace{\frac{\partial}{\partial t}\left(\rho\overline{\acute{u}_i\acute{u}_j}\right)}_{Local\ time\ derivative}+\underbrace{\frac{\partial}{\partial x_k}\left(\rho u_k\overline{\acute{u}_i\acute{u}_j}\right)}_{convection}\\
&=\underbrace{-\frac{\partial}{\partial x_k}\left[\rho\overline{\acute{u}_i\acute{u}_j\acute{u}_k}+\overline{\acute{p}\left(\delta_{kj}\acute{u}_i+\delta_{ik}\acute{u}_j\right)}\right]}_{Turbulent\ Diffusion}\\
&+\underbrace{\frac{\partial}{\partial x_k}\left[\mu\frac{\partial}{\partial x_k}\left(\overline{\acute{u}_i\acute{u}_j}\right)\right]}_{Molecular\ Diffusion}\underbrace{-\rho\left(\overline{\acute{u}_i\acute{u}_k}\frac{\partial u_j}{\partial x_k}+\overline{\acute{u}_j\acute{u}_k}\frac{\partial u_i}{\partial x_k}\right)}_{Stress\ Production}\underbrace{-\rho\beta\left(g_i\overline{\acute{u}_j\theta}+g_j\overline{\acute{u}_i\theta}\right)}_{Buoyancy\ Production}\\
&+\underbrace{\overline{\acute{p}\left(\frac{\partial\acute{u}_i}{\partial x_j}+\frac{\partial\acute{u}_j}{\partial x_i}\right)}}_{Pressure\ Strain}-\underbrace{2\mu\overline{\frac{\partial\acute{u}_i}{\partial x_k}\frac{\partial\acute{u}_j}{\partial x_k}}}_{Dissipation}\underbrace{-2\rho\Omega_k\left(\overline{\acute{u}_j\acute{u}_m}\varepsilon_{ikm}+\overline{\acute{u}_i\acute{u}_m}\varepsilon_{jkm}\right)}_{Production\ by\ System\ Rotation}\\
&+User\ defined\ source\ term\end{aligned}$$

Modified transport equation for the turbulent dissipation rate in realizable $k-\varepsilon$ model

$$\frac{\partial}{\partial t}(\rho\varepsilon)+\frac{\partial}{\partial x_j}(\rho\varepsilon u_j)=\frac{\partial}{\partial x_j}\left[\left(\mu+\frac{\mu_t}{\sigma_\varepsilon}\right)\frac{\partial\varepsilon}{\partial x_j}\right]+\rho C_1S\varepsilon-\rho C_2\frac{\varepsilon^2}{k+\sqrt{\nu\varepsilon}}+C_{1\varepsilon}\frac{\varepsilon}{k}C_{3\varepsilon}G_b+S_\varepsilon$$

$$C_1=\max\left[0.43,\frac{\eta}{\eta+5}\right],\eta=S\frac{k}{\varepsilon},S=\sqrt{2S_{ij}S_{ij}}\quad S_{ij}=\frac{1}{2}\left(\frac{\partial U_j}{\partial x_i}+\frac{\partial U_i}{\partial x_j}\right)$$

Profile function of inlet stratification pipe channel geometry

$$\begin{aligned}y_1&=-\frac{92}{9}-\frac{20}{3}a-\frac{40}{9}b\\
&\quad+x\left[\frac{64}{3}+6a+\frac{17}{3}b+x\left[-8-\frac{7}{4}a-\frac{9}{4}b+\left(\frac{8}{9}+\frac{5}{30}a+\frac{25}{90}b\right)x\right]\right]\end{aligned}$$

For $x \leq 4$

$$y_2=4+\left[b+\left(\frac{1}{3}.\left(\frac{-4}{3}-b\right)+\frac{1}{3}.\left(\frac{4}{9}+\frac{1}{3}.\left(\frac{4}{3}+b\right)\right)\right).(-7+x)\right).(-4+x)\right].(-4+x)$$

For $x \geq 4$

UDF for calculation of effective thermal conductivity due to advection in storage tank

```
/*******************************************************************
***
   The following code provides the parameters for calculation of
effective thermal conductivity due to advection effect in charging
process of a thermal storage tank applied in adsorption heat pump
cycle. The required parameters for calculation are stored in user-
defined memory and after post-processing in Ansys Fluent are used to
calculate the effective thermal conductivity.
*******************************************************************
***/

#include "udf.h"

DEFINE_ON_DEMAND(Keff)
{
   Domain *d; /* declaration of domain as a variable */

   /* type declaration of variables */

   real temp;
   real volume;
   real vol_tot;
   real vol3d;
   real vol_tot3d;
   real u;
   real v;
   real cp;
   real dens;
   float tempgrd_x;
   float tempgrd_y;
   double udtx;
   double udty;
   double udt_tot;
   double conv;
   double Q;


   /* definition of the variable PI as Pi number*/

 #define PI 3.1415926

  /* access the information about the cell zones by pointer to cell
thread */

   Thread *t;
   cell_t c;
   d = Get_Domain(1);     /* Get the fluid domain pointer using
ANSYS FLUENT utility */

   /* Looping over all cell threads in the fluid domain */

   thread_loop_c(t,d)
     {
     /* getting cell flow variables using cell macros*/
```

```
     /* Looping over all cells  */
     begin_c_loop(c,t)
       {
         volume = C_VOLUME(c,t);
         temp = C_T(c,t);
         dens = C_R(c,t);
         cp = C_CP(c,t);
         u = C_U(c,t);
         v = C_V(c,t);
         vol_tot += volume;
         vol_tot3d = (2*PI*vol_tot);




     /* getting flow variable reconstruction gradient using RG
vector macros*/
      /* Looping over all cells  */


         tempgrd_x = C_T_G(c,t)[0]; /* get cell temperature gradient
in X direction */
         tempgrd_y = C_T_G(c,t)[1]; /* get cell temperature gradient
in Y direction */


       /* calculation of required parameters*/


         vol3d = (2*PI*volume);
         udtx = (u*tempgrd_x);
          udty = (v*tempgrd_y);
          udt_tot= udtx+udty;

   /* calculation of advective heat transfer*/

         conv = fabs(vol3d*udt_tot);
         Q = (dens*cp*conv);

          /* store the parameters in user defined memory*/

         C_UDMI(c,t,0) = Q;
         C_UDMI(c,t,1) = tempgrd_x;

       }
       end_c_loop(c,t)
     }
}
```

Appendix B: Additional results

Additional results of the simulation of storage tank without stratification device

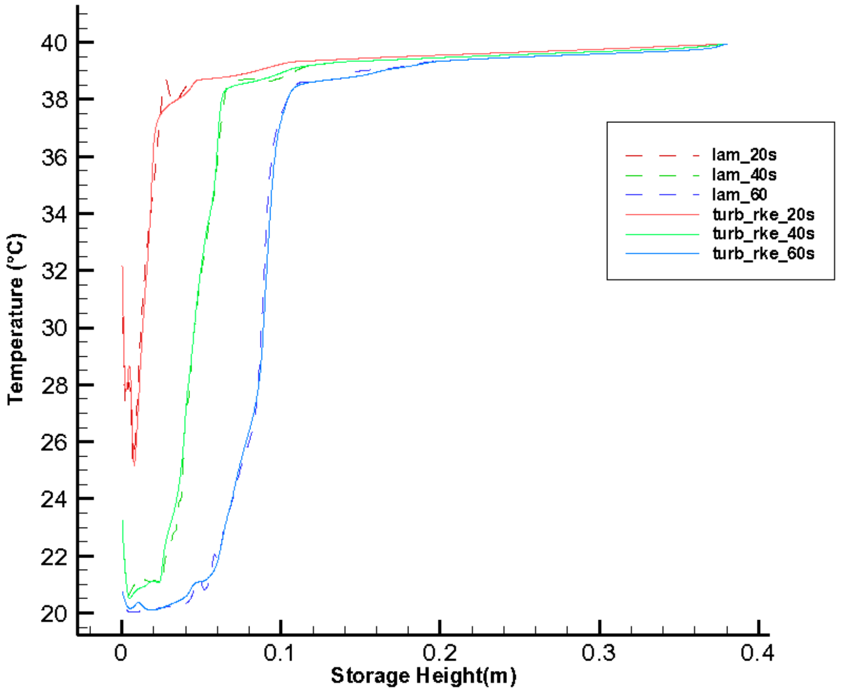

Average temperature distribution in laminar and turbulent simulation with realizable $k-\varepsilon$ model for ΔT= 20 K (simulation according to experimental setup)

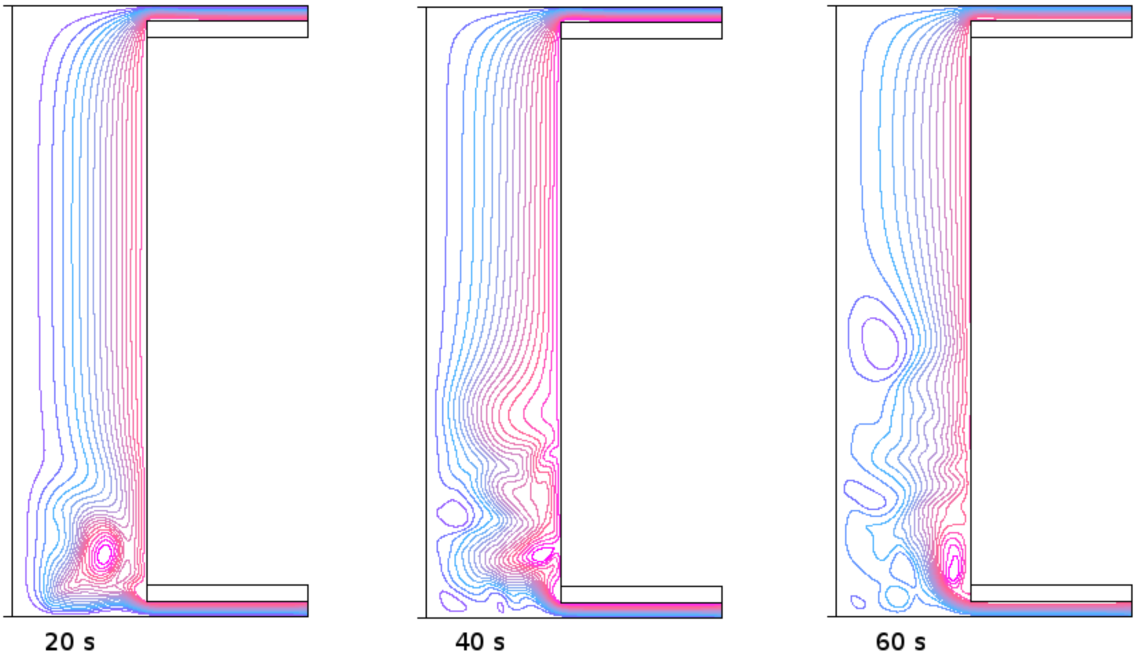

Streamline for charging flow of 3 lpm in laminar simulation at different charging times for ΔT= 5 K (simulation according to experimental setup)

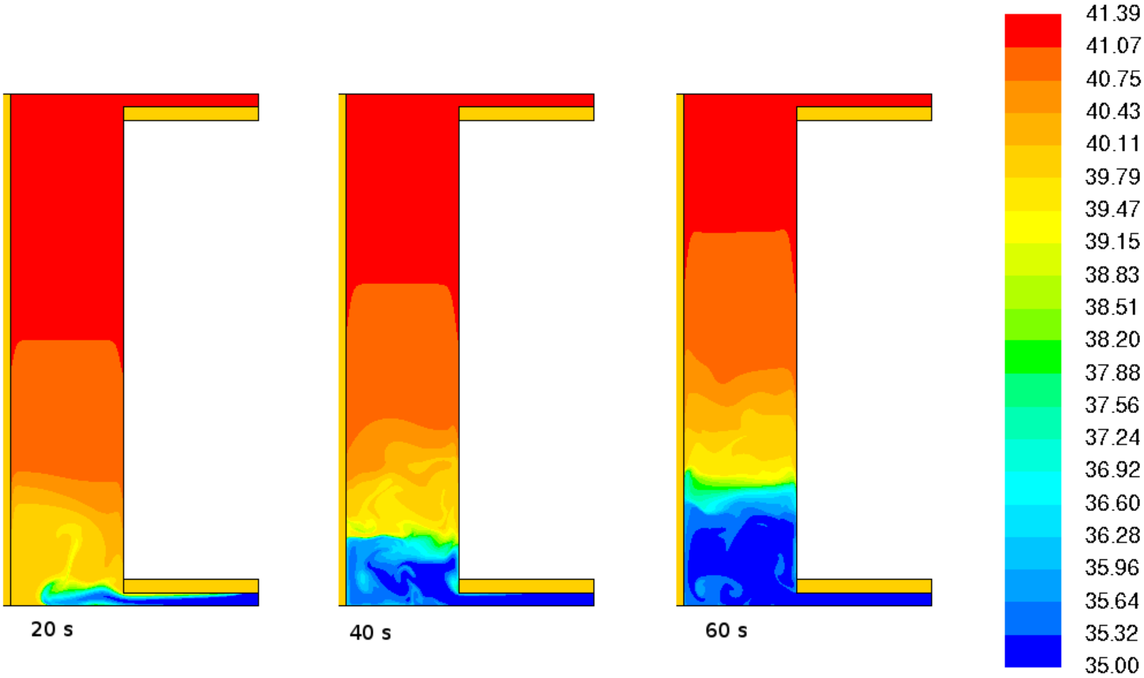

20 s 40 s 60 s

Temperature contours (°C) at different charging times for laminar simulation for ΔT= 5 K

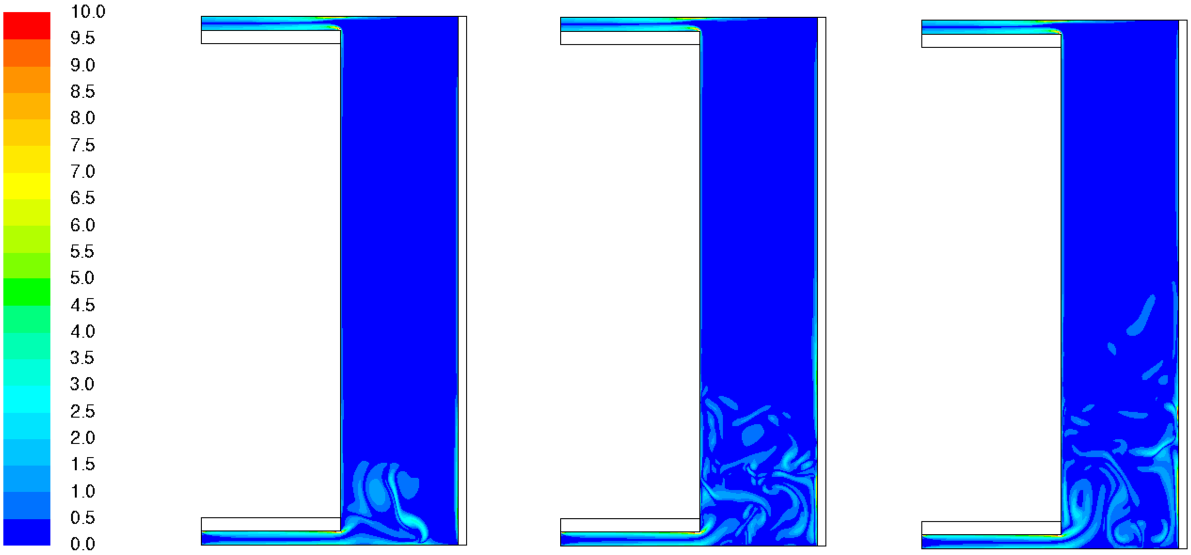

20 s 40 s 60 s

Vorticity contours (1/s) for charging with 3 lpm in laminar simulation for ΔT= 5 K

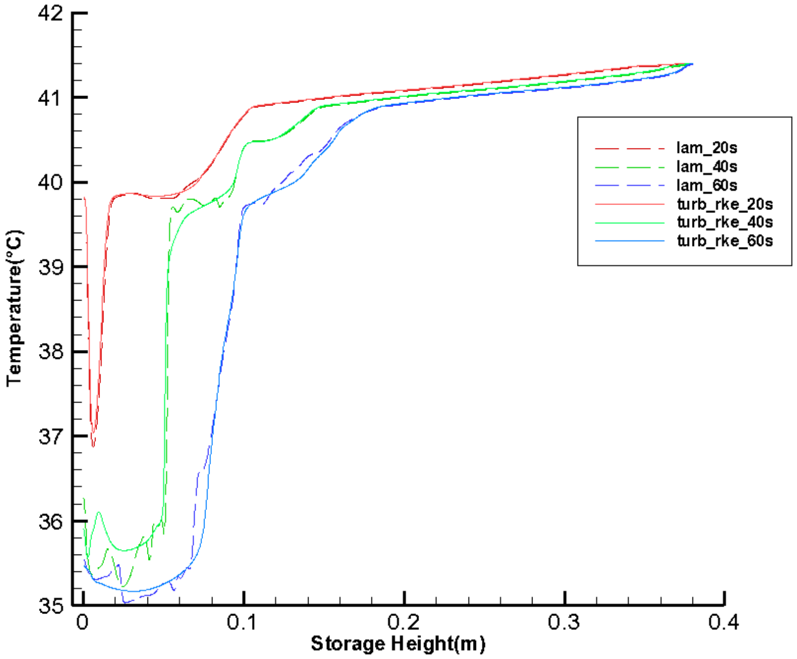

Temperature comparison between laminar and turbulent calculation with realizable $k-\varepsilon$ model in vertical direction with 3 cm distance from central axis of the storage tank at the temperature sensors position for ΔT=5 K

Additional results of simulation of storage tank with inlet stratification pipe

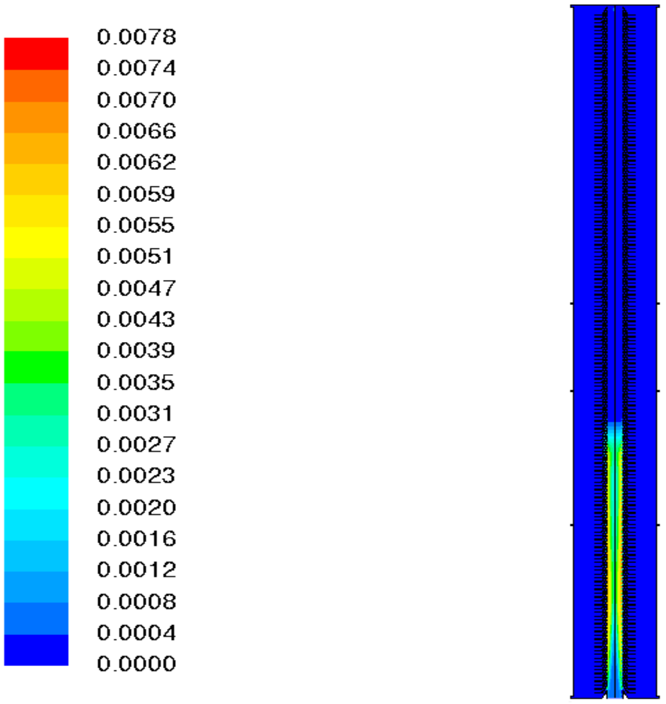

Turbulent kinetic energy ($\frac{m^2}{s^2}$) contour after 4 s charging with 0.2 kg/s mass flow rate and 119 °C in stratified storage tank with initial linear stratification from 38 °C at the bottom to 200 °C at the top (applied turbulence model: realizable $k-\varepsilon$)

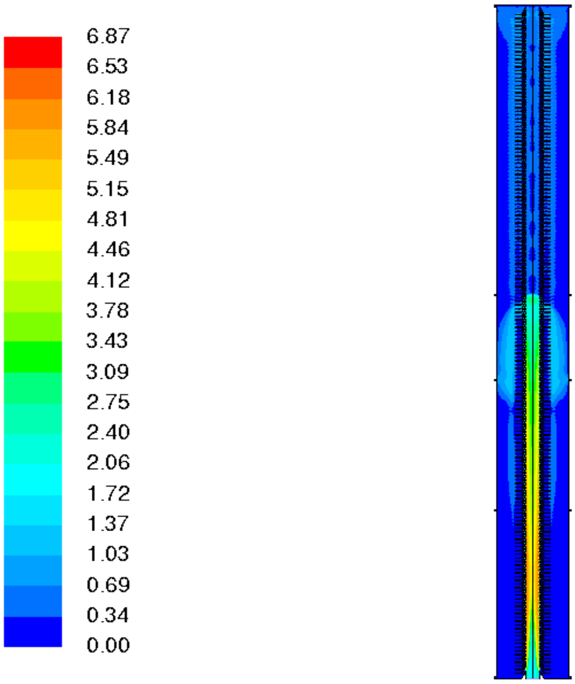

Turbulent intensity contour (-) after 1 minute charging with 0.2 kg/s charging mass flow rate (simulation with realizable $k-\varepsilon$ model)

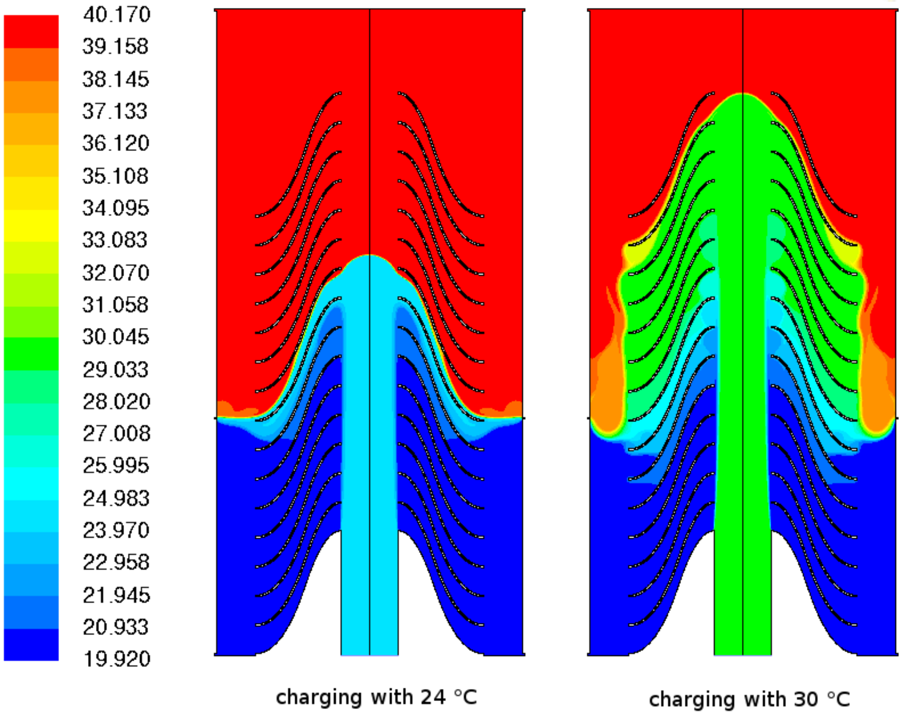

charging with 24 °C

charging with 30 °C

Temperature contour (°C) for charging with 24 °C and 30 °C in laminar simulation of TES with modified geometry of the stratification pipe (a=0, b= -3, c=15)

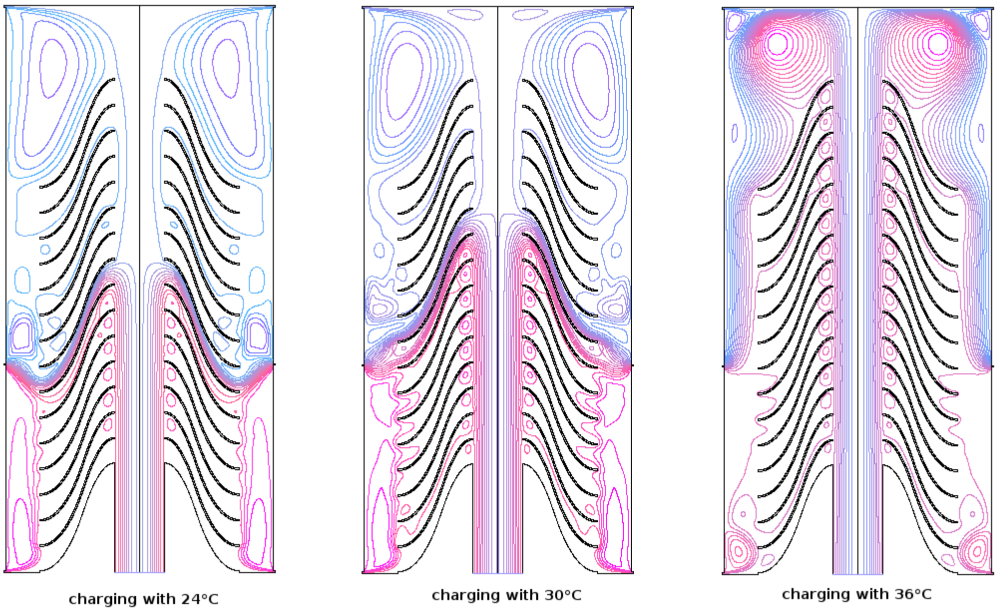
charging with 24°C

charging with 30°C

charging with 36°C

Streamline for different charging flow temperatures in turbulent simulation with realizable $k - \varepsilon$ model (a=0, b= -3, c=15)

Additional results of the simulation of storage tank with free jet charging and free jet charging with implemented foam

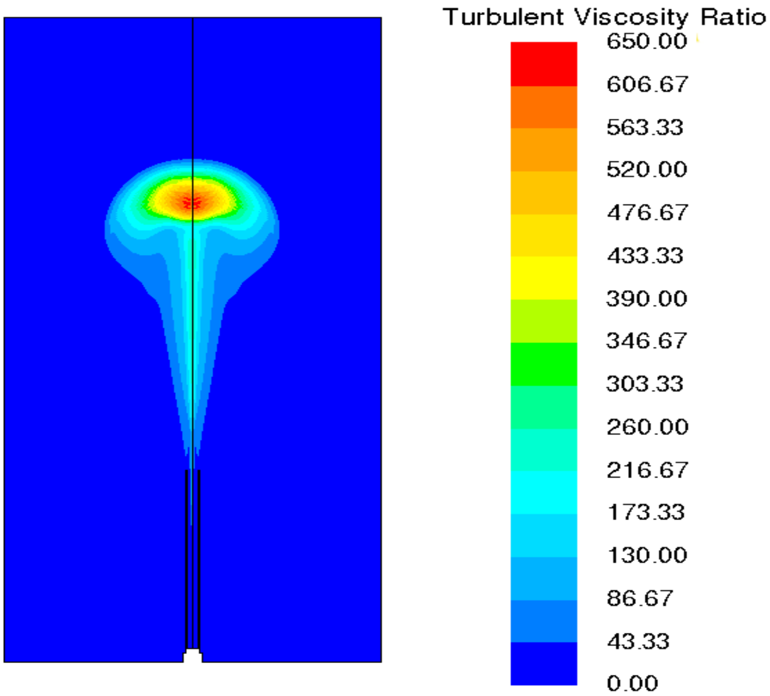

Turbulent viscosity ratio (-) calculated for charging with 40 °C after 20 s charging time with realizable $k - \varepsilon$ model

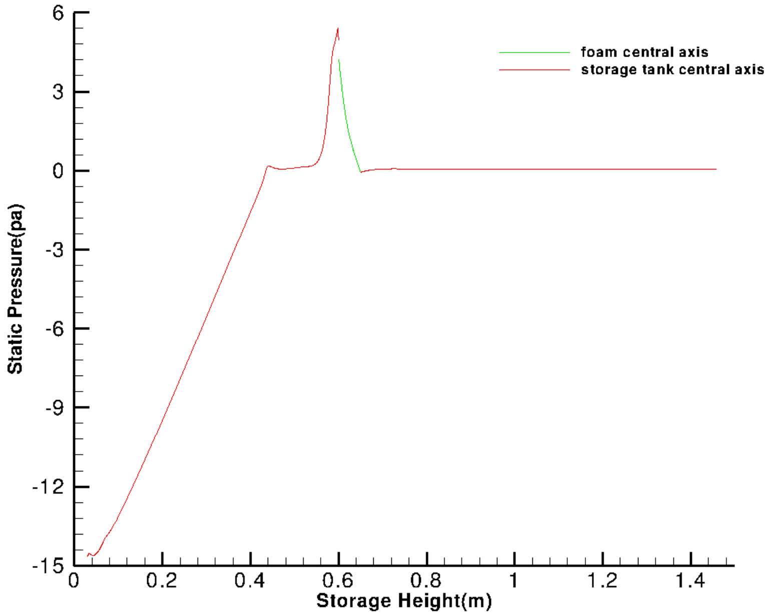

Pressure distribution along the central axis of the storage tank (red) and central axis inside of the foam(green) after 20 s charging with 40 °C in simulation with realizable $k-\varepsilon$ model (storage tank initial temperature: 20 °C)

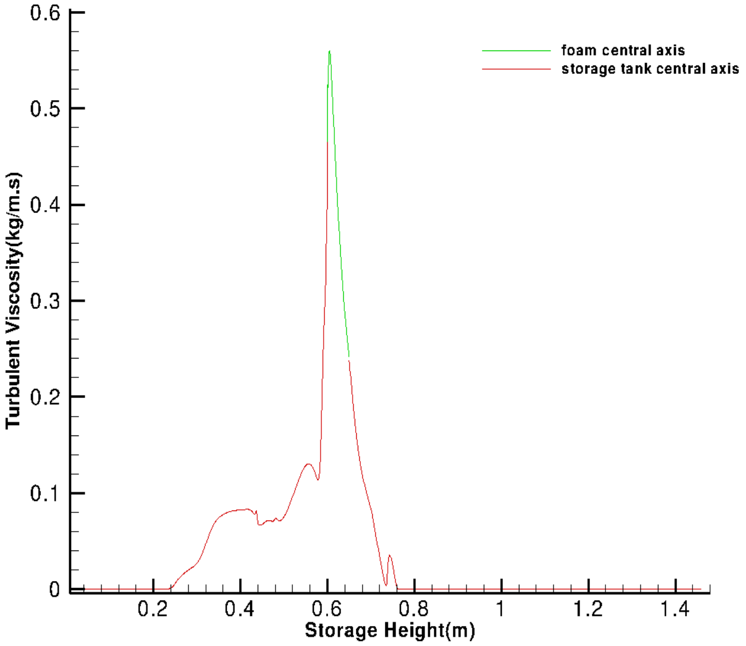

Turbulent eddy viscosity distribution along the central axis of the storage tank (red) and central axis inside of the foam (green) after 20 s charging with 40 °C in simulation with realizable $k-\varepsilon$ model (storage tank initial temperature: 20 °C)

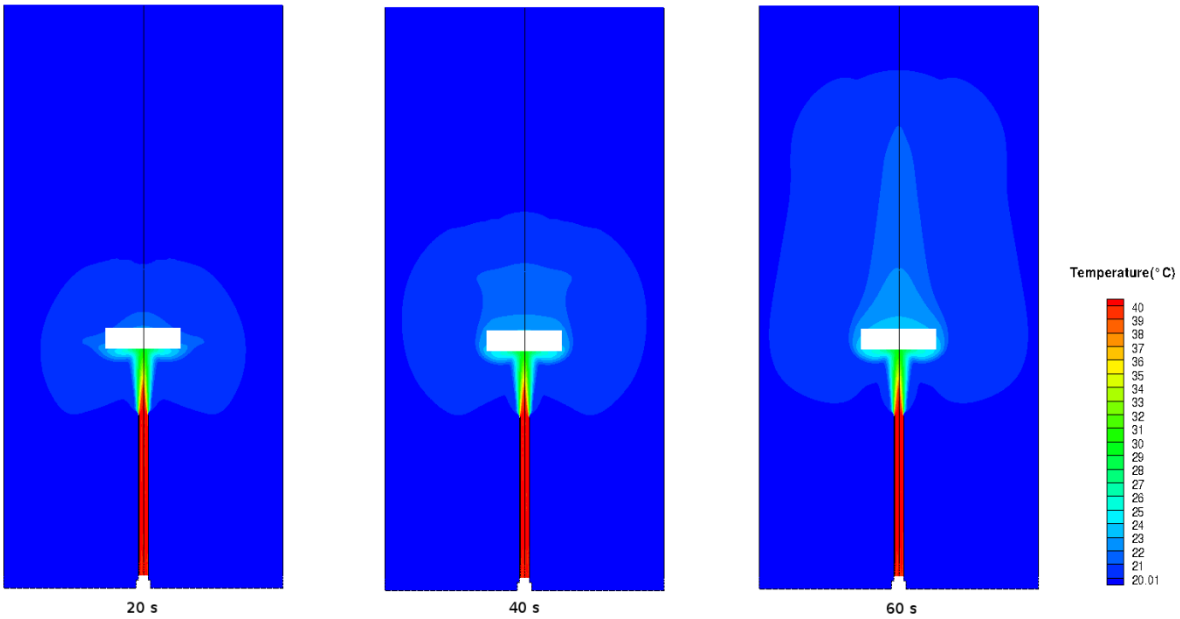

Temperature contours for different charging times in simulation with Reynolds stress model

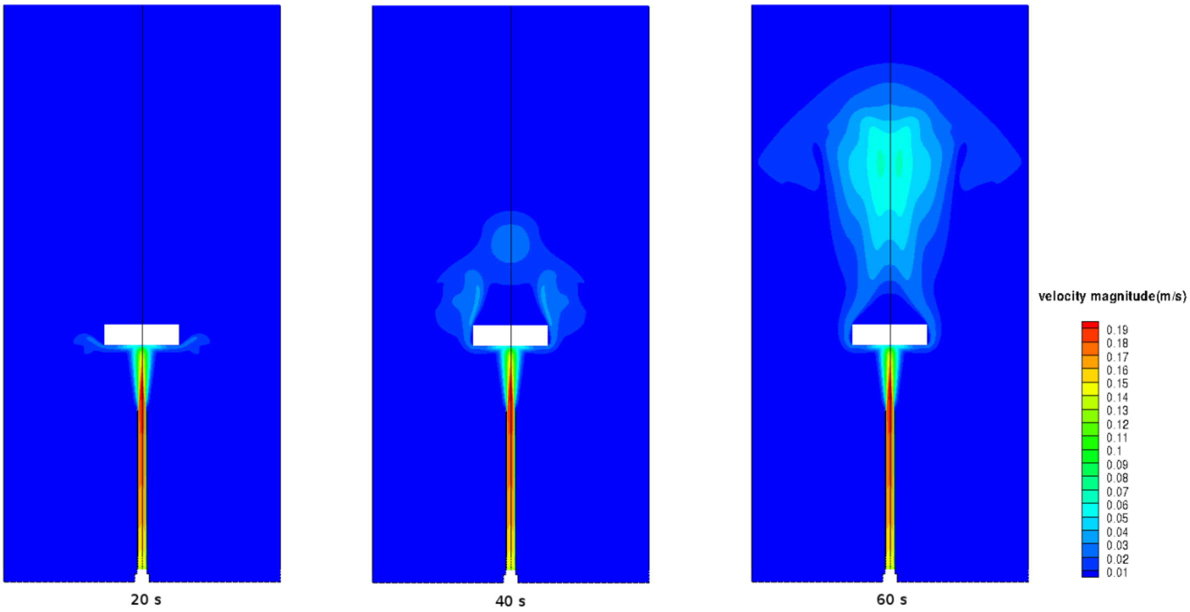

Velocity contours for different charging times in simulation with Reynolds-stress model

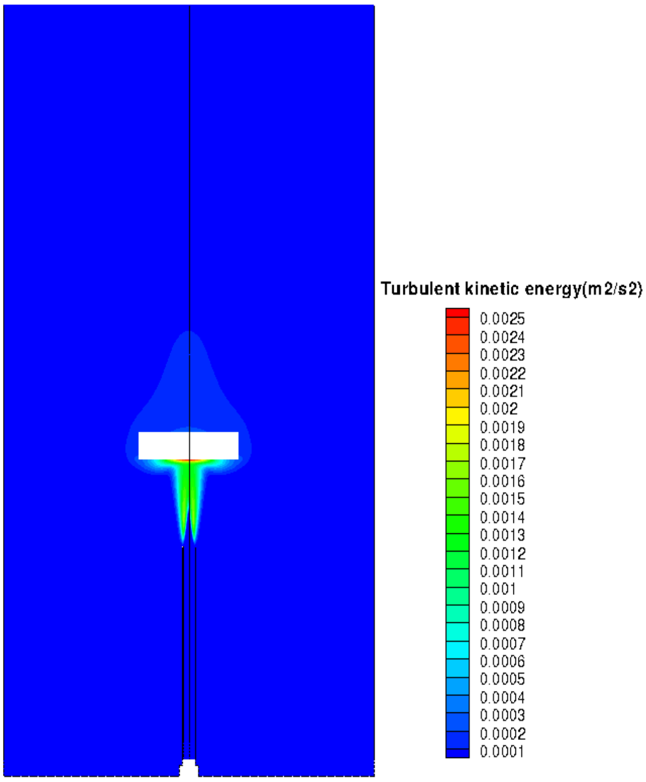

Turbulent kinetic energy after 60 s charging in simulation with Reynolds stress model

Appendix C: Technical data sheets

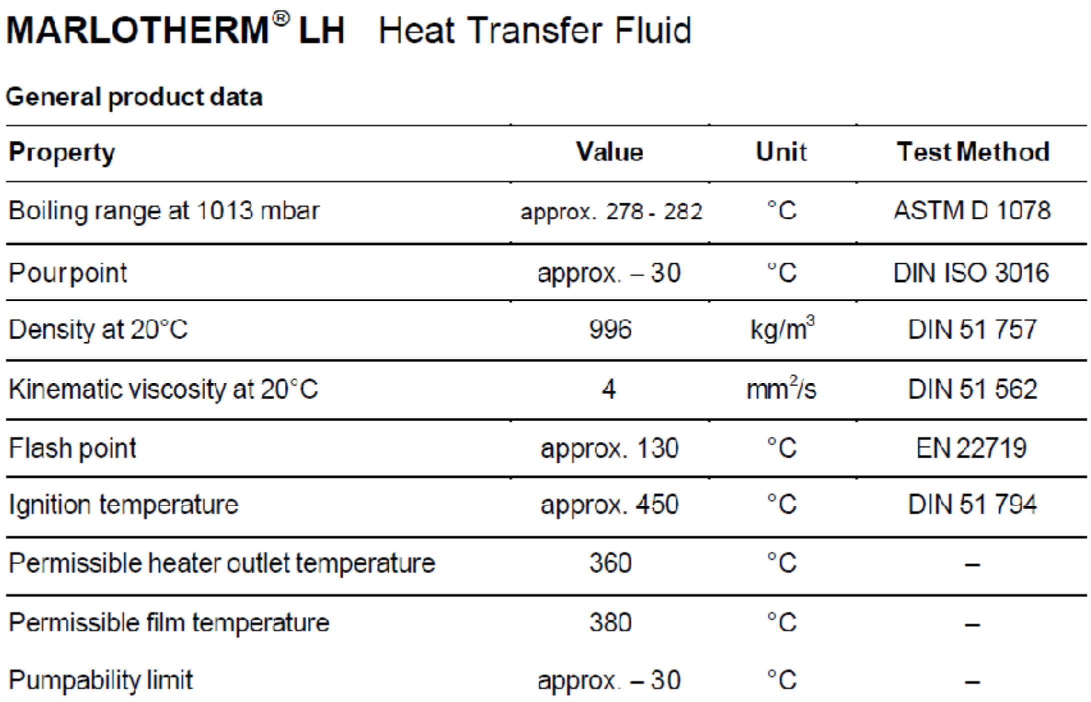

MARLOTHERM® LH Heat Transfer Fluid

General product data

Property	**Value**	**Unit**	**Test Method**
Boiling range at 1013 mbar	approx. 278 - 282	°C	ASTM D 1078
Pourpoint	approx. – 30	°C	DIN ISO 3016
Density at 20°C	996	kg/m^3	DIN 51 757
Kinematic viscosity at 20°C	4	mm^2/s	DIN 51 562
Flash point	approx. 130	°C	EN 22719
Ignition temperature	approx. 450	°C	DIN 51 794
Permissible heater outlet temperature	360	°C	–
Permissible film temperature	380	°C	–
Pumpability limit	approx. – 30	°C	–

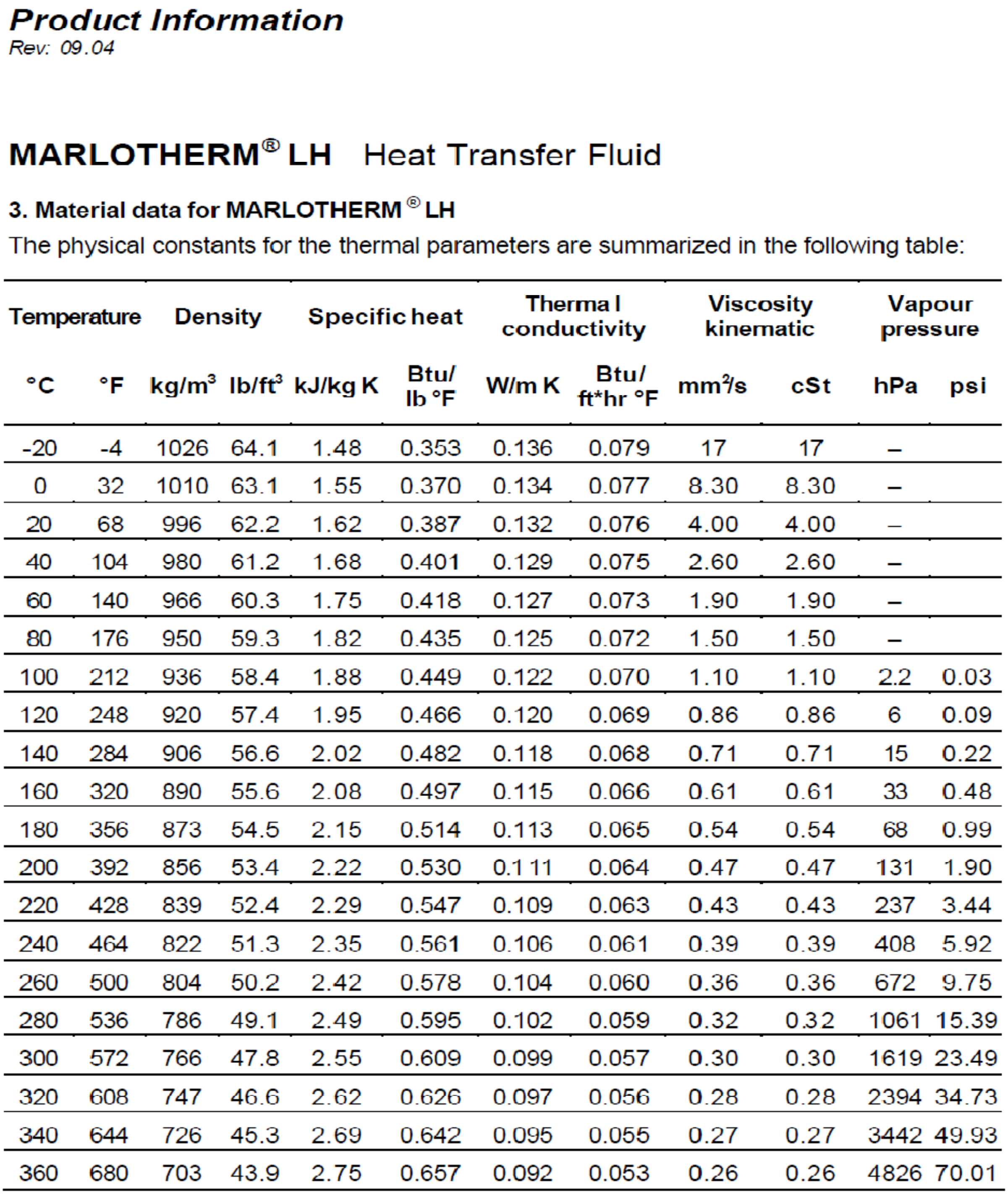

Product Information

Rev: 09.04

MARLOTHERM® LH Heat Transfer Fluid

3. Material data for MARLOTHERM® LH

The physical constants for the thermal parameters are summarized in the following table:

Temperature		**Density**		**Specific heat**		**Thermal conductivity**		**Viscosity kinematic**		**Vapour pressure**	
°C	**°F**	**kg/m³**	**lb/ft³**	**kJ/kg K**	**Btu/ lb °F**	**W/m K**	**Btu/ ft*hr °F**	**mm²/s**	**cSt**	**hPa**	**psi**
-20	-4	1026	64.1	1.48	0.353	0.136	0.079	17	17	–	
0	32	1010	63.1	1.55	0.370	0.134	0.077	8.30	8.30	–	
20	68	996	62.2	1.62	0.387	0.132	0.076	4.00	4.00	–	
40	104	980	61.2	1.68	0.401	0.129	0.075	2.60	2.60	–	
60	140	966	60.3	1.75	0.418	0.127	0.073	1.90	1.90	–	
80	176	950	59.3	1.82	0.435	0.125	0.072	1.50	1.50	–	
100	212	936	58.4	1.88	0.449	0.122	0.070	1.10	1.10	2.2	0.03
120	248	920	57.4	1.95	0.466	0.120	0.069	0.86	0.86	6	0.09
140	284	906	56.6	2.02	0.482	0.118	0.068	0.71	0.71	15	0.22
160	320	890	55.6	2.08	0.497	0.115	0.066	0.61	0.61	33	0.48
180	356	873	54.5	2.15	0.514	0.113	0.065	0.54	0.54	68	0.99
200	392	856	53.4	2.22	0.530	0.111	0.064	0.47	0.47	131	1.90
220	428	839	52.4	2.29	0.547	0.109	0.063	0.43	0.43	237	3.44
240	464	822	51.3	2.35	0.561	0.106	0.061	0.39	0.39	408	5.92
260	500	804	50.2	2.42	0.578	0.104	0.060	0.36	0.36	672	9.75
280	536	786	49.1	2.49	0.595	0.102	0.059	0.32	0.32	1061	15.39
300	572	766	47.8	2.55	0.609	0.099	0.057	0.30	0.30	1619	23.49
320	608	747	46.6	2.62	0.626	0.097	0.056	0.28	0.28	2394	34.73
340	644	726	45.3	2.69	0.642	0.095	0.055	0.27	0.27	3442	49.93
360	680	703	43.9	2.75	0.657	0.092	0.053	0.26	0.26	4826	70.01

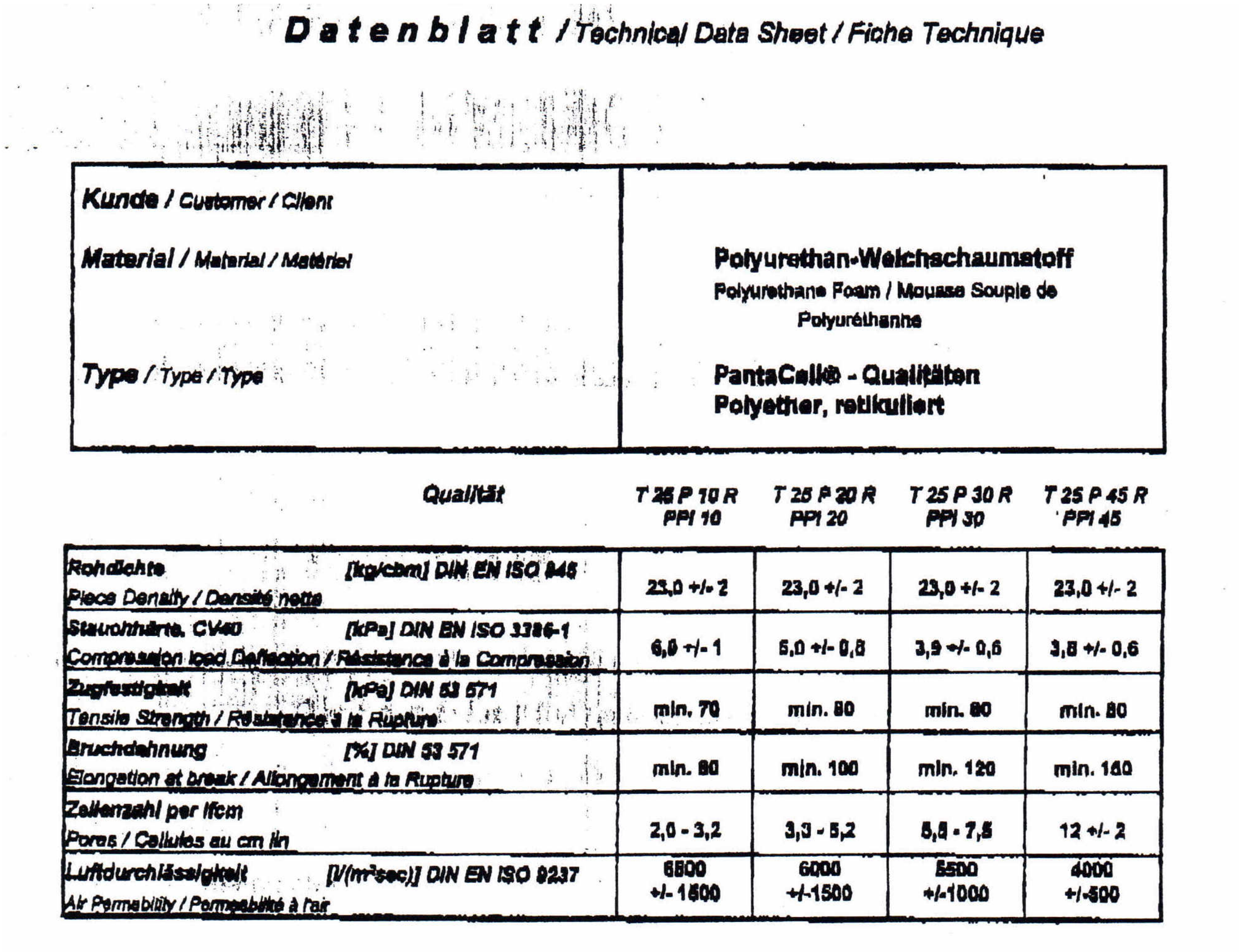

Datenblatt / Technical Data Sheet / Fiche Technique

Kunde / Customer / Client	
Material / Material / Matériel	**Polyurethan-Weichschaumstoff** Polyurethane Foam / Mousse Souple de Polyuréthanne
Type / Type / Type	**PantaCell® - Qualitäten** **Polyether, retikuliert**

Qualität	*T 25 P 10 R* *PPI 10*	*T 25 P 20 R* *PPI 20*	*T 25 P 30 R* *PPI 30*	*T 25 P 45 R* *PPI 45*
Rohdichte [kg/cbm] DIN EN ISO 845 *Piece Density / Densité nette*	23,0 +/- 2	23,0 +/- 2	23,0 +/- 2	23,0 +/- 2
Stauchhärte, CV40 [kPa] DIN EN ISO 3386-1 *Compression load Deflection / Résistance à la Compression*	6,0 +/- 1	5,0 +/- 0,8	3,9 +/- 0,6	3,8 +/- 0,6
Zugfestigkeit [kPa] DIN 53 571 *Tensile Strength / Résistance à la Rupture*	min. 70	min. 80	min. 80	min. 80
Bruchdehnung [%] DIN 53 571 *Elongation at break / Allongement à la Rupture*	min. 80	min. 100	min. 120	min. 140
Zellenzahl per lfcm *Pores / Cellules au cm lin*	2,0 - 3,2	3,3 - 5,2	5,5 - 7,5	12 +/- 2
Luftdurchlässigkeit [l/(m²sec)] DIN EN ISO 9237 *Air Permability / Perméabilité à l'air*	6500 +/- 1500	6000 +/-1500	5500 +/-1000	4000 +/-500